Theory of the microfluidic channel angular accelerometer for inertial measurement applications

by

H. Jurgens Wolfaardt

A dissertation submitted in partial fulfillment of
the requirements for the degree of
Master of Engineering (Mechanical)
University of Pretoria
2005

Supervisor : Prof. P. S. Heyns
Department : Mechanical and Aeronautical Engineering

Summary

The angular accelerometer is a versatile inertial instrument with applications ranging from stabilization to navigation and satellite pointing. The performance state-of-the-art in angular accelerometry is set by the large fluid-rotor concept with low bandwidth while Micro-Electromechanical System (MEMS) angular accelerometers offer a compact lower accuracy option. A novel angular accelerometer is proposed by the author to improve on contemporary angular accelerometers and MEMS gyroscopes. The sensor consists of spiral channels micromachined into multiple wafers to construct a spiral helix fluid column with high angular pressure generating potential. The two ends of the fluid column are joined at a central measurement chamber where a diaphragm-based pressure transducer outputs a signal proportional to the applied angular acceleration. The objective of this research is to derive and synthesize the theory necessary for simulation of the sensor and thereafter investigate the potential of the sensor. A wave speed corrected discrete multi degree of freedom model simulates pressure generation and -propagation. The pressure theory is verified by means of a 200mm diameter spool using 3mm polyurethane tubing with diesel or water as the inertial fluid. Accelerations of up to 480rad/s^2 are imposed on 1.5m and 20m tube lengths using a rate table and the generated pressure sampled at 2kHz. Channel flow is simulated by means of a model directly derived from Szymanski's unsteady laminar flow theory, while the pressure transducer diaphragm model is based on linear flat plate theory. Two pressure transducers are studied, the strain-gaged plain circular diaphragm and a piezo-based transducer with an annular diaphragm. All sensor theory is synthesized into a linear sensor model and the dynamic response optimized by means of the Kuhn-Tucker method. The application of the optimization routine is somewhat restricted by the presence of multiple minima in the sensor's cost function and selection of various starting conditions points out available envelopes of sensor design. Designer judgment is applied within these local envelopes to achieve the desired sensor performance. When referenced against a noise level of $1\mu\mathrm{V}/\sqrt{\mathrm{Hz}}$, a sensor with resolution of $6\mu rad/s^2$ and bandwidth of 50Hz is simulated as feasible in a sensor of 22mm diameter by 22mm height.

Keywords: angular accelerometer, microfluidic channel, inertial navigation

Opsomming

Die hoekversnellingsmeter is 'n veelsydige inersiële instrument met toepassings wat strek van stabilisering na navigasie en satelietrigting. Die huidige tegnologies toonaangewende hoekversnellingsmeter is die vloeistofrotorkonsep met lae bandwydte terwyl Mikro-Elektromeganiese Stelsel (MEMS) hoekvernellingsmeters 'n kompakte opsie met laer akkuraatheid bied. 'n Nuwe hoekversnellingsmeter word voorgestel deur die outeur om te verbeter op hedendaagse hoekvernellingsmeters en MEMS giroskope. Die sensor funksioneer deur gebruik te maak van mikrogemasjineerde spiraalkanale in veelvoudige skyfies om 'n spiraalheliks te konstrueer met hoë drukgenerasie tydens hoekversnelling. Die twee eindpunte van die vloeistofkolom ontmoet by 'n sentrale meetkamer waar 'n diafragma-gebaseerde druksensor 'n sein eweredig aan die toegepaste hoekversnelling lewer. Die doel van hierdie navorsing is om die teorie benodig vir simulasie van die sensor af te lei en saam te stel en daarna die potensiaal van die sensor vas te stel. 'n Golfspoed-aangepaste diskrete multivryheidsgraad model simuleer drukopwekking en -voortplanting. Die drukteorie is bevestig deur middel van 'n 200mm diameter spoel gewen met 3mm polieuretaan pyp. Diesel of water is gebruik as traagheidsvloeistof. Versnellings van tot 480rad/s^2 is toegepas op 1.5m en 20m pyplengtes met behulp van 'n tempotafel en die resulterende drukke is teen 2kHz gemonster. Kanaalvloei word gemodelleer deur middel van teorie direk afgelei van Szymanski se ongestadigde laminêre vloeiteorie, terwyl die drukomsetter diafragmamodel gebasseer is op linieëre platplaat teorie. Twee drukomsetters word bestudeer, die rekstrokie met 'n gewone sirkelvormige diafragma en 'n piezo-gebaseerde drukomsetter met 'n annulêre diafragma. Alle teorie is saamgestel in 'n lineëre sensormodel en die dinamiese respons geoptimiseer met behulp van die Kuhn-Tucker metode. Die toepassing van die optimisasieroetine is ietwat beperk deur die teenwoordigheid van veelvoudige minima in die sensor kostefunksie en verskeie beginkondisies het beskikbare sensorontwerpgebiede uitgewys. Ontwerpersoordeel is toegepas binne hierdie lokale gebiede om die verlangde werkverrigting te verkry. 'n Sensor van 22mm diameter en 22mm hoogte met $6\mu rad/s^2$ resolusie en 50Hz bandwydte is gesimuleer as lewensvatbaar as die sensoruitset teen 'n agtergrondruis van $1\mu\mathrm{V}/\sqrt{\mathrm{Hz}}$ verwys word.

Sleutelwoorde: hoekversnellingsmeter, mikrovloeïdiese kanaal, inersiële navigasie

Acknowledgements

I owe my gratitude to the following people who contributed to the completion of this work:

- Prof. P. Stephan Heyns for his guidance and willingness to supervise this work.
- Theuns Coetzee, Paul van der Merwe and Willie Klinck for the use and calibration of measurement equipment.
- Louis Boshoff for use of his data acquisition equipment.
- Denel Aerospace Systems for the access to their facilities, funding of the experimental hardware and promoting the research.
- Rob Hudson, Spook van der Merwe and Ernst Pretorius for advice in matters electronic.
- My wife Delia, Henriëtte van Eeden and my family, who formed my motivational support during this period.
- God Almighty, for the creation, out of which this work ultimately originated.

Table of contents

Nomenclature

Lower case symbols

(Bold symbols denote vectors or matrices)

a	Linear acceleration (m/s^2), outside radius of cylindrical channel (m) or speed of sound (m/s)
α	Angular acceleration (rad/s^2), coefficient of decay for a wave or angle where transition arc starts in linear pseudo-spirals (rad) or the Womersley flow parameter
α_k	Roots of J_0
α_t	Angular acceleration sensitivity or threshhold (rad/s)
β	Angle where transition arc ends in linear pseudo-spirals
d	Channel diameter (m)
δ	Deflection of a point in an elastic body (m), or angle to discontinuity in linear pseudo-spiral with a transition arc of zero
e	Inertial measurement drift error
e_0	Wheatstone bridge output (V)
ε	Angle between channel and local acceleration (rad) or material strain
f	Frequency (rad/s or Hertz) or friction factor (dimensionless)
h	Linear pressure potential (m)
h_{ang}	Angular pressure potential (m^2/rad)
h_f	Laminar steady state head loss (m)
η	Dimensionless time-length variable for flow, or Wheatstone non-linearity factor
k	Spring rate (N/m), gain or constant of linear equation in general
λ	Wave length (m)
m	Slope of line (dimensionless) or mass of body of matter (kg)
μ	Dynamic viscosity of fluid (Ns/m^2)
ν	Kinematic viscosity of fluid (m^2/s) or Poisson's ratio
π	The ratio of the circumference of a circle to its diameter
p	Cost function power
q	Differential pressure across diaphragm (Pa)
θ	Angle of a line measured from the x-axis upwards in the first quadrant
r	Radial position or distance of a point from the origin (m)
ρ	Mass density (kg/m^3)
s	Arc length (m)
σ	Material stress (Pa)
t	Time (in seconds) or diaphragm thickness (m)
τ	Shear stress (Pa)
τ_w	Shear stress at channel wall (Pa)
ω	Velocity vector of flow (m/s in all directions) and the frequency of the harmonic pressure input to Womersley flow (rad/s)
ω_n	Fundamental natural frequency (rad/s)
x	Horizontal Cartesian coordinate
$\mathbf{x}$	State vector or system input parameters in the case of optimization
y	Vertical Cartesian coordinate or deflection of diaphragm (m)
$\mathbf{y}$	Output state vector (may be scalar as well)

Upper case symbols

(Bold symbols denote vectors or matrices)

A	Area (m^2) or horizontal offset of circle from the origin
$\mathbf{A}$	State-space system matrix
B	Horizontal offset of circle from the origin
$\mathbf{B}$	State-space input matrix
$\mathbf{C}$	State-space output matrix
D	Diaphragm plate constant (Nm)
$\mathbf{D}$	State-space direct feed-through matrix
E	Young's modulus of elasticity (Pa)
Δ	Prefix to a symbol signifying the difference between two cases
Fo	Fourier number of flow (seconds)
Φ	Wave speed constant (m^2)
G	Gravitational acceleration of Earth (9.81 m/s^2)
G_0	Flow impetus constant for unsteady flow
J_0	Zero'th order Bessel function of the first kind
J_1	First order Bessel function of the first kind
K	Bulk modulus of fluid (N/m^2)
L	Length of curve or channel (m)
M	Moment in diaphragm (Nm), or total mass of body of matter (kg)
N	Flow constant of first order flow development
P	Fluid pressure (Pa)
P_w	Wetted perimeter on cross section of fluid containing channel (m)
Q	Volume flow (m^3/s)
Q_{ss}	Steady state flow (m^3/s)
R	Radius of circle (m)
R_0	Outside radius of diaphragm
R_c	Radius of transition arc for linear pseudo-spiral
T	Time constant of first order step response
U	Flow speed (m/s)
V	Volume (m^3) or rigid body velocity (m/s)

Abbreviations

AHRS	Attitude-Heading Reference System
CAC	Conventional Arms Control
DETF	Double Ended Tuning Fork
DC	Direct Current
DTG	Dynamically Tuned Gyroscope
DOF	Degree of Freedom
ESG	Electrostatic Gyroscope
FET	Field Effect Transistor
FOG	Fibre-Optic Gyroscope
FRAA	Fluid Rotor Angular Accelerometer
FS	Full Scale
G	Gravitational acceleration of Earth (9.81 m/s^2)
GPS	Global Positioning System
IC	Integrated Circuit
ICBM	Intercontinental Ballistic Missile
IO	Input/Output
ITAR	International Traffic in Arms Regulations
INS	Inertial Navigation System
LTI	Linear Time Invariant
ppm	parts per million
MEMS	Micro Electro-Mechanical System
MFCAA	Microfluidic Channel Angular Accelerometer
MDOF	Multi Degree of Freedom
MTCR	Missile Technology Control Regime
mph	mile per hour
nmph	nautical mile per hour
ODE	Ordinary Differential Equation
NP	Nuclear non-Proliferation
PCB	Printed circuit board
PDE	Partial differential equation
RLG	Ring Laser Gyroscope
RLSN	Recursive Linear Smoothed Newton
rms	root-mean-squared
SDOF	Single Degree of Freedom
VSG	Vibrating Structure Gyroscope

Chapter 1

Introduction and literature survey

1.1 Introduction

Navigation is the art of obtaining knowledge of an object's location and velocity. Dependence on information from outside the vehicle's confines in order to perform navigation constitutes non-inertial navigation. This method is in fact the one that early maritime navigators used, because they used the stars often to acquire their position. The light of the star traveling onto the eye of the navigator is information crossing the confines of the ship; hence this type of navigation is non-inertial. The sailors had to have sight of the stars to do their navigation in this manner. When no stars were visible, navigators had to approximate their current position by using only the compass and the last known position. Even the compass is non-inertial since the enveloping magnetic field of the earth is also information passed to the ship.

Navigation, whether inertial or not, is done by a process called dead-reckoning. Dead-reckoning is the process of using the latest available information on position to calculate the vehicle's current position by taking account of the path traveled since departure from that point: a type of extrapolation of space in time. Heading and speed are therefore important quantities to acquire as well as time elapsed. If navigation is purely inertial, the starting point is the only place where the current position is recorded and set as the starting point by a non-inertial method. An example of this is an autonomous submarine that performs its whole mission underwater and only resurfaces on return to its pen. It is more common though that navigation is a mixture between inertial and non-inertial technology. Commercial or civilian aircraft is an example here since commercial aircraft rely on inertial systems as well as outside information from radio beacons/satellites or fed via a two-way radio from air-traffic control towers.

Pure inertial navigation rarely occurs today, but most navigational systems possess inertial equipment of some sort. In fact, commercial aircraft flights are in the great majority purely non-inertial in the sense that position updates are constantly received via satellite. Not even during landing, when the pilot has sight of the landing strip do the transmissions stop. The Instrument Landing System (ILS) that gives the pilot the correct ingress and approach angle is constantly fed with information from radio beacons. Yet none of these aircraft fly without inertial equipment on board.

1.1.1 Inertial navigation

Inertial navigation has its foundations firmly set in applications where systems either have no way of extracting information of its position from its environment. (like submarines), or the system is a weapon that needs to be failsafe and autonomous (like Inter-Continental Ballistic Missiles, also known as ICBMs. Gates (1968) and Stovall (1997)). The applications have since expanded to vehicles that have non-inertial navigation systems on board, but require redundancy from an independent system like an Aircraft Heading Reference Systems (AHRS) in modern aircraft. Systems with autopilots also benefit from angular acceleration feedback by improving stability or accuracy of navigation.

According to Kayton and Fried (1969), inertial navigation has the following advantages:

1) Its indication of position and velocity is instantaneous and continuous.
2) It is completely self-contained since it is based on measurements of acceleration made within the vehicle itself. It is non-radiating and non-jammable.
3) Navigation information (including azimuth) is obtainable at all latitudes (including the polar regions), in all weather, and without the need for ground stations.
4) Navigation information is substantially independent of vehicle manoeuvres (in contrast to, for example, Loran and Doppler systems).
5) The inertial system provides outputs of position, groundspeed, azimuth and vertical. It is the most accurate means of measuring azimuth and vertical on a moving vehicle.

The disadvantages are:

1) The position-and-velocity information degrades with time. This is called drift, and occurs whether the vehicle is moving, or is stationary.
2) The equipment is expensive and relatively difficult to maintain. This is truer of the older inertial systems. Strapped-down solid-state gyros and accelerometers are mass produced and very cheap relative to the old stabilised platforms.
3) Initial alignment is necessary. Alignment is simple on a stationary vehicle at moderate latitudes, but it degrades at latitudes greater than 75° and on moving vehicles.

While navigation is performed, the location of the object is generalized to be in three-dimensional space; hence three displacement quantities are needed to describe its position. This is the function of the accelerometer cluster, which may be either stabilized or "strapped-down". A stabilized platform is designed to keep its orientation fixed to an external reference, which may be the local vertical, or a fixed point like a star. This has the advantage that each accelerometer always measures in the same orthogonal direction in inertial space relevant to the user. The disadvantage of this configuration is of course high cost. Strapped-down systems eliminate the need for a stable platform by fixing the accelerometers to the body of the vehicle and resolving the correct components of the acceleration by means of an on-board computer, with knowledge of the vehicle orientation.

Orientation is obtained by means of any device that can provide the direction the vehicle is pointed in. An inertial device capable of doing this, whether close to earth or in outer space, is the gyroscope. A "gyroscope" (loosely Greek for turn-measure) is a term that is generally understood to output an angle by default. This is partly due to the fact that this is indeed the most desirable output for navigational purposes, but also because the first rotor gyroscopes gave this output by default. An inertial device that outputs angular velocity, by this lore, is called a rate-gyroscope. Devices that output angular acceleration are called angular-accelerometers and not "acceleration-gyroscopes", but the function is exactly that of a gyroscope only in another dependent kinematical quantity. The reason for calling them angular-accelerometers stems from their evolution from modified linear accelerometers rather than gyroscopes. Angular displacement, -velocity and -acceleration are quantities dependent on successive differentiation or integration. In theory, if a person obtains any one of these quantities, any one of the others is obtainable.

In practice, this is unfortunately not as easy as a quick integration or differentiation. The reasons for this are:

1) Differentiation (to transform displacement to velocity to acceleration to jerk) is a noise-amplifying operation. Seemingly good data of displacement may be totally noise-corrupted when differentiated twice to obtain acceleration.
2) Integration is a noise attenuating operation, but may have gain problems when used inside control loops. Even more importantly, it introduces drift that is difficult to control.

3) Differentiation, integration and filtering take time and introduces filter lag. In feedback loops that require up-to-date data this may be a problem. The problem is addressed with predictive-filtering, which introduces some uncertainty to the system, especially in highly dynamic systems.
4) Integrating twice to obtain angular information from angular acceleration causes drift (angular error) adding up with the square of time instead of a normal gyroscope's drift that increases linearly with time. This has been the main obstacle in an angular accelerometer being used as a gyroscope. If an angular accelerometer is used for navigation the cross-track error can be found in Anthony (1993):

$$e = \frac{\alpha_t V t^3}{6} \tag{1.1}$$

where α_t is the angular acceleration threshold, V the vehicle velocity and t the mission time.

It is therefore preferable that the kinematical quantity required is measured directly. If this is not possible, the operation that is performed to obtain it should rather be integration to avoid noise problems. In spite of this, circumstances sometimes necessitate both indirect measurement and differentiation to be performed. Examples of this are given in following pages.

1.1.2 Strapped-down inertial systems

The gimbaled stabilized platform is an expensive, complex mechanization for accomplishing inertial navigation. Development of cheaper and simpler strapped down systems was already under way in the sixties. A computer performs the function of the stabilized platform in strapped-down systems by resolving the accelerometer outputs into local level coordinates. The resolved accelerometer outputs can then be processed as if they originated from a stabilized platform.

The first challenges to be met are that the gyroscopes must be able to output any angle accurately since they will be fixed to the arbitrary orientation of the vehicle. Such a "wide-angle" gyro or even "infinite-angle" gyro is often a solid-state type of sensor. High angular rates and the varying gravitational vector on the sensor are further complications in strapped-down mechanization. Strapped down systems only really became practicable in the 1970s. The Ring Laser Gyroscope (RLG) was the first gyro technology widely applied to this field.

1.1.3 General inertial measurement industry

Due to the historical preference for displacement or rate gyros (drift error being the main reason for this), the use of angular accelerometers in inertial navigation applications is far less prevalent. Applications for the direct measurement of angular acceleration for non-navigational purposes include:

1) Stabilization of computer hard disk heads. Angular acceleration feedback allows more robustness against shock in portable computers. (Hernden, 2000).
2) Road vehicle stabilization and testing. Extensive use is made of angular accelerometers for this application since the advent of MEMS. Insalaco (2000) describes one such application.
3) Ship roll-stabilization. Samoilescu and Radhu (2002) describe methods available.

4) Aircraft stabilization and testing, particularly for elevator and aileron control. Hartzell (1985) describes one example of successful application of an angular accelerometer as a gyroscope in aircraft testing.

Navigational angular acceleration measurements are commonly used in:

1) Satellite pointing systems. Le Du (1995) documents an example of an accurate satellite payload pointing.
2) Navigation of many aerial vehicles including aircraft and missiles (Khivrich and Belkin, 1985).
3) Increasing accuracy of gyro-stabilized platforms. (Neusypin, 1991).

Beyond the angular accelerometer, the domain of the gyroscope starts, which is much older and more celebrated. As mentioned above, the gyroscope outputs a kinematical quantity that is closely related to angular acceleration. When reference is made to a "gyroscope", this quantity is by and large understood to mean either angular rate, or displacement. The angular accelerometer may therefore be used for gyroscopic measurements, and vice versa. The gyroscope represents the historical and contemporary industry into which the angular accelerometer is introduced. As such, it is prudent to include an account of the current and expected near-future state of the art in gyroscopes.

1.1.4 Gyroscopes

Gyroscopes fall in two categories, mechanical gyroscopes and optical gyroscopes.

1.1.4.1 Mechanical gyroscopes

The mechanical types include the:

1) Conventional Gyro
   A Gyroscope functioning on the gyroscopic precession principle of a spinning mass supported on a single gimbal in the case of single degree of freedom (SDOF) gyros. The modern derivative of this type of gyro is the Dynamically Tuned Gyro (DTG), which is a two degrees of freedom (2DOF) gyro also referred to as a "free" gyro. The main advantage of this mid 1960s technology is that it does not require a flotation liquid or precise temperature control.

2) Floated and Levitated Gyros
   Some gyroscopes make use of spinning inertias that are levitated by some means to limit friction. This could be accomplished with superconducting suspension coils in the case of superconducting gyroscopes (a.k.a. cryogenic gyros) or capacitor plates in the case of the Electrostatic Gyros (ESGs). These gyroscopes may be "free" (in which case the spinning inertia has no mechanically constrained degrees of freedom) or only partially free as with air-bearing gyros.

3) Vibrating Structure Gyro (VSG)
   This solid-state technology is now used for micromachined gyros (by BAe Systems, among others). Coriolis effect is utilized on a vibrating resonator to measure angular rate.

4) MEMS Gyros
   Like VSGs, MEMS Gyros are late additions to the art and Coriolis force sensing is used for angular rate measurement. Tuning fork rate gyros are one of the earlier

successful MEMS devices. The simplicity of the sensor allows micromachining to be done on a mass-production scale.

1.1.4.2 Optical gyroscopes

Optical Gyros function on the Sagnac principle, which occurs due to differences in the propagation time (or beam path length) between clockwise and counter-clockwise beams of light about a closed optical path. Optical Gyroscopes include the:

1) Ring Laser Gyro (RLG)
   A relatively large and heavy device that is selfresonating; the RLG utilizes three mirrors of high optical quality (low beamscatter) to construct the closed optical path. A corner prism is used to reflect the beam onto the detector. The RLG in its passive form may experience problems at low rates where the two counter propagating beams are locked together in frequency, causing an effective deadband. To overcome this problem, periodic switching is used to change the effective optical pathlength of the two beams. This may be done by one of numerous methods, some of which are mechanical dithering (predominant method), an intracavity quartz crystal or saturable absorber.

2) Fiber-optic gyroscope (FOG)
   A more compact interferometric device where coherent light is injected into the system. In its simplest, passive form the closed optical path is built out of a coil of fiber-optic wire and the counterpropagating light beams are generated by a central beamsplitter. Appropriate placement of a spatial filter and polarizer ensures that the beams transverse the same path in the coil. The beams mix in the coil and fall onto the detector, which measures cosinusoidal intensity changes caused by rotation.

Many other types of gyroscopes exist, some only on experimental or demonstration level and others on prototype or product level. A chronicle of all gyroscopes ever devised is not the intent of this section, but rather the performance and cost that the current state of the art entails. For this goal, the gyroscopes mentioned above are adequate since they have become entrenched in gyroscope design through many years of representing the state of the art. This has been accomplished through constant evolution of the basic concepts and the components used in their construction. MEMS gyros are the exception in this respect as it is still a relatively late addition.

1.1.5 Contemporary inertial navigation industry

Ingram (2003) gives a strategic point of view on the inertial measurement industry. From this perspective, an inertial sensor is not only a decision of performance vs. cost, but also a matter of the strategic autonomy of a nation to provide in its own inertial measurement requirements. Inertial measurement is an essential technology in military applications and is thus export-controlled beyond certain performance levels. The objective of the restrictions is to limit distribution of gyros suitable for military use, and thus the regulations are in essence application specific. The contents of regulations (which include International Traffic in Arms Regulations (ITAR), Nuclear non-Proliferation (NP), Conventional Arms Control (CAC), Wassenaar Arrangement and the Missile Technology Control Regime (MTCR)) reflect this objective, but enforcement requires quantification to distinguish between military- or commercial use gyros. Currently, the MTCR limit is a drift rate stability of less than 0.5 degree/hour in a 1G environment. Due to the increase in performance of the mass-produced MEMS devices, these restrictions are set to be relaxed somewhat. Still, MEMS devices are far from satisfying all industry requirements, especially on the high performance end. This makes the type of gyro technology used still very much application dependent.

Figure 1.1 shows gyroscope applications and their required accuracies. The required scale factor stability and bias stability covers a range of many orders of magnitude. Bias stability refers to the fraction of bias (erroneous output at zero instrument input, in parts per million) that cannot be corrected by bias estimation techniques during instrument initialization because of continuing change after sensor initialization. Scale factor stability refers to the instrument scale factor (ratio of a change in output to a change in input) that cannot be correctly characterized by instrument calibration because of continuing change after sensor initialization. The overlap in required performance is clear from the figure, especially in lower performance gyros. In recent years, the overlap of the sensors used in commercial and military applications has been increasing making the control on military suitable gyros more difficult.

Figure 1.2 shows the performance and cost inherent to the principal gyroscope types. The MEMS range of gyros can be seen only to marginally satisfy the performance critical to some military applications, though this does not preclude military application of MEMS products. Commercially available MEMS accelerometers are in fact used as gun-hardened sensors for artillery rounds and many other weapons. The high performance gyro applications are still firmly seated in more mature non-MEMS technologies. The DTG covers the greatest range of performance. This may be attributed in part to the length of time this has been developed and applied, as it originates from the earliest gyro technology used.

The same performance expansion tendency may be expected from the MEMS gyros as they mature. The main driving forces behind the use of MEMS are size and cost, while the performance criterion is slightly compromised relative to other gyroscope types. In state-of-the-art applications where cost and size is of smaller importance, MEMS is not as likely to impose on other technologies. One of the few technologies where size and mass come at high enough premiums for the displacement of large accurate devices to occur is satellites and space travel. The cost of putting mass in space is still astoundingly expensive, but even this is set to become cheaper as more conventional aircraft reaches orbit. The successful flight of SpaceShipOne in June 2004 is a case in point. Furthermore, the drive for higher performance gyroscopes has almost ceased after the Cold War. With the advent of Global Positioning Systems (GPS) the focus is shifting to cheaper lower performance equipment to be used in conjunction with non-inertial technologies.

The cost and complexity of floated gyros and RLGs make them other candidates for replacement by something cheaper. MEMS devices reaching this level of performance is still leaps away, although far from impossible. The scale factor of MEMS gyros is the clear challenge in this respect, as well as the stability thereof. Ingram (2003) predicts the performance levels below for the period leading up to 2010. These predictions provide a benchmark for what performance would make a new technology worthwhile in the near future.

RLG	Drift rate stability < 0.005 °/h for <10G Drift rate stability < 25 °/h for 10 – 100G RLG system performance from 1nmph to 0.1nmph. System performance implies the integrated inertial measurement unit performance with vehicle position as output, in other words the user-level output.
FOG	Drift rate stability < 0.01 °/h for <10G Drift rate stability < 0.25 °/h for 10 – 100G FOG system performance from 2nmph to 0.4nmph
MEMS	2000: 100°/h @ $50 2002: 10°/h offset stability 2005-2010: Drift rate stability < 0.05 °/h for <10G 2005-2010: Drift rate stability < 0.5 °/h for 10 – 100G

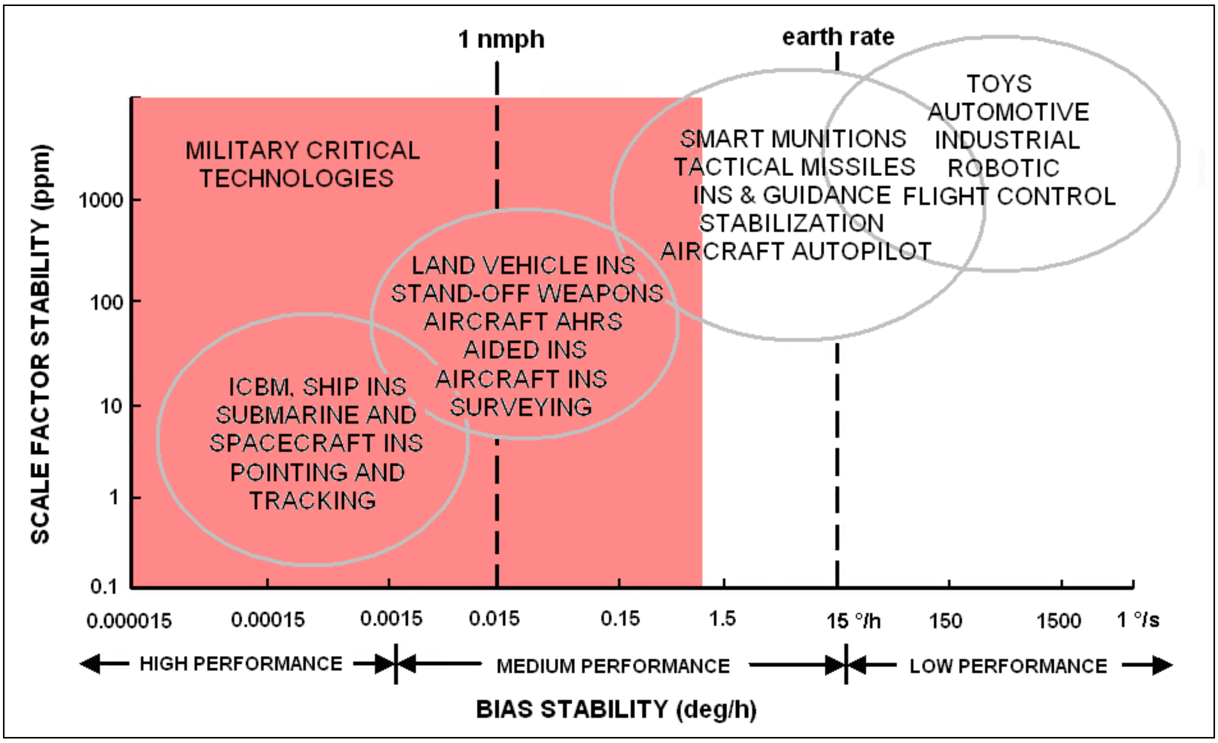

Figure 1.1: Gyroscope applications and their required performance. (Adapted from Ingram, 2003)

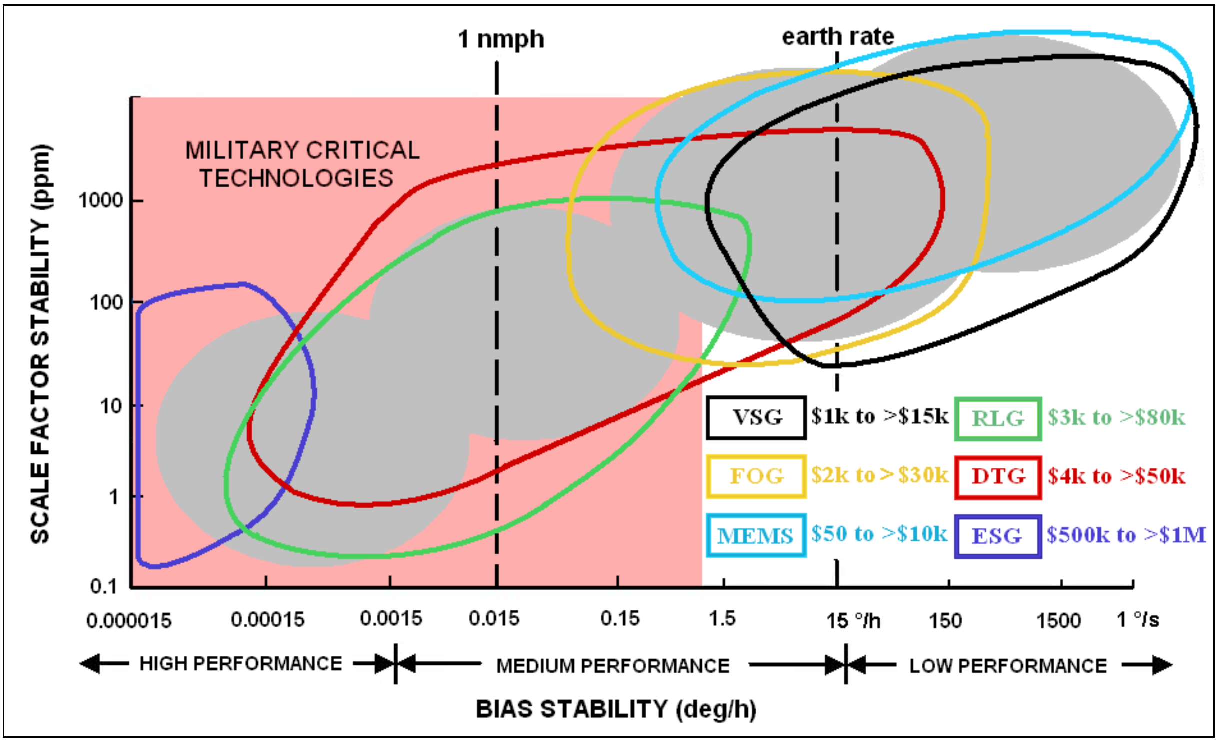

Figure 1.2: Principal gyroscope technologies in use today and their approximate cost per measured gyro axis. (Adapted from Ingram, 2003)

1.2 Angular acceleration measurement literature survey

Ovaska and Väliviita (1998) did a review on angular accelerometry inside and beyond inertial applications. The emphasis in this paper is on delay-sensitive real-time applications, which make it especially relevant for the current field of study. The authors are quoted in the next sentence: "Direct measuring of linear acceleration is in wide everyday use, but the angular acceleration sensors, especially those with unlimited rotation angle, can still be considered as emerging devices. "

1.2.1 Indirect angular acceleration measurement

Ovaska and Väliviita give an account of methods available for indirect angular acceleration measurement. These include:

1) Differentiation with Predictive Postfiltering
   A technique normally performed in the discrete time domain where easing constraints can be placed upon the incoming signal characteristics in the shape of low order polynomials. The required output is differentiated and filtered. The methods available here include the *p*-step predictive filter and the Recursive Linear Smoothed Newton (RLSN) predictor. Examples may be found in Pasanen et al. (1994). Vainio and Ovaska present an analogue filter (1997).

2) Linear State Observation
   Well-known as a "Kalman-filter", which originates from state space theory. This method is attractive when no assumption on the polynomial nature of the acceleration curve is possible. A stochastic state space model is developed with zero-mean white noise imposed on the acceleration. For the use of state space methods on guided projectiles see Burchett (2001). More specific examples on angular acceleration estimation are found in Bèlanger (1992) or Schmidt and Lorenz (1992).

A MEMS version of the vibration beam concept was developed by Roszhart et al. (2000) for inertial navigation application at Kearfott Guidance and Navigation Corporation. A single flexure mounted proof mass functions as a coupled-mode Coriolis sensor and an accelerometer. In this manner, both linear acceleration and angular rate is measured about one common axis. To obtain angular acceleration, the rate output may be differentiated and postfiltered. A system similar in function was developed by Hulsing (1988). Because this document's emphasis is placed on direct measurement of angular acceleration, the list is limited to these although many other examples exist. Ovaska and Väliviita also includes a researched base of application tailored methods that are seated firmly in rotating machinery disciplines of various types and are thus non-inertial in nature. This is elaborated on in the next section.

1.2.2 Non-inertial angular acceleration measurement

As mentioned above many situations arise where angular acceleration may be measured from non-inertial reference frames. Ovaska and Väliviita (1998) report on some of these methods. For navigational purposes these methods may not have direct application, but important uses may even be found in this document's scope in the ground testing of inertial systems. Non-inertial ground-based rotational systems can be made extremely accurate. Inertial problems like drift and noise are easily eliminated in optical encoders, and thus are more than ten times more accurate than an inertial system, so that it may be used as a verifying measurement. For an example of angular accelerometer testing see McDonnel (2001). The more conventional angular displacement measuring equipment is omitted from this list, which includes theodolites and inclinometers.

Restivo and Gomes de Almeida (2004) describe a method of measurement of either linear- or angular relative acceleration. The difficulties experienced in getting relative angular acceleration have incited direct measurement of the quantity. The sensor functions on the formation of eddy currents (Foucault currents) within a conductor when moving through magnetic flux. The current generated will be proportional to the velocity of the conductor and the magnetic field that originated the current. Changes in the relative velocity cause changes in the current. A pick-up coil in this conductor is used as a sensing element to generate a voltage proportional to the relative acceleration.

Measurement of angular acceleration (and other kinematical quantities) with an optical encoder is covered by Kadhim et al. (1992). The measurement of acceleration by this method proved difficult when acceleration in excess of 50 rad/s^2 was present.

A passive fiber-optic class angular accelerometer was developed by Listvin et al. (1993). Development of calibration equipment and the characterization of the sensor are also discussed. An angular displacement sensitivity of 4x10^{-10}rad/Hz$^{1/2}$ was obtained. Sensitivity is defined here as the ratio of a change in output to a change in an undesirable or secondary input, which is in this case white noise. White noise in turn is measured in V/Hz$^{1/2}$, an undesirable voltage output (in root mean squared magnitude) when measured with a noiseless bandpass filter of certain bandwidth in Hz. Noise is discussed further in section 6.7.

Hancke and Viljoen (1990) treated a special case in rotating machinery where only one speed reference signal per revolution is available. Emphasis is placed on the measurement of low values of rotational speed and acceleration. Extrapolation of the last two pulses is used to calculate the value of speed and acceleration between consecutive pulses. The success in using this method is partially attributable to the fact that high inertia components (as found in a turbo generator plant) were measured. Applicability must therefore be reserved.

Another method for the measurement of angular acceleration is using diffraction grating interferometry. Two improved methods (based on homodyne and heterodyne techniques) are described by Täubner and von Martens (1998). The application of grating interferometry to the calibration of angular accelerometers is also described.

1.2.3 Direct inertial angular acceleration measurement

Meydan (1997) gives a survey of direct linear and angular acceleration measurement, where short descriptions on most of the concepts mentioned below may be found. Accelerometers in general may classify among the following sensors that may be customized for linear or angular measurements:

1) Piezoelectric accelerometers
2) Strain-gage accelerometers
3) Piezoresistive accelerometers
4) Capacitive accelerometers
5) Reluctive accelerometers
6) Cantilever magnetic accelerometers
7) Clamped-Clamped magnetic accelerometers

The dedicated angular accelerometers are:

1) Amorphous wire angular accelerometers
2) Fluid rotor angular accelerometers

Most of the above may fall in either the open loop or servo (closed loop) categories. The generic concept contribution from the angular side of accelerometry clearly confirms the finding of Ovaska et al. on the low presence of angular accelerometers relative to their linear counterparts. A survey on the state of angular accelerometry revealed the following angular accelerometer sensors developed mostly from the mid-eighties onwards:

Brosnihan et al. (1995) describe a surface micromachined force feedback angular accelerometer for computer hard drive applications. The use of angular acceleration feedback has the advantage of reducing the positioning overshoot of the read/write head and so reduce seek times by 10% when compared to previously used methods. In this application, the MEMS approach to accelerometers proves to be ideal because it brings down both the cost and size of the product. The whole package is chip integrated. Unlike MEMS gyroscopes, these angular accelerometers contain no vibratory motion so the direct effect of acceleration is measured. The pick-up is capacitive in nature and the accelerometer includes an analogue feedback to improve scale factor. The first generation sensor has a scale factor of 0.24 μVrms/(rad/s^2) with a noise floor of 75 rad/s^2/Hz$^{1/2}$.

Other chip-integrated packages may also contain useful processing functions like temperature sensors, analogue-to-digital signal conversion, pulse width modulated output, filtering and interface functions to improve scale factor. The LIS1RO2 (L6671) Rotational Accelerometer system by Gola et al. (2000) from ST Microelectronics provides a digital output with an included interface chip. The interface chip enhances the scale factor of the sensor by use of a single bit electromechanical $\Sigma\Delta$ conversion loop. This enables the measurement of acceleration as low as 2.5rad/s^2. By use of feed-forward compensation on external disturbances acting on HDD packaging, the system keeps the read/write head on track, which in turn allows greater track densities in portable computers.

Another micromachined sensor that includes a linear sensor and possibly two axes of angular sensitivity was proposed by Mizuno et al. (1997). The seismic mass is ring-shaped and surrounds a central pillar. The ring is suspended to the pillar by means of a pair of flexible torsion bars in the case of one axis of angular sensitivity, and by a gimbal structure incorporating two pairs of torsion bars for two axes of sensitivity. The sensor was proposed as open loop with an envisaged future closed loop (force-balance) sensor to improve angular bandwidth. In an alternative configuration even angular rate is measurable, but a question was raised on how the device's sensitivity to angular rate can be discriminated from its sensitivity to angular acceleration.

For the measurement of the rotational degrees of freedom in a large dynamic system (like automotive studies), Insalaco (2000) describes two different angular accelerometers. The first type of angular accelerometer is a high sensitivity bimorph piezoelectric concept that is capable of simultaneously measuring linear and angular acceleration for general low shock experimental studies. The bimorph is coupled to a remote signal processor to accommodate sensor element deficiencies. An earlier version of the bimorph system of Insalaco is the Translational-Angular-Piezobeam (TAP) system described by Bill and Wicks (1990). The system contains two identical beams which each consists of a bilaminar piezoceramic flexure with polarization direction normal to the beam axis. Charge amplifiers are integrated into the sensor yielding an output proportional to one axial and one rotational sensitive axis. The second angular accelerometer for use in crash testing consists of a rugged quartz shear element. Correct design of the shear element's fundamental parameters eliminates the need for post-processing in this sensor. The quartz shear concept only measures angular acceleration, which necessitates the addition of linear sensors if linear acceleration measurement is desired.

Lassow and Meydan (1995) developed an angular accelerometer using a seismic mass on ferromagnetic amorphous wire. Angular acceleration causes torsional stress in the wire, which in turn causes a Matteucci voltage over the clamps of the wire. A solenoid-magnetized, highly magnetostrictive amorphous wire is required to obtain the voltage that is modulated and measured. The main advantage of this angular accelerometer over a piezoelectric derivative is superior low frequency response and less supporting electronics. A scale factor of 0.56 mV/rad/s^2, non-linearity of 0.19% full scale (FS) and repeatability of 4.62% FS was obtained.

Shirron et al. (1996) developed a monolithic superconducting angular accelerometer capable of resolving angular acceleration in one axis to 10^{-10} rad/s^2/Hz$^{1/2}$. Angular acceleration is sensed by changes in inductance of superconducting coils near a proof mass of niobium. The proof mass is attached to the housing via a torsional spring and operated at a temperature below 9.2K so that the proof mass becomes superconducting. The angular accelerometer has a very low bandwidth and was designed for use with a superconducting gravity gradiometer at frequencies below 1Hz. The supporting systems required to operate this device is considerable, but the advantage of accuracy is clear.

An earlier superconducting accelerometer capable of measuring both linear and angular acceleration was developed at the University of Maryland, by Canavan et al. (1991). This accelerometer functions by magnetically levitating the proof mass against gravity, or any other proof force. The relative positions and orientations with respect to the levitation platform are measured with six superconducting inductance bridges sharing one amplifier. All six degrees of freedom is measured simultaneously in this way, thus the sensor offers a full inertial measurement unit. The sensor is servoed by feeding sensed deviations back to the levitation coils and so improves the sensor’s linearity and dynamic performance. Expected intrinsic noise is $4x10^{-12}$ $m/s^2/Hz^{1/2}$ for linear acceleration, and $3x10^{-11}$ $rad/s^2/Hz^{1/2}$ for angular acceleration.

Where Lassow et al. and Shirron et al. uses a torsional wire to support the seismic mass, Minbang and Pen (1992) use a fluid floated mass that is force balanced to obtain a resolution of up to 10^{-4} rad/s^2. The sensor is temperature compensated.

Evans (1970) describes a triaxial angular accelerometer by use of a seismic mass suspended in a buoyant fluid. The neutral buoyancy is set up by temperature control of the suspension fluid with heating from a printed circuit heater. The system also contains a float centering system serving as active internal feedback.

Hartzell (1985) built another fluid based system. Here the fluid assumes the function of the seismic mass. Statham (1957) patented this concept. The functioning of the sensor is based on the rotation of a suspended paddled mass that rotates due to the inertia of the fluid when angular acceleration is applied. The fluid is contained in an annularly shaped channel coupling the fluid inertia with the paddles, and a DC servomotor directly driving the paddles provides feedback. A washout integrator electronic circuit is used to take the sensor output to angular displacement.

Marat-Mendez et al. (1999) developed two dedicated angular accelerometer tranducers, one with a pre-polarized PVDF film and the other with a polymer/ceramic piezo-composite, and compared the results. The research extended only as far as the transducers and no sensor electronics are mentioned, hence the sensor output is in Coulomb. The sensitivities achieved varied from 0.03 $pC/rad/s^2$ to 0.06 $pC/rad/s^2$. One conclusion of the research was that the measurement error obtained from PVDF is lower than the composite piezoelectric.

Other force transducers have also been used to devise angular accelerometers. The Double Ended Tuning Fork (DETF) is a resonating device that generates a frequency shift proportional to applied force. A characterization of the DETF is given by Cheshmehdoost, Jones and O' Connor (2001).

Current commercially available angular accelerometers and angular displacement devices include:

1) Endevco Model 7302B: a 5000 and 50 000 rad/s^2 sensor for high shock applications.
2) BEI Technologies Model 8301 Fluid Rotor angular displacement device: a highly accurate device operating within a range of ±10 mrad or ±10 μrad.
3) ST Microelectronics L6674.
4) Columbia Sensors SR-107VFR. Full-scale range of between 1 and 100rad/s^2 and resolution as good as 50 $\mu rad/s^2$.

5) Jewell ASXB10

The Columbia sensors, Jewell and BEI Technologies accelerometers use fluid rotor technology.

1.2.4 Survey conclusions

From the literature survey, direct angular acceleration measurement can be divided into two main categories. The first category of sensor is a small, cheap micromachined sensor that is mass-produced for applications where low scale factor is satisfactory, like the automotive industry. The second category sensor is a large elaborate device with high scale factor and cost. Between these two types of sensors a niche exists that can be exploited. The high-performance end of angular accelerometers has large size, high cost and also limited rotation angle (in some cases) as the biggest drawbacks.

1.3 Scope of research

A niche has been identified in the angular accelerometer industry for a high scale factor MEMS device. The available range of truly dedicated angular accelerometers is limited and the high performance sensors have prominent disadvantages of large size and low bandwidth:

1) Dimensions from 40mm diameter and 60mm length are the norm when mounting structure is excluded.
2) Sensors exceeding 30Hz bandwidth are likely to be low scale factor, or non-dedicated devices.

It is proposed that fluid inertia could be used to achieve high angular acceleration sensitivity inside a small package with suitable bandwidth for most inertial measurement applications, thereby improving on the two main drawbacks of the fluid rotor angular accelerometer (FRAA). The design of the proposed sensor will endeavor to contain fluid in the optimum manner for pressure generation in one axis of angular acceleration input. The pressure generation must be insensitive to linear acceleration in any direction and angular acceleration on the two non-sensitive angular axes. The generated pressure is transduced into a signal proportional to the input acceleration by a central pressure transducer.

The research done in the remainder of this document addresses the theory necessary for the modeling of the sensor. The aim of this research is to theorize a concept offering a worthwhile performance, size or cost improvement on current angular accelerometer varieties, thus increasing the scope of application for MEMS-based inertial products. The attempted contribution of the sensor is an increase in scale factor offered by current MEMS angular inertial devices. The attempt will be embarked on with the Microfluidic Channel Angular Accelerometer (MFCAA) concept defined in chapter 2.

The aims of this document are:

1) Acquisition, development, synthesis and verification of the theory necessary to develop an MFCAA and evaluate its potential.
2) Perform a trade-off and/or optimization of important variables in the sensor.
3) Study the viability of such a sensor and recommend applications for which it might be favored.
4) Make recommendations on further work to be done.

The research focus is on mechanical theory pertaining to the MFCAA, but electronics is addressed as far at it influences the feasibility and potential of the sensor. The detail and spectrum of theory is also governed by the requirements set by successful modeling of the sensor. New fundamental theory presented here will be verified by experiment.

1.4 Overview of research

Chapter 2 presents the function and general structure of the envisaged angular accelerometer conceptually. This allows identification of the fundamental natural phenomena relevant to the sensor. The mathematical description of these natural phenomena is the subject of chapters 3 to 6 and 8.

Chapter 3 addresses matters regarding the pressure in the spiral-helical channels. The fundamentals of steady acceleration-generated pressure are covered first. A general mathematical description of a spiral's dimensions is presented in 3.3 and angular pressure potential is defined in Cartesian and polar coordinates in 3.4. Sections 3.5 onward cover the propagation of pressure through the channels by using a discrete model. Some inherent deficiencies of this model is addressed by a modification performed in 3.6.

Chapter 4 studies various spiral shapes as candidates for use in the sensor. The mathematical theory of chapter 3 is used to generate and compare various spiral schemes. Three spirals are proposed to allow a trade off between ease of manufacture and performance.

Chapter 5 studies flow in the sensor channels arising from the pressure differences predicted by chapter 3 that interacts with the finite stiffness of the pressure transducer. The expected laminar flow regime is described in 5.2 and an analytical solution for the limiting case of flow with constant pressure gradient starting from rest is reproduced in 5.3 (from the solution first derived by Szymanski). A more general solution is developed from this limited analytical solution in the shape of a transfer function in section 5.4.

Chapter 6 covers the pressure transducer. Sections 6.1 to 6.5 study a strain-gage based transducer used with a plain circular diaphragm while sections 6.6 to 6.9 study the characteristics of the piezo-based pressure transducer with an annular diaphragm. A Wheatstone bridge (section 6.3) is used to measure change in resistance of the strain-gage and a charge amplifier (section 6.6.2) is used to measure piezo crystal deformation. Noise of the charge amplifier is covered superficially in section 6.7.

Chapter 7 experimentally verifies the pressure generation theory presented in chapter 3. Urethane tubing wound on a spool is used on a rate table to input angular acceleration and generate pressure. The pressure is measured absolutely at the two tube ends by means of an integrated circuit (IC) sensor and subtracted to obtain differential pressure. The effect of free air and radial offset of the spool is studied in section 7.4. Experimental results for 1.5m and 20m tubes are presented in 7.5. The theory of chapter 3 is used directly to predict pressure versus time and then compared with the measured pressure.

Chapter 8 synthesizes the sensor theory of chapter 3 to 6 into a mathematical model of the whole sensor. Sensor DC characteristics are described in 8.4 and the dynamical model architecture in 8.2. General sensor characteristics versus main sensor parameters are described in 8.6. In section 8.7 a sensor optimization is performed to satisfy a high- and low-bandwidth requirement.

Chapter 9 concludes the research and makes recommendations on further work.

Chapter 2

Proposed microfluidic channel angular accelerometer concept

2.1 Principle of operation

The MFCAA aims to utilize fluid inertia to measure angular acceleration. The main result of fluid inertia in an acceleration field is variation of pressure in the fluid, which is transduced to a signal in the MFCAA as a measure of angular acceleration. The principle of operation is clarified by starting with the effect of linear acceleration on a body of fluid.

Any body of fluid undergoing steady linear acceleration different to that of the local gravity field eventually causes a steady pressure in the fluid due to that acceleration. A fluid falling to earth (in the absence of drag) generates no such pressure because the fluid acceleration equals the gravitational acceleration. An acceleration differential has to be caused in order to generate a pressure. The acceleration differential is defined as the difference between the gravitation and translational acceleration subtracted as vectors. The generated pressure increases linearly in the direction of the acceleration differential.

The body of fluid under consideration has to be contained to sensibly cause an acceleration differential. Consider a stationary beaker containing a fluid as shown in figure 2.1. The container contents give a color representation of the pressure in the fluid. Increasing brightness of red indicates an increase in pressure from atmospheric level, while a blue brightness scale indicates a drop in pressure. White indicates atmospheric or nominal pressure. The beaker in figure 2.1 has an open top; hence the free surface of the fluid is at atmospheric pressure. The gravitation pull of the earth causes an increasing pressure in the direction of the acceleration differential (which is downward in this case due to the stationary container). The pressure at the bottom of the beaker equals atmospheric pressure plus the gravitational pressure of $\rho\, a_{pot}\, h$. Here ρ is the fluid density and a_{pot} is the acceleration differential, which can also be expressed as $a_{pot} = G - a$. The factor a_{pot} is in this case simply G (the gravitational acceleration) because a (the body acceleration) is zero. h is the depth of the fluid parallel to the acceleration differential.

The acceleration differential direction can be changed into any direction by applying linear acceleration to the beaker. To illustrate this, consider figure 2.2. The beaker is completely filled with liquid with an airtight lid on top. Furthermore, the support is removed and a force is applied downward. The beaker will accelerate downward faster that the local gravitational acceleration, reversing the acceleration differential. If no lid were in place, the fluid would spill out the top but now a pressure is generated in the constrained fluid. Unlike figure 2.1 the pressure increases upward (due to the reversed acceleration differential) but a drop in pressure is found at the opposite end of the beaker. The drop in pressure is caused by the lid, which prevents pressure equalization of the fluid's free surface with the atmosphere. Since the amount of fluid in the beaker is constant under constant temperature, the increase in pressure against the lid comes at the cost of pressure elsewhere.

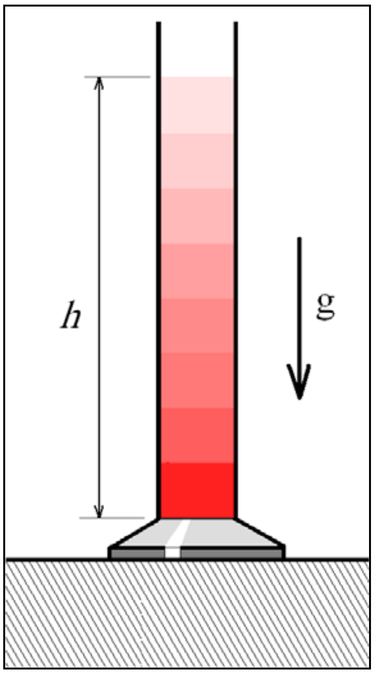

Figure 2.1 Pressure distribution in stationary, open-top beaker.

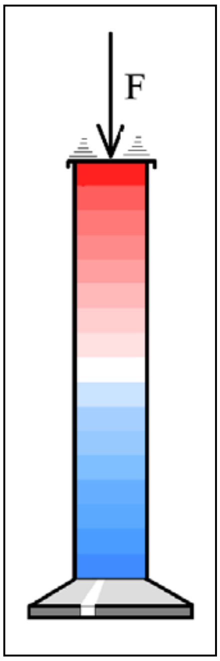

Figure 2.2 Pressure distribution in downward accelerated closed beaker.

The pressure still increases in the direction of the acceleration differential (upwards), and the pressure difference between the top and bottom is still $\rho \, a_{pot} \, h$. In the examples above, gravity plays an important role in the pressure generated. Linear accelerometers have no way of distinguishing between gravity and kinematic acceleration also due to this effect. Dedicated angular accelerometers should however not be influenced by the earth's gravitational pull. To accomplish this, the MFCAA does not measure absolute pressure but rather differential pressure. The following paragraphs explain how.

A fluid filled thoroidal (circular and endless) tube is shown in figure 2.3. The tube is stationary initially, and all the fluid inside as well. A blockage is also shown in the tube, preventing any flow inside. If the blockage and any internal friction were absent and the tube was rotated about its Z-axis as shown, the fluid inside would remain stationary. With the blockage present in the tube, the inertia of the fluid will generate a pressure in the event of angular acceleration.

Figure 2.4 shows what occurs at the start of counterclockwise angular acceleration around the Z-axis with a blockage present. A high-pressure wave propagates from the blockage in the direction of the angular acceleration and a low-pressure wave propagates in the opposite direction.

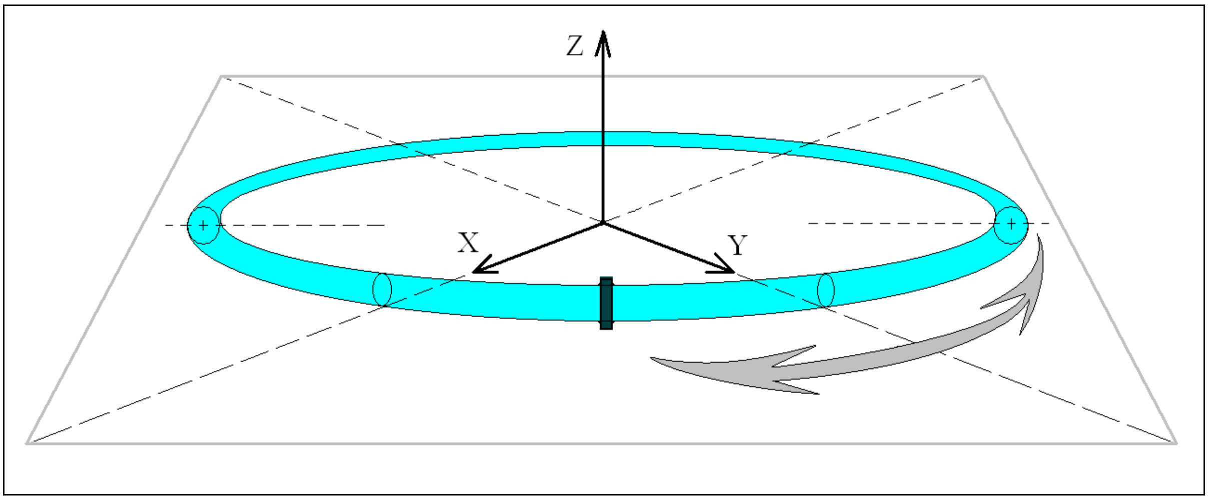

Figure2.3: A thoroid-shaped tube filled with liquid.

These pressure waves propagate at the speed of sound in the fluid. The fluid at the top experiences no pressure change yet. Eventually the pressure waves will damp out due to various mechanisms and assume the steady state pressure distribution in figure 2.4B.

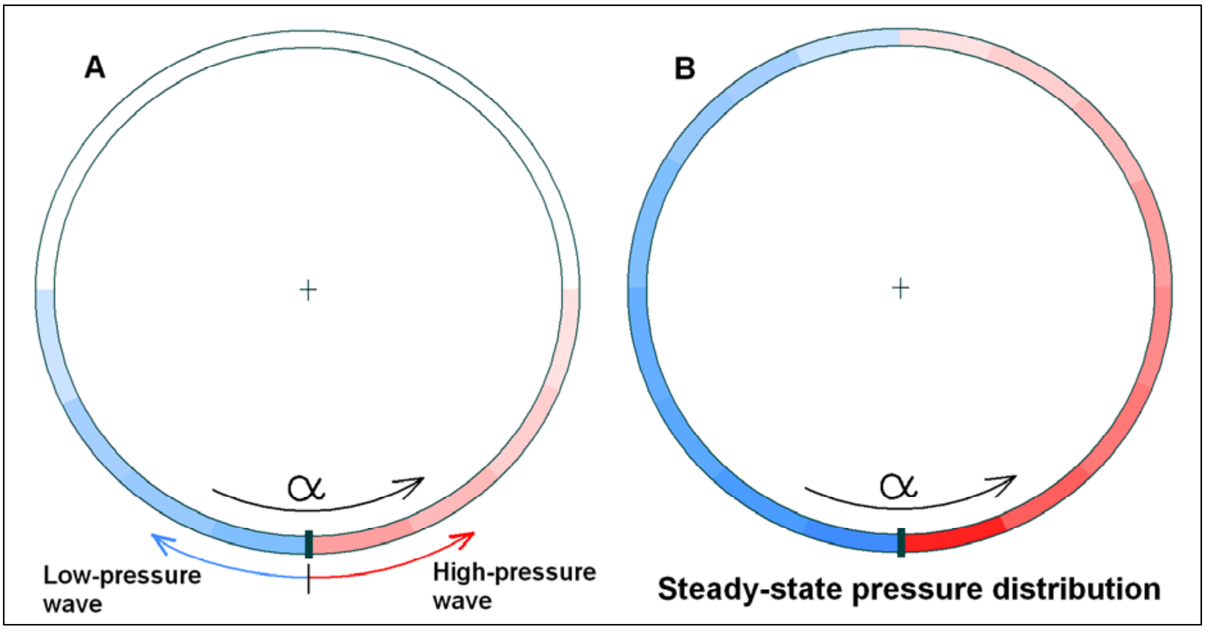

Figure 2.4: Thoroidal tube under angular acceleration about axis orthogonal to tube plane. A) Immediately after start of angular acceleration input B) After pressure transients have decayed.

The pressure distribution of figure 2.4B is exactly that of figure 2.2 except that it applies to angular and not linear acceleration. The mechanism for the generation of pressure in figure 2.4B is also linear acceleration, but here it is caused at a distance from the center of the angular acceleration. The difference in steady pressure across the blockage is a measure of the imposed steady angular acceleration on the tube. This is the principle of operation of the MFCAA. An MFCAA aims to maximize the differential pressure generation across a diaphragm (channel blockage) due to angular acceleration input about the sensitive axis. In figure 2.3 the Z-axis is therefore the sensitive axis.

A rigid body can reasonably approximate the tube, if suitably supported. A single rigid body contains six degrees of freedom (DOFs), three translational and three rotational. To make the MFCAA a successful angular accelerometer it has to be possible to distinguish between pressures generated by angular acceleration about its sensitive axis and accelerations in the other five DOFs. The MFCAA is particularly well suited to this requirement.

In Figure 2.3, the tube is shown in the XY-plane. Linear acceleration of the tube along the Z-axis will clearly not generate a differential pressure across the blockage since the pressure would increase along the Z-axis. Similar scenarios occur for angular acceleration in the X or Y axes. Pressure distributions for acceleration and angular velocity in two degrees of freedom is shown in figure 2.5. The top two drawings show linear acceleration in the X and Y axes respectively while the bottom drawings do the same for angular velocity input. The tube obstructions have been removed to see the pressure distribution clearly. As a matter of fact, the pressure distributions would essentially be the same with or without obstructions for these inputs. The pressure distributions in figure 2.5 do not generate flow in the absence of a blockage and hence will not generate a differential pressure across a blockage. Any combination of the acceleration or velocity motions in figure 2.5 (or linear acceleration in the Z axis) will also not contribute to the differential pressure across the blockage. Since linear acceleration in any axis is rejected, gravity is also rejected. The tube differential pressure therefore rejects all angular or linear accelerations except that of the sensitive axis, and is insensitive to angular velocity in any axis.

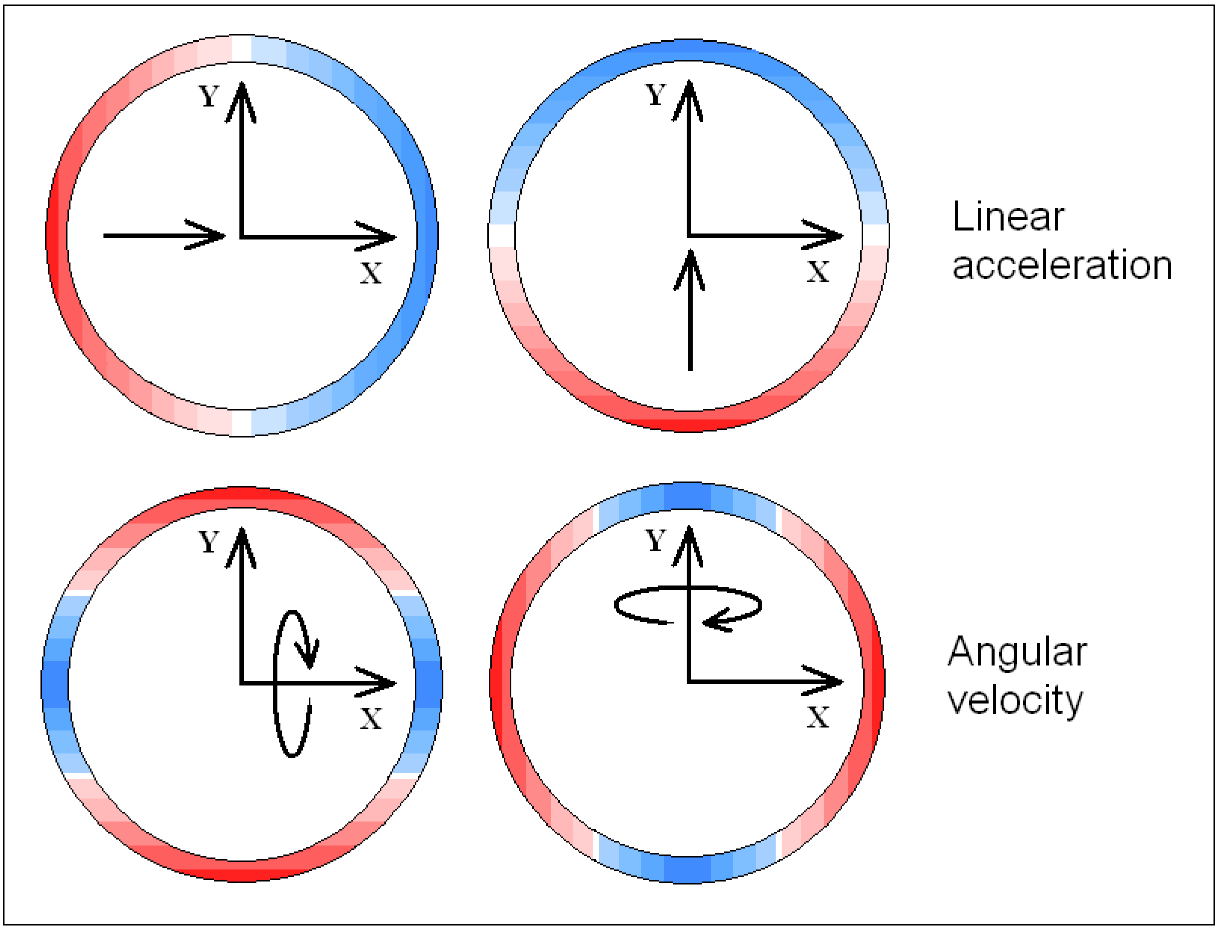

Figure 2.5: Pressure distributions generated by kinematics in the degrees of freedom of the XY plane.

The rejection of unwanted inputs is due to the closed infinite loop construction. Any distance between the ends of a broken loop causes failure of the closed loop assumption and indeed causes differential pressure for various kinematic inputs.

2.2 Micromachined spiral helix channels

The MFCAA customizes the tubular loop shape of section 2.1 into a helix shaped micro-fluidic channel that is optimized to generate pressure for angular acceleration inputs. The MFCAA is still designed to disregard linear accelerations (including gravity) and angular acceleration input to the non-sensitive axes. In order to maximize pressure generation, the single loop tube is replaced by a system of channels. The channels are etched from wafers with micro-machining techniques and then bonded to form the spiral-helix. Figure 2.6 shows a coarse scheme of the wafers to illustrate the concept. The channels are built up out of two wafers differing only in port position and the direction of the spiral. A spiral is used on each wafer to maximize pressure generation; while a central area is left for the measurement chamber. Bonding an alternating set of wafers in an equal number completes the channel array. The machined wafers complete a continuous helix by lining up the ports for each wafer to feed onto a subsequent wafer. The top wafer is covered with a lid that contains a port leading to the top chamber feed chute. The top and bottom ends of the fluid channel are thus fed to the measurement chamber where the pressure is transduced into a signal proportional to the applied angular acceleration. The channels are square in cross-section, therefore the wafer thickness depends on the channel width. Narrower channel width allows a longer spiral and thinner wafer so that the total channel length increases inversely proportional to the square of channel width (on the same annular area).

2.3 Working fluid

The working fluid could be any fluid that is liquid in the sensor's temperature range, but mercury is especially suitable due to the following reasons:

1) Mercury has a density of 13550 kg/m^3 (the highest of any fluid at room temperature) and a dynamic viscosity of 1.561x10^{-3} kg/ms. The pressure generated in the channels is proportional to the fluid density, but high viscosity adversely influences fluid flow. Mercury presents the most favorable ratio between density and viscosity (kinematic viscosity) of any fluid.
2) Mercury has a very low vapor pressure of 1.1x10^{-3} Pa. This allows the pressure at the low-pressure end of the diaphragm to drop farther than any other fluid before the mercury boils, allowing a greater angular acceleration range in the sensor.

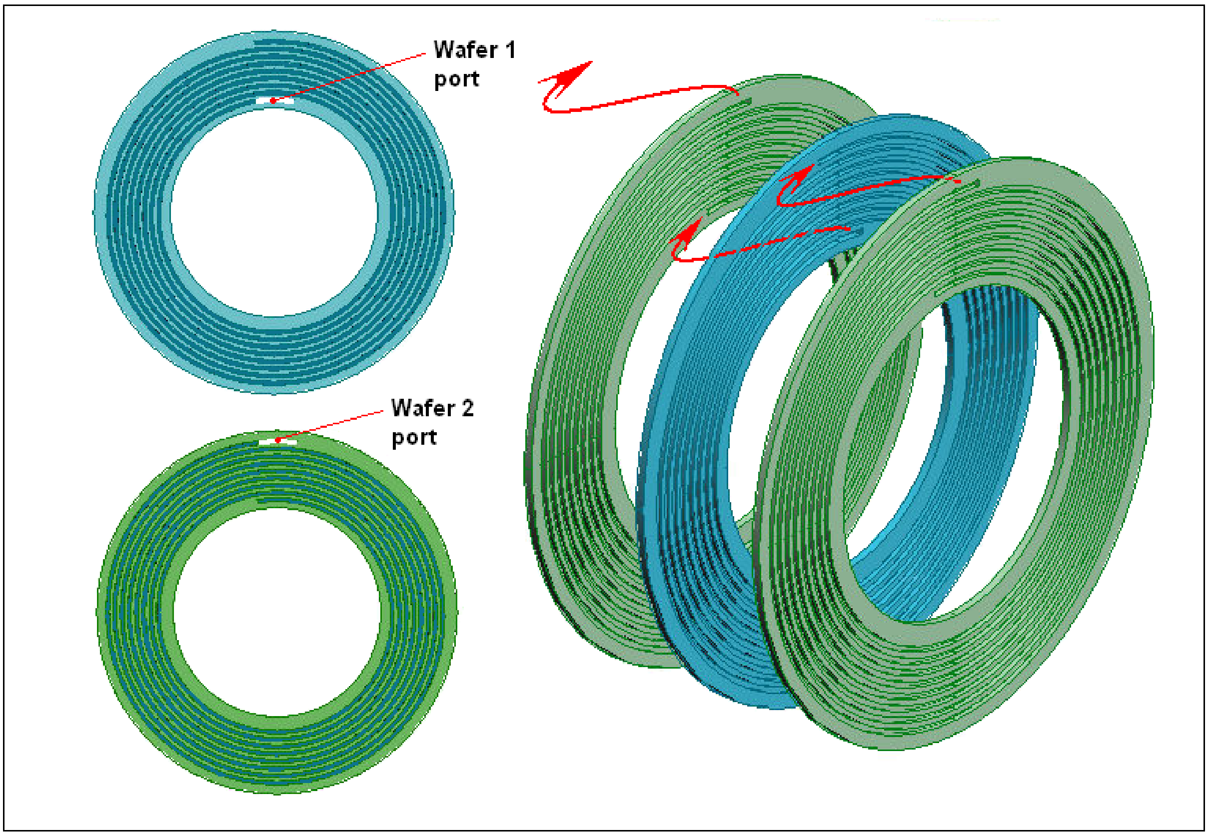

Figure 2.6: Illustration of the use of two wafers to build a spiral-helix.

Contrary to the expected, mercury does not have a very high wave propagation speed. The speed of sound in mercury is in fact lower than that of water at some temperatures. The high density of mercury is the reason for this, even though the bulk modulus of mercury is an order of magnitude higher than that of water.

2.4 Measurement chamber

The center of the sensor would not generate linear acceleration during angular rotation so this region is used for the pressure transducer. The wafers are thus manufactured to occupy a cylinder with an annular cross-section. Figure 2.7 shows one whole view and one sectioned view of the resulting bonded wafer structure. The measurement chamber has a cross-sectional area much larger than that of the channel, making the flow negligible in this volume. The chamber contains the diaphragm with a transducer, which may be a piezo-electric crystal, diaphragm mounted strain-gage or any other displacement/deformation transducer. In the case of a piezo-crystal, internal support would be needed against which the crystal can deform. One possible configuration is shown in figure 2.8. The support for the piezo-crystal is shown at the top, and one baffle on either side of the diaphragm. The baffle is a possible measure under consideration to minimize the effect of unsteady pressure waves on the measurement chamber. In a strain-gaged diaphragm there would be no support rods necessary, except if baffles are used.

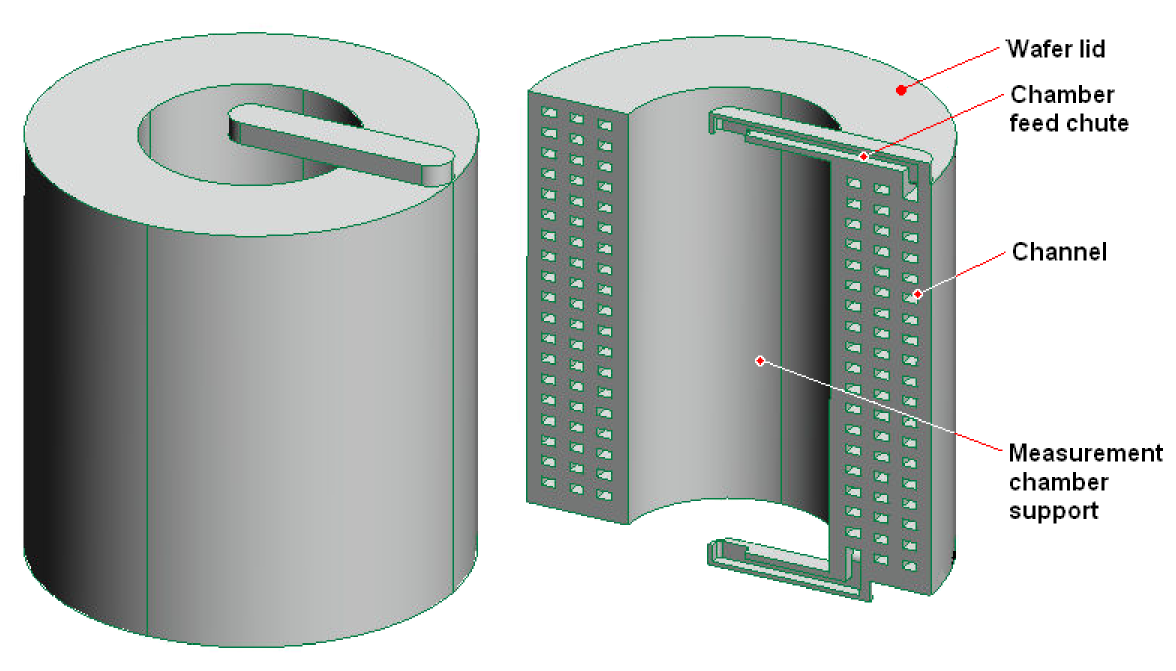

Figure 2.7: Set of bonded wafers showing the top and bottom chamber feed chutes. Half-sectioned view on the right shows channel detail.

2.5 Bladder system

A gas-filled bladder system is also included to perform the following functions:

1) Allow for expansion of the working fluid. The thermal volumetric expansion coefficient of mercury is significant at $1.82\text{x}10^{4}$ K^{-1}. This is considerably higher than glass or silicone, which is what the channels will probably be fabricated from. Without the bladder present, the sensor stands risk of bursting at higher temperatures than it was filled at. Conversely, evaporation bubbles may form inside the channels under lower temperatures that at which the sensor was filled at. The use of a bladder will provide for this volume change by compression and expansion of the gas inside it.
2) Provide passive damping of wandering pressure waves inside the fluid. The differential pressure applied inside the sensor is low relative to the yield of the material and low damping materials are used. The deformation and damping contributed by the wall material may therefore not be sufficient to obtain a favorable pressure transient response. The bladder will be much more deformable with higher damping.
3) Allow for bleeding of the working fluid during assembly to avoid gas bubbles in the channels. Any bubbles in the channels will be very undesirable since a gas-fluid boundary will result in surface tension, which in turn will cause considerable flow losses. Gas also has a significant effect on the pressure wave propagation.
4) Pre-pressure the working fluid to alleviate under-pressure problems, which also causes localized boiling of the fluid. This is caused by the dropping pressure on the one side of the diaphragm, which compromises fluid column continuity and may even cause cavitation of the channel walls.

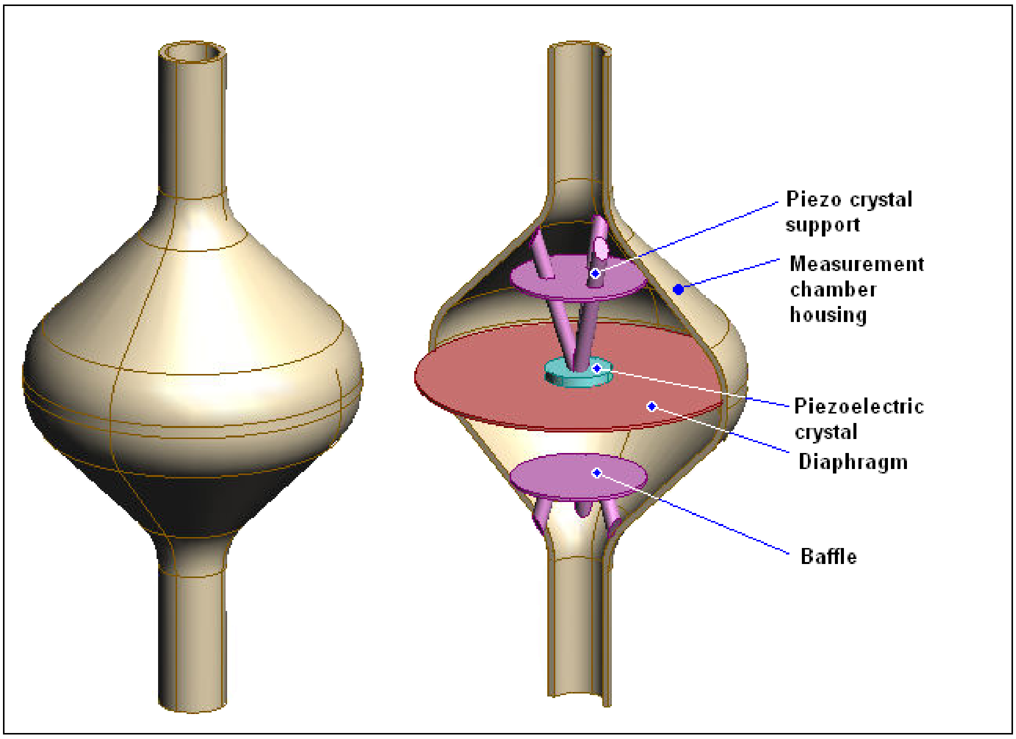

Figure 2.8: Pressure transducer chamber.

An illustration of the bladder is shown in figure 2.9. The gas filled bladder is shown in a slender thoroidal shape. The bladder will require a sealed interface to the outside for filling of the gas. The bladder will have one inlet (not shown) leading to the measurement chamber to allow exchange of working fluid. This interface has to be designed to also allow pressure waves to enter the bladder and thus achieve damping. A third inlet may be required for additional working fluid during the bleeding operation in the assembly of the sensor. The bladder may also be installed inside the measurement chamber to simplify the assembly. All the necessary inlets would then be installed on the measurement chamber walls.

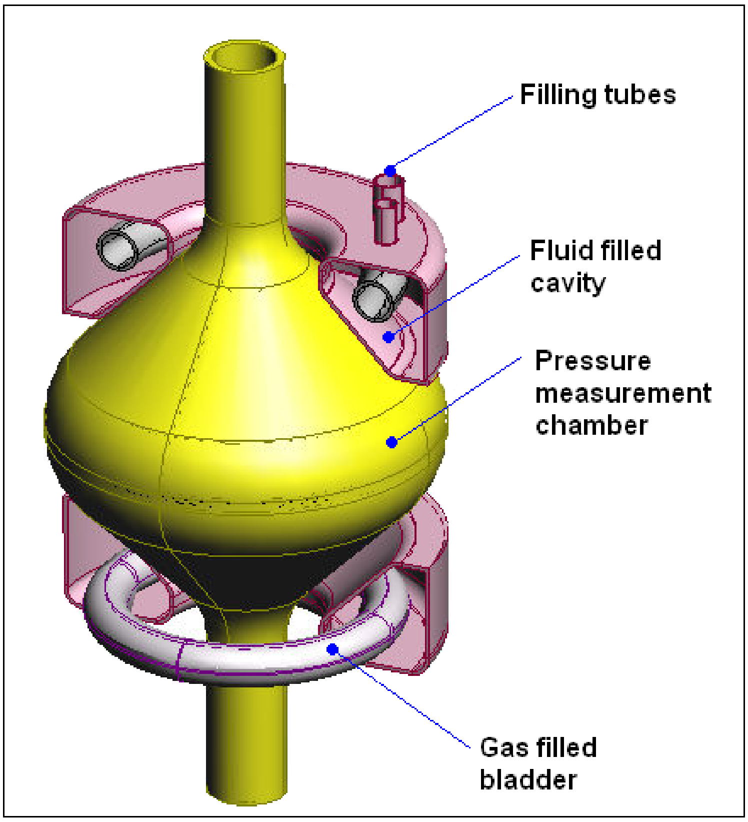

Figure 2.9: Two installed bladders, above and below the measurement chamber.

Figures 2.10 and 2.11 show the integrated sensor, which will be hermetically sealed with high internal pressure. Using a closed fluid column in this manner prevents linear acceleration from causing differential pressure in the measurement chamber. Only an angular component in acceleration around the sensitive will cause a differential pressure by means of the inertia of the working fluid. Maximizing the length of channel perpendicular to the local acceleration field, (within the limits of imposed constraints) maximizes the differential pressure generated in the sensor.

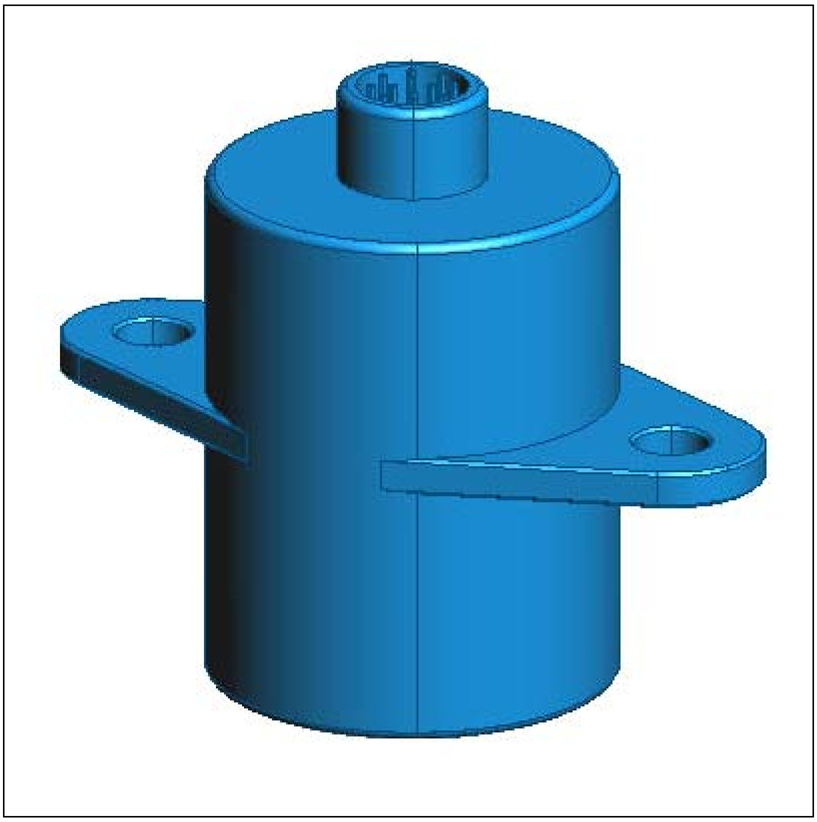

Figure 2.10: Sensor packaging.

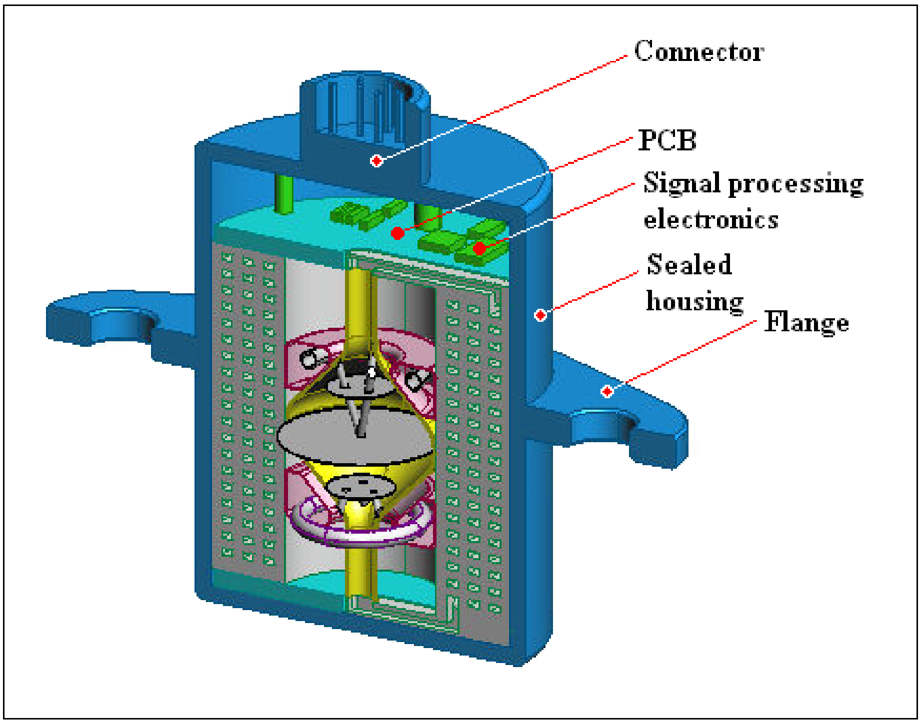

Figure 2.11: Section view of whole MFCAA sensor assembly.

Chapter 3

Pressure generation and propagation theory

3.1 Introduction

The only purpose the spiral has in the angular accelerometer is creating the maximum possible pressure differential in the smallest possible space. Increasing the differential pressure generated across the diaphragm per unit angular acceleration is the key method for increasing sensor scale factor. Pressure generation is therefore central to the function of the MFCAA. The relation of fluid pressure in a finite length closed channel to the imposed angular acceleration on the channel is covered in this chapter.

The aims of this chapter are:

1) The development of a method for the description of channel characteristics that is amenable to quick calculation for use in optimization.
2) Modeling of the pressure inside the channels (both transient and steady state) for real fluids and channel wall materials.

An angular accelerometer utilizes inertia to measure angular acceleration. Exactly the same method is used universally in linear accelerometers, except that linear inertia is the mechanism and not rotational inertia. In recent years some angular accelerometers have been constructed by directly mounting two linear accelerometers a known distance apart to measure angular acceleration. Any accelerometer (be it angular or linear) uses linear inertia on a fundamental level to measure acceleration. To make this simple connection consider the length of a circular arc, which is:

$$s = r\theta \tag{3.1}$$

where r is the radius of the arc, s is the arc length and θ is the arc angle in radians. Differentiating s with respect to time gives:

$$\frac{d^2}{dt^2}s = r\frac{d^2}{dt^2}\theta$$

$$\Rightarrow \quad a = \alpha\ r \tag{3.2}$$

with α the angular acceleration and a the tangential acceleration in the channel. Equation 3.2 states that the magnitude of linear acceleration, due to rotational acceleration increases linearly with the radius of rotation. Using this information from the outset to design an angular accelerometer makes it possible to design a more sensitive and compact angular accelerometer than those derived from linear accelerometers.

Since most of the curves worked with (in deriving their pressure potential) will be spiral in nature, it is logical to expect that the curves would need to be expressed in polar co-ordinates to efficiently handle them. In textbook calculus the applications for polar co-ordinates are usually clear-cut polar graphs to explain their usefulness best, but unfortunately the boundaries fade for this application. The expression of some seemingly “polar-natured” curves (like an off-centre circle) is an unexpected laborious matter in polar co-ordinates, while it is simple in Cartesian co-ordinates.

Some equations will thus need to be transformed from Cartesian co-ordinates into the polar system. For this purpose, the following equations that relate Cartesian to polar co-ordinates are useful.

$$x = r \cos\theta = f(\theta)\cos\theta \tag{3.3}$$

$$y = r \sin\theta = f(\theta)\sin\theta \tag{3.4}$$

From equations 3.3 and 3.4, the polar equation for any Cartesian curve can be derived. Furthermore, the slope of a straight line can be related to its polar angle by:

$$m = \frac{y}{x} = \tan\theta \tag{3.5}$$

According to Pythagoras, the distance of any point from the origin is:

$$r = \sqrt{x^2 + y^2} \tag{3.6}$$

3.2 Pressure generated by angular acceleration

Fluid pressure in a static body of fluid close to earth changes with the depth of the body of fluid along the gravity vector. The equation describing this pressure is:

$$\Delta P = \rho \ a_{dif} \ \Delta h \tag{3.7}$$

with ΔP the pressure difference between the two points in question, a_{dift} the acceleration differential and Δh is the difference in pressure potential height between the two points. The fluid density is ρ.

In equation 3.7, the pressure is generated due to earth's gravity field or applied acceleration, but it could also be generated by kinematical acceleration of the fluid as in section 2.1. Analogous to equation 3.7, if a fluid in a straight channel of finite length ΔL is accelerated linearly, without any rotation or gravity present, the pressure difference between the two endpoints of the channel is:

$$\Delta P = \rho \ a \ \Delta L \ \cos\varepsilon \tag{3.8}$$

with ε the angle between the linear acceleration field and the channel, and a the linear acceleration. Equation 3.8 is of course written on the assumption that the linear acceleration is constant in the entire channel, but according to equation 3.2 this is often not the case when rotational acceleration is present. Another complication is that a straight channel is likely to constitute a small portion (or none) of the total spiral length. The solution to both these problems is the creation of a Riemann sum to derive an integration formula. With a Riemann sum, the curve can be meaningfully divided into small pieces that are easy to handle mathematically and then added up to derive the integral, or directly added numerically in a computer routine. Consider a general curve in a plane as depicted in figure 3.1.

When the curve is divided up into small pieces, it is reasonable to assume firstly, that each small piece approximates a straight line, which will comply with the assumption of equation 3.7. In addition to this, each line segment (a distance r from the centre of rotation) is then inside an approximately constant acceleration field. Therefore, provided a small line segment is considered, the pressure difference that a segment of line contributes is well approximated by equation 3.8.

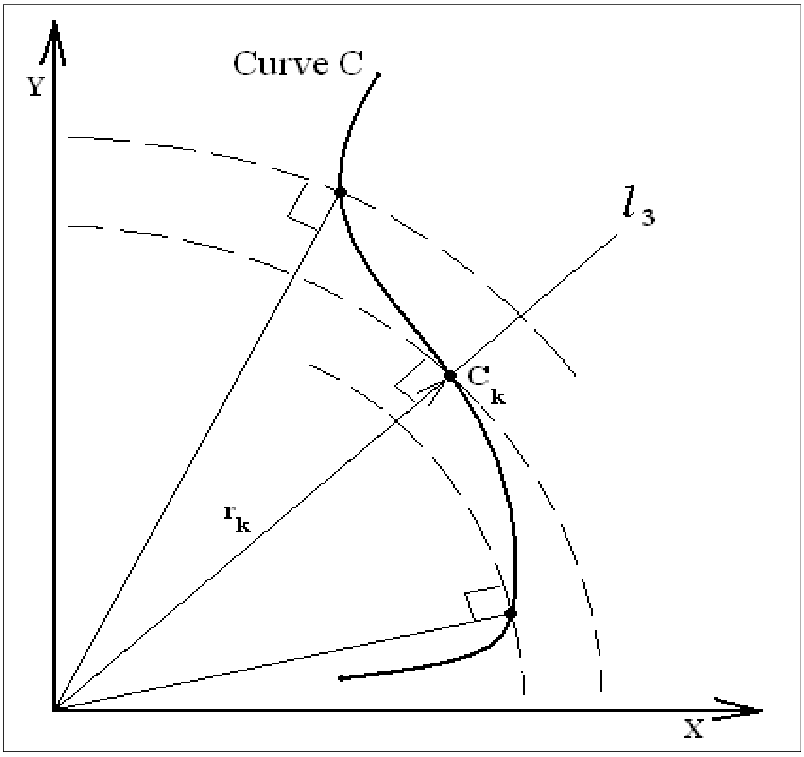

Figure 3.1: A two dimensional curve in a plane that contains an angular acceleration field about the origin.

In figure 3.1, line l_3 from the origin intercepts the curve C at the point C_k. Two other intercepts are also shown. An arc about the origin, which is placed at the centre of rotation of the proposed spiral, defines the local acceleration field. The placement of this arc relative to the spiral is arbitrary (as far as the integral of pressure generation is concerned), if the sensor is successful at disregarding linear acceleration effects. It is prudent to base the decision of origin placement on the effort required to describe the entire spiral from that proposed position. If the point C_k is considered closer on an infinitesimal scale, it would correspond to the schematic shown in figure 3.2:

Line l_1 is the infinitesimal line segment at point C_k.
Line l_2 is the direction of the local acceleration field of point C_k.
Line l_3 runs from the origin to C_k and is orthogonal to l_2.

Equation 3.2 is substituted into equation 3.7 to yield, for the k'th segment:

$$\Delta P_k = \rho \; r_k \alpha \; \Delta L_k \cos \varepsilon_k \tag{3.9}$$

Equation 3.9 states the pressure contributed by one infinitesimal channel segment in the channel for a general case.

3.3 Spiral length

The following derivation conveys the spiral length in terms of both Cartesian and polar co-ordinates and is taken from Ellis and Gulick (1994). This is expanded separately to provide the length of the fluid column resulting from a spiral. The development of the length formula is first made in Cartesian co-ordinates and then transformed to polar co-ordinates.

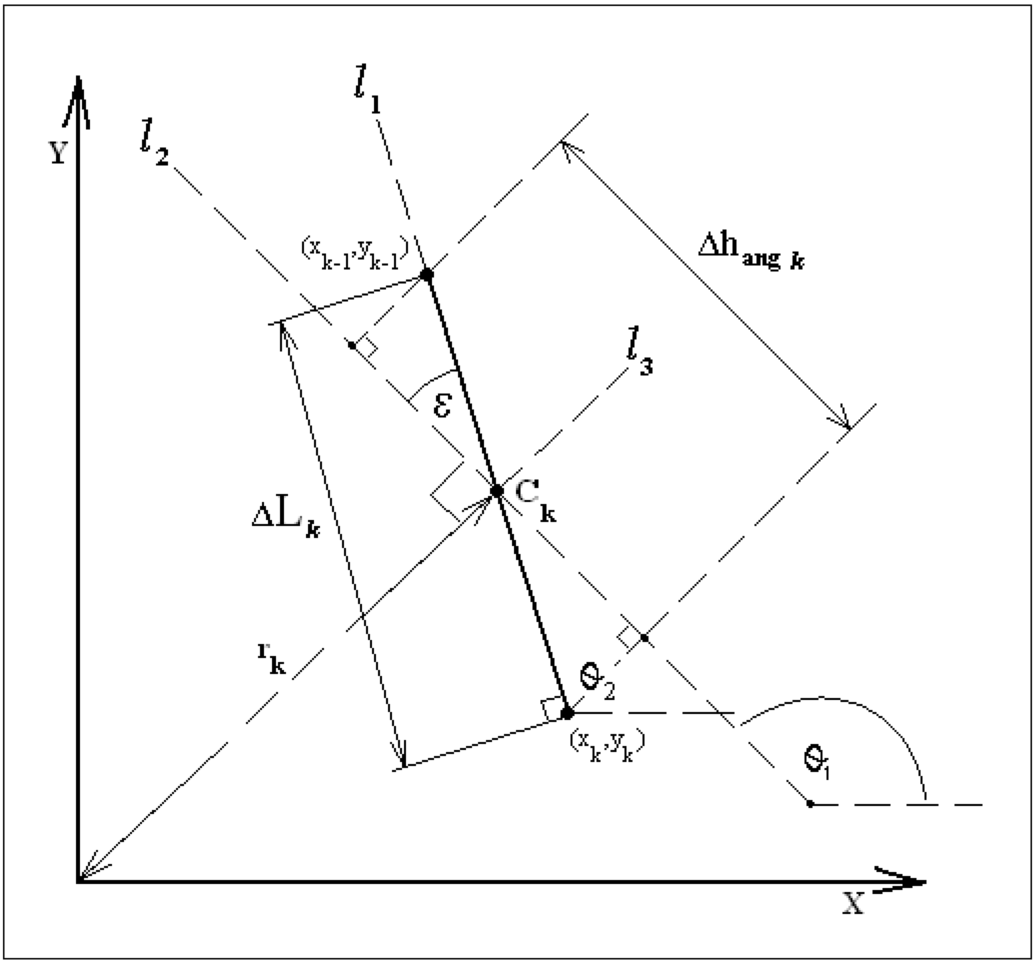

Figure 3.2: View of infinitesimal line segment at point C_k.

Suppose the channel curve *C* is parametrically represented by:

$$x = f(t) \quad \text{and} \quad y = g(t) \quad \text{for} \quad a \leq t \leq b$$

where both the functions have continuous derivatives on $[a,b]$. Now let $P = \{t_0, \ t_1, \ \ldots\ldots \ t_n\}$ be a partition of $[a,b]$ and for $1 \leq k \leq n$ let $(x_k, y_k) = (f(t_k), f(t_k))$ be the corresponding point on *C*. Let ΔL_k be the portion of the curve joining (x_{k-1}, y_{k-1}) and (x_k, y_k). If Δx_k is small, ΔL_k is approximately equal to the line segment joining (x_{k-1}, y_{k-1}) and (x_k, y_k), or in other words:

$$\Delta L_k \approx \sqrt{(x_k - x_{k-1})^2 - (y_k - y_{k-1})^2}$$

By the Mean Value Theorem $= \sqrt{(f(t_k) - f(t_{k-1}))^2 - (g(t_k) - g(t_{k-1}))^2}$ there are numbers t'_k and t''_k in $[t_{k-1}, t_k]$ such that $f(t_k) - f(t_{k-1}) = f'(t'_k)\ \Delta t_k$ *and* $g(t_k) - g(t_{k-1}) = g'(t'_k)\ \Delta t_k$. Therefore the total length L of the graph of the curve ΔL_1, ΔL_2 ….. , ΔL_3, should be approximately:

$$\sum_{k=1}^{n} \sqrt{[f'(t'_k)]^2 + [g'(t''_k)]^2} \ \ \Delta t_k \tag{3.10}$$

Now follows that:

$$\lim_{\|P\| \to 0} \sum_{k=1}^{n} \sqrt{[f'(t'_k)]^2 + [g'(t''_k)]^2} \ \ \Delta t_k = \int_a^b \sqrt{[f'(t'_k)]^2 + [g'(t''_k)]^2} \ \ dt$$

Therefore the length of the curve can be defined as:

$$\therefore \qquad L = \int_a^b \sqrt{[f'(t_k')]^2 + [g'(t_k'')]^2} \; dt$$

which is in Leibniz notation expressed as:

$$L = \int_a^b \sqrt{\left(\frac{dx}{dt}\right)^2 + \left(\frac{dy}{dt}\right)^2} \; dt \tag{3.11}$$

In equation 3.11, t represents any parameter, and may be θ as well. So if a nonnegative polar graph is considered on $[\alpha, \beta]$, equation 3.11 can be applied if f' is continuous on $[\alpha, \beta]$. Then the length is defined in Cartesian co-ordinates as:

$$L = \int_\alpha^\beta \sqrt{\left(\frac{dx}{d\theta}\right)^2 + \left(\frac{dy}{d\theta}\right)^2} \; d\theta$$

But from equations 3.3 and 3.4:

$$x = r \; \cos\theta = f(\theta)\cos\theta$$

$$y = r \; \sin\theta = f(\theta)\sin\theta$$

By differentiating the terms it yields:

$$\begin{aligned} L &= \int_\alpha^\beta \sqrt{[f'(\theta)\cos\theta - f(\theta)\sin\theta]^2 + [f'(\theta)\sin\theta + f(\theta)\cos\theta]^2} \; d\theta \\ &= \int_\alpha^\beta \sqrt{(f'(\theta))^2\left(\cos^2\theta + \sin^2\theta\right) + (f(\theta))^2\left(\sin^2\theta + \cos^2\theta\right)} \; d\theta \\ &= \int_\alpha^\beta \sqrt{(f'(\theta))^2 + (f(\theta))^2} \; d\theta \end{aligned}$$

So the length of a polar graph is given by:

$$L = \int_\alpha^\beta \sqrt{(f'(\theta))^2 + (f(\theta))^2} \; d\theta$$

and in Leibniz notation it becomes:

$$L = \int_\alpha^\beta \sqrt{r^2 + \left(\frac{dr}{d\theta}\right)^2} \; d\theta \tag{3.12}$$

3.4 Angular pressure potential

The formula for pressure potential of a spiral is now derived. First, the angular pressure potential is defined in general:

$$h_{ang} = \frac{P}{\rho \; \alpha} \tag{3.13}$$

with P the pressure generated by the spiral or helix, ρ the fluid density and α the angular acceleration imposed on the spiral in rad/s^2. h_{ang} has the unit m^4/rad. The angular pressure potential is defined in this manner to obtain the same equation form as for linear pressure potential, which is defined by a rearrangement of equation 3.7:

$$h_{lin} = \frac{\Delta P}{\rho \ a}$$

Formulas for $\mathrm{h}_{\mathrm{ang}}$ will now be derived for any curve that is expressed in either Cartesian or polar form.

3.4.1 Pressure potential in Cartesian coordinates

The derivation for a Cartesian curve is included here for cases where a polar equation of a channel is not available. In some cases, a graph that is simple in Cartesian form is not even a function in polar form (the converse is also true). As may be expected intuitively, the derivation of the pressure potential is quite involved in Cartesian form due to the polar nature of angular acceleration.

Consider equation 3.9: $\Delta P_k = \rho \ r_k \alpha \ \Delta L_k \cos \varepsilon_k$

If the density and acceleration terms are taken to one side of the equation to rearrange to the form of equation 3.13, it yields.

$$\frac{\Delta P_k}{\rho \ \alpha} = \Delta h_{ang \ k} = r_k \ \ \Delta L_k \ \ \cos \varepsilon_k \qquad (3.14)$$

The partition $P = \{t_0, t_1, \ldots\ldots\ldots, t_n\}$ of $[a,b]$ on $1 \le k \le n$ used in section 3.3 is also valid here, so the length ΔL_k that has already been derived in equation 3.10 may be substituted:

$$\Delta h_{ang \ k} = r_k \ \sqrt{[f'(t'_k)]^2 + [g'(t''_k)]^2} \ \ \cos \varepsilon_k \ \ \Delta t_k$$

Equation 3.6 is now substituted for the radius of each segment:

$$\begin{aligned} h_{ang \ k} &= \sqrt{[f(t_k)]^2 + [g(t_k)]^2} \ \sqrt{[f'(t'_k)]^2 + [g'(t''_k)]^2} \ \ \cos \varepsilon_k \ \ \Delta t_k \\ &= \sqrt{\left[[f(t_k)]^2 + [g(t_k)]^2\right] \ \left[[f'(t'_k)]^2 + [g'(t''_k)]^2\right]} \ \cos \varepsilon_k \ \ \Delta t_k \qquad (3.15) \end{aligned}$$

Strictly speaking, $\sqrt{[f(t_k)]^2 + [g(t_k)]^2}$ is the radial position of the one end of the segment and not the centre of the segment. The assumption is reasonable though for a fine partition.

The core of the rest of the derivation is finding ε, the angle between the channel and the local acceleration. To find ε for each segment, it is best to simplify ε as a function of a single variable so that integration can be performed. ε is expressed first in terms of the slopes of the lines l_1 and l_2 (in figure 3.2).

Firstly, from the trigonometric identity:

$$\tan(A \pm B) = \frac{\tan A \ \pm \ \tan B}{1 \ \mp \ \tan A \tan B}$$

$$\therefore \ \tan \varepsilon \ = \ \tan(\theta_2 - \theta_1) = \frac{\tan \theta_2 - \tan \theta_1}{1 + \tan \theta_1 \tan \theta_2}$$

where θ_1 and θ_2 is defined in figure 3.2. But from equation 3.5:

$$\tan\ \theta_n = m_n$$

$$\Rightarrow \tan \varepsilon_k = \frac{m_2 - m_1}{1 + m_1 m_2} \tag{3.16}$$

This applies only where the two lines l_1 and l_2 are:

- Not perpendicular: because the product of the slopes equals –1 and thus makes the denominator zero.
- Non-vertical: because slope is infinite for vertical lines in Cartesian co-ordinates.

Line l_1 is on the integrated function, so m_1 is simply *f'(x)*. Line l_2 is not dependent on the function, but rather on its position relative to the origin. This complicates matters even more, and is a further reason why polar equations are more readily integrated for the pressure potential of the spiral. The gradient of l_2 for each line segment has to be found by locating to one end of the segment in both x and y co-ordinates, which is now done.

If the angle is taken from point *k* on the partition, the gradients for point *k* is:

$$m_{3k} = \frac{y_k}{x_k}$$

Lines l_2 and l_3 are perpendicular so:

$$m_{2k}\ m_{3k} = -1$$

$$\therefore m_2 = \frac{-x_k}{y_k} \tag{3.17}$$

Equation 3.17 is substituted into 3.16 and solved for ε:

$$\varepsilon_k = \tan^{-1}\left[\frac{\left(-{x_k}/{y_k}\right) - f'(x_k)}{1 - f'(x_k)\left({x_k}/{y_k}\right)}\right] \tag{3.18}$$

Equation 3.18 is now in turn substituted into equation 3.15, and the result is:

$$h_{ang\ k} = \sqrt{\left[[f(t_k)]^2 + [g(t_k)]^2\right]\ \left[[f'(t_k')]^2 + [g'(t_k'')]^2\right]}\ \cos\left[\tan^{-1}\left[\frac{\left(-{f(t_k)}/{g(t_k)}\right) - f'(t_k)}{1 - f'(t_k)\left({f(t_k)}/{g(t_k)}\right)}\right]\right] \Delta t_k \tag{3.19}$$

The limit is now taken where the partition size approaches zero:

$$\lim_{\|P\|\to 0} \sum_{k=1}^{n} \sqrt{\left[[f(t_k)]^2 + [g(t_k)]^2\right]\ \left[[f'(t_k')]^2 + [g'(t_k'')]^2\right]}\ \cos\left[\tan^{-1}\left[\frac{\left(-{f(t_k)}/{g(t_k)}\right) - f'(t_k)}{1 - f'(t_k)\left({f(t_k)}/{g(t_k)}\right)}\right]\right] \Delta t_k$$

resulting in the integral:

$$h_{ang} = \int_a^b \sqrt{\left[[f(t)]^2 + [g(t)]^2\right]\ \left[[f'(t)]^2 + [g'(t)]^2\right]}\ \cos\left[\tan^{-1}\left[\frac{\left(-{f(t)}/{g(t)}\right) - f'(t)}{1 - f'(t)\left({f(t)}/{g(t)}\right)}\right]\right] dt \tag{3.20}$$

3.4.2 Pressure potential in polar coordinates

Taking equation 3.14 again: $h_{ang\ k} = r_k\ \Delta L_k\ \cos\varepsilon_k$

The first variable r is already in the correct form for integration in polar co-ordinates since r is already a function of angle for a polar graph. A formula for ΔL_k has also been derived (equation 3.12), so the only outstanding variable to be elaborated on is ε_k.

From figure 3.2 it is found that, for a fine partition:

$$\tan\varepsilon = \frac{dr}{rd\theta}$$

$$\therefore \quad \varepsilon = \tan^{-1}\left(\frac{dr}{rd\theta}\right) = \tan^{-1}\left(\frac{f'(\theta)}{f(\theta)}\right) \tag{3.21}$$

If equation 3.12 and equation 3.21 is substituted into equation 3.14 and the limit taken as before:

$$h_{ang} = \int_\alpha^\beta f(\theta)\ \sqrt{(f'(\theta))^2 + (f(\theta))^2}\ \cos\left[\tan^{-1}\left(\frac{f'(\theta)}{f(\theta)}\right)\right] d\theta$$

or in Leibniz notation:

$$h_{ang} = \int_\alpha^\beta r\ \sqrt{\left(\frac{dr}{d\theta}\right)^2 + r^2}\ \cos\left[\tan^{-1}\left(\frac{dr}{rd\theta}\right)\right] d\theta \tag{3.22}$$

This equation is clearly a lot simpler than equation 3.20. This may often be reason enough to go to considerable lengths to get a Cartesian equation into polar form. When coding spirals in a finite difference procedure, equation 3.16 may be used directly from Cartesian coordinates to find ε_k, so the trouble of using either equation 3.20 or equation 3.22 is avoided. When doing this, the following must be ensured:

1) Care must be taken to comply with the caveats of equation 3.16. The first requisite of non-verticality is easily ensured by using an angular difference between two consecutive points as a fraction of π. The irrational nature of π makes a vertical line element very unlikely. The second requisite of non-perpendicularity has to be satisfied by an exclusion statement in the routine that assumes full efficiency of rotation-centered circles.

2) Each element must be sufficiently small to make the finite difference procedure feasible. When calculating general spiral characteristics, an angular difference between two consecutive points of $\pi/100$ (31 mrad) was found to give sufficient accuracy (without overwhelming a standard 2004 AMD-based personal computer).

3.5 Pressure propagation in the channels

The generation of pressure potential is only part of the theory required to simulate channel operation. If incompressibility of the working fluid is assumed (as in the case for flow), the speed of wave propagation through the fluid has to be infinite. This is of course not possible. The assumption of infinite wave speed (which results in a relation of pressure to acceleration the same as in equation 3.7) would result in a grossly over-optimistic time response of the sensor. Depending on the length of the channels used, the realization of the maximum pressure potential for constant angular acceleration input may take considerable time. The main challenge of the sensor's modeling is to capture the time dependence of all variables accurately.

In this section the following objectives are set:

- To find an accurate relation of the differential pressure generated across the diaphragm due to an arbitrary angular acceleration input to the sensor channels.
- To obtain theory for the propagation of the pressure beyond the confines of the measurement section where the diaphragm is situated, and to understand the propagation of pressure waves past imperfections in the channel and changes in cross sectional area.

All fluids are compressible to a greater- (in the case of gasses) or lesser extent (in the case of liquids). The compressibility of a liquid is defined as the change in fluid pressure experienced because of a change in volume (without the addition of liquid):

$$\Delta P = K\frac{\Delta V}{V} \tag{3.23}$$

where K is called the bulk modulus of the liquid. The bulk modulus is quite similar to the modulus of elasticity (Young's modulus) used for solids. The bulk modulus is also assumed as linear around the state of rest, which is generally taken to be atmospheric pressure. The formation of a wave through a liquid when pressure is applied to a fluid is partially due to the presence of this inherent compressibility and also in part due to deformation of the fluid container.

The analysis of pressure wave propagation through matter can be subdivided into two main sub-categories, steady harmonic excitation and arbitrary excitation. Harmonic excitation theory originated primarily through the study of sound of which a major contributor was Lord Rayleigh with his 1877 treatise "The Theory of Sound". Later (in the twentieth century) the theories of harmonic pressure propagation through fluids were considered more closely. Publications of pressure wave propagation are ever expanding to account for novel materials and boundary conditions.

3.5.1 Harmonic excitation models

The main advantage of using a harmonic excitation as input to the system is the simplifying assumption of harmonic output. This allows an analytically exact answer from the Partial Differential Equations (PDEs) for a linear infinite degree of freedom system and yields a very useful result for many engineering disciplines. Of these, acoustics and electricity are the principal ones.

The earliest authors recognized the analogy between general vibration and sound propagation. Henceforth some of the results obtained from harmonic assumptions are directly applicable in the pressure propagation through the sensor's channels. Rayleigh derived solutions for the longitudinal vibration of a bar for the two cases of both extremities being either fixed or free. The fixed-fixed scenario is more comparable to the fluid column used than the free-free case. For the ends-fixed bar model a result for the deflection of any point in the bar is given as the infinite series:

$$\delta = \alpha \frac{x}{L} + \sum_{i=1}^{\infty} \sin \frac{i\pi x}{L} \left[A_i \cos \frac{i\pi at}{L} + B_i \sin \frac{i\pi at}{L} \right] \tag{3.24}$$

where δ is the displacement at a point x along the bar of length L. A and B are arbitrary constants found by application of the initial values of δ and its derivative. The speed of sound wave propagation is a. For the case of both extremities of the bar being free, the first term of equation 3.24 is simply omitted.

Equation 3.24 results in a series of tones (or harmonic scales, one for every integer i) of which the one with lowest frequency and longest wavelength is for $i = 1$. The period of this fundamental wave is the time taken for the wave to travel twice the length of the rod. Although this solution cannot directly be used in the modeling of the pressure propagation in the channels, it allows the important deduction that the lowest natural frequency of the system is directly linked to the speed of wave propagation by:

$$a = \frac{L\omega_n}{\pi} \tag{3.25}$$

where ω_n is the fundamental (lowest) natural frequency of the system in radians/second.

3.5.2 Pressure wave speed in a fluid

The speed of wave propagation in a fluid predicted in equation 3.25 is not of much use unless the fundamental frequency of the system is known. A formula for the wave speed propagation based on fluid properties is therefore required. The result is taken from theory in the study of the waterhammer phenomenon, which occurs in pipes when any change in flow rate occurs. For the complete derivation refer to Pickford (1969).

Pickford relates the wave speed for fluid in a rigid channel as:

$$a = \sqrt{\frac{K}{\rho}} \tag{3.26}$$

Pickford also gives the speed of wave propagation for other boundary conditions. Stiffer pipes may cause faster fluid propagation only up to the maximum value predicted by equation 3.26 for a rigid pipe. A more in-depth analysis of the channel array may show that channel deflection causes flow in adjacent channels. This implies that wave propagation may not only be due to applied acceleration but also due to inter-channel relationships. These effects are assumed to be negligible in the current analysis and this assumption may be improved upon in subsequent work done on the matter. The influence of the wall material type and channel support method on the wave speed can however not be neglected since the effect is undisputedly large. The impact of pipe stiffness on the wave speed velocity is included by means of a modified bulk modulus. Taking into account the longitudinal and circumferential stresses and strains in an elastic cylindrical pipe, the modified bulk modulus of the fluid filled pipe is:

$$\frac{1}{K'} = \frac{1}{K} + \frac{dc}{eE} \tag{3.27}$$

where d is the pipe inside diameter and e is the pipe wall thickness while c is a constant dependent on the method of pipe anchoring:

$c = 1$ in cases where the longitudinal stress is negligible

$c = \left(\frac{5}{4} - \nu\right)$ for a pipe free to move longitudinally

$c = 1 - \nu^2$ for a pipe constrained against longitudinal movement

$c = 1 - \frac{\nu}{2}$ for a pipe with expansion joints

The wave speed in an elastic pipe becomes:

$$a = \sqrt{\frac{K'}{\rho}} = \sqrt{\left(\frac{\rho}{K} + \frac{\rho d c}{e E}\right)^{-1}} \tag{3.28}$$

From equation 3.28 the wave speed is seen to be dependent on:

1) Pipe size: a smaller diameter results in larger wave speed. This is a direct result of a smaller pipe having greater stiffness than a larger pipe with the same wall thickness. Thicker walls result in a higher wave speed.

2) Liquid: the density and bulk modulus of the liquid is important.

3) Pipe material stiffness: Young's modulus varies greatly in materials used for pipes. Polycrystalline silicon used commonly to do etching has a modulus of 168GPa and glass (also used for fabrication of microfluidic channels) has a Young's modulus of 48-83 GPa.

4) Temperature: the density and bulk modulus of fluids are affected by temperature and therefore the wave speed as well.

5) Pressure: at high pressures the bulk modulus tends to increase which increases the wave speed. The pressures implied here are too high to be of use inside the sensor.

6) Free gas in fluid: gas will cause a marked drop in bulk modulus. Whether or not this results in extra damping is dependent on the flow caused by the lower modulus.

3.5.3 Wave damping in a fluid

The chief reason for pressure loss in fluids is the presence of shear. Sir Rayleigh did an analysis of wave attenuation in fluids due to viscosity. To simplify the analysis, Rayleigh assumes harmonic input and thus may assume that the axial flow in the channel varies as:

$$u = Ae^{-ax}\cos(nt - \beta x)$$

where:

$$\beta^2 - \alpha^2 = \frac{n^2 a^2}{\alpha^4 + \frac{16\nu^2 n^2}{9}} \quad \text{and} \quad 2\alpha\beta = \frac{4\mu n^3 \big/ 3\rho_0^2}{\alpha^4 + \frac{16\nu^2 n^2}{9}}$$

The coefficient of decay is α. For most fluids (and especially mercury) the magnitude of ν is small and thus its square is negligible. Furthermore, the factor n is replaced by $2\pi a\lambda^{-1}$ (with λ the wave length) to yield:

$$\alpha = \frac{8\pi^2 \nu}{3\lambda^2 a}$$

This shows that the coefficient of decay is strongly dependent on the wavelength. Shorter wavelength waves will decay sooner and over shorter distances. The decay constant can also be represented versus frequency where $f = a\lambda^{-1}$:

$$\alpha = \frac{8\pi^2 \nu \ f^2}{3a^3}$$

In mercury, the following is valid:

$a = 1450 \ \ m/s$

$\mu = 1.56 \text{ x}10^{-3} \ \ Ns/m^2$

$\rho = 13550 \ \ kg/m^3$

If an input frequency of 100Hz is assumed, a very small α of 3.92x10^{-10} results. The time for the pressure wave to damp out half of its amplitude, based only on fluid shear, is then >1.2e6 seconds. In this time the wave will have traveled a total length of >1.7e9 m. The damping to be expected in the frequency range where the sensor will be operated is clearly negligible.

Damping of pressure waves is greatest when acoustical waves of high frequency are sent through fluids. Of course, other mechanisms for wave damping exist. The main damper of waves in the MFCAA is flow caused by the strain of the diaphragm. Deformation of the fluid container may also present damping and the designer can introduce chambers where damping is added similar to surge tanks that damp out pressure waves.

If considerable oscillation of induced pressures is still present, other measures may be taken to “clean up” the pressure signal, which include:

- The flow area expansions necessary for transition from the channel diameter to the diaphragm diameter will afford considerable reflection of the pressure wave.
- A wave reflection baffle inside the test section to prevent waves from reaching the diaphragm.
- Places of wave reflection can be inserted in the channel at intervals to create high frequency standing waves that damp out more rapidly than the applied acceleration input frequency.

The low inherent damping of the fluid column is in a sense fortunate for the designer of the sensor since it provides some control over the damping that is present. The added damping may assume the form of a passive unit inside the sensor or an active control loop. The clear result of this analysis is that the matter of damping in the channels cannot be ignored. If no extra damping is present, the pressures fed to the measuring chamber will accumulate into a gradually increasing noise floor, since acceleration long gone still make itself felt through transient pressures at the diaphragm.

3.5.4 Arbitrary pressure excitation models

Finding a solution to the pressure at any position in a channel for an arbitrary acceleration cannot be approached as easily in an analytical manner as the case for the steady harmonic input. The options available to model the pressure is:

1) **The use of Computational Fluid Dynamics (CFD) in a time-marching scheme:** This would also consider all flow characteristics, and thus make any need for further flow theory redundant. The CFD software would have to be able to simulate

compressibility (wave propagation) in addition to flow if the whole sensor model is to be included. A numerical solution, via CFD in a time-marching scheme is possible, but requires massive computational power and coding to efficiently calculate results in an optimization routine. Each optimization run would require its own solution convergence and if the optimization is to run independently from user-input, many 3D models and meshes will have to be computer generated. The result obtained from a CFD calculation will also (at best) be in the time domain; the user will have to write postprocessing code in order get the required result. Another limitation of contemporary CFD is the types of boundary conditions available, which does not yet include unsteady pressure inlets and outlets. CFD does however provide a convenient method for a supplementary answer to the flow theory of chapter 5 in the case of unsteady flow for a step pressure input.

2) **A single degree of freedom (SDOF) approximation of the acceleration to pressure transfer function:** A simple second order system results for which the theory is simple and fast to code and process in a computer. This method stands at the opposite extreme of the CFD option and is an over-simplification of the pressure propagation at work here. This would give an idea of the pressure transients involved if formulated properly, but since proper reformulation of the second order model is needed to fit the fluid column anyway, another model that better represents the infinite DOF fluid column is more suited

3) **A multi degree of freedom (MDOF) model of the fluid in the channel:** The MDOF system is an apt analogy for the pressure propagation taking place within the channels because the compression of the fluid closely resembles the compression of springs between masses. The connection between the one dimensional MDOF system and the three dimensional channels is possible since the designer is only interested in the differential pressure across the diaphragm (in the test section) to know what the flow potential is. The pressure in the channels is assumed only dependent on the one-dimensional length along the channel. Since the channels feed into the relatively massive test section, the dependence of the pressure upon the radial position of the channel fades, and only the integral effect is substantive. The model adopted is shown in figure 3.3.

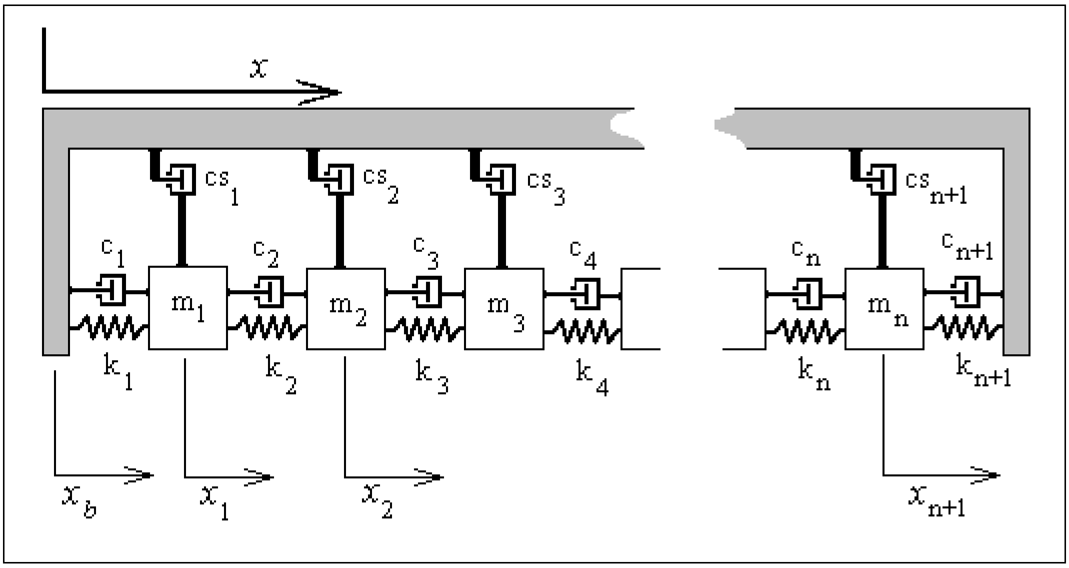

Figure 3.3: Multi degree of freedom model of pressure generation in channels.

The designer makes the decision regarding the number of masses used in the model according to the complexity of frequency response desired. The order of the MDOF model transfer function would be twice the number of degrees of freedom permitted. A minimum of four orders (for a single mass model) would exist, since the body of the sensor also constitutes a degree of freedom. The MDOF model shown in figure 3.3 is drawn as if linear acceleration is applied. This is permissible by the definition of angular pressure potential in equation 3.13, which is of the same form as equation 3.7 for the linear case. The transformation is accomplished by including channel radial displacement into the gross angular pressure potential. Each mass represents a section of the working fluid, and obeys rigid body motion caused by forces from two springs and three dampers. The springs represent the bulk modulus of the fluid, thereby permitting wave propagation. One shear damper (c_{s1} ,c_{s2}… c_{sn}) is inserted per mass to account for flow shear losses and the inter-mass dampers (c_1 , c_2...c_{n+1}) convey inter molecular damping to the system. All boundaries are assumed rigid. The deflection of the pressure transducer is handled separately from pressure generation (in chapter 6).

Requirements for MDOF approximation

To make the MDOF system similar to the infinite degree of freedom fluid column, the following requirements are set:

1) The speed of wave propagation in the MDOF system must be similar to that of the real fluid column.
2) The steady state pressure predicted must be identical to the value predicted by equation 3.13.

$$P = \rho \ \alpha \ h_{ang}$$

3) The modes of the true fluid column must be reproduced in the frequency range of interest. This will also provide a realistic transient wave shape. The range of frequency input is assumed to extend only up to 150 Hz.

3.5.5 Fluid column to spring-damper array analogy

The force exerted by a spring is by the MDOF analogy similar to the pressure experienced at a specific point in the fluid column. The number of points where the pressure is approximated by a spring is therefore only as much as the number of springs present. The only pressure in the system the designer is truly concerned with is the differential pressure across the diaphragm. The simplest model of this pressure would comprise of a single mass with a spring on either side. This will satisfy requirement two above, but probably not the rest. Provision must be made to include many degrees of freedom so that the infinite degree of freedom fluid column may be approximated and studied further.

The first relation needed is the pressure caused by a spring if its force were to be uniformly distributed to cause pressure. The predicted pressure caused by a spring is simply:

$$P_n = \frac{k_n \ \Delta x_{kn}}{A_{channel}} \tag{3.29}$$

where P_n is the pressure, k_n is the spring stiffness, $A_{channel}$ is the channel cross sectional area. In order to fulfill requirement 1, a relation must be found between the bulk modulus and the spring stiffness.

From equation 3.23:

$$\Delta P = K \frac{\Delta V}{V}$$

If the pressure is assumed to be constant across the cross section then:

$$\Delta P = K\frac{\Delta V}{V} = K\frac{\Delta L}{L} = \frac{F}{A} = \frac{k_{tot}\Delta x_{tot}}{A} \tag{3.30}$$

Hence:

$$\frac{K}{L} = \frac{k_{tot}}{A} \tag{3.31}$$

where k_{tot} is the combined stiffness of all the springs in the array and Δx_{tot} is the total deflection under force F. Furthermore, the stiffness of a set of springs in series is:

$$\frac{1}{k_{tot-series}} = \sum_{j=1}^{n}\frac{1}{k_j} \tag{3.32}$$

for a set of n springs in series. When all the springs have the same stiffness, the equation reduces to:

$$k_{tot-series} = \frac{k}{n} \tag{3.33}$$

The stiffness for each spring by this analogy is then:

$$k_n = \frac{KA\ n}{L} \tag{3.34}$$

where n is the number of springs used. The total fluid mass is divided equally between the inserted masses. The masses will then each have inertias of:

$$m_n = \frac{\rho A h_{ang}}{n-1} \tag{3.35}$$

Equation 3.35 enables conformance to the steady state pressure predicted in equation 3.13 despite the fluid column model being a linear one. The total column length would simply be substituted for the angular pressure potential, if the fluid column had been a linear one as in figure 3.3.

3.5.6 Dynamics of multi degree of freedom system

A numerical model is now derived for the discrete fluid column representation of figure 3.3. The solving of the equations of motion for the MDOF system may be done by two main methods. The first method is a matrix representation of the dynamic system into separate stiffness, mass, damping, force and displacement matrices. The matrix system is then reformulated into a set of first order differential equations called Hamilton's canonical equations to make them treatable with matrix algebra.

The second method similarly transforms the system into a set of first order differential equations, but matrix representation is done according to the State Space method (borrowed from control system theory). This may be done directly from the equations of motion. If the system is linear and time invariant (an LTI system), these matrices are constant according to the equations:

$$\begin{aligned}\dot{x} &= Ax + Bu\\ y &= Cx + Du\end{aligned} \tag{3.36}$$

where A is the system matrix or characteristic matrix which defines the system and x is the state vector. B is the input matrix defining how the input u is applied to the system. C is the output matrix and contains any constants contributing to the system output vector y, and also determines which states become outputs. D is the direct feedthrough matrix which relates the contribution of inputs that are not influenced by A but rather directly adds to the output.

In a system of N degrees of freedom the matrices will have the following sizes, representing the system as a set of N first order differential equations. Matrix A will be of size 2NX2N, which is the minimum size to fully describe the system, namely two states per degree of freedom in this one dimensional case. These two states will be displacement and velocity for this model. Matrix B will have $2N$ rows and the same number of columns as the system has inputs. With acceleration as the only input required for the system in figure 3.3, B will be a vector. C also has $2N$ rows, with columns depending on the outputs required up to a maximum of $2N$. Figure 3.3 has no direct feedthrough; hence matrix D will be an empty one of a size the same as the product of C and x.

The model starts off with the equations of motion for the system in figure 3.3:

$$\sum_{i=1}^{n} F_x = m_i\ddot{x}_i \tag{3.37}$$

$$Mass\ 1:\ -k_1(x_1 - x_b) + k_2(x_2 - x_1) - c_1(\dot{x}_1 - \dot{x}_b) + c_2(\dot{x}_2 - \dot{x}_1) + cs_1(\dot{x}_b - \dot{x}_1) = m_1\ddot{x}_1$$

$$Mass\ 2:\ -k_2(x_2 - x_1) + k_3(x_3 - x_2) - c_2(\dot{x}_2 - \dot{x}_1) + c_3(\dot{x}_3 - \dot{x}_2) + cs_2(\dot{x}_b - \dot{x}_2) = m_2\ddot{x}_2$$

$$Mass\ 3:\ -k_3(x_3 - x_2) + k_4(x_4 - x_3) - c_3(\dot{x}_3 - \dot{x}_2) + c_4(\dot{x}_4 - \dot{x}_3) + cs_3(\dot{x}_b - \dot{x}_3) = m_3\ddot{x}_3$$

$$Mass\ n:\ -k_n(x_n - x_{n-1}) + k_{n+1}(x_b - x_n) - c_n(\dot{x}_n - \dot{x}_{n-1}) + c_{n+1}(\dot{x}_b - \dot{x}_n) + cs_n(\dot{x}_b - \dot{x}_n) = m_n\ddot{x}_n$$

$$Body:\quad k_1(x_1 - x_b) - k_{n+1}(x_b - x_n) + c_n(\dot{x}_1 - \dot{x}_b) - c_{n+1}(\dot{x}_b - \dot{x}_{n+1}) + \sum_{i=1}^{n} Fcs_i = m_b\ddot{x}_b$$

The term $\sum_{i=1}^{n} Fcs_i$ in the body's equation of motion is the sum of all the shear dampers' force experienced by the body. Since N is any positive integer corresponding to the total degrees of freedom, this term can be any size (N=n +1). For the sake of this document the term is condensed. The number of terms condensed here is as many as the number of masses included in the model.

A choice is now made for the state vector x. Note that only the states contained in this vector can be used as outputs. To get equations 3.37 into state space form, a simple state vector is first chosen so that minimum manipulation is necessary. The state vector chosen is:

$$x = [x_1 \quad x_2 \quad x_3 \quad .... \quad x_n \quad \dot{x}_1 \quad \dot{x}_2 \quad \dot{x}_3 \quad .... \quad \dot{x}_n]' \tag{3.38}$$

which results in the system matrix:

$$A = \left[\begin{array}{c:c} [0] & I \\ \hdashline [J] & [F] \end{array}\right] \tag{3.39}$$

The product Ax directly simplifies to the left hand side of equation 3.37, except for the "body" equation, which accounts for the first empty row in J. The top left matrix is an empty array while I is the identity matrix that links the deflections of the various masses with their first derivatives. The dotted lines subdivide A into four sub-matrices of equal size.

The J and F matrices are:

$$J = \begin{bmatrix} 0 & 0 & 0 & 0 & 0 & \ldots & 0 & 0 \\ \frac{k_1}{m_1} & \frac{-k_1-k_2}{m_1} & \frac{k_2}{m_1} & 0 & 0 & \ldots & 0 & 0 \\ 0 & \frac{k_2}{m_2} & \frac{-k_2-k_3}{m_2} & \frac{k_3}{m_2} & 0 & \ldots & 0 & 0 \\ 0 & 0 & \frac{k_3}{m_3} & \frac{-k_3-k_4}{m_3} & \frac{k_4}{m_3} & 0 & \ldots & 0 \\ \ldots & \ldots & \ldots & \ldots & \ldots & \ldots & \ldots & \ldots \\ 0 & 0 & \ldots & 0 & \frac{k_{n-2}}{m_{n-2}} & \frac{-k_{n-2}-k_{n-1}}{m_{n-2}} & \frac{k_n}{m_{n-2}} & 0 \\ 0 & 0 & \ldots & 0 & 0 & \frac{k_{n-1}}{m_{n-1}} & \frac{-k_{n-1}-k_n}{m_{n-1}} & \frac{k_n}{m_{n-1}} \\ \frac{k_{n+1}}{m_n} & 0 & \ldots & 0 & 0 & 0 & \frac{k_n}{m_n} & \frac{-k_n-k_{n+1}}{m_n} \end{bmatrix}$$

$$F = \begin{bmatrix} 0 & 0 & 0 & 0 & 0 & \ldots & 0 & 0 \\ \frac{c_1+c_{s1}}{m_1} & \frac{-c_1-c_2}{m_1} & \frac{c_2}{m_1} & 0 & 0 & \ldots & 0 & 0 \\ \frac{c_{s2}}{m_2} & \frac{c_2}{m_2} & \frac{-c_2-c_3}{m_2} & \frac{c_3}{m_2} & 0 & \ldots & 0 & 0 \\ \frac{c_{s3}}{m_2} & 0 & \frac{c_3}{m_3} & \frac{-c_3-c_4}{m_3} & \frac{c_4}{m_3} & 0 & \ldots & 0 \\ \ldots & \ldots & \ldots & \ldots & \ldots & \ldots & \ldots & \ldots \\ \frac{c_{sn-2}}{m_{n-2}} & 0 & \ldots & 0 & \frac{c_{n-2}}{m_{n-2}} & \frac{-c_{n-2}-c_{n-1}}{m_{n-2}} & \frac{c_n}{m_{n-2}} & 0 \\ \frac{c_{sn-1}}{m_{n-1}} & 0 & \ldots & 0 & 0 & \frac{c_{n-1}}{m_{n-1}} & \frac{-c_{n-1}-c_n}{m_{n-1}} & \frac{c_n}{m_{n-1}} \\ \frac{c_{n+1}+c_{sn}}{m_n} & 0 & \ldots & 0 & 0 & 0 & \frac{c_n}{m_n} & \frac{-c_n-c_{n+1}}{m_n} \end{bmatrix}$$

The first row of the J and F matrices are empty when the body acceleration is chosen as input to the system. This removes the body equation of motion from the A matrix and takes the input acceleration as a single parameter to the B matrix, which thus becomes:

$$B = \begin{bmatrix} 0 & 0 & \ldots & 0 & \vdots & 1 & 0 & .. & 0 \end{bmatrix}' \tag{3.40}$$

The input u in equations 3.36 is the applied acceleration, which is multiplied with B. The C matrix contains information about which states are taken as outputs and any modification of the output is done here. In the current case, the spring deflection has to be transformed to the predicted pressure by using the equation:

$$P_n = \delta_n k_n / A \tag{3.41}$$

The C matrix is a NX$2N$ empty matrix with the only exception being the states taken for output. The choice of the state vector (containing positions and velocities) in equation 3.38 is however not yet suitable to define a useful C matrix yet. In the MDOF model, the pressure is approximated by spring deformation and not the absolute positions of masses provided by equation 3.38. To get sensible pressure output, the absolute positions of neighboring masses may be subtracted to obtain spring deformation. This method is elaborate and causes calculation with very large numbers because most accelerations cause ever-increasing displacements. A better method is to transform the state vector in equation 3.38 to a more favorable one, namely spring deformation and its derivative. If the state vector is x and the required state vector that x must be transformed into is z then the transformation matrix is defined by:

$$z = Tx \tag{3.42}$$

and if *T* is a non-singular matrix:

$$x = T^{-1}z \tag{3.43}$$

Equation 3.36 may then be transformed to an equivalent system:

$$\begin{aligned} \dot{z} &= \overline{A}z + \overline{B}u \\ y &= \overline{C}z + \overline{D}u \end{aligned} \tag{3.44}$$

where:

$$\begin{aligned} \overline{A} &= TAT^{-1} \\ \overline{B} &= TB \\ \overline{C} &= CT^{-1} \\ \overline{D} &= D \end{aligned} \tag{3.45}$$

For this transformation to succeed, *T* must be non-singular. As an example, when the system is transformed to a state vector:

$$z = [\delta_1 \quad \delta_2 \quad \ldots \quad \delta_{n+1} \;\vdots\; \dot{\delta}_1 \quad \dot{\delta}_2 \quad \ldots \quad \dot{\delta}_{n+1}] \tag{3.46}$$

This enables the system to output any spring deflection within the system but results in a singular *A* matrix that makes the transformation impossible. Another state vector is recommended for any system with an even number of masses that gives a non-singular state vector.

$$z = [x_b \quad \delta_1 \quad \delta_1 \quad \ldots \quad \delta_{n+1} \;\vdots\; x_b \quad \dot{\delta}_1 \quad \dot{\delta}_2 \quad \ldots \quad \dot{\delta}_{n+1}] \tag{3.47}$$

The new state vector *z* still has a length of 2(*N*+1). To make space for the included two body states, the *δ*-term of the centre spring is omitted. The deflection of the centre spring is zero for any input anyway so its output is redundant. The only requirement for this system is that it must have an even number of masses so that a centre spring is present. The transformation matrix is now found from substitution of equation 3.47 into equation 3.42:

$$T = \begin{bmatrix} Ta & [0] \\ [0] & Ta \end{bmatrix} \tag{3.48}$$

with:

$$Ta = \begin{bmatrix} 1 & 0 & 0 & 0 & 0 & \ldots & 0 & 0 \\ -1 & 1 & 0 & 0 & 0 & \ldots & 0 & 0 \\ 0 & -1 & 1 & 0 & 0 & \ldots & 0 & 0 \\ 0 & 0 & -1 & 1 & 0 & \ldots & 0 & 0 \\ \ldots & \ldots & \ldots & \ldots & \ldots & \ldots & \ldots & \ldots \\ 0 & 0 & \ldots & 0 & 0 & -1 & 1 & 0 \\ 0 & 0 & \ldots & 0 & 0 & 0 & -1 & 1 \\ 1 & 0 & \ldots & 0 & 0 & 0 & 0 & -1 \end{bmatrix} \tag{3.49}$$

The diagonal starting at the top left corner ends at row (*N*+1)/2 rounded up to the closest integer. In the row after that, the bottom right diagonal starts. The reader will find that this transformation gives reasonable results for systems with an uneven number of masses too at high degrees of freedom. The most marked error by using and uneven number of masses is an erroneous steady state gain, or unstable step response for the case of one mass. The frequency response will not exhibit any obvious errors.

With the availability of a suitable state vector, a suitable C matrix can be selected. To single out the first and last spring deflection, C will be an empty *N*X2*N* matrix with k_n/A (from equation 3.41) entered at the 22 and *NN* positions, in order to output P_1 and P_{n+1}. The difference between these two pressures is the diaphragm differential pressure.

3.6 Transfer function

With the state space system definition complete, the transfer function can be calculated from:

$$H(s) = C(sI - A)^{-1}B + D \tag{3.50}$$

This results in (*N*+1) transfer functions of which only the second and last transfer functions are of interest, corresponding to the deflection of the first and last spring. From these transfer functions, the following is clear:

1. The transfer functions are mirror images of each other. The differential pressure can therefore be approximated simply by multiplying one of the transfer functions by two, and the appropriate sign.
2. The coefficients of the transfer functions are exceedingly large and become even larger when more degrees of freedom are added. This is typical of a badly conditioned system for which a matrix balancing exercise would be beneficial. Matrix balancing makes the *A* matrix more diagonal and thus more docile during inversion.
3. Depending on the damping, the transfer function goes unstable at a certain degree of freedom where the matrices become too badly conditioned for the inversion required by the transfer function calculation.

The matrix condition problem makes the use of the transfer function less attractive for calculation of dynamic responses.

An evaluation of the quality of the formulation is now made for a 10m long channel. A very low damping of 1% of critical is taken to make the natural frequencies more perceptible. The damping is half shear damping and half inter-molecular damping.

STIFFNESS: Each spring is from equation 3.34:
314.4 N/m for the 2 mass system.
524 N/m for the 4 mass system.
733 N/m for the 6 mass system.

MASS: The inertia of each mass is calculated from equation 3.35 to be:
2.71e-3kg for the 2 mass system.
1.355e-3kg for the 4 mass system.
9.033e-4kg for the 6 mass system.

SOUND SPEED: Using equation 3.26, the speed of sound in the fluid is predicted to be 1390.53 m/s. This is slightly lower than the quoted 1450 m/s for mercury that the reader will find in literature. A higher bulk modulus will have to be assumed to reach the quoted speed of sound. The fundamental frequency caused by this sound speed is from equation 3.25 calculated to be 69.527 Hz.

The transfer functions are shown in a magnitude Bode graph in figure 3.4.

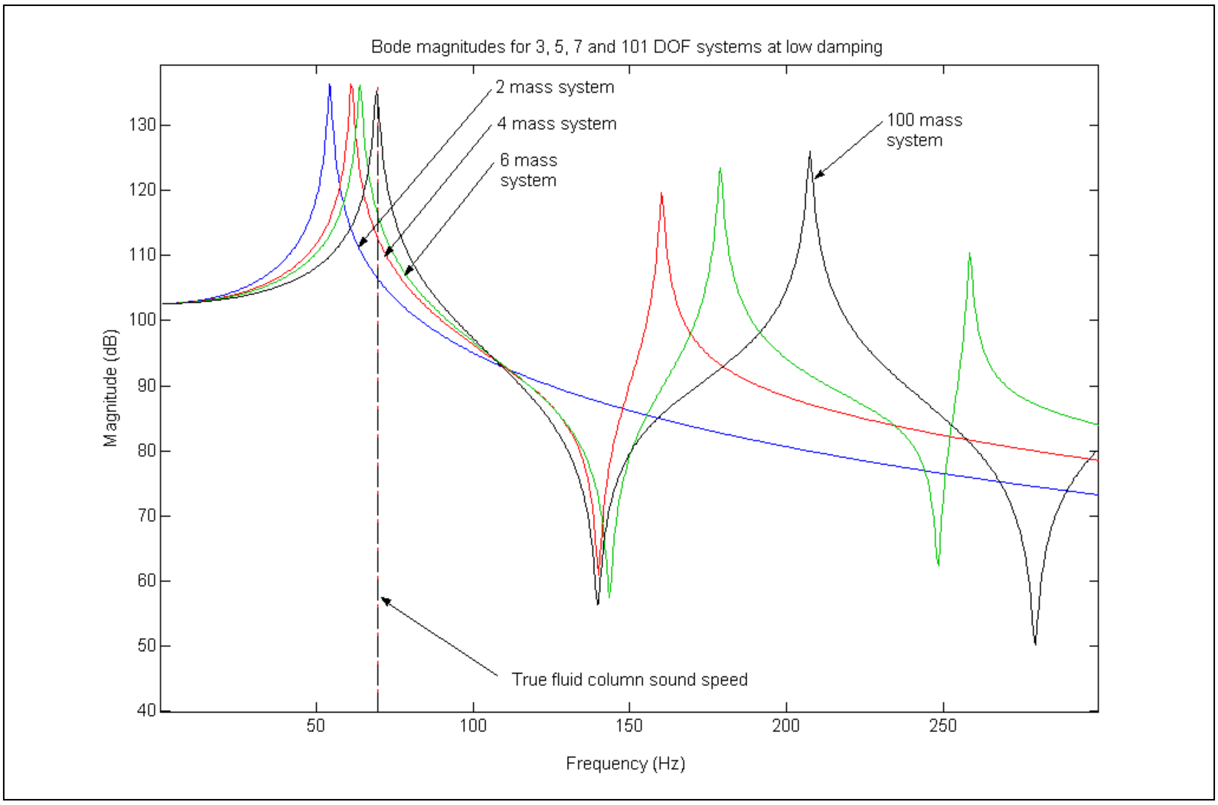

Figure 3.4: Bode magnitude plot for MDOF approximation for a 10m long fluid column showing the frequency predicted for speed of sound in mercury.

The following is clear from figure 3.4:

1) The first natural frequency increases asymptotically toward the sound speed as the degrees of freedom increase. At 101 degrees of freedom, the wave propagation speed is 99.5% of the true value. The frequency of subsequent resonances is even more in error than the first.
2) As the degrees of freedom increase, more resonances are added into the Bode plot. More mode shapes are therefore accounted for in higher DOF systems.
3) The higher resonances occur at lower amplitudes than that of the fundamental frequency. This is typical of a homogenous infinite degree of freedom system.

A true fluid column will essentially be an infinite DOF system and hence if a finite DOF system is used to model a fluid column:

1) The wave propagation speed is under-estimated.
2) Only a finite number of resonances and mode shapes are predicted
3) The frequency intervals (bands) between resonances are under-estimated.

These inherent errors must be eliminated or controlled in order for the MDOF approximation to be successful. An obvious solution is to use a very large DOF system, say a 1000-DOF system. This would result in a transfer function with a numerator and denominator potentially containing 1001 terms each, which take prohibitively long to calculate. In addition to this, it would only be possible to calculate the transfer function if mathematical stability of the matrices could be assured. To make dynamical simulation of the system possible, a more conveniently sized system has to be addressed in its deficiencies.

3.6.1 Wave speed error correction

The following relation, which equation 3.26 also obeys, expresses the wave speed for a more general system:

$$a = \Phi\sqrt{\frac{\text{stiffness}}{\text{inertia}}} \tag{3.51}$$

where Φ is a dimensionless coefficient called the wave speed constant.

Any measure of the system stiffness and inertia in the system may be used as reference in equation 3.51. For the following analyses, the individual spring stiffness and point-mass inertias are substituted for these two variables. To increase the wave speed to a more acceptable level, the stiffness can be increased, or the inertia decreased. It is preferred that the stiffness is increased as opposed to decreasing the mass, since any increase in stiffness will still predict the correct steady state pressure by virtue of equation 3.41 (or equivalently 3.29). A decrease in mass would necessitate other modifications to the modeling equations to make this possible. If Φ is known for a system, a corrected stiffness can be selected to give any wave speed by rearranging equation 3.51 into:

$$k_{corr} = \frac{a^2 m_n}{\Phi^2} \tag{3.52}$$

Equation 3.52 replaces equation 3.33 with the assumption that the correct Φ is available. Note that the true wave speed is calculated by means of equation 3.25, where ω_n is the first natural frequency in radians per second.

$$a = \frac{L\omega_n}{\pi}$$

In a state space system, the natural frequencies are found by finding the system eigenvalues. This is achieved by solving for λ in:

$$\left|A - \lambda I\right| = 0 \tag{3.53}$$

Equation 3.53 results in a polynomial in λ with 2(N+1) terms, called the characteristic equation. The characteristic equation will clearly be an arduous one to solve on paper for higher number DOF systems. Each λ gives one pole of the system and the natural frequency corresponding to that pole is found from:

$$\omega_n = \sqrt{(\text{real}\lambda)^2 + (\text{imag}\lambda)^2} = |\lambda| \tag{3.54}$$

Φ_{LN}, referenced to any k and m is then found from:

$$\Phi_{LN} = \frac{L\omega_{nN}}{\pi\sqrt{k/m}} \tag{3.55}$$

where k and m can be any positive real values for the stiffness and mass used. N is the number of degrees of freedom used in the MDOF approximation and L the length of the channel being approximated. ω_{nN} is therefore the natural frequency of any N-DOF system with the configuration of figure 3.3.

The transformation performed on the system in equations 3.42 to 3.49 requires the use of an even number of masses in order for a center spring to be present. This requirement hampers the search for a relation between the number of DOFs and the natural frequency since half of the possible configurations are prohibited. The transformation does not change the characteristics of the system; it simply rearranges the matrix for a different set of states to become available in an equivalent system. A successfully transformed system is identical to the original, also in terms of its natural frequencies. Hence, in order to find the natural frequencies for a system with an even or uneven number of masses, the untransformed system is now used. To find ω_{nN}, the corresponding λ_N is first found by solving equation 3.53. Exact solutions for λ_N is shown below for the first nine systems. N refers to the degrees of freedom, hence λ_2 applies to a single mass system. The first nonzero pole is found from equation 3.53 for a single mass system to be:

$$\lambda_2 = \sqrt{\frac{-2k}{m}}$$

The negative square root argument makes the pole complex as indeed all the non-zero poles are. Applying equation 3.54 to λ_2, the natural frequency for this pole is:

$$\omega_{n2} = \sqrt{\frac{2k}{m}} \tag{3.56}$$

From elementary vibration theory, a single excited mass-spring combination is known to have a natural frequency of $\sqrt{\frac{k}{m}}$. The system described by equation 3.56 has two springs in parallel resulting in twice the stiffness; hence a factor 2 is present.

The fundamental poles of the higher DOF systems are now found in order to find a relation between the DOF of the system and its natural frequency. All poles occur in conjugate pairs, and only the positive pole is extracted here for the purpose of finding natural frequency. The complex conjugates of the exact answers result in the same natural frequencies. The fundamental poles up to the ninth possible system are:

$$\lambda_3 = \sqrt{-\frac{k}{m}}$$

$$\lambda_4 = \sqrt{\frac{(\sqrt{2}-2)k}{m}}$$

$$\lambda_5 = \sqrt{\frac{(\sqrt{5}-3)k}{2m}}$$

$$\lambda_6 = \sqrt{\frac{(\sqrt{3}-2)k}{m}}$$

$$\lambda_7 = \sqrt{\frac{\left(-\frac{5}{3} + \frac{1}{6}\sqrt[3]{-28+84\sqrt{3}i} + \frac{14}{3}\sqrt[3]{-28+84\sqrt{3}i}\right)k}{m}}$$

$$\lambda_8 = \sqrt{\frac{\left(-2+\sqrt{2+\sqrt{2}}\right)k}{m}}$$

$$\lambda_9 = \sqrt{\frac{\left(-2+\frac{1}{2}\sqrt[3]{4+4\sqrt{3}i} + \frac{2}{\sqrt[3]{4+4\sqrt{3}i}}\right)k}{m}}$$

$$\lambda_{10} = \sqrt{\frac{\left(-2+\frac{1}{2}\sqrt{10+2\sqrt{5}}\right)k}{m}}$$

Larger systems become too elaborate or numerically unbalanced for an exact answer as shown above. Diagonalization of the characteristic matrix may provide limited help in this regard, but still no clear indication could be deduced from the exact answers on the function that describes λ_N's dependence on N.

Only the following is clear from the exact answers: Each pole λ_N includes a factor k/m so Φ_{LN} is proportional to L and N but independent of k and m, which is eliminated from by the square-rooted k/m in the denominator of equation 3.55. Any values for k and m can therefore be employed to plot Φ_{LN} versus N. Φ_{LN} is plotted in figure 3.5 up to 201 degrees of freedom for an L of 1m. The wave speed constants plotted in figure 3.5.

The wave speed constant seems to be either a hyperbolic-, power-, or exponential function of N. Surprisingly, the function does not fit even one of these satisfactorily enough to be used in equation 3.52. The fit may be visually gratifying for either the power or exponential function, but the square present in equation 3.52 amplifies the error and gives a mediocre result.

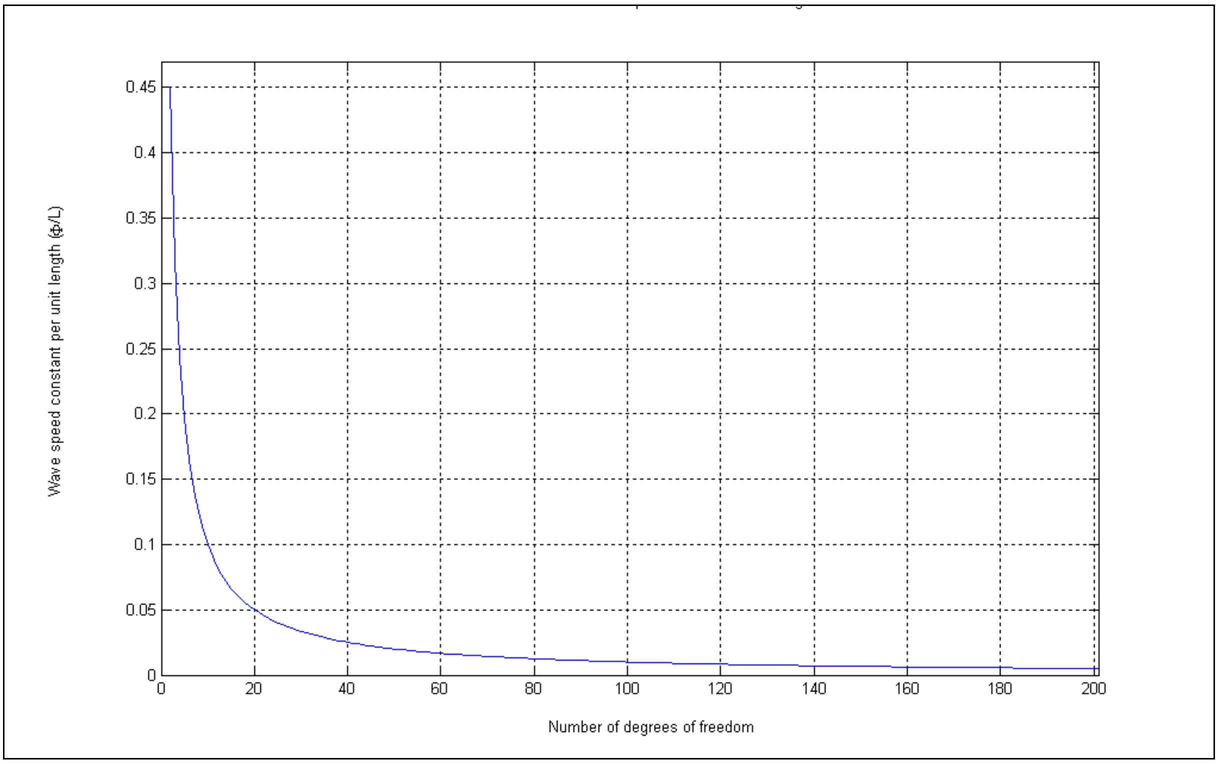

Figure 3.5: Wave speed constant for a 3 - 201 DOF system.

A good fit is found in the shape of a rational function of two polynomials. The fit was performed by the sum-of-least-squares method and results in:

$$\Phi_{LN} = \frac{L(N-1)+\dfrac{L}{1.21852}}{(N-1)^2+1.822(N-1)+1.21852} \tag{3.57}$$

Equation 3.57 offers an alternative in cases where a table of Φ_{LN} cannot be generated. A table for an even number of fluid column masses up to 200 is given in appendix A.1.

3.6.2 Higher mode fluid column resonances

Requirement 3 of section 3.5.4 for successful modeling of the fluid column is the only one left to be satisfied, and the most difficult. There is no way to make a finite DOF system have an infinite number of modes and resonances. The designer must decide where the frequency range of interest lies and make a compromise to approximate the true fluid column in this range.

The first modal frequency is corrected for, so the only errors under consideration here are from the second resonance and onwards. The frequency range chosen is taken conservatively as a first approximation to be 150Hz. This will account for the most dynamic systems devised in inertial navigation and will exceed the achievable sensor bandwidth by a great margin. After the sensor potential is clearer, the frequency range may be decreased.

If the system is kept in its state space LTI form, a computer can very efficiently calculate the response and provide considerable freedom for degrees of freedom available. The type of response desired is also of great importance. For harmonic inputs it will be important to match the bode plot of the true fluid column. For step or impulse inputs it is far less important since the transients for systems with widely varying DOFs show similar transient responses. The number of degrees of freedom required will increase as the length of the fluid column approximated increases. This occurs because the first resonance mode decreases in frequency with increasing fluid column length.

3.6.3 Real fluid columns

Despite the measures taken thus far in this chapter to make the theoretical fluid column model of figure 3.3 simulate a real fluid column, there are still differences.

Vapor pressure limits: In real fluid columns, the differential pressure generated does not faithfully follow increasing acceleration without limit. The fluid at the low-pressure end of the diaphragm will boil if the pressure there drops below the vapor pressure of the fluid. The low vapor pressure of mercury (1.1×10^{-3} Pa at 20°C) makes this fluid suitable even in this respect. The use of hydraulic oils can decrease the impact of vapor pressure, albeit at a great cost to the fluid density.

Channel array shape: The fluid column model originates from a one-dimensional column with acceleration longitudinal to the column (see figure 3.3). The pressure potential of the modeled spiral-helix is calculated by use of equation 3.14. The assumption is still made that the linear acceleration in the channels resulting from angular acceleration of the sensor is the same along any position in the channel. This is not the case. By definition, a spiral has channel sections at varying radii and thus it has channel section in varying linear acceleration fields (according to equation 3.2). Equation 3.14 serves to give the total differential pressure regardless of the channel shape – not pressure generated at a specific channel end. Two spiral channels of the same pressure potential and fluid but different shape will always provide the same differential pressures. The only difference between the channels is the fraction of total pressure contributed by each end of the channel. For an asymmetric channel, the generated outputs will also be asymmetric. Only the total differential pressure is of interest to the sensor's function. In the theory verification of chapter 7, an asymmetric channel is used with asymmetric outputs.

Free gas: The observation made in section 3.6 that the generated gage pressures at the two ends of the channel are symmetric is also dependent on the continuity of the medium in the channel. The model assumes that the fluid column has constant bulk modulus throughout the fluid. If free gas is present in the fluid, the pressures at the two ends of the channel will not be symmetric. Gas that is distributed in perfect symmetry with respect to the two channel ends will have no effect on pressure symmetry but this is of course not the tendency. A good indication of free gas presence in the fluid column is therefore an asymmetric output (if channel shape is already taken into account). This will only be discernable from other effects if the pressures are measured separately.

Chapter 4

Spiral planform shape

4.1 Introduction

Angular acceleration is measured in the sensor. Angular acceleration creates linear acceleration proportional to the radius from the center of rotation that is tangent to an arc around the center of rotation. Intuitively the planform shape (top view) of a spiral should be circular in shape around the center of the accelerometer; the shape used in the Fluid Rotor angular accelerometer. Geometrically however, a circular arc will only be able to have an angular span of 360 degrees taking it back where it started, completing a circle. This limits the spiral length to a single revolution. One possible scheme to maximize pressure generation around one axis of rotation with the use of a circle is to use a helix. The planform view of a mathematical helix is a circle; hence the pressure would be generated in a circular arc relative to the axis of rotation.

This would be ideal from efficiency point-of-view, but a lot of space would go to waste where extra measurable pressure potential could be generated. If more pressure potential length is desired (as is the case here) a spiral of some sort is needed at different levels to create an array of spirals inside a helix. The helix can be subdivided into different levels with one spiral at each level. The shape of the spiral at each level of the helix needs to be optimized, as well as the transitions to different levels.

The objective of this chapter is:

1) To model different spiral concepts with a view to maximizing pressure potential generation and manufacturability of the sensor.
2) To compare different spiral shapes in terms of their efficiency at generating pressure potential during angular acceleration.

Before any losses are taken into account, a better understanding should be formed of the gross pressure generation capability of a spiral.

First consider equation 3.9: $\Delta P_k = \rho \ r_k \alpha \ \Delta L_k \cos \varepsilon_k$

The fluid density ρ and angular acceleration α do not describe the channel. It is clear that the channel "shape-and-size" variables in equation 3.9 (that also govern the pressure generated) is r the radius from the center of rotation, L the length of the spiral, and ε the angle between a section of channel and the local acceleration.

Furthermore, r and L describe mainly the size of the spiral and ε describes only the shape. The last portion of the equation contains a cosine, which can only vary between unity (if the angle is zero) and zero (where the angle is 90 degrees). The cosine term in effect expresses the fraction of the channel that generates pressure at any point. From this, the pressure potential efficiency is defined. The flow loss in the spiral is kept aside for the moment, as it will be addressed in a later section. The pressure potential efficiency is defined as:

$$\text{Pressure potential efficiency} = \frac{\text{Length of channel tangent to rotation}}{\text{Total length of channel}} \qquad (4.1)$$

4.2 Spiral shapes

The pressure potential efficiency will be analyzed for various spiral shapes:

1) The Archimedes spiral
2) The pseudo-spiral with straight-line transitions
3) The circular arc pseudo-spiral.

The attributes of these spirals are now elaborated on.

4.2.1 Archimedes spiral

This is a simple continuous spiral that gains constant radius with each revolution. It is described by the equation $r = k\theta$ with r the radius from the origin, k the radius gained per angle rotation and θ the angle rotated. The Archimedes spiral is a continuous polar function through any real angle. If an Archimedes spiral of both positive and negative angle is plotted, the spiral causes a mirror image on itself as shown in figure 4.1.

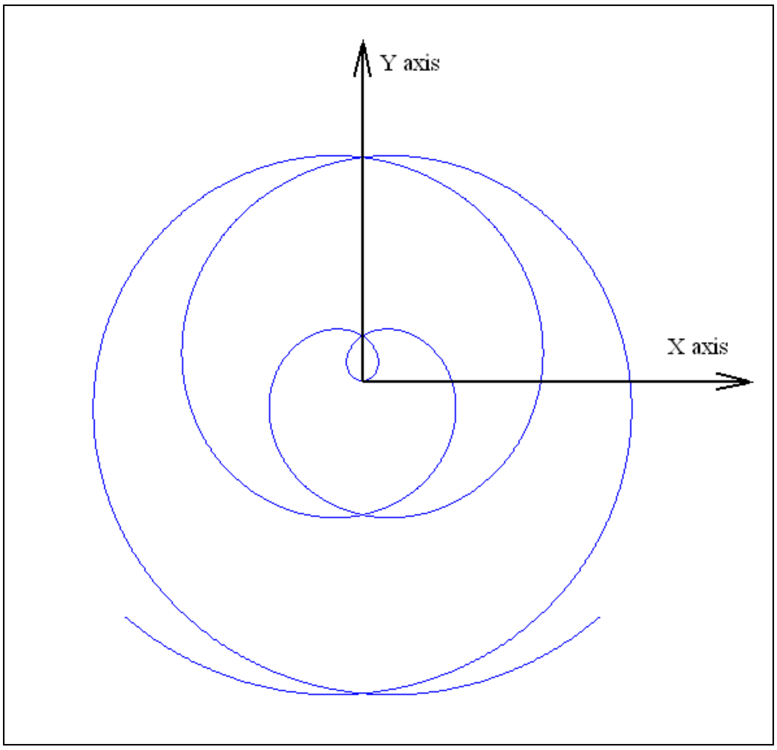

Figure 4.1: The spiral of Archimedes.

4.2.2 Pseudo-spiral with straight line transitions

The linear pseudo-spiral consists of a set of concentric circles and uses a tangent straight line to progress from one circle to the next. The objective of a linear pseudo-spiral is to simplify manufacturing of the channel array. The linear channel portions aid in the fabrication and alignment of the inports and outports of the wafers. The concentric circles minimize loss of efficiency and are also a simple geometric shape to fabricate. A diagram of the pseudo-spiral for one transition between two concentric circles is shown in figure 4.2. The transition (in red) shows two different ways for the transition to take place. If only a straight line is used as a transition, a discontinuity results in each circle in the spiral at point P on the larger circle. To remove the discontinuity, a second circular arc may be used as also illustrated in red. The transition arc is placed so that the one end is tangent to the straight line and the other end tangent to the larger circle, which results in a circle that is off-center with the origin. This tangency requirement limits the radius of the transition arc to the radial difference between two consecutive circles. The transition arc improves pressure potential efficiency and has the added advantage that flow losses are also less.

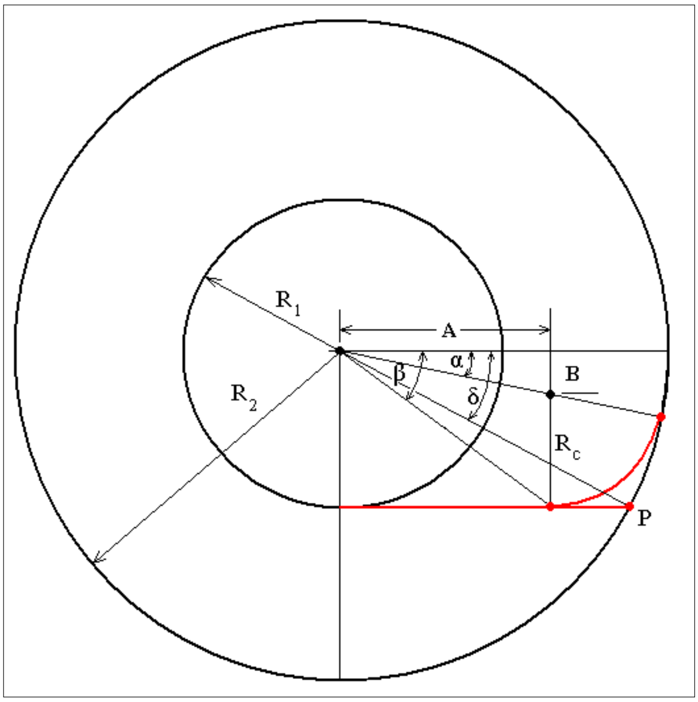

Figure 4.2: A pseudo-spiral with straight-line transitions.

The geometry of the transition arc is now defined for use in equation 3.9. The angles α and β (measured below the horizontal) between which the transition arc exists is found from analysis of figure 4.2:

$$\alpha = \tan^{-1}\left(\frac{R_1 - R_c}{\sqrt{(R_2 - R_c)^2 - (R_1 - R_c)^2}}\right)$$

$$\beta = \tan^{-1}\left(\frac{R_1}{\sqrt{(R_2 - R_c)^2 - (R_1 - R_c)^2}}\right) \tag{4.2}$$

Relative to the main concentric circles, the transition circle is offset by (A ; -B). The transition circle is shown in figure 4.3. In order to find the contribution of the channel in the transition circle to h_{ang}, the radial displacement must be found for entry into equation 3.14. For the moment, the negative sign on B is dropped, it may be added later when the resulting formula is used. To obtain the distance of any point on the transition circle from the origin, the circle is best described in polar coordinates. The off-center circle in Cartesian coordinates is then simply:

$$(x - A)^2 + (y - B)^2 = R_c^2$$

To change this equation to polar coordinates, the x and y variables are replaced by their polar equivalents:

$$(R\cos\theta - A)^2 + (R\sin\theta - B)^2 = R_c^2$$
$$\therefore \left(R^2\cos^2\theta - 2RA\cos\theta + A^2\right) + \left(R^2\cos^2\theta - 2RB\sin\theta + B^2\right) = R_c^2$$

Rearrange to obtain:

$$\left(\cos^2\theta + \sin^2\theta\right)R^2 - (2A\cos\theta + 2B\sin\theta)R - \left(R_c - A^2 - B^2\right) = 0$$
$$\therefore R^2 - (2A\cos\theta + 2B\sin\theta)R - \left(R_c - A^2 - B^2\right) = 0$$

The roots of this equation give the required radial displacement at θ, which is:

$$R(\theta)=\frac{(2A\cos\theta+2B\sin\theta)\pm\sqrt{(-2A\cos\theta-2B\sin\theta)^2+4(R_c-A^2-B^2)}}{2} \tag{4.3}$$

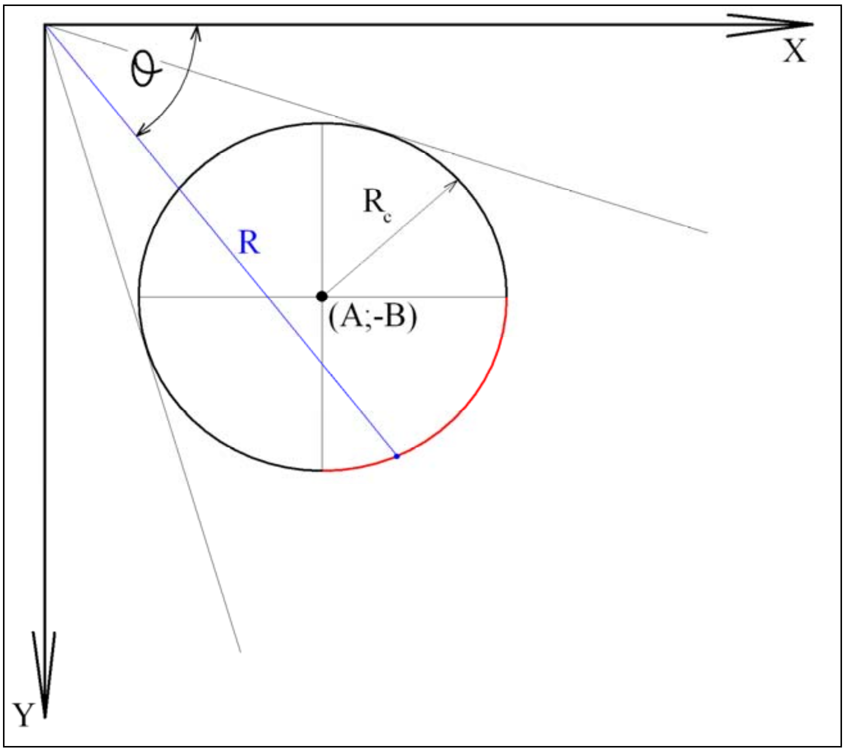

Figure 4.3: Transition circle, showing the required radius in blue. The maximum portion of the circle that may be used for the transition is shown in red.

The larger of the two solutions is R in figure 4.3. Equation 4.3 is only valid between angles where the intersection of a straight line is possible with the circle. Care must also be taken that only the fourth quadrant of the circle is used, so that equation 4.3 is not used beyond its applicability.

When no transition arc is used, a discontinuity will result at point P in figure 4.2. The negative angle from the horizontal to this point (δ) is then:

$$\delta=\tan^{-1}\left(\frac{R_1}{\sqrt{R_2^2-R_1^2}}\right) \tag{4.4}$$

4.2.3 Circular arc pseudo-spiral

The circular arc spiral is the only spiral that consists only of circular arcs. This spiral aims to simplify the construction of the channel by using only circular arcs with maximum pressure potential and flow efficiency. A constant gain in radius per revolution is achieved by using circles of increasing radius, each placed off-center to achieve a continuous curve. A schematic of the circular pseudo-spiral is shown in figure 4.4. The top and bottom arcs in figure 4.4 are both semi-circles.

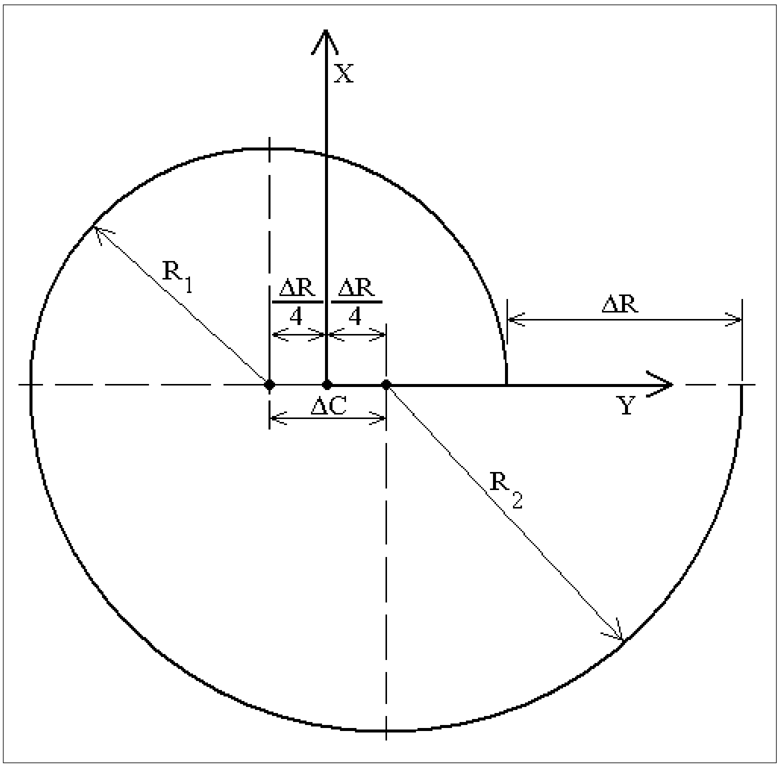

Figure 4.4: The circular arc pseudo-spiral.

4.3 Spiral comparison

4.3.1 Spiral shape

Four spirals that illustrate the general shape are plotted in figure 4.5. The four plots are done according to the same spiral parameters and on the same axes to highlight the differences between the spirals.

1) The Archimedes spiral evenly distributes the change in radius on each rotation, but is never a rotation-centered circular arc (which is the ideal shape for angular pressure potential).
2) The pseudo-spiral with linear transitions aims to maximize the use of concentric circles and concentrates the deviation from a circular arc in one region. The refined version of this installs an arc where the discontinuity is, since the deviation from the circle is most severe in that position.
3) A circular-arc pseudo-spiral compromises the concentricity of the arcs in order to build the entire spiral out of circular arcs. A circular arc spiral and an Archimedes spiral with the same parameters can be seen to closely resemble each other. The difference in shape is more apparent at the center of the spiral as shown in figure 4.6.

Due of the adverse efficiency effects of starting spirals close to the origin; a spiral of the shape in figure 4.6 is not feasible. At large radii the two types of spirals are almost identical; hence the differences plotted in figure 4.6 are not apparent in applicable spirals.

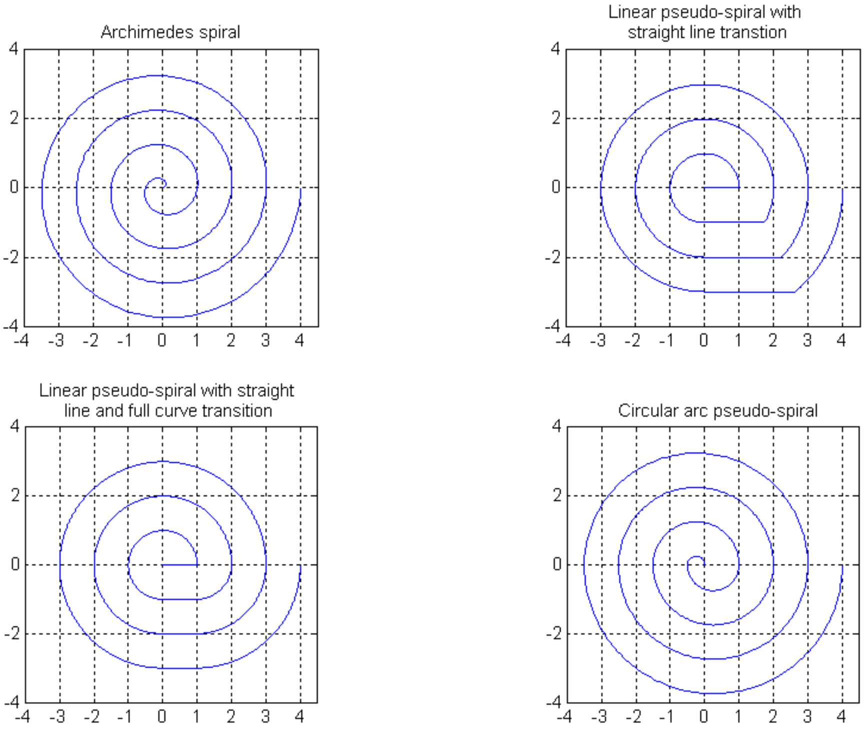

Figure 4.5: Plots of the four types of spirals over four revolutions with a line spacing of unity.

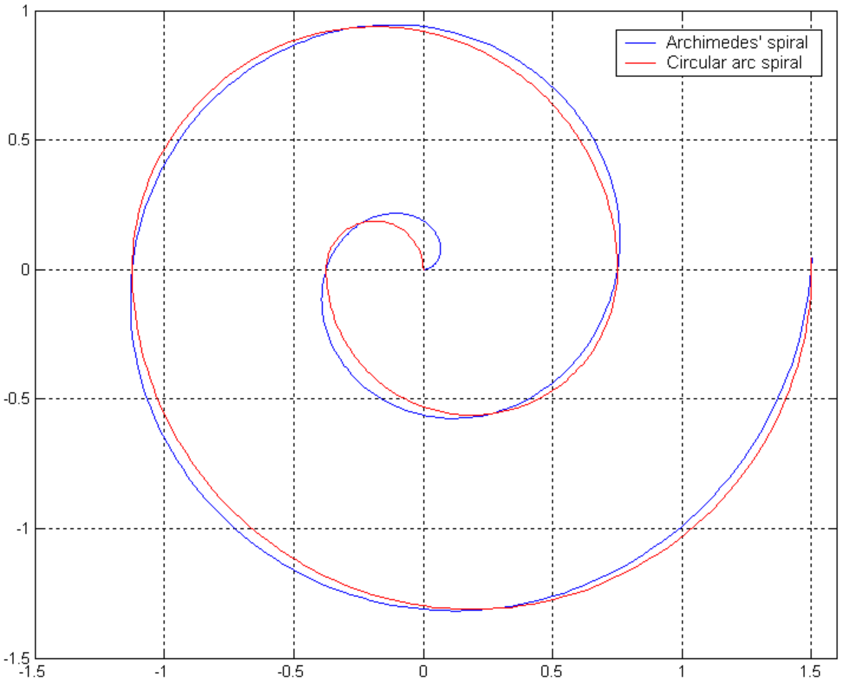

Figure 4.6: Archimedes spiral and circular arc pseudo-spiral starting at the origin.

4.3.2 Spiral shape efficiencies

A plot of the pressure potential efficiency (equation 4.1) is made of these four types of spirals in figure 4.7. It can be seen that the general efficiency of all the spirals are high. The Archimedes spiral and the circular spiral have only a small difference in terms of efficiency, while the linear and curved-linear spiral show a more significant drop in efficiency at high angles. At very low angles, close to the center of the spiral, the linear spirals are perfectly efficient. This difference would be even more evident for a sub-single rotation spiral, although the utilization of such a spiral is highly unlikely in this application.

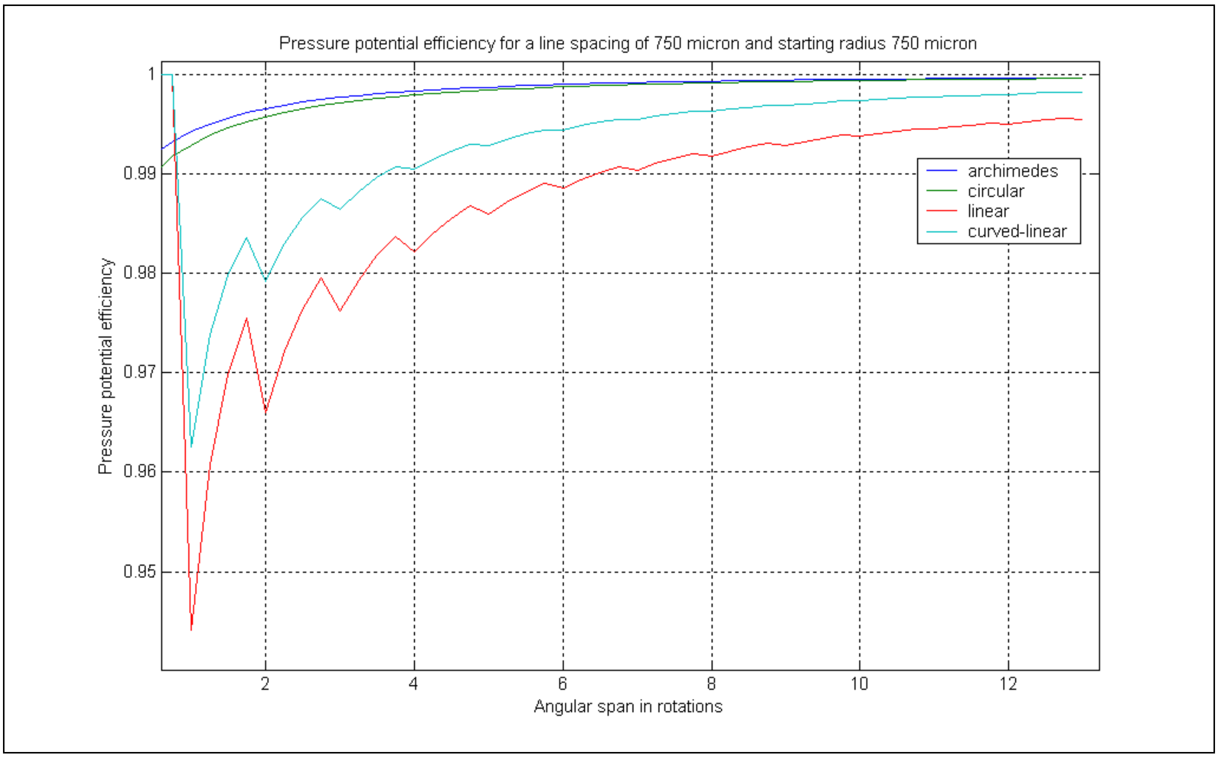

Figure 4.7: Pressure potential efficiencies for spirals starting at a radius equal to the line spacing. The plot shows the graph from one revolution onwards. Angular span denotes the total angular domain (or sweep) of the spiral.

A plot of the tangency (angle to the tangent of a rotation-centered arc) shows where the efficiency of each spiral is lost. A higher tangency angle corresponds to lower efficiency, with zero efficiency at a tangency angle of 90 degrees. Clearly, the Archimedes spiral is the best choice in terms of pressure potential efficiency at high rotations for the graphs plotted. However, there is an exception.

The Archimedes spiral is only efficient far from the origin in a spiral with a small difference in radius per turn. In fact, the Archimedes spiral has zero efficiency at the origin (tangency angle of 90 degrees). It is therefore possible for cases where very low flow losses are experienced that the areas in the center of the spiral may also be utilized for pressure generation. If this were the case, an Archimedes spiral or circular spiral would be used on the outside only, while a curved linear spiral would be better for the center region. If the sensor has a very stiff pressure sensing system or a good feedback system, then the flow would be further minimized which makes the length of useful spiral longer. Therefore, there may be several types of spirals involved on a single level. The port alignment advantages of the linear pseudo-spiral may be obtained by only constructing the innermost and outermost loop of the spiral in this shape.

Figures 4.7 and 4.8 are valid for any spiral with constant line spacing. To make any further deduction of the size and type of spiral that is optimal, a good understanding of the minor flow losses involved is required. A detail design of the spiral and subsequent CFD analysis of the through-ports will be the subject of a prototype design.

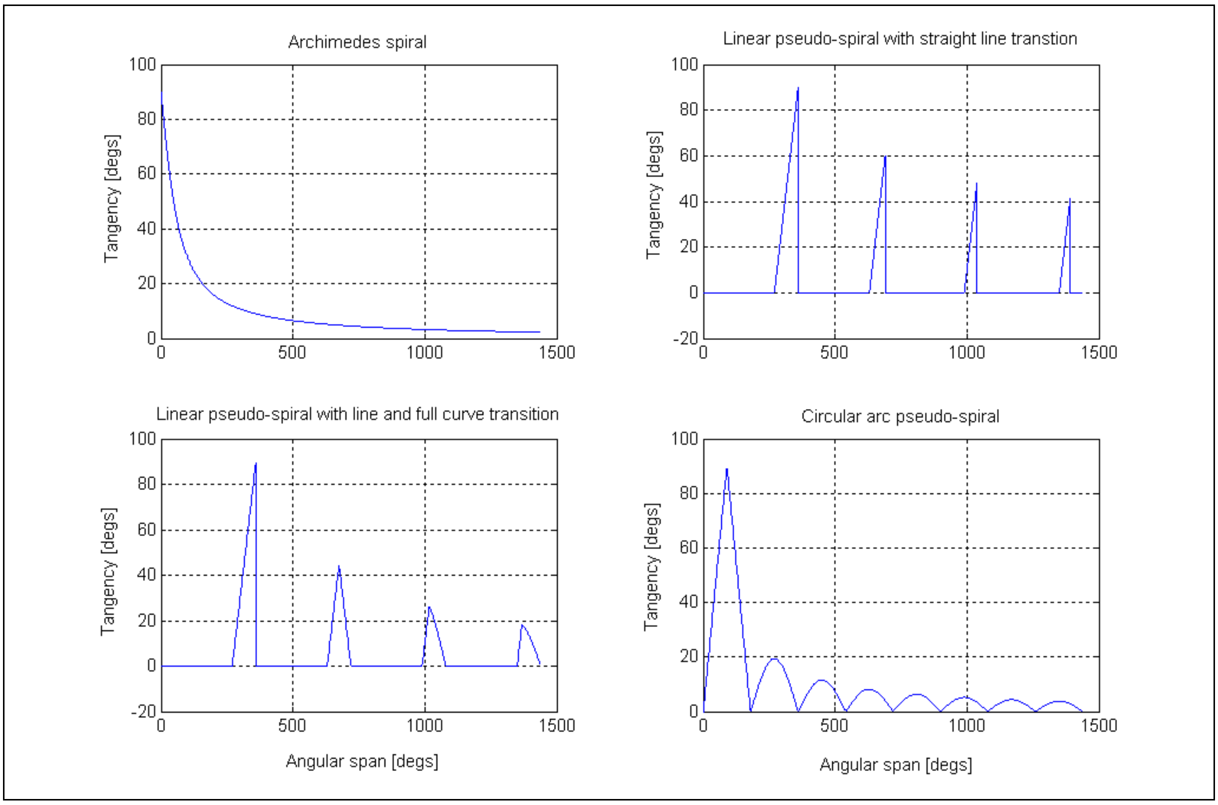

Figure 4.8: Tangency angles of the four spiral types. Angular span denotes the total angular domain (or sweep) of the spiral.

4.4 Conclusions on planform shape

Various planforms have been proposed to make trade-offs between efficiency and manufacturability possible. The three types of spirals presented have very similar efficiencies at large radii, which make the use of any type feasible in the channels envisaged for the sensor. For subsequent calculations and simulation, the Archimedes spiral will be assumed as the default planform. For a channel of width 0.2mm starting at a radius of 5mm, the angular span is 25 revolutions, which makes the loss of efficiency negligible for any spiral type (figure 4.7).

Chapter 5

Flow in sensor channels

5.1 Introduction

If the fluid contained in the channels had zero viscosity, flow modeling would be a simple matter of applying Newton's second law without regard for a boundary layer formation or flow losses. The motion of the fluid would be very similar to rigid body motion. The viscosity in the fluid has the effect of causing a shear force proportional to any velocity gradient in the flow, which always opposes the motion of the fluid. The velocity gradient is in turn caused by a no-slip condition imposed at the wall. This is unfortunately unavoidable. The only way to limit pressure loss is to limit flow so that a large velocity gradient does not form. This places a requirement on the diaphragm to stay rigid if no pressure losses are to occur. Of course, any diaphragm used in the sensor transduces the pressure generated by the helical channels into a signal by deflecting. The deflection might be very small, but does exist nonetheless and this causes flow in the channels, and thus also pressure loss. The only option left to the designer is to limit that flow to as small a value as possible, and so maximize the measured differential pressure. Due to pressure loss, fluid viscosity is generally an undesirable attribute of the working fluid, but viscosity also provides valuable sensor damping without which no measurement is possible. A fluid with large bulk damping (to provide pressure wave damping) and negligible viscosity (to limit pressure loss due to flow) would be ideal in terms of pressure transmission and flow. Of course, other fluid attributes like density also play an important role and must be considered. The ratio of dynamic viscosity to density is a better benchmark of fluid suitability, in which mercury is the clear choice.

The aims of this chapter are:

1) Identify the variables governing the flow in the sensor channels to gain an understanding of the mechanisms involved.
2) Describe flow mathematically in a manner amenable to rapid simulation of the sensor.

5.2 Characteristics of flow

The flow is expected to have the following characteristics:

5.2.1 Laminar flow

Flow can be taken as laminar below a Reynolds number of 2300 for most conditions. The Reynolds number for flow is defined as:

$$\mathrm{Re} = \frac{\rho U L}{\mu} = \frac{U L}{\nu}$$

where ρ is the fluid density, U is the characteristic flow velocity, L is the characteristic length, μ is the fluid's dynamic viscosity and ν is the fluid's kinematic viscosity. For channel flow, another version of the Reynolds number Re_d is adopted where the channel diameter d is substituted for the characteristic length. For a non-circular cross-section channel the hydraulic diameter concept was derived to use as the duct diameter. The hydraulic diameter is:

$$D_h = \frac{4A}{P_w}$$

with A, the flow cross-sectional area, and P_w the wetted perimeter around the flow area. The wetted perimeter is described as the total length around the flow on which shear stress is acting. The hydraulic diameter concept is unfortunately only accurate to ±40% and used in fully developed flow rather than for flow transients. Laminar, fully developed flow has considerable simplifications that make the application of its theory tempting even though it's clear that transient flow dominates the regime. The flow rate at steady state can be found from application of Bernoulli's principle for a horizontal pipe, which results in:

$$Q_{ss} = \frac{\Delta P \pi a^4}{8\mu L} \tag{5.1}$$

with a the outside radius of the channel. In fully developed laminar flow in a straight circular channel, the velocity profile will be:

$$U = U_{\max}\left(1 - \frac{r^2}{a^2}\right) \tag{5.2}$$

with r the radial ordinate anywhere along the channel. This is known as Hagen-Poiseuille flow, or simply Poiseuille flow. Around 1859 E. Hagenbach and F. Newman gave the head loss in a circular channel for Poiseuille flow as:

$$h_{f,lam} = \frac{8\nu L U_{ave}}{ga^2} = \frac{8\nu LQ}{\pi g a^4} \tag{5.3}$$

where Q is the volume flow, and all other variables the same as before and the average flow speed for Poiseuille flow is half of the maximum. Unfortunately this is only for flow that has reached steady state (fully developed), but the linear simplicity and availability of the formula makes a trial application of this head-loss formula hard to resist. The application of this formula is not as limited as may be first expected because it gives a good representation of the flow loss at the two extremes of laminar flow, namely zero flow and when the flow has reached steady state. A fluid, by definition, has no resistance to shear force so there cannot be any flow loss at zero flow. On the other extreme, a laminar flow cannot contain higher velocity gradients for a specific applied pressure gradient than at steady flow where its pressure loss equals the applied pressure gradient. This is clear since the flow has stopped accelerating and hence the losses must equal the applied gradient to ensure force equilibrium.

It has been found by experiment (by Coulomb in 1800) that the effect of channel wall roughness in channels with laminar flow is negligible. Moreover, there is readily available data on many cross-section shapes. It is here that the hydraulic diameter concept is successfully employed, but as mentioned the accuracy leaves something to be desired. It is envisaged that the channel cross section will be square. White (1994) recommends a hydraulic diameter correction for laminar flow in a rectangular channel. This correction is necessary to account for varying wetted area shape of the channel. For a square channel it is recommended that the following be used:

$$D_h = \left(\frac{256}{56.91}\right)\frac{A}{P_w}$$

5.2.2 Incompressible flow

The compressibility of the fluid undergoing a specific flow regime is of great importance because of the simplifications made possible by the incompressible flow assumption. For incompressible flow to occur, the following two conditions have to be met:

> **Requirement 1**: The Mach number ($M=v/c$ with v the flow speed and c the speed of sound in the fluid) must be low, which is the most important requirement.
> **Requirement 2**: The flow must occur within adiabatic boundaries. Hence no heat transfer must take place between the fluid and its environment.

Generally, a truly incompressible fluid has the following characteristics:

1) The innate result of incompressible flow is that the density (ρ in kg/m^3) remains constant throughout the flow. When this condition is substituted into the equation of continuity:

$$\frac{\partial \rho}{\partial t} + \mathrm{div}(\rho\omega) = 0$$

where ω is the velocity vector $\omega =$ u i + v j + w k, it is found that:

$$\mathrm{div}(\omega) = 0$$

2) From the flow speed requirement (requirement 1 above) it follows that if flow does occur (with u, v or w a finite value), the speed of sound inside the fluid must equal infinity to ensure incompressibility. It is important to note that no fluid possesses an infinitely large speed of sound, and that the true speed of sound of the fluid (however large) should be used to calculate pressure transfer delays.

The flow occurring in the sensor ducts will be a negligible fraction of the fluid's sound speed even at extreme acceleration frequencies, which satisfies the first requirement for incompressibility. Furthermore, the second requirement will be met by the fact that the ducts will be in thermal equilibrium with its surroundings with no possibility of kinetic heating in the ducts caused by high speed flows.

5.2.3 Newtonian flow

The general Navier-Stokes equation which form the basis of analytical fluid mechanics, assumes a linear relation between the shear stress in the fluid and the slope of the velocity profile in the flow according to:

$$\tau = \mu \frac{du}{dy} \tag{5.4}$$

where μ signifies a constant viscosity and u is the flow speed.

Not all fluids exhibit a linear relation as in equation 5.4. The shear characteristics of each fluid considered should be taken into consideration as the Newtonian fluid assumption can be in gross error at high strain rates (for dilatants, pseudoplastics and plastics) and even at zero strain rates for a Bingham plastic. Non-Newtonian fluids may also have other deviations from the linear assumption such as a time varying viscosity. Here, an increasing viscosity is referred to a rheopectic fluid whereas a thinning fluid is thixotropic. Deviations such as these will often disqualify a fluid only due to this unfavourable idiosyncrasy alone so that the choice of a Newtonian fluid for the sensor is probable.

5.3 Analytical unsteady flow solutions

The flow in the channels is highly dependent on the deflection of the diaphragm. As mentioned before, it is desirable that the diaphragm deflects as little as possible to limit flow losses, which demands high diaphragm stiffness. The diaphragm stiffness in turn results in a self-centering diaphragm that causes unsteady flow even if the acceleration input is steady. Unfortunately, flow theory is best developed for steady state flow cases where the velocity profile in the channel (boundary layer) is fixed in time. Any flow starting from rest requires a certain time to reach steady state and since the flow under consideration occurs over very short distances, it will rarely reach steady state and the parameters governing transient flow, i.e. inertial forces, will dominate.

An inherent ambiguity exists in the term “unsteady flow”. In general technical literature, this may firstly refer to internal flow that possesses velocity derivatives in time for a wall-fixed inertial frame. For a particle fixed inertial frame, such a flow will also contain time derivatives. On the other hand, unsteady flow may also refer to velocity derivatives with respect to length in the direction of flow for a fixed inertial frame. This can be done because in the particle fixed reference the equations of flow will contain time derivatives and so justly be called “unsteady”. Hence any flow that changes its average velocity in space or in time may be called “unsteady” depending on the inertial reference considered. The former type of flow is the one analyzed here, while the latter type is flow that transitions through channels of changing sectional area or around objects in external flow. The second type of “unsteady” flow in fact may not contain a time derivative in its Navier-Stokes formulation at all. The absence of a time derivative in the Navier-Stokes equation simplifies the process of finding an exact solution. The application of such solutions is also more common than ones containing time derivatives, which makes these sources prevalent. Hence to avoid any confusion: In all references to unsteady flow in this document it is implied that a substantial time derivative is present in the flow when analyzed in the channel fixed inertial frame. To make matters more interesting, the flow analyzed in this document will in fact also occur through varying cross sections and is unsteady due to both effects. The entrance effects are expected to be of small consequence though and are neglected as far as pressure loss is concerned.

The first analytical resource for channel transient flow is the solution derived by Szymanski (1932). Szymanski derived velocity profiles for sudden imposition and maintenance of a pressure gradient on a liquid in a cylindrical pipe. The solution involves a method that employs Bessel functions and persists (to some extent) even in solutions obtained in the 21st century. Russian contribution to this theory starts in 1955 with a comprehensive analytical publication by Slezkin (1955) on incompressible fluids. Slezkin simplifies the theory started by Szymanski but still only gives a solution for the one-dimensional, cylindrical case. The latest additions to exact analytical solutions in unsteady flow were made by Avramenko (2001) who expanded the solvable geometries to rectangular and curvilinear ducts. All solutions rely heavily on symmetry, thus a general geometry analytical solution for the Navier Stokes equation is still very much elusive. For more on unsteady flow see Bernardin (1999) who gave solutions for the unsteady Couette flow formed by a cylinder rotating concentrically inside another. The work of Bernardin is especially applicable to the fluid floated rotor, like the sensor proposed by Minbang and Pen (1992) or the traditional gyroscope, which is described in Gates (1968). For general theory on unsteady incompressible flow see Ladyzhenskaya (1969).

It is probable that the flow generated in the accelerometer will rarely (if ever) reach steady state. Furthermore, a pressure gradient reversal may often be imposed long before the boundary layer is fully developed. This flow is closely related to the problem of Szymanski, except for the differences of pressure gradient imposition and maintenance. In the angular accelerometer the pressure would not be instantaneously applied as Szymanski and Avramenko assumes. The pressure in the channel will be generated by an applied angular acceleration via the inertia of the fluid inside and thus; the nature of the pressure increase is entirely dependent on the dynamic system measured. The solutions of Szymanski and Avramenko give an applicable solution for the flow at different levels of flow development, which is applicable regardless of the governing variables that brought the flow to that stage. This is clear since for a laminar Newtonian fluid (equation 5.4) the shear (and pressure loss) is only dependent on the slope of the velocity profile at the wall.

5.3.1 Slezkin's flow solution for channel flow starting from rest

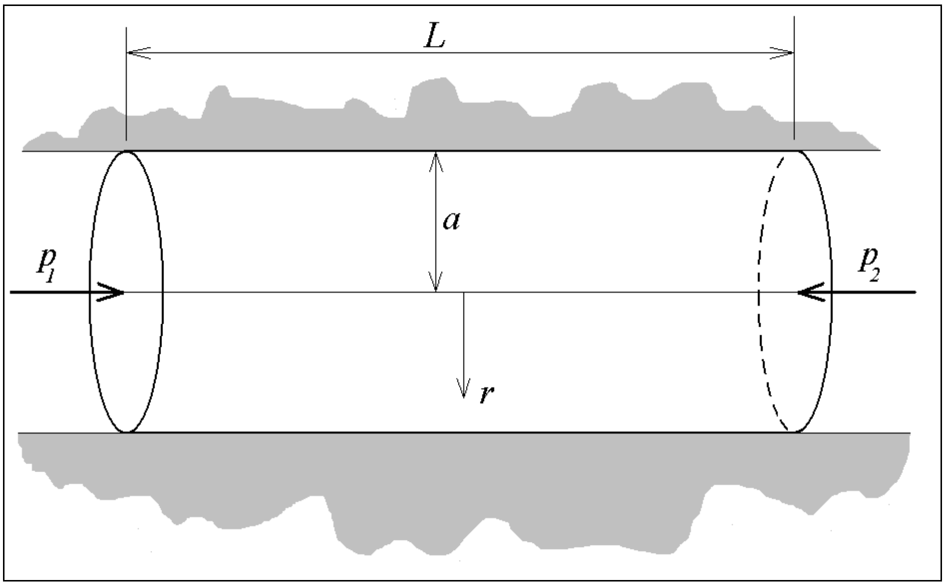

Figure 5.1: Cylindrical channel for which transient flow is solved by Szymanski and Slezkin.

Slezkin derives the transient flow solution for a straight cylindrical channel, hence the Navier-Stokes equation is used in cylindrical coordinates:

$$\frac{\partial u}{\partial t}=\nu\left(\frac{\partial^2 u}{\partial r^2}+\frac{1}{r}\frac{\partial u}{\partial r}\right)-\frac{1}{\rho}\frac{\partial p}{dx} \tag{5.5}$$

The time derivative is clear in equation 5.5, so there is no doubt that the flow is in fact unsteady. The last term is assumed constant during the flow and non-existent before the flow starts. That is:

$$\frac{1}{\rho}\frac{dp}{dx}(t)=\begin{cases}0 & t\le 0\\ P_1 & t>0\end{cases}$$

Furthermore:

$$P_1=-\frac{dp}{dx}\frac{1}{\rho}=\frac{-(p_1-p_2)}{\rho\ L}$$

The solution for this case is given as:

$$u(r,t)=P_1\frac{a^2}{4\nu}\left[1-\frac{r^2}{a^2}-8\sum_{k=1}^{\infty}\frac{J_0\left(\alpha_k\dfrac{r}{a}\right)}{\alpha_k^3 J_1(\alpha_k)}\exp\left(-\nu\frac{\alpha_k^2}{a^2}t\right)\right] \tag{5.6}$$

with J_0 and J_1 Bessel functions of the first kind (zero and first order respectively) and α_k the zeros of J_0. Equation 5.6 may be simplified by making some substitutions that have become customary. As will be seen shortly, the degree of development of the boundary layer depends on the factor $\nu t/a^2$. This factor is called the Fourier number of the flow or:

$$Fo = \frac{\nu\, t}{a^2}$$

The Fourier number is measured in seconds and is as such a time constant of the flow. The variable P_1 and Fo is substituted into equation 5.6, which yields:

$$u(r,t) = -\frac{dp}{dx}\frac{a^2}{4\mu}\left[1 - \frac{r^2}{a^2} - 8\sum_{k=1}^{\infty}\frac{J_0\left(\alpha_k \dfrac{r}{a}\right)}{\alpha_k^3 J_1(\alpha_k)}\exp\left(-\alpha_k^2 Fo\right)\right] \tag{5.7}$$

The effect of density on the flow acceleration (that seems to be included with the formulation for P_1) has apparently disappeared. This is a false impression since density still makes itself felt in the Fourier number. Equation 5.7 is plotted in figure 5.2 for a series of Fourier numbers. The Bessel series is solved for the first 10^4 roots calculated to a tolerance of 10^{-6}. Convergence errors are most apparent at zero Fourier number, so a measure of the quality of the convergence is to test the maximum flow speed at zero Fourier number. The accuracy of the convergence will improve approximately by an order of magnitude if the number of zeros used increases also by an order of magnitude.

The following is clear from the figure:

1) In the first stages of flow, the boundary layer is still thin and only reaches the central regions of the flow as the flow develops.
2) The steady state flow (at infinite Fourier number) has the parabolic velocity distribution of Poiseuille flow (equation 5.2).
3) The velocity gradient for each Fourier number is maximal at the channel wall (after motion has started). The highest gradient is reached at infinite Fourier number. According to equation 5.4, the wall shear is therefore also a maximum at steady state and hence the flow pressure loss is also a maximum at steady state. Equation 5.3 gives the maximum pressure loss for laminar flow in a circular pipe for a certain pressure gradient.
4) At the start of motion (Fo=0) there is no velocity gradient because there is no flow. The wall shear and pressure loss are zero for this case.
5) The flow at a Fourier number of 0.75 is very close to full development. (The maximum normalized velocity at Fo=0.75 is 98.5%.) A flow with a Fourier number of unity can thus be safely assumed as steady state for speed profile purposes. (At Fo=1 the maximum normalized velocity is 99.66%.)

The flow rate is found by integrating equation 5.7 over the cross sectional area:

$$Q = \int_0^{2\pi}\int_0^{a} u(r,t)\; r\,dr\,d\theta = -\frac{dp}{dx}\frac{\pi a^4}{8\mu}\left[1 - 32\sum_{k=1}^{\infty}\frac{\exp\left(-\alpha_k^2 Fo\right)}{\alpha_k^4}\right] \tag{5.8}$$

Equation 5.8 is normalized to unity (like equation 5.7 in figure 5.2), which is plotted in figure 5.3. Like flow speed, the flow rate levels off at a Fourier number of one. Equation 5.8 gives the best indication of how mass is transferred inside the channel and shows directly the application of Newton's second law in laminar flow with viscous pressure losses taken into account. This is advantageous when simulating the flow because of the elimination of pressure loss feedback (as a function of flow speed) as an additional applied pressure.

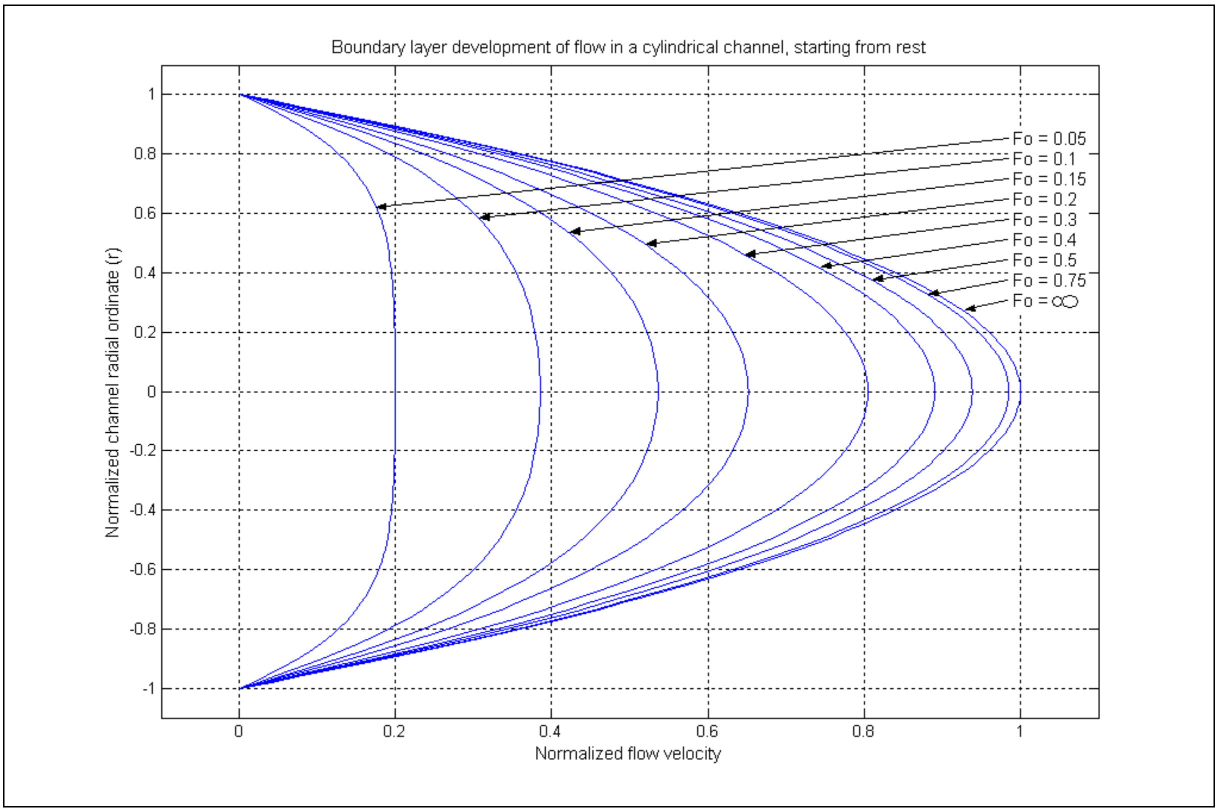

Figure 5.2: Szymanski's solution for unsteady flow in a cylindrical channel starting from rest, plotted from Slezkin's solution (equation 5.7).

5.3.2 Pressure loss

The pressure loss generated by developing flow is now derived (as a function of time) by means of evaluating equation 5.4 at the channel wall for the flow described by equation 5.7:

$$\tau = \mu\left(\frac{du}{dr}\right)_{r=a} = \frac{1}{2}\frac{dp}{dx}a\left[1-4\sum_{k=1}^{\infty}\frac{\exp\left(-\alpha_k Fo\right)}{\alpha_k^2}\right] \tag{5.9}$$

According to the Darcy-Weisbach equation (which is derived from momentum conservation) the head loss of duct flow at steady state is:

$$h_f = f\frac{L}{d}\frac{U^2}{2g} \tag{5.10}$$

With f the Darcy friction factor (a dimensionless value), d the channel diameter and U the average flow speed. The shear induced pressure loss is:

$$\Delta P_{shear} = \rho g h_f \tag{5.11}$$

The friction factor is derived from dimensional analysis to be:

$$f = \frac{8\tau_w}{\rho U^2} \tag{5.12}$$

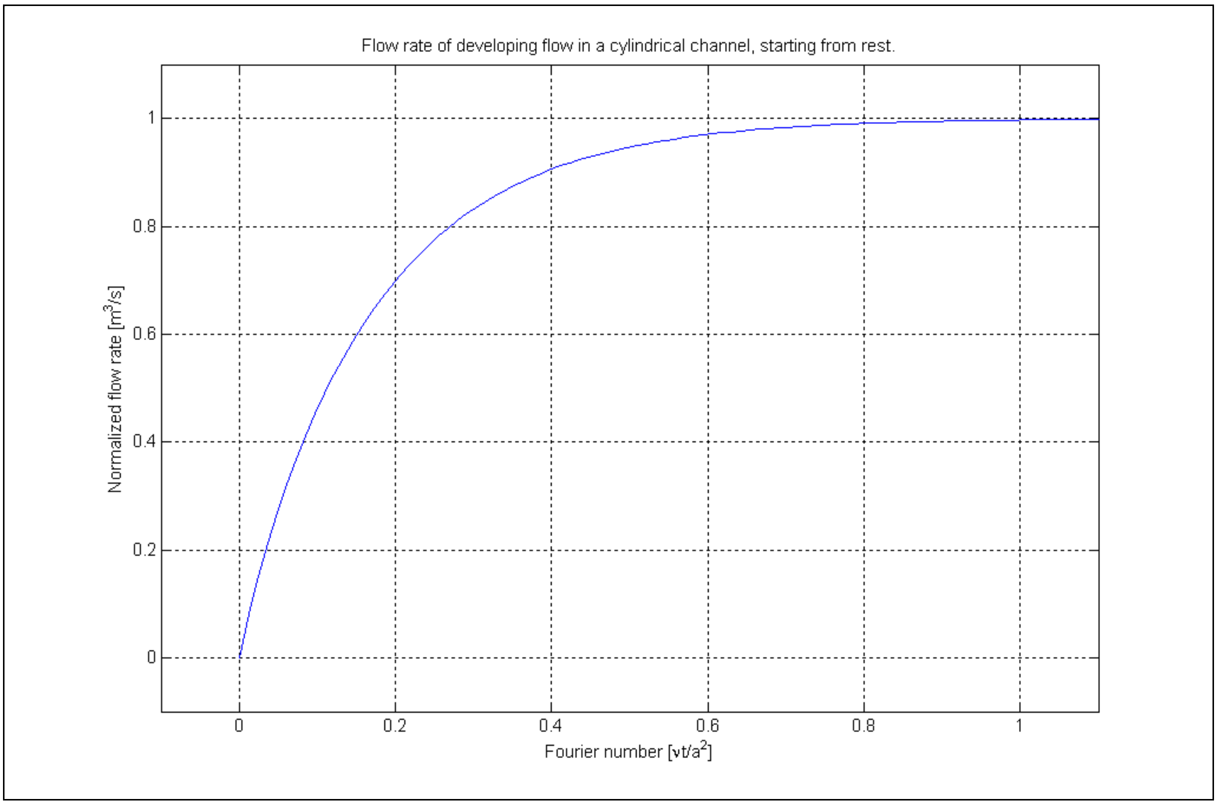

Figure 5.3: Flow rate versus Fourier number for Slezkin's solution for unsteady flow starting from rest.

Equation 5.10 and 5.12 is substituted into equation 5.11, which makes the shear induced pressure loss in the channel:

$$\Delta P_{shear} = \frac{4\tau_w L}{d} \tag{5.13}$$

Substituting equation 5.9 into equation 5.13 yields:

$$P_{shearloss} = L\frac{dp}{dx}\left[1 - 4\sum_{k=1}^{\infty}\frac{\exp(-\alpha_k Fo)}{\alpha_k^2}\right] \tag{5.14}$$

This result could have been anticipated at equation 5.9 already because as mentioned before, the pressure loss must equal the applied pressure at steady state. Unlike the flow speed, the pressure loss is independent of the radial position in the channel, but directly proportional to the channel length and pressure gradient that caused the flow. The effects of time, viscosity, density and pipe diameter are contained in the Fourier number as before. After full development, all terms in the square brackets add to unity. A normalized result of equation 5.14 is shown in figure 5.4.

Figure 5.4 shows a pressure loss of 93.7% at a Fourier number of unity even though the maximum flow speed is at 99.66% of the Poiseuille distribution according to equation 5.7. For the purposes of pressure loss a Fourier number of 2.5 may be assumed as the maximum possible flow development (99.8%) whereas a Fourier number of one is sufficient for flow speed, or volume rate purposes.

Equations 5.7 and 5.14 are pressure gradient dependent, but equation 5.3 is not (since developed flow is assumed). Yet the result of equation 5.14 at an infinite Fourier number must equal the result of equation 5.3. This is used as a verification of the validity of equation 5.14.

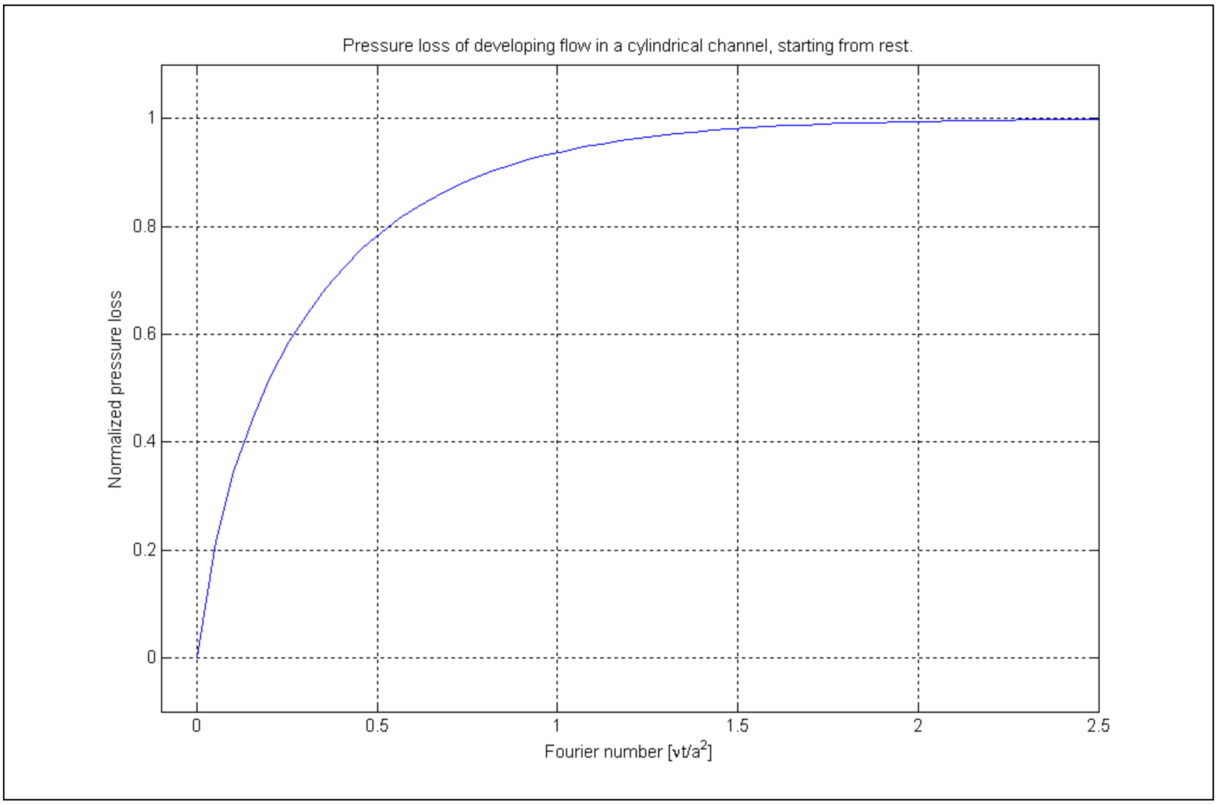

Figure 5.4: Pressure loss in unsteady flow expressed as a fraction of the maximum steady state loss predicted by Hagen-Poiseuille flow.

5.3.3 Avramenko's solutions for flow starting from rest

The derivation of the previous set of equations for unsteady flow dates from as early as 1932 and into the 1950s for the equations of Slezkin. With the enormous rise of numerical flow analysis in recent years relative to analytical flow analysis, it is somewhat surprising that a significant publication on incompressible unsteady flow solutions was done by Avramenko in 2001. It covers laminar and turbulent flow for many differently shaped channels in one and two dimensions. Curvilinear channels are also covered, which is where this document finds interest because the channels manufactured into the wafers will mostly be curved. The ratio of the channel effective diameter to the curve diameter will be below 1 percent, thus straight channel theory will be applied in this document. Yet, at smaller channel curvatures it may become necessary to have more apt theory for curved channels.

From the conditions set in previous sections, namely Newtonian, incompressible, laminar flow the Navier-Stokes equation describing the dynamics of the flow is:

$$\frac{\partial u}{\partial t} = -\frac{1}{\rho}\frac{dp}{dx} + \nu\frac{\partial^2 u}{\partial y^2}$$

The first term on the right of contains the pressure gradient that causes motion in the fluid. This pressure gradient (assumed as constant by Szymanski and Slezkin) is expanded to a more general case by Avramenko. The first right hand term now becomes:

$$-\frac{1}{\rho}\frac{dp}{dx}(t) = \begin{cases} 0 & t \le 0 \\ G_0 t^n & t > 0 \end{cases}$$

The pressure gradient becomes an exponential function of time. Avramenko provides ordinary differential equations for many cases, of which the curvilinear channel is most relevant to this document's scope. The channel has an inner curve radius of R_1 and an outer radius of R_2. Avramenko proposes the following ordinary differential equation for one-dimensional curvilinear flow that may be solved with a boundary value problem method:

$$\frac{d^2u}{d\eta^2}+\left(\frac{\eta}{2}+\frac{1}{\eta}\right)\frac{du}{d\eta}-u\left(n+\frac{1}{2}+\frac{1}{\eta^2}\right)=-\frac{B}{\eta}$$

$$\eta=\frac{r}{\sqrt{\nu\ t}} \quad \text{and} \quad B=G_0\nu^{-n-2}h^{2n+2}$$

where u is the normalized flow as a fraction of the maximum flow. The boundary conditions for the problem is:

$$1)\ u=0 \qquad \text{for} \qquad \eta=\eta_1=\frac{R_1}{\sqrt{\nu\ t}}$$

$$2)\ u=0 \qquad \text{for} \qquad \eta=\eta_2=\frac{R_2}{\sqrt{\nu\ t}}$$

A two dimensional curvilinear solution is also provided, in partial differential equation form:

$$\frac{\partial^2u}{\partial\eta^2}+\frac{\partial^2u}{\partial\xi^2}+\left(\frac{\eta}{2}+\frac{1}{\eta}\right)\frac{\partial u}{\partial\eta}+\frac{\xi}{2}\frac{\partial u}{\partial\xi}-u\left(n+\frac{1}{2}+\frac{1}{\eta^2}\right)=\frac{B}{\eta}$$

where $\xi=\frac{z}{\sqrt{\nu\ t}}$, which gives the self-similar variable for the second dimension. All other variables are as before. The two dimensional problem is solved with the four boundary conditions:

$$1)\ u=0 \qquad \textit{for} \qquad r=R_1$$

$$2)\ r=R_2$$

$$3)\ u=0 \qquad \textit{for} \qquad z=0$$

$$4)\ z=b$$

5.4 Modeling of flow

Equations 5.7, 5.8 and 5.14 are not directly useful for simulating flow in a finite time difference scheme because a very large series will have to be solved for each time step. Another complication is that these equations are only valid for step pressure gradient inputs. In an optimization exercise the simulation may be required to handle many varied types of inputs.

Two options exist for the mathematical modeling of the flow in a simulation. The first method entails the calculation of the Fourier number based on flow conditions and applying a change in flow in each time step taken from the derivative of equation 5.8. The simulation for this method requires an exceedingly large relational logic base to remove pressure singularities and assure the correct flow changes take place for all conditions.

The more effective method that readily befits any shape input is a transfer function, which gives the output of a process for any input. A transfer function is generally derived from first principles according to the physics of the problem. An ordinary differential equation of the system is first derived which includes time derivatives of all relevant states. A Laplace transformation is then used to transform the differential equation into an algebraic equation and so derive the transfer function itself. In the case of unsteady flow, a differential equation (namely the Navier Stokes equation) is already available, but unfortunately it is a partial differential equation that is not so easily treatable by a Laplace transformation. It is due to the difficulty of solving the Navier Stokes equation that Bessel functions are employed to solve the flow. The result for flow rate given in equation 5.8 is a time-based solution to which a suitable transfer function must be fitted so that proper simulation of the flow may be done.

On first glance of figure 5.4, the flow rate development looks remarkably like either that of a first order system, or an over damped second order system. Where figure 5.4 differs notably from a second order step response is in its time derivatives. The volume flow rate in figure 5.4 has an initial maximum rate that decays to zero at steady state whereas a second order system by default starts with zero rate. The flow development therefore better fits a first order system that also starts with maximum rate. This does not imply that flow development is in fact perfectly first order. The fit quality of the flow rate development to a first order system transfer function has to be tested.

5.4.1 Test for first order system

By virtue of the fact that the pressure imposition is a step input, a test may be done to ascertain whether the system is in fact first order as suspected. In order to determine experimentally whether a system is of first order, the curve of $log|c(t) - c(\infty)|$ is plotted where $c(t)$ is the system output as a function of time (or Fourier number in this case). If the curve is a straight line, the system is of first order.

Equivalently, it may be more convenient to plot $|c(t)-c(\infty)| \,/\, |c(0)-c(\infty)|$versus t on a semilog scale. A first order the transfer function is:

$$R(s) = \frac{1}{Ts+1} C(s) \tag{5.15}$$

of which the step response is:

$$c(t) = 1 - \exp\left(\frac{t}{T}\right) \tag{5.16}$$

where T is the time constant, s is the Laplace operator, $R(s)$ and $C(s)$ is the Laplace transformed output and input respectively. Assuming a system passes the first order test, the time constant can be found as the time T that satisfies the relation:

$$c(T) - c(\infty) = 0.368 \;\; [c(0) - c(\infty)] \tag{5.17}$$

Also, when taking the derivative of equation 5.16 at time zero:

$$\left.\frac{dc}{dt}\right|_{t=0} = \left.\frac{1}{T} e^{-t/T}\right|_{t=0} = \frac{1}{T} \tag{5.18}$$

Thus the time constant can also be found as the reciprocal of the starting slope of the output. Note that both the methods for calculating the response time constant assumes first order response, so when using equation 5.18 to calculate the time constant a good first order fit is required at time zero.

The flow relation of equation 5.8 is now subjected to the test for a first order system and plotted in figure 5.5. Figure 5.5 confirms that unsteady volume flow response is indeed close to first order. Although figure 5.5 seems to be perfectly straight, the plot is now investigated closer for linearity errors. Figure 5.6 shows the slope error of figure 5.5 as a measure of the deviation from a straight line. The slope error presents more clearly than visual inspection of figure 5.7 because the error is amplified by the derivative.

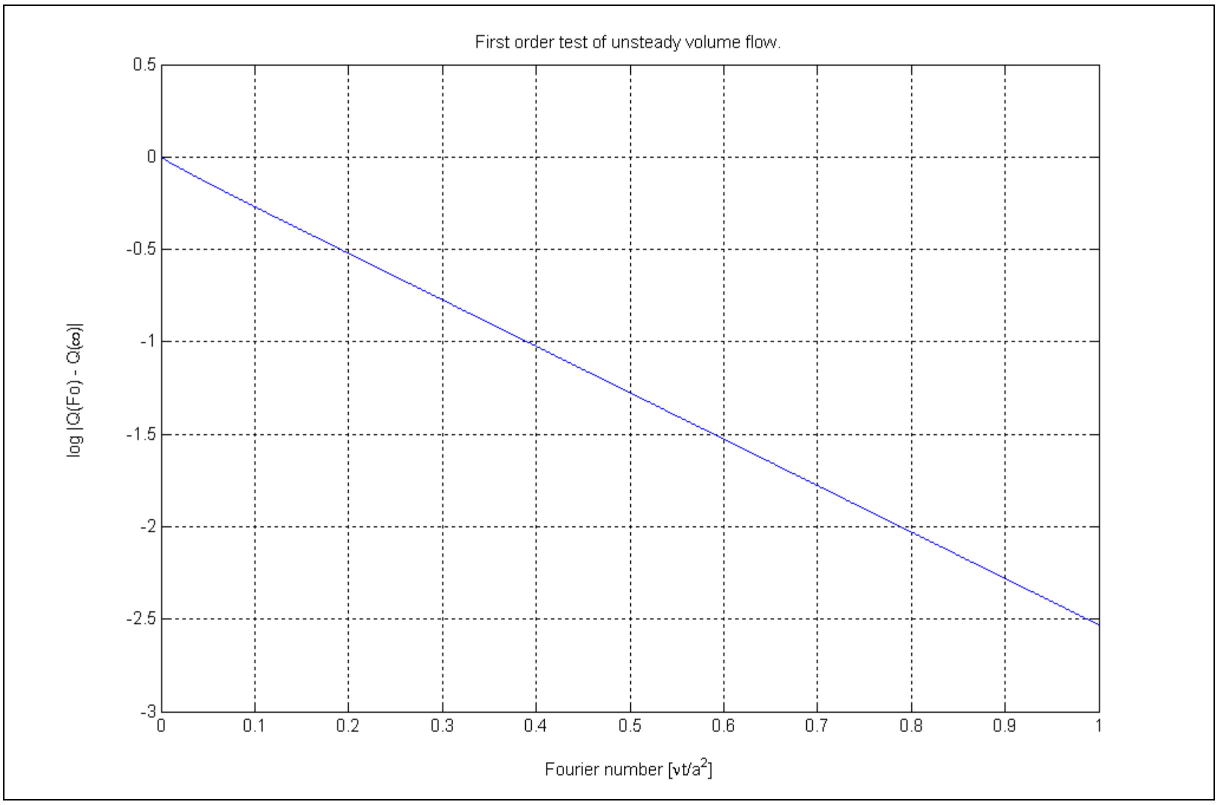

Figure 5.5: Test for first order response of unsteady volume flow versus Fourier number.

Figure 5.6 shows that the flow response fit to a first order system is worst at the start of flow, but improves to good linearity beyond a Fourier number of 0.2. The deviation from the straight line is still minimal at low Fourier number (as shown in figure 5.5) yet due to the slope deviation at the start of flow the Fourier number region of 0 to 0.2 should not be used for the purpose of determining time constants. The slope error at *Fo*=0.205 is 0.1%.

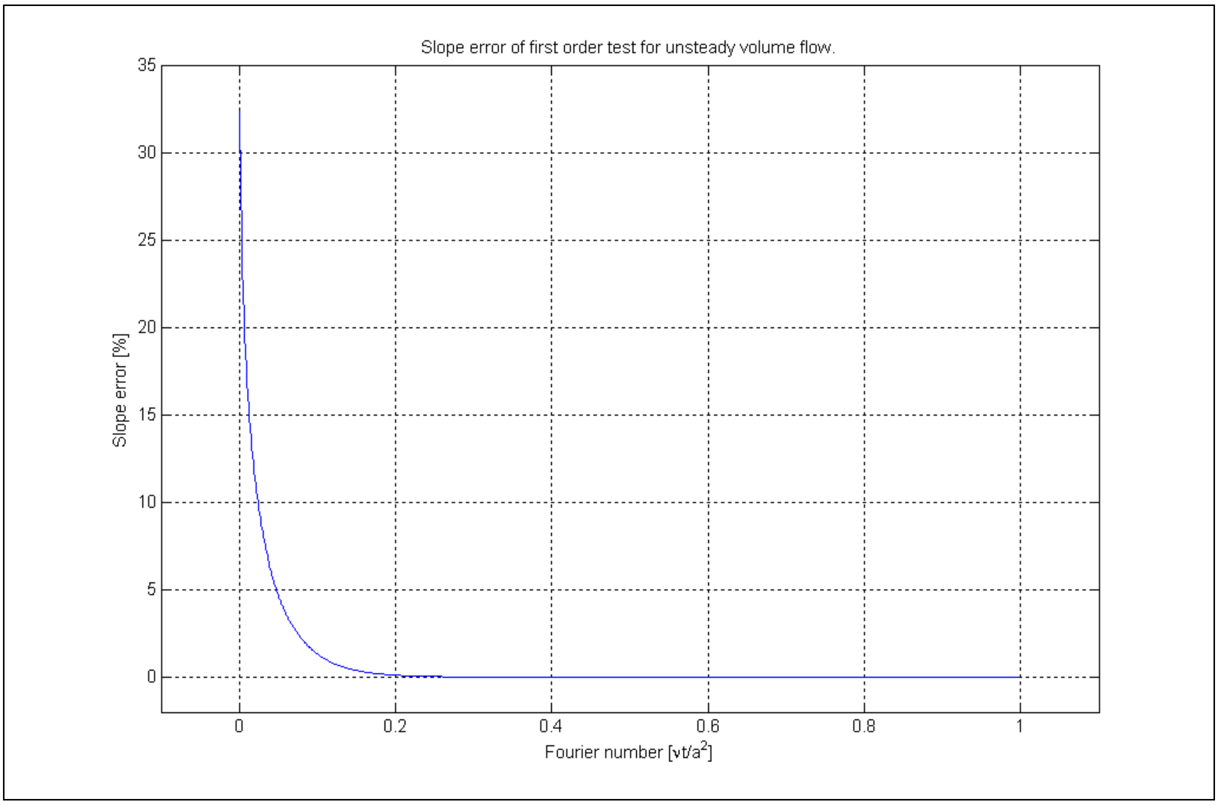

Figure 5.6: Deviation from first order response for volume flow.

5.4.2 First order model of flow

Equation 5.8 is now fitted to a first order response with account for the limitations set by the linearity test. When the flow response to a constant pressure gradient is assumed as first order in nature, the flow develops according to a modification of equation 5.16:

$$Q = -\frac{dp}{dx}\frac{\pi a^4}{8\mu}\left[1-\exp\left(-Fo\ N\right)\right] \tag{5.19}$$

where N is a dimensionless constant that allows the time constant of equation 5.16 to be set according to the correct Fourier number. In order to fit equation 5.19, it is normalized by dividing by the steady state quotient on both sides:

$$\begin{aligned}\frac{Q}{Q_{ss}} &= 1-\exp\left(-Fo\ N\right)\\ &= 1-\exp\left(-\frac{\nu\ t\ N}{a^2}\right)\end{aligned} \tag{5.20}$$

where Q_{ss} is the flow at steady state. The transfer function's time constant T then becomes:

$$T = \frac{a^2}{\nu\ N} = \frac{a^2\rho}{\mu\ N} \tag{5.21}$$

The information contained in figure 5.3 is substituted into equation 5.20 to find N for any Fourier number and cross-referenced normalized flow. The N calculated in this method will make the flow development line run through the selected point and assumes first order response everywhere else. Figure 5.7 shows the constant N calculated for the whole range of development.

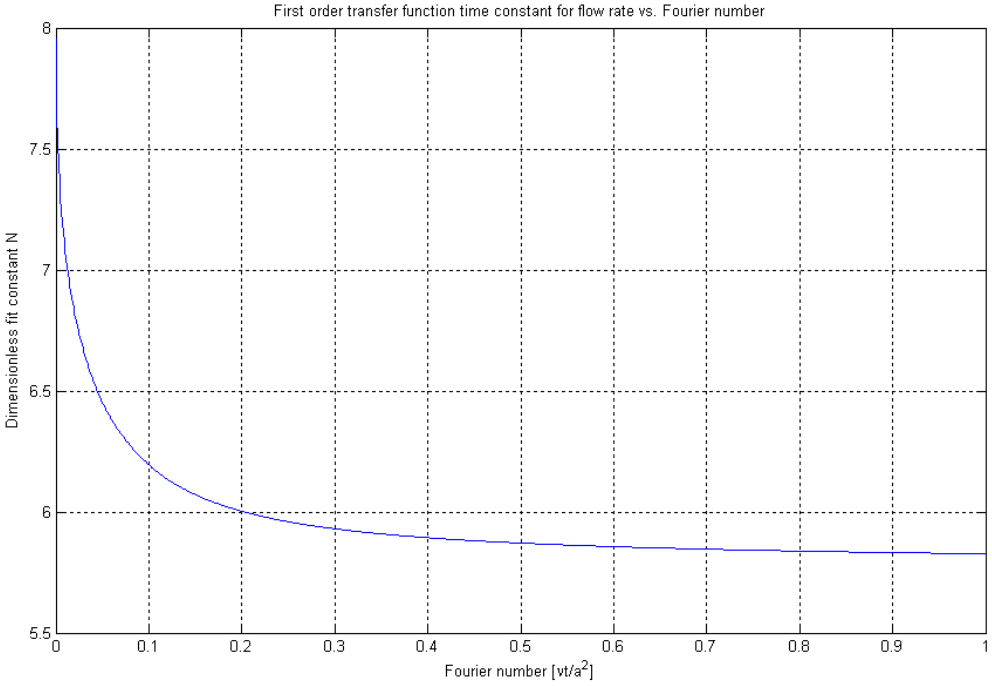

Figure 5.7: Dimensionless constant for fitting of flow theory to first order response.

The decision on which Fourier number to take is the designer's, but for unsteady flow that may reach full development, a good fit is required over the whole range. The main impact of different *N* factors is on the starting slope and the time taken to reach steady state. A fit at any Fourier number will start at zero and reach the same steady state because the steady state error on any first order system for a step input is zero. For this reason, it is advantageous to take the smallest *N* possible that still represents a realistic flow settling time since it implies the smallest starting slope error. A good fit is acquired at *Fo*=0.21 just beyond the domain of high linearity errors predicted by figure 5.6. The fit is plotted in figure 5.8.

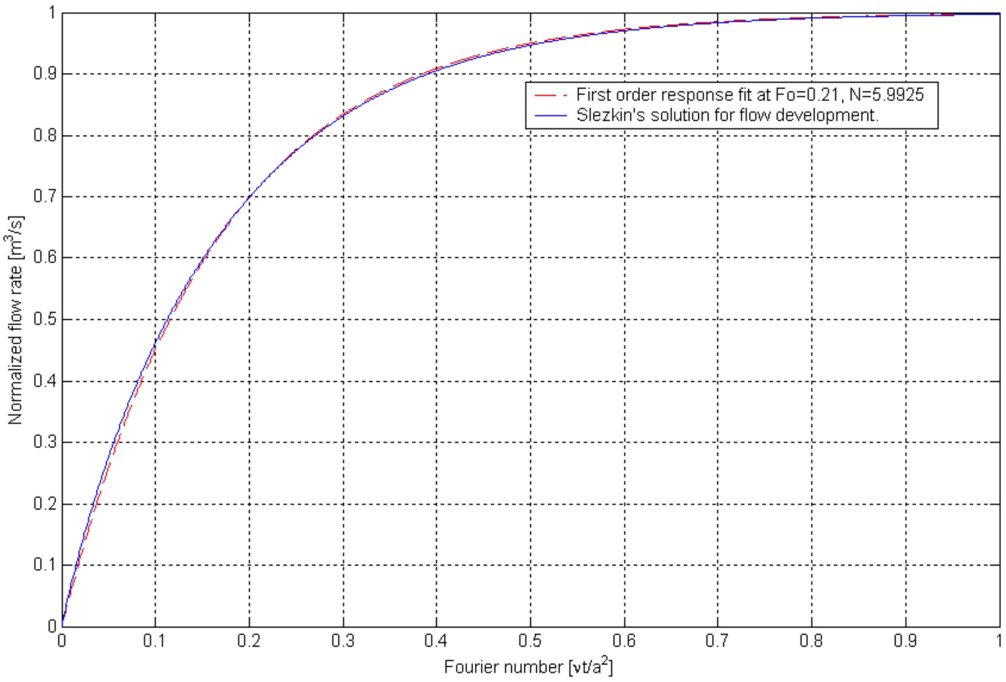

Figure 5.8: Fit of first order response to flow data for an *N* of 5.9925.

As intended, the fit is perfect at *Fo* = 0.21, but deviates slightly on either extreme. The starting slope error can be seen to be minor with this fit and may be improved at the expense of quality in fit elsewhere.

5.5 Validation and conclusions on flow relations

Whether unsteady flow is indeed prevailing in this application can be tested with the Fourier number. The time required for mercury to reach a Fourier number of 2.5 for up to 0.2mm diameter is shown in figure 5.9.

Steady state can take considerable time to achieve, which means that the sensor will function in unsteady flow conditions, even with small channels at low frequencies. The necessity for unsteady flow theory is confirmed by this graph. The recommended transfer function for pressure gradient input to flow output is:

$$\frac{Q(s)}{P(s)} = \frac{\pi a^4 / 8\mu L}{\left(\dfrac{a^2 \rho}{\mu \; 5.9925}\right) s + 1} \tag{5.22}$$

with $Q(s)$ and $P(s)$ the Laplace transforms of the flow and differential pressure respectively. The numerator originates from the steady state flow defined in equation 5.1.

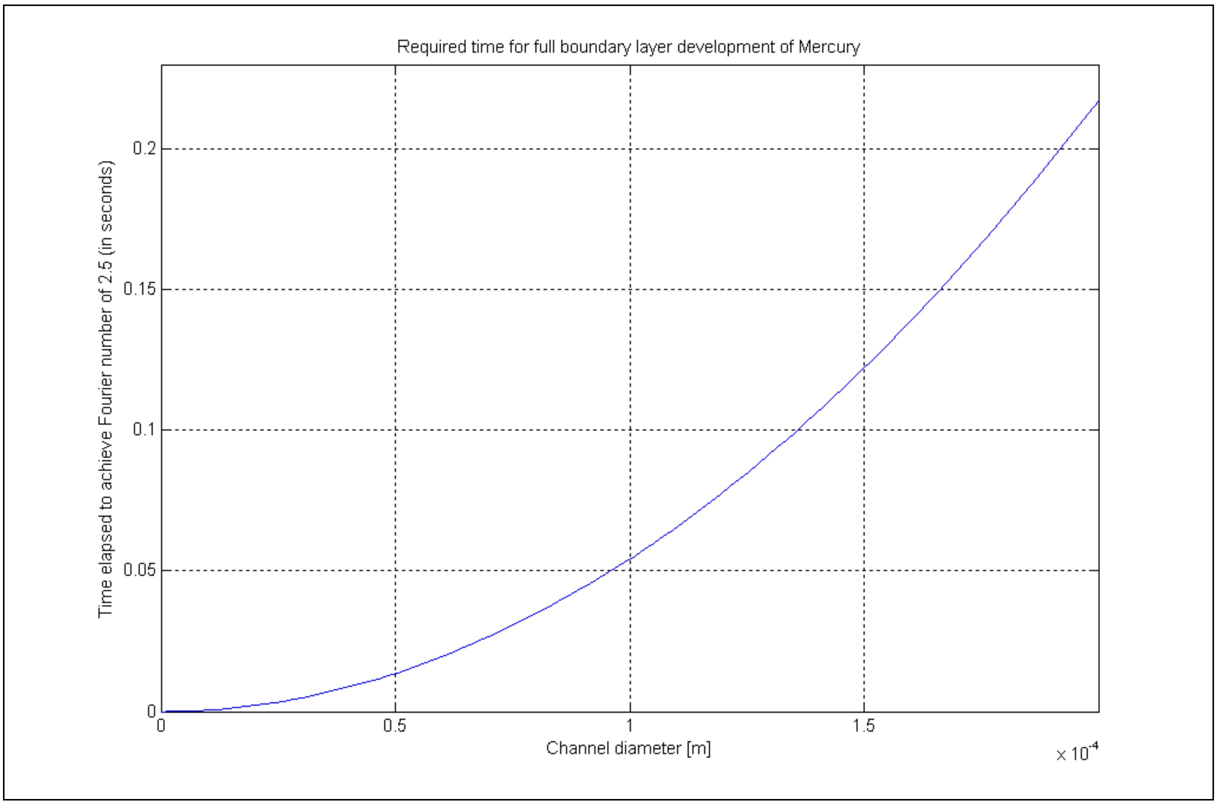

Figure 5.9: Time required (in seconds) for mercury to reach pressure loss steady state. Volume flow steady state is reached earlier at a Fourier number of unity.

Because no experimental verification is to be done on the flow relations in this document, the Szymanski flow fit (equation 5.22) is now compared to another unsteady flow regime, namely harmonic pulsatile flow to determine the validity of the assumptions made. The pulsatile flow of blood in arteries has been studied by Womersley (1955). The pressure input is assumed harmonic in the form:

$$\frac{dp}{dx} = A\exp(i\omega\, t) \tag{5.23}$$

where A is a constant representing the amplitude of the applied pressure gradient, ω is its frequency in rad/s and t is time is seconds. According to Womersley the resulting flow for the layout illustrated in figure 5.1 is:

$$Q = \frac{\pi\ a^2 A\exp(i\omega\ t)}{i\omega\rho}\left[1 - \frac{2J_1\left(i^{\frac{3}{2}}\alpha\right)}{i^{\frac{3}{2}}\alpha\ J_0\left(i^{\frac{3}{2}}\alpha\right)}\right] \tag{5.24}$$

where $\alpha^2 = \dfrac{a^2\omega\rho}{\mu}$ and i is the imaginary number. α is known as the Womersley number; an unsteady analogue to the Reynolds number. Womersley models flows resulting from non-harmonic pressure inputs (like that resulting from the human heart) by approximating the non-harmonic input with a Taylor series. The solution assumes that the harmonic flow rate has reached steady state, thus no initial condition is applicable like the stationary fluid initial condition of Szymanski. This assumption befits cardiac output modelling well and many of the scenarios that the MFCAA will be subjected to, therefore a comparison to the first order fit of Szymanski flow is illustrative of the quality of the fit.

The harmonic nature of the Womersley solution makes a Bode plot readily calculable to be compared to the Szymanski fit. Since Womersley flow is harmonically steady at any time no transients have to be accounted for. The flow potential is taken as input to the system for the bode plot, while volume flow is the output hence a transfer function of unity (0dB) indicates steady flow. The first order Szymanski fit is also easily converted to a Bode plot, which is compared to that of Womersley flow for a $500\mu m$ outer diameter pipe in figure 5.9.

The two graphs coincide at zero frequency because both flows assume the Poiseuille steady flow scenario. At higher frequency the graphs diverge slightly, with the Szymanski fit offering lower magnitude and more lag than the Womersley response. Compared to Womersley flow theory, the Szymanksi flow fit is therefore conservative throughout its frequency response. With larger pipe diameters the phase response of Womersley flow approaches that of the Szymanski fit with increasing frequency, confirming the 1st order dominant nature of unsteady flow. The good correlation verifies the suitability of the Szymanski flow fit for use in dynamic simulation of the sensor channel flow.

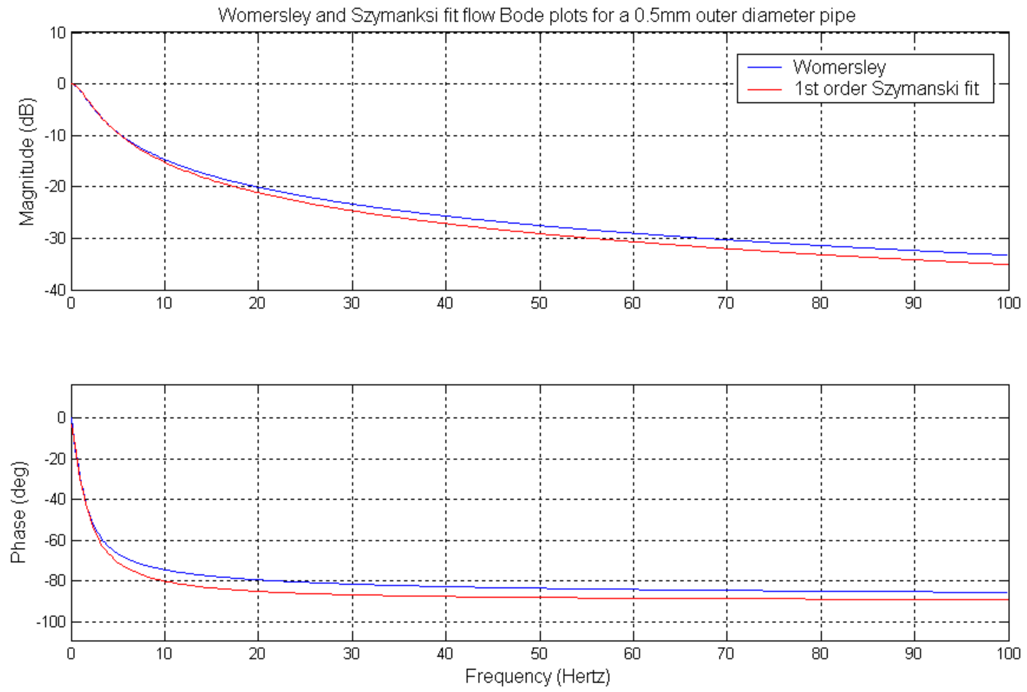

Figure 5.9: A comparison between the Womersley flow model and the 1st order Szymanski flow fit of equation 5.22 for a $500\mu m$ outer diameter pipe.

Chapter 6

Pressure transducer

6.1 Introduction

The type of pressure transducer is a decision of great implication to the sensor performance, and there are a myriad of methods to measure pressure that can be self-contained in a small volume. In the decision of the transducer type, the following priorities are set (in no particular order):

1) Signal to noise ratio: The only motive for the existence of the transducer is the output of a linear, clean signal. High output sensitivity and low noise across the frequency range is thus important.
2) Low frequency response: The pressure transducer should have a DC response, or at least response down to very low frequencies. This is an important requirement for inertial navigation.
3) Stiffness is of high importance to the bandwidth of the sensor. A stiffer transducer will cause less flow, which is where most bandwidth is lost or gained.
4) The pressure transducer must be contained within the channel array. Larger ultra-sensitive pressure transducers do exist that would have to be installed externally, but this is in conflict with the sensor objective of miniaturization.

Two concepts are evaluated in this chapter. The Strain-gaged diaphragm is the first, and the the piezo-electric transducer, which is very popular in dynamic pressure measurement systems is the second. The piezo concept will still contain a diaphragm to transmit the pressure from the fluid to the piezo crystal; hence diaphragm theory is still applicable here, although most of the transducer stiffness is obtained from the piezo crystal itself.

The aim of this chapter is to acquire necessary theory for the design theory for the design of the strain-gaged diaphragm, and the piezo-diaphragm pressure transducer. The suitability of each concept will be evaluated in chapter 8.

6.2 Strain-gaged diaphragm pressure transducer

The strain-gage is essentially a displacement (strain) to signal transducer. The strain-gage functions on the principle of the change in a conductor's resistance when it is deformed longitudinally. A wire under tension will reduce in thickness due to Poisson's ratio, which in turn increases the wire's resistance. Similarly, a wire under longitudinal compression will decrease in resistance. Generally the strain is miniscule and the change in resistance as well. Electric circuits are available to measure this small change in resistance; the most popular of which is the Wheatstone bridge. The diaphragm central to the MFCAA experiences strain when differential pressure is generated across it, which makes a strain-gage a candidate in this application.

For the MFCAA, the strain-gaged diaphragm has the following pros:

- Cheap and simple to implement.
- Minimal supporting electronics.
- One gage provides measurement of differential pressure in any direction.

and cons

- Low stiffness, which degrades sensor bandwidth.
- Low sensitivity.
- Temperature instability.

A strain-gaged diaphragm may use many types of strain-gages, even ones generally used for beam, rod or bar deformation since it also deforms in similar modes. Strain-gages do exist that that are specifically designed for diaphragms though, that are just as readily available as normal ones. They have the following features:

1) One full Wheatstone-bridge is completed by using one diaphragm strain-gage foil. This provides for temperature compensation in the bridge while only using one face of the diaphragm.
2) One gage measures both compressive and tensile strains simultaneously and averages it across the diaphragm. Sensitivity for a diaphragm is therefore optimized for use with a diaphragm.

An example of an implementation of a diaphragm strain-gage into a simple Wheatstone-bridge arrangement is shown in figure 6.1.

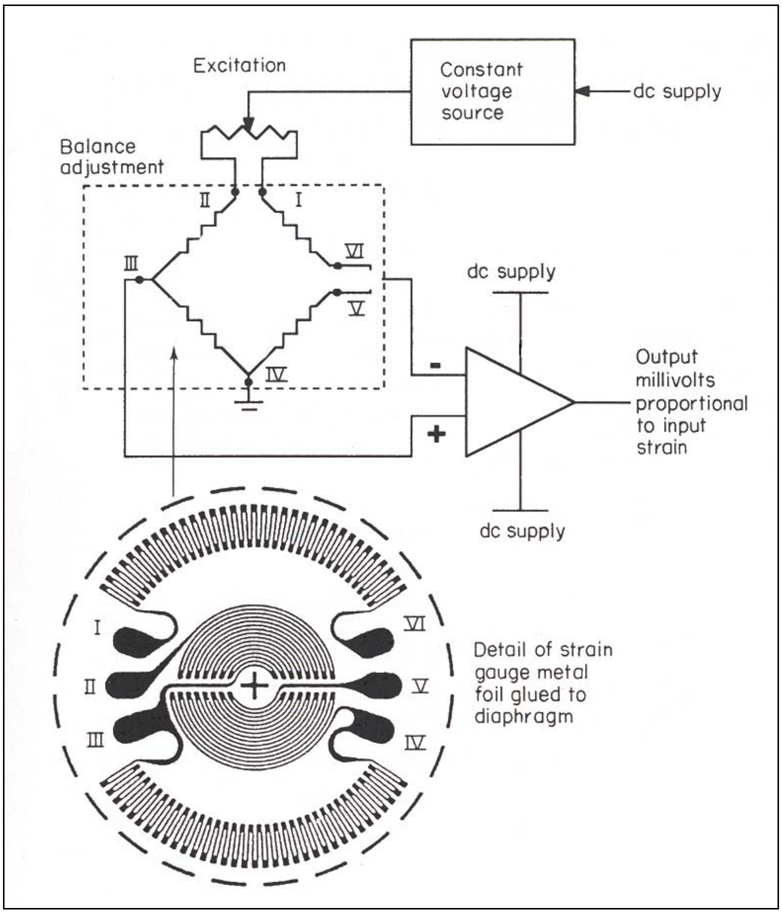

Figure 6.1: A diaphragm strain-gage.
(Taken from Sydenham and Hancock (1989))

An unfortunate result of using a diaphragm is that its linearity leaves much to be desired, even at very small deflections. A general rule to achieve good linearity is for the maximum diaphragm deflection not to exceed the diaphragm thickness. For 0.3% linearity this has to be limited to a quarter of the thickness. This doesn't leave much room for deformation of the diaphragm in a linear system. In the MFCAA application, the diaphragm will probably only be used well within its linear range since flow has to be limited anyway. The small linear range of the diaphragm is therefore not a direct drawback; it has to be ensured due to other considerations too. The issue of linearity is addressed further in the following section.

6.2.1 Circular diaphragm stress and strain

Using a thinner diaphragm for a more sensitive measurement will cause bigger deflection and bigger flow losses and linearity errors. These two conflicting requirements are the main trade-offs being made in the diaphragm; the only way to partially avoid this conflict is a proper internal control system that controls diaphragm deflection even for very thin diaphragms. This is the main reason for the inclusion of such a control system.

The aim of this section is to provide optimization inputs for the strains and stresses in the diaphragm and their relation to the flow in the system. As is the case many scenarios in structural design, the main analytical source of theory for diaphragms is found in Young and Budynas (2002). For a solid circular plate (diaphragm) that is loaded with constant pressure over its entire surface and fixed at its edge, Young and Budynas gives the deflection of the diaphragm as:

$$y = y_c + \frac{M_c r^2}{2D(1+\nu)} - \frac{qr^4}{64D} \tag{6.1}$$

where M_c is the diaphragm center moment, q is the pressure across the diaphragm, ν is Poisson's ratio and r is the radius from the diaphragm center. The diaphragm center deflection is y_c and D is the plate constant, which is defined as:

$$D = \frac{Et^3}{12(1-\nu^2)} \tag{6.2}$$

where E is Young's modulus, t is the diaphragm thickness. Furthermore, the center deflection of the diaphragm is:

$$y_c = -\frac{qR_0^4}{64D} \tag{6.3}$$

where R_0 is the diaphragm outside radius. Bending stress in the diaphragm is related to the moment at that point according to the formula:

$$\sigma_{bend} = \frac{6M}{t^2} \tag{6.4}$$

The moment at the center of the diaphragm is:

$$M_c = \frac{qR_0^2(1+\nu)}{16} \tag{6.5}$$

While at the edge the moment is:

$$M_{R_0} = \frac{-qR_0^2}{8} \tag{6.6}$$

In most cases the stress at the edge of the diaphragm will govern the design. The diaphragm deflection shape according to linear theory is shown in figure 6.2.

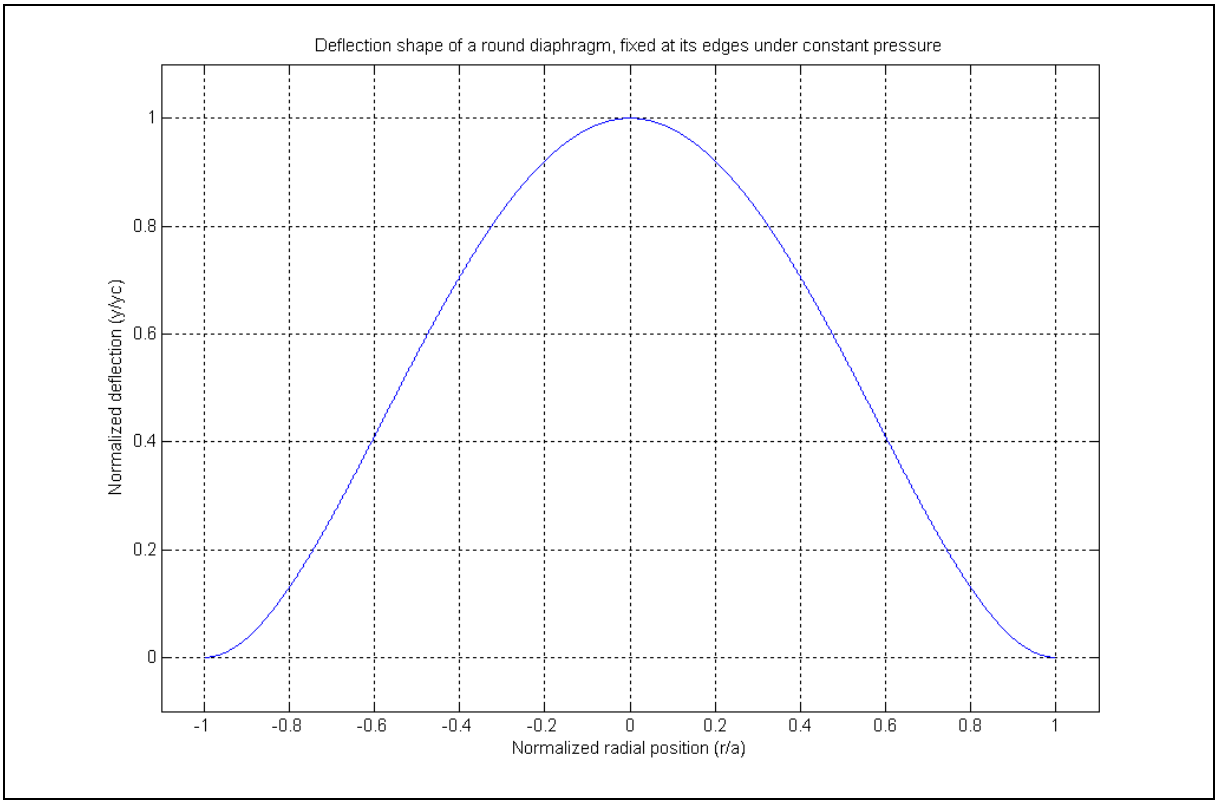

Figure 6.2: Deflection shape of the diaphragm under linear theory.

The maximum strain experienced by the diaphragm in linear theory is the radial strain at the edges of the diaphragm according to:

$$\varepsilon_{ra} = -\frac{3qR_0^2\left(1-\nu^2\right)}{4t^2E} \tag{6.7}$$

The strain becomes a design limitation, among other reasons, due to the fatigue characteristics of strain-gage materials. A higher strain promotes sensitivity of the measurement at the cost of durability of the strain-gage. Although the strain-gage's cost presents a very small portion of the cost of the measurement system, it will be difficult to replace in the MFCAA's case. The gage durability becomes more important when the sensor reaches maturity and has to function for prolonged periods in dynamic environments.

6.2.2 Circular diaphragm non-linear theory

All the theory given thus far by Young and Budynas is under linear assumptions. The fact that only the bending stresses (equations 6.4-6.6) are accounted for in the calculation of stress is the first indication that the diaphragm stresses are in fact ignored completely. This assumption can only reasonably be done for maximum deflections smaller than half the diaphragm thickness, as mentioned in the introduction of this section. The addition of the diaphragm stress enables the diaphragm to carry some of the load in direct tension and makes the diaphragm stiffer at higher strains, making the load deflection and load stress relation non-linear. For maximum deflections larger than half the diaphragm thickness these effects have to be taken into account.

Care must be taken here not to apply the non-linear theory without cognizance of all the effects of a non-linear diaphragm. Although the non-linear theory may predict the true stress and strain of the diaphragm and the optimization occurs correctly, the sensor will have greatly degraded performance in the non-linear region.

The following formulas give these non-linear relations of stress and strain according to Young and Budynas. The diaphragm stress is now taken into account so that the maximum stress is that of bending and tension combined:

$$\sigma_{\max} = \sigma_{dia} + \sigma_{bend}$$

Then:

$$\frac{qR_0^4}{Et^4} = \frac{5.33y}{\left(1-\nu^2\right)t} + \frac{2.6}{\left(1-\nu^2\right)}\left(\frac{y}{t}\right)^3 \tag{6.8}$$

For stresses at the center of the plate:

$$\frac{\sigma\ R_0^2}{Et^2} = \frac{2y}{\left(1-\nu\right)\ t} + 0.0976\left(\frac{y}{t}\right)^2 \tag{6.9}$$

And for stresses at the edge:

$$\frac{\sigma\ R_0^2}{Et^2} = \frac{4y}{\left(1-\nu^2\right)\ t} \tag{6.10}$$

6.2.3 Volumetric deflection of plain circular diaphragm

The relations given above must be integrated to find the volume displaced by a deflected diaphragm. Only the linear case is treated.

$$\begin{aligned}
\text{Vol} &= \int_0^{2\pi}\int_0^{R_0} r\left(y_c + \frac{M_c r^2}{2D(1+\nu)} - \frac{qr^4}{64D}\right) dr d\theta \\
&= \int_0^{2\pi}\int_0^{R_0}\left(ry_c + \frac{M_c r^3}{2D(1+\nu)} - \frac{qr^5}{64D}\right) dr d\theta \\
&= \int_0^{2\pi}\left[\frac{r^2 y_c}{2} + \frac{M_c r^4}{8D(1+\nu)} - \frac{qr^6}{384D}\right]_0^{R_0} d\theta \\
&= \int_0^{2\pi}\frac{R_0^2 y_c}{2} + \frac{M_c R_0^4}{8D(1+\nu)} - \frac{qR_0^6}{384D}\ d\theta \\
&= 2\pi\left[\frac{R_0^2 y_c}{2} + \frac{M_c R_0^4}{8D(1+\nu)} - \frac{qR_0^6}{384D}\right] && (6.11)
\end{aligned}$$

But according to equation 6.3: $y_c = -\frac{qR_0^4}{64D}$, which is substituted into equation 6.11 to give:

$$\text{Vol} = 2\pi\left[\frac{R_0^2 y_c}{2} + \frac{M_c R_0^4}{8D(1+\nu)} + \frac{R_0^2 y_c}{6}\right] \tag{6.12}$$

The second term in brackets can be simplified in the following manner with equation 6.5:

$$\frac{M_c R_0^4}{8D(1+\nu)} = \frac{qR_0^6(1+\nu)}{128D(1+\nu)} = -\frac{R_0^2 y_c}{2}$$

which is substituted back into equation 12 to give:

$$\text{Vol} = 2\pi\left[\frac{R_0^2 y_c}{2} - \frac{R_0^2 y_c}{2} + \frac{R_0^2 y_c}{6}\right]$$

$$\therefore \quad \text{Vol} = \frac{\pi R_0^2 y_c}{3} \tag{6.13}$$

6.3 The Wheatstone bridge equations

A diaphragm type strain-gage (with a gage factor of two) gives an output e_0 when wired in a full Wheatstone-bridge as shown in the following figure:

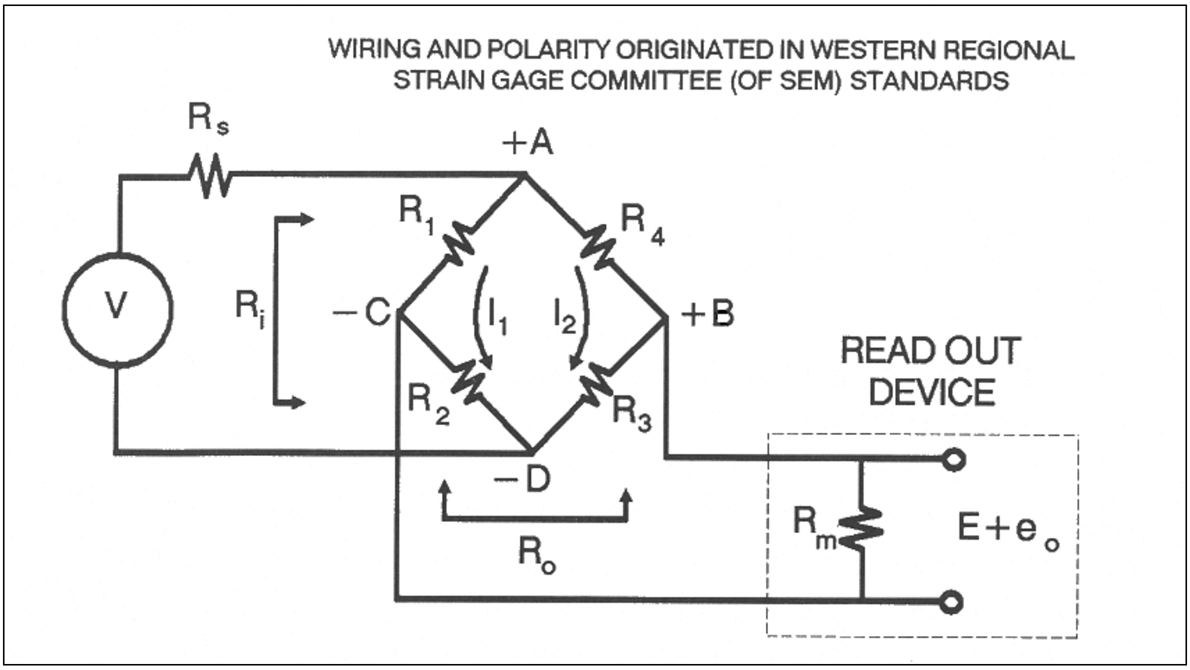

Figure 6.3: The Wheatstone bridge (taken from Wright (1994)).

The bridge equations can be found in most books on measurement systems or strain-gages and are well known. The total bridge output for the Wheatstone bridge is:

$$e_0 = V\left(\frac{1}{1+R_s/R_1}\right)\left(\frac{1}{1+R_0/R_m}\right)\left(\frac{a}{(1+a)^2}\right)\left[\frac{\Delta R_1}{R_1} - \frac{\Delta R_2}{R_2} + \frac{\Delta R_3}{R_3} - \frac{\Delta R_4}{R_4}\right](1-\eta) \tag{6.14}$$

In the third bracket, a is defined as $R_2/R_1 = R_3/R_4$ for a symmetric/balanced bridge. In general this will not be remain true for the bridge when one of the gauges (resistors) are strained, hence the bridge is normally operated in an unbalanced state. In this mode of operation, resistance changes in the arms cause changes in the currents I_1 and I_2 (in figure 6.3), which causes non-linearity. The last bracket contains the non-linearity term. And if $r = R_y/R_x$, with R_y the gauge resistance after deformation and R_x the resistance before, the non-linearity is written:

$$\eta = \frac{\left[\frac{(r_1 + ar_2)(r_1 - r_2)}{1 + a + r_1 + ar_2}\right]\left[\frac{(r_4 + ar_3)(r_4 - r_3)}{1 + a + r_4 + ar_3}\right]}{(r_1 - r_2 + r_3 - r_4)} \tag{6.15}$$

In most mechanical applications it does not influence equation 6.14 significantly since a strain gauge can only deform about 3% (hence r generally varies between 0.97 and 1.03). To find the output for a diaphragm gage the strain distribution has to be averaged across the tangential strain and radial strain sections that is used by the gage. This empirical formula is provided by the gage manufacturer, Vishay Measurements Group, which is:

$$e_o = 0.82 \frac{qR_0{}^2\left(1-\nu^2\right)}{t^2 E} \tag{6.16}$$

6.3.1 Strain-gaged diaphragm relations

From equation 6.16 it is important to note the following: The output is directly dependent on the strain levels in the strain-gage. Deciding on a specific output (which is similar to sensitivity) of the strain-gage sets the level of the maximum strain regardless of anything else, whether it is pressure, diaphragm thickness, or type of material. Equation 6.16 changes the diaphragm thickness to the required value to provide the scale factor. This is more evident in equation 6.7, which is reproduced here:

$$\varepsilon_{ra} = -\frac{3qR_0^2\left(1-\nu^2\right)}{4t^2 E}$$

The diaphragm maximum strain and gage output is in fact directly proportional according to:

$$e_0 = -1.0933 \ \varepsilon_{ra} \tag{6.17}$$

The output must of course be maximized for a favorable signal to noise ratio, and the price of that output is felt as:

1) A thinner diaphragm that is more difficult and costly to manufacture.
2) High strain levels in the gage that limits its fatigue life and causes unwanted channel flow.

Equation 6.16 is more useful when the thickness is solved for, which results in:

$$t = \sqrt{\frac{0.82qR_0{}^2\left(1-\nu^2\right)}{e_0 E}} \tag{6.18}$$

Equation 6.16 applies to the steady state where the diaphragm has settled at a position governed by the pressure. For dynamic applications it is better to get the output in terms of the diaphragm center deflection:

$$e_0 = \frac{4.3733 y_c t}{R_0^2} \tag{6.19}$$

More can be deduced from the equations. Since the material is used in its linear range, the maximum strain also has to be directly proportional to the maximum stress. The maximum stress level is found from equation 6.6 into equation 6.4.

$$\sigma_{\max} = -\frac{3qR_0^2}{4t^2} \tag{6.20}$$

From equation 6.7 can be shown that:

$$\varepsilon_{ra} = -\frac{\sigma_{\max}\left(1-\nu^2\right)}{E} \tag{6.21}$$

6.4 Strain-gaged diaphragm design and characteristics

Going through a design exercise the equations will be utilized in the following manner:

STEP 1: The diaphragm diameter and maximum pressure that is to be measured is decided on.
STEP 2: Equation 6.17 is used to decide on the maximum possible output that will still provide sufficient fatigue life in the strain-gage and not cause too much flow.
STEP 3: Calculate the maximum stress (equation 6.21) for the strain from equation 6.17. It is here that the material properties (Young's modulus and Poisson's ratio) come into play first. Hence a specific material is chosen here.
STEP 4: Equation 6.18 is used to calculate the diaphragm thickness based on parameters found in steps 1 to 3.
STEP 5: Check for maximum diaphragm deflection to confirm whether linear theory is applicable. The deflection shall not exceed half the diaphragm thickness.

The first step where the material parameters are used is now investigated closer to understand its effect on the rest of the design. Poisson's ratio is in fact quite constant in a vast range of completely different materials. Most Poisson's ratios are 0.3, and seldom reaches 0.35 (in polymers and composites). It makes sense to leave the Poisson ratio's contribution out of a relational study because Young's modulus varies roughly by a factor 200 in engineering materials. When Young's modulus is varied from 1 to 200GPa and the diaphragm thickness, deflection, stress and strain is plotted the result is shown in figure 6.4. A strain gauge factor of 2 is assumed with a sensitivity of 2mV/V. Applied pressure is 1kPa.

From figure 6.4 the following is clear:

1) The diaphragm thickness drops in a hyperbolic fashion as the material becomes stiffer, which is intuitively expected.
2) The diaphragm strain is constant for all elasticities. This confirms equation 6.17's prediction that strain is independent of stiffness for implied output.
3) The maximum stress increases linearly as stiffness increases. The cause of this can be seen most clearly in equation 6.21 for a constant strain and increasing stiffness.
4) The diaphragm deflection increases for increasing stiffness. A designer will in fact have to use a less stiff material to get a smaller maximum diaphragm deflection.

When equation 6.3 is written out with the plate constant substituted it becomes:

$$y_c = -\frac{3qR_0^4\left(1-\nu^2\right)}{16Et^3} \tag{6.22}$$

The elasticity is in the denominator of equation 6.22, so how is it possible that deflection decreases as *E* increases? The thickness used in equation 6.22 is calculated be means of equation 6.18. Equation 6.22 can thus also be written as:

$$\begin{aligned} y_c &= -\frac{3qR_0^4(1-\nu^2)}{16E\left(\dfrac{0.82PR_0{}^2\left(1-\nu^2\right)}{e_0E}\right)^{\frac{3}{2}}} \\ &= -\frac{3qR_0^4(1-\nu^2)\sqrt{E}}{16\left(\dfrac{0.82PR_0{}^2(1-\nu^2)}{e_0}\right)^{\frac{3}{2}}} \end{aligned} \tag{6.23}$$

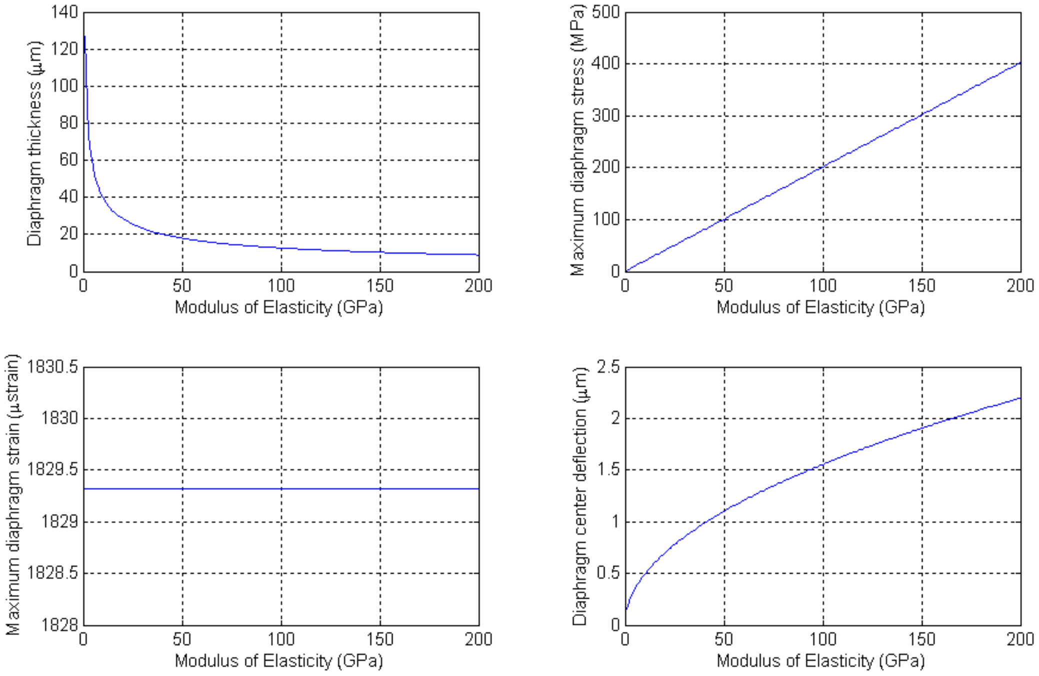

Figure 6.4: The influence of Young's modulus (from 1Gpa to 200GPa) on diaphragm design according to linear theory.

Equation 6.23 confirms the shape of the right bottom graph in figure 6.4 and confirms that a lower Young's modulus indeed results in smaller diaphragm deflections. The diaphragm strain-gage governs the dimensions of the sensor to a certain extent because of the limited number of gage sizes available. It must be known what options exist for the diaphragm so that the optimization can be done with these values in mind. The following are available:

HBM supplies diaphragm strain-gages with nominal gage factors (strain sensitivity) of two. The transducer gages are available in sizes 10, 15 and 25mm at resistances from 120Ω to 350Ω. Micro-Measurements corp. supplies gages in sizes of 5mm, 6.4mm, 10mm and 13mm and at resistances of 350Ω to 1kΩ. The choice of gage resistance is a trade-off of temperature sensitivity versus signal/noise ratio. Gages with smaller resistance will generate less noise, but will be more susceptive to generate internal heat and cause temperature drive problems. A 350Ω gage is generally accepted as the fair choice for most applications but the 120Ω option may be necessary to build a sensitive enough system.

On the matter of size: It must be kept in view that the outside diameter size constraint is 20mm. This is not a strictly enforced requirement though, because the sensor will still be small relative to most requirements in envisaged applications if kept within 30mm. The sensitivity of the sensor will increase for larger diaphragms because larger size provides volume to build a higher pressure potential generating system. Using a larger diaphragm may be tempting, but it increases sensor size as well. One constraint of using a strain-gage is the limited sizes they are available in.

6.5 Strain-gaged diaphragm conclusions

1) The output available from a strain-gage is governed only by the maximum strain available. These two variables are linearly dependent.
2) A diaphragm may be designed for a certain output for any value of pressure, however small. The diaphragm will simply be thinner to account for this. Consequences of a thinner diaphragm are manufacturability problems and high diaphragm stresses. One other caveat on an exceptionally thin diaphragm is that the strain-gage gluing may be

difficult, especially if roughing of the surface finish is required. The added stiffness of the strain-gage may also have to be taken into account.

3) The material stiffness must be minimized to a) make a diaphragm of a more readily manufacturable thickness and b) limit the diaphragm deflection and thereby limiting flow pressure loss.
4) Diaphragm stress will be less for low stiffness materials, which makes the softer materials also feasible for use in a diaphragm. For very low stiffness materials, the added stiffness of the installed strain-gage may have to be taken into account.
5) The constraints caused by available strain-gage sizes and the required diaphragm strain to operate these gages places a lower limit on the volumetric deflection of the diaphragm and therefore also the flow for a specific channel width.

The plain circular diaphragm may also be applied in other pressure transducer concepts. Capacitive sensing is common in pressure transducers, but is not covered in this document in favour of the piezo electric transducer. Capacitive sensing is widely associated with servoed sensors since the plates used for sensing can also be applied as actuators of the sensitive element. This concept can be further developed when a servoed sensor option is considered.

6.6 Piezo-electric pressure transducer

6.6.1 Piezo-electric characteristics

The constraints placed on the designer by strain-gaged diaphragm diameter and deflection may prove to be too limiting. Great bandwidth losses are experienced with strain-gaged diaphragms where the ratio of channel width to diaphragm diameter drops below 10 percent. Another limitation of strain-gages is the sizes they are available in. This makes the application of a strain-gaged diaphragm limited to macro scale channels. Generally, small sensors will require much stiffer pressure transducers to limit flow, thus making the use of small channels possible and reducing the size of the sensor.

The piezo-electric pressure transducer has the following main pros:

- High stiffness.
- Good sensitivity.

and cons

- More complex design. The diaphragm has to be braced against the piezo-crystal for force transference.
- Higher manufacturing accuracies are required.
- Higher cost.
- Piezo-electric transducers have no DC response. This is the most important drawback because the MFCAA sensor is inclined toward low frequency application due to the long narrow channels that places an upper limit on bandwidth. Using a piezo-electric transducer places an extra trade-off into the optimization challenge.

The piezo pressure transducer functions on the basis of a piezo crystal that generates charge proportional to strain. Many crystals ranging from quartz to ordinary sugar exhibits this phenomenon. The main trade-off made in deciding on piezo material is between output and temperature stability. Quartz is stable with low output while Rochelle salt provides high output, but has to be protected from moisture and temperatures above 45°C. The applied strain can be of any type (thickness, shear or even transverse strain) but since the crystal only generates charge it has to be connected parallel to a shunting capacitor. A very high impedance circuit amplifies the capacitor voltage (to limit charge leakage). The impedance of this circuit will always be finite, so charge leakage will always occur. For this reason, piezo-transducers are best suited to inputs of high frequency that require no DC response.

This can be illustrated by the following example: The stiffness afforded by the crystal when used in compression or tension is:

$$k_c = \frac{E_p A_p}{L_p} \tag{6.24}$$

where A_p is the stressed area, E_p is Young's modulus for the crystal and L_p is the unstressed length of the crystal. The reaction force generated by the crystal is thus:

$$F_p = k_c x \tag{6.25}$$

with x the crystal deflection under force F_p. The piezo element and its equivalent circuit may be illustrated as in figure 6.5: The crystal generates a charge directly proportional to the applied force:

$$q = k_p F_p \tag{6.26}$$

or proportional to imposed deflection (equation 6.25). Equation 6.26 becomes:

$$q = k_p k_c x = K_{piezo} x \tag{6.27}$$

Differentiating equation 6.27 results in:

$$i_t = \frac{dq}{dt} = \frac{K_{piezo} dx}{dt} \tag{6.28}$$

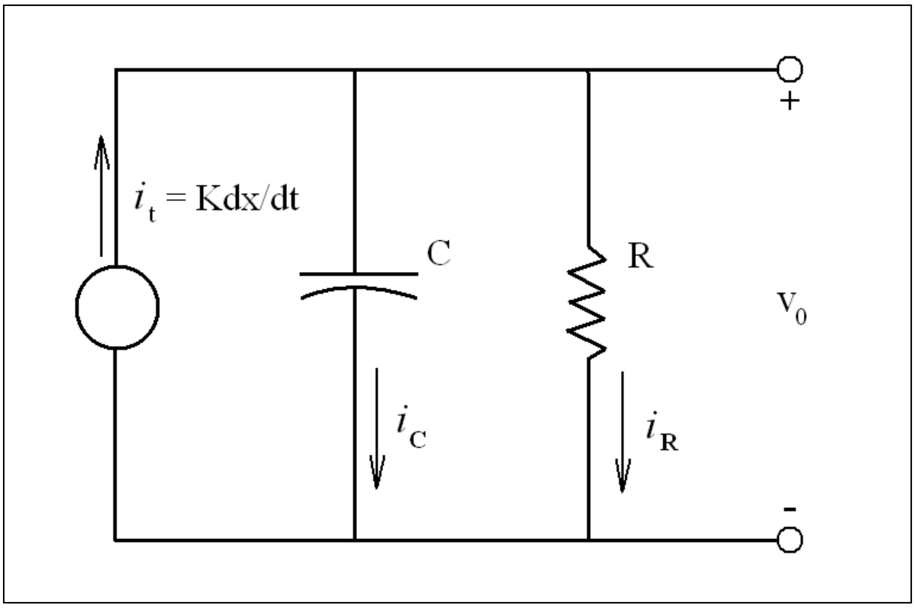

Figure 6.5: Transducer equivalent circuit of piezoelectric element.

From figure 6.5:

$$i_t = i_C + i_R \tag{6.29}$$

$$v_o = v_C = \int \frac{i_C dt}{C} = \int \frac{(i_t - i_r)}{C} dt \tag{6.30}$$

$$C\frac{dv_o}{dt} = i_t - i_R = K\frac{dx}{dt} - \frac{v_0}{R} \tag{6.31}$$

In the frequency domain equation 6.30 becomes:

$$\frac{V_o(j\omega)}{X(j\omega)}=\frac{K_s j\omega\tau}{j\omega\tau+1} \tag{6.32}$$

The time constant τ is equal to the product RC of the circuit and $K_s = {}^{K}\!/_{C}$. The steady state response is for the transducer is zero. The resonance frequency is set by the stiffness of the transducer and inertia of the system while the low cut-off frequency in Hertz is:

$$f_{-3dB}=\frac{1}{2\pi RC} \tag{6.33}$$

Increasing RC (the time constant) will decrease the cut-off frequency, but increasing C also decreases nominal output sensitivity. Increasing the capacitance of the feedback capacitor (and of the wiring) unfortunately also increases the noise in the amplifier, see Purdy (1979).

With regards to the piezo sensor output, some assumptions are made in its modeling:

1) The piezo element is assumed only to output charge due to its thickness change deformation (also called the longitudinal or d33 direction): The top and bottom of the crystal is bonded to the piezo support and to the diaphragm respectively, and is therefore not wetted by the working fluid. The diaphragm reacts the differential pressure upon it (in shear and bending) against the crystal, which causes a thickness change in the crystal. The thickness change causes a corresponding transverse change (also called the d31 mode) according to Poisson's ratio. Thickening of the crystal will cause transverse contraction and thinning of the crystal will cause transverse expansion. The crystal however will also deform due to direct fluid pressure on its circumference where it is exposed to the fluid. When the sensor experiences an increase in pressure (in which case the other side of the diaphragm will experience a drop in pressure) the diaphragm will act to lengthen the piezo film in the d33 direction, causing transverse contraction. The increased direct circumferential fluid pressure will assist this transverse contraction and increase the sensor output. The opposite occurs when the sensor experiences a drop in pressure, in which case the direct fluid pressure also assists the sensor output. The direct fluid pressure causing this change is not amplified by the diaphragm area however but does add to sensor output. The extra output is extremely small however, and should only contribute about 4% of the output for a $100\mu m$ thick film if the transverse degree of freedom is entirely free to deform. Since the piezo film is bonded on its top to the piezo support and on its bottom to the diaphragm, any transverse change is reacted in shear across the bonded surface. Therefore the crystal cannot be assumed free in the transverse direction and the small d31 contribution thereby ignored. For thicker piezo sensors, this assumption may need to be revised and the transverse output included.
2) The measurement chamber is assumed rigid. The pressure chamber has to be made from a finite stiffness material like all other systems in the sensor. Flow entering the measurement chamber will deflect the diaphragm, compress the measurement chamber diameter fluid and expand the measurement chamber itself. In this document the flow is assumed to compress the chamber fluid and deflect the diaphragm. Due to the low stiffness of the diaphragm relative to the envisaged stiffness of the measurement chamber this assumption is reasonable, but can be improved upon when the measurement chamber is designed.

6.6.2 Piezo electric signal conditioning

Amplification of the transducer output may be done with voltage- or charge-amplification. The more popular of these is the charge amplifier because of the independence of its low frequency response on the transducer parameters. Within limits, the system performance is only dependent on the feedback resistance and capacitance of the amplifier. Figure 6.6 shows a schematic of a charge amplifier installation.

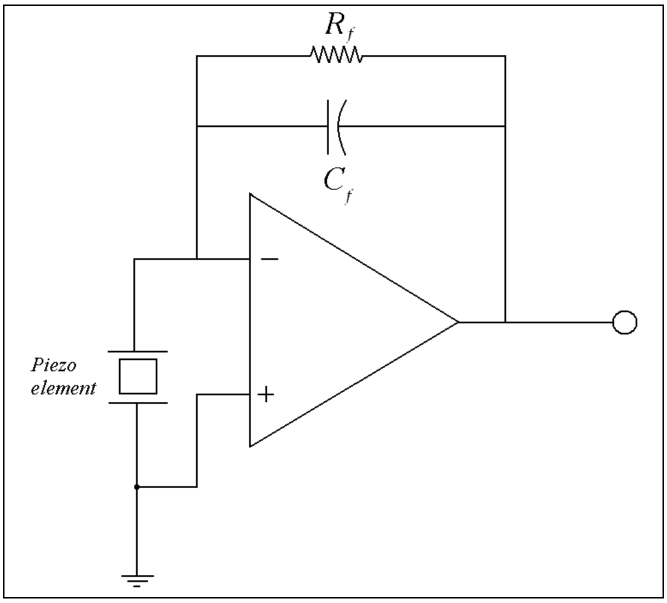

Figure 6.6: Piezo transducer with charge amplifier.

The output voltage of the amplifier is then:

$$v_o = \frac{-1}{C_f}\int_0^t \left(\frac{Kdx}{dt}\right) dt = \frac{-Kx}{C_f} \tag{6.34}$$

This does not imply that DC response is possible. The feedback resistor R_f must be added to prevent drift and saturation of the operational amplifier by its input bias currents. The addition of the feedback amplifier reintroduces the $R_f C_f$ circuit high-pass characteristic, so DC response is still not attained. The frequency response caused by the charge amplifier starts off with a 20dB/decade slope. At f_{-3dB} the response reaches 71% of the nominal scale factor level of K_s where it levels off. The true response will also contain resonant structural frequencies beyond the nominal scale factor, but these are not reflected by equation 6.32. This resonance are not of much consequence for the MFCAA because of the high frequencies they occur at.

6.7 Noise of charge amplifier

Noise is still to be covered, and this is only done for the charge-amplifier coupled with the piezo crystal. Noise in the strain-gage is omitted because the perceived potential for this is limited.

For a treatment of noise in amplifiers in general, see the Analog Devices technical notes on the subject by Kester et al. Noise is of utmost importance in the design of the sensor and is considered in detail when the electronics of the system is designed. As background to the decisions made and the results obtained in this document, the sources and character of noise in the sensor is covered. The results of chapter 8 must be seen as illustrative against this background. A larger scale factor for example will only be beneficial to resolution and drift if the signal/noise ratio increases. Charge amplifier noise can be subdivided into "white" noise, with a flat spectrum and low frequency "1/f" noise (also known as pink noise or flicker noise) that increases with the inverse of frequency.

In this document the impact of noise is indirectly expressed as the sensor resolution. Resolution is defined as the smallest increment of change in angular acceleration that can be determined from a change in sensor output voltage. As a lower limit of the noise, the inescapable sources of noise are used which are all white in nature. Other sources of noise do exist, and is more often than not the dominating noise. The MFCAA is a very low frequency application by electronic standards, which makes 1/f the probable dominating type of noise. Interference noise is not covered in this chapter because it is inherent to the actual electronic layout, which is beyond the scope of this document. Interference noise is also manageable by proper layout, component selection and filtering as opposed to white noise, which is inescapable. Flicker noise is also dependent on frequency (therefore filterable) and depends greatly on resistor construction.

6.7.1 Charge amplifier white noise

The white noise of the charge amplifier in combination with the transducer comes from three irreducible sources (see Hamamatsu technical notes). All are expressed in $V_{rms}/\sqrt{Hz}$, therefore the rms noise level of the sensor depends on the bandwidth (or rather "bandpass" frequencies of interest):

1) Thermal noise of the first stage Field Effect Transistor (FET) is proportional to the square root of temperature:

$$N_{T1} = \sqrt{\frac{8}{3}\frac{KT}{gm}} \tag{6.35}$$

where K is the Boltzmann constant, *gm* is the transconductance of the first-stage FET, and T is the absolute temperature in Kelvin. Usually a first stage FET is chosen with a relatively large transconductance (which is equivalent to the FET gain) while the FET input capacitance is matched with the detector capacitance.

2) Shot noise caused by the gate current of the first stage FET and dark current of the piezo crystal. Shot noise is caused by the fundamental discrete nature of current; the flow of current is not absolutely smooth and causes statistical fluctuations in true current. The shot noise in the charge amplifier is:

$$N_S = \sqrt{2q(I_G + I_D)} \tag{6.36}$$

where q is one electron charge, I_G is the gate leakage current of the first-stage FET, I_D is the dark current of the piezo crystal. The dark current of a sensor can vary from values in the order of electrons/second to μAmps. FETs with gate leakages of 1pA are available.

3) Thermal noise caused by resistances in the circuit. This is also known as Johnson noise and is unavoidable at non-zero absolute temperatures. Johnson noise sets a lower limit on the noise voltage in any detector. All resistances in the circuit will generate thermal noise but in a charge amplifier the feedback resistor is the natural main culprit. The Johnson noise is expressed by:

$$N_{TR} = \sqrt{4KTR_f} \tag{6.37}$$

The variables are the same as in equation 6.35 except for R_f, which is the feedback resistance.

The total charge amplifier white noise in mean squared complex representation then becomes:

$$N_{amp}^{2}(j\omega)=N_{T1}\left(1+\frac{C_{in}}{C_{f}}\right)^{2}+\frac{1}{(j\omega C_{f})^{2}}\left(N_{S}^{2}+\left(\frac{N_{TR}}{R_{f}}\right)^{2}\right) \tag{6.38}$$

where C_{in} is the input capacitance to the charge amplifier. Multiplying equation 6.38 by $e^{j\omega t}$ and taking the real part yields the actual mean squared noise voltage:

$$N_{amp}^{2}(t)=\cos(\omega t)\left[N_{T1}\left(1+\frac{C_{in}}{C_{f}}\right)^{2}-\frac{1}{(\omega C_{f})^{2}}\left(N_{S}^{2}+\left(\frac{N_{TR}}{R_{f}}\right)^{2}\right)\right] \tag{6.39}$$

The amplitude of equation 6.39 is of real interest to the resolution, while the integral of equation 6.39 causes sensor drift. The term $\left(1+{}^{C_{in}}\!/_{C_{f}}\right)$ is known as the noise gain. The input capacitance of the charge amplifier is the capacitance of the piezo-film in parallel with the input capacitance of the first stage FET. The piezo film capacitance is proportional to the active electrode area and inversely proportional to the film thickness. As an example, an AMP DT-1 standard piezo film's specific capacitance is 1.0889 x 10^{-10} F/m. The input stage FET input capacitance is generally matched with the piezo film capacitance. Due to the small size of the piezo film, the charge amplifier input capacitance used will probably be less than 2pF, which brings noise gain down significantly.

The shot noise and resistive thermal noise is independent of input capacitance, but decreases with the square of frequency and feedback capacitance. Both a high feedback capacitance and high feedback resistance is beneficial for low noise. Of course it's only the resistance that will be maximized in order to achieve low piezo leakage. The capacitance will be a low value to reach high sensor scale factor. From the envisaged parameters in the charge amplifier, the expected white noise will be low relative to flicker noise.

6.7.2 Charge amplifier flicker noise

Flicker noise is expected to dominate in the MFCAA application due to the low frequencies applied. Flicker noise is the result of fluctuations in resistance generating an additional noise voltage. This noise depends on the resistive material used and in particularly the end-cap connections of resistors. For an op-amp, the frequency at which the 1/f noise spectral density equals the white noise rms (root mean squared) level is known as the 1/f corner frequency. Higher quality amps have lower corner frequencies; hence this parameter is fixed by the selection of the op-amp. High accuracy bipolar op-amps reach corner frequencies of less than 1Hz. Frequency dependent noise (like 1/f noise) can be filtered out and is by default filtered to some extent by the low frequency cut-off of a piezo transducer. The Hamamatsu H4083 charge amplifier has the noise spectrum shown in figure 6.7.

The noise spectrum of the H4083 is used as a benchmark to calculate sensor resolution. The charge amplifier will definitely be operated below 1 kHz, hence a constant spectrum of 1 $\mu V/\sqrt{Hz}$ is taken as the reference noise spectrum. All quoted values of resolution in chapter 8 are therefore referenced to 1 $\mu V/\sqrt{Hz}$.

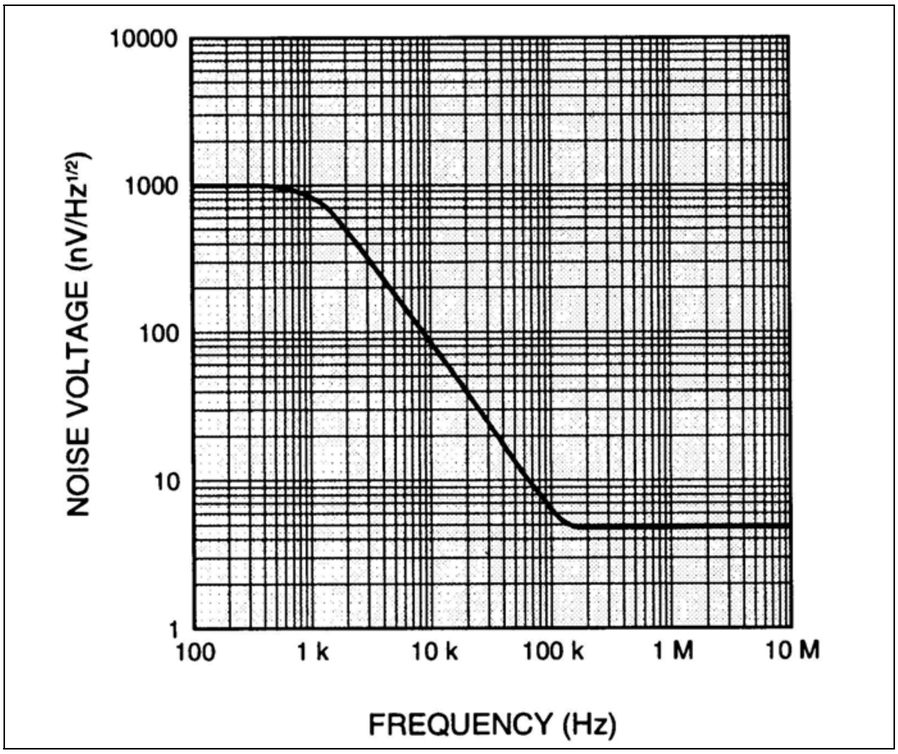

Figure 6.7: Hamamatsu H4083 charge amplifier noise spectrum.

6.8 Strain of piezo-diaphragm combination

With the addition of the piezo-film, the stiffness contributed by the diaphragm becomes somewhat secondary in importance. Contrary to the diaphragm, the piezo-film is a very stiff body, being as thin as 9µm with a Young's modulus of higher than 100 GPa. The diaphragm will be supported at its center by the piezo-film, and fixed at its perimeter. The addition of the piezo-film will thus not only change the diaphragm deflection magnitude but also the deflection shape. This influences the volumetric deflection and the induced flow significantly.

The area that the generated differential pressure is applied to is decreased because the piezo-film has to be supported with a pillar, though only on the one side of the diaphragm. The pillar area will match the stressed piezo film area. The decreased available diaphragm area will have a negative effect on the sensor scale factor.

6.8.1 Fixed-fixed annular diaphragm

The diaphragm is assumed to be rigidly bonded to the piezo-film and its supportive structure, which is also assumed to be rigid. No moments are therefore present in the diaphragm where it is bonded to the piezo-film and the deflection shape does not have any curvature in this region either. If (for the moment) it is assumed that pressure is only transmitted to the annular diaphragm, the following relations are applicable. The pressure transmitted opposite the piezo sensor's bonded area will be accounted for in section 6.8.4.

These assumptions coupled with a flexible diaphragm (of steel less than about 100µm thick) closely resembles an annular diaphragm that is fixed at its inner and outer diameters. For this assumption to apply, the great majority of the deflection must reside within the diaphragm and not the piezo-film support. This assumption will apply for thin pliant diaphragms mounted on very stiff supportive structure. The deflection shape diaphragm with such a boundary support is shown in figure 6.8.

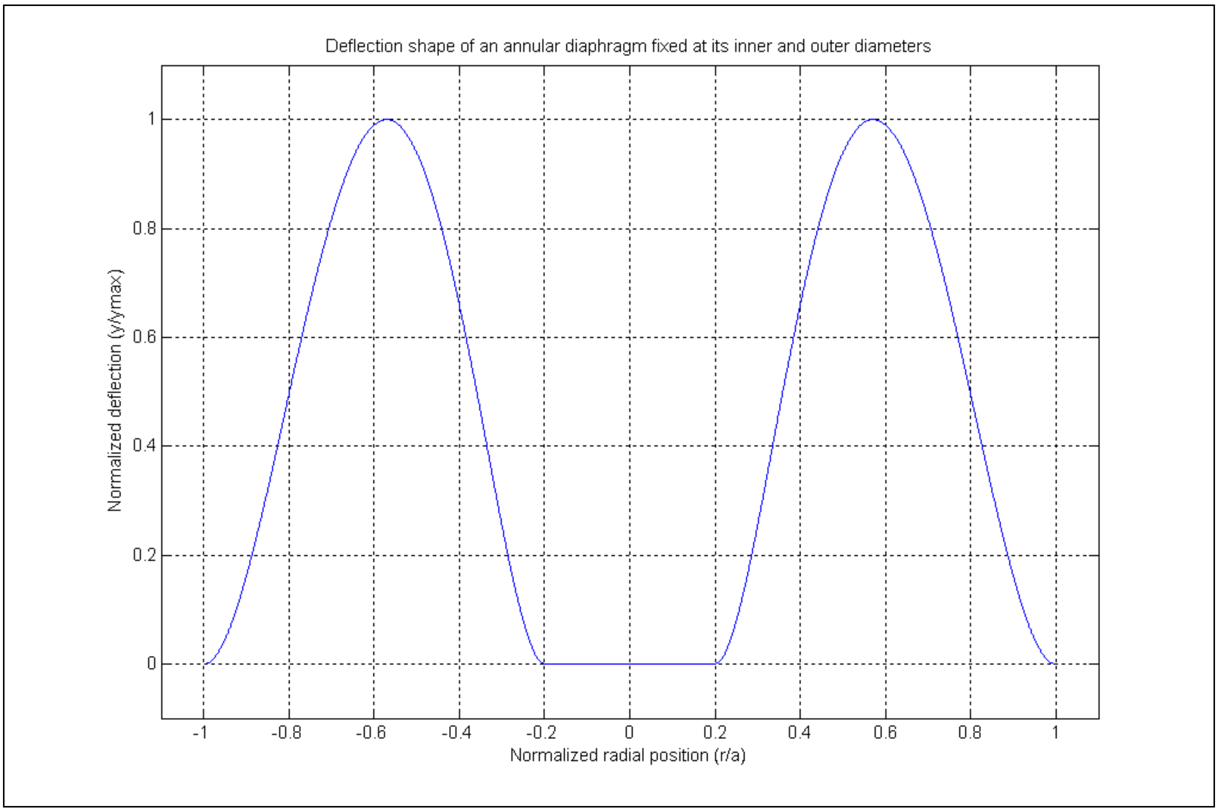

Figure 6.8: Deflection shape of an annular diaphragm fixed at both its edges. The piezo crystal is shown supported on the inside 20% of the diaphragm diameter.

The shape in figure 6.8 is of course greatly exaggerated in favor of the deflection direction due to normalization. In a real diaphragm the deflection will be about 6 orders smaller than the diameter. The constraints enforced on the diaphragm will cause shear forces in the diaphragm at both the inner and outer diameter. The shear forces add up to balance the applied forces due to the applied pressure and is therefore proportional to the diaphragm area and applied pressure:

$$\pi a Q_a + \pi b Q_b = -q\pi\left(a^2 - b^2\right)$$

where Q_a and Q_b is the shear force on the outer and inner diameter respectively (in N/m), a is the outer radius of the diaphragm and b the inner radius. Q_a and Q_b is found in Young and Budynas after substitution to be:

$$Q_a = \frac{q(3a^6 + 5a^2b^4 + 4a^4b^2\log(a/b) - 7b^2a^4 - b^6 - 4a^2b^4\log(a/b) - 16a^4b^2\log(a/b)^2)}{8a(-2a^2b^2 + a^4 + b^4 - 4a^2b^2\log(a/b)^2)} \qquad (6.40)$$

$$Q_b = \frac{q(a^6 + 7a^2b^4 - 4a^4b^2\log(a/b) - 5b^2a^4 - 3b^6 + 4a^2b^4\log(a/b) + 16a^2b^4\log(a/b)^2)}{8b(a^4 + b^4 - 4b^2\log(a/b)^2a^2 - 2a^2b^2)} \qquad (6.41)$$

Q_a and Q_b is plotted in figure 6.9. As the inner diameter increases relative to the outer diameter the total shear decreases and becomes zero when the radii are equal. This is clear since the diaphragm area is zero for this case. The fraction of the total shear attributed to the inner edge also increases as its radius increases up to where it equals the outer shear (when $a = b$, even though both are zero at this point). Q_b is an edge-distributed force that adds up to the force experienced by the piezo crystal, and should thus be as large as possible to maximize scale factor. This maximum is seen in figure 6.9 to occur when the inner diameter is 34.6% of the outer diameter. At this diametrical ratio, the inner diaphragm edge carries 37% of the shear, which is 88% of the total shear that would be present if no diaphragm area were lost to the piezo support.

Another important assertion can be made from equations 6.40 and 6.41. The shear experienced by the diaphragm's edges is independent of the diaphragm thickness. This means that the diaphragm can be made thicker (and so limit flow in the sensor channels) without compromising sensor scale factor. This is unfortunately only true within limits. If the diaphragm is made thick enough, the stiffness it contributes will start to dominate and the deflection shape under pressure will not resemble that of figure 6.8. For a very thick diaphragm with a relatively limp center support, the portion of the shear allocated to the inner diameter will start to vanish because the diaphragm carries the shear internally. The design of the piezo support is therefore important, which includes the stiffness of the material used for the support.

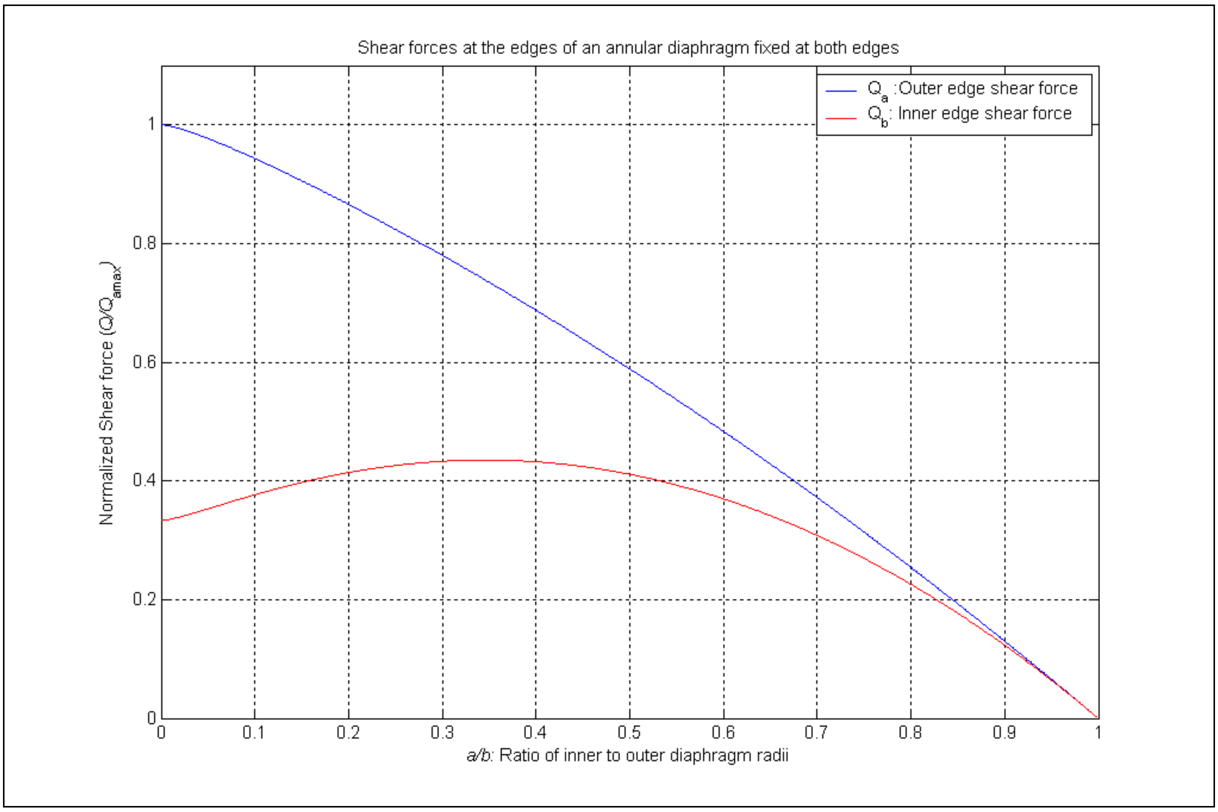

Figure 6.9: Shear forces on an annular diaphragm fixed on both edges.

The *b/a* ratio of 34.6% represents the optimal potential for force generation at the piezo-film. But this does not mean that a significant force is generated at the inner diaphragm; this depends on the relative stiffness of the diaphragm to its center support.

6.8.2 Fixed-guided annular diaphragm

If the majority of the deflection resides within the piezo support, the deflection shape will resemble that of figure 6.10, which shows an annular diaphragm with a guided inner diameter instead of a fixed one while the outer diaphragm remains fixed. As in 6.8.1 only the effect of the annular pressure on the diaphragm itself is considered.

The solution of the deflection shape is:

$$y_b = \frac{3qa^2(1-b^4/a^4-4(b^2/a^2)\log(a/b))r^2(1-v^2)(1-b^2/r^2(1+2\log(r/b)))}{8(1-b^2/a^2)Et^3}\ldots$$
$$-\frac{qr^4(1-v^2)(1+4b^2/r^2-5b^4/r^4-4b^2/r^2(2+b^2/r^2)\log(r/b))}{4Et^3} \qquad (6.42)$$

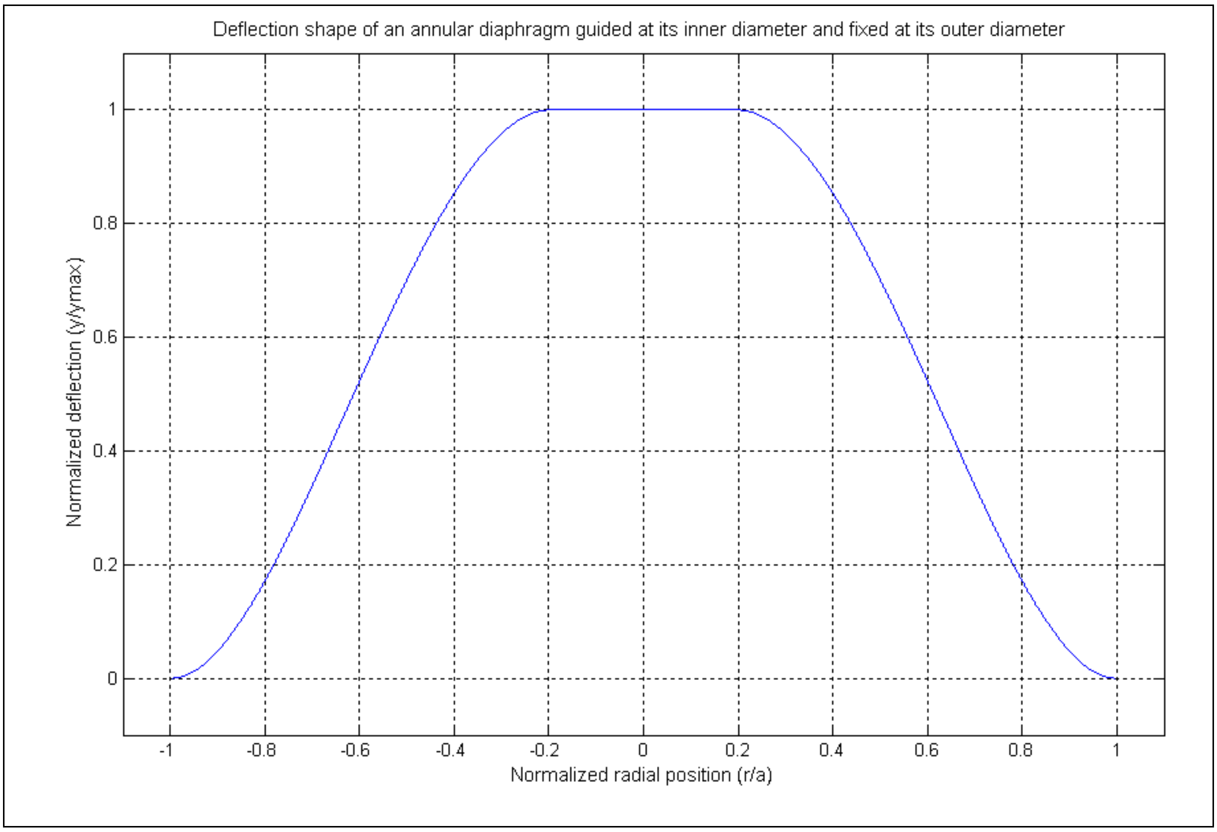

Figure 6.10: Deflection shape of an annular diaphragm fixed at the outer edge and guided at the inner edge. The piezo-crystal is shown supported on the inside 20% of the diaphragm diameter.

The solution for the deflection of the diaphragm is unfortunately not as elegant as the plain circular diaphragm in equation 6.3. In this scenario there exists no shear at the inner edge (only a moment, which causes the bending) since the edge can freely move vertically. This scenario would apply if no stiffness is contributed by the piezo support, and is thus at the other extreme from figure 6.8. Even with only a guided inner edge, the annular diaphragm is still significantly stiffer than a circular diaphragm. Figure 6.11 shows the relative deflection under the same net force for the two cases (i.e. the lost area of an annular diaphragm is accounted for). As the inner edge diameter approaches that of the outer edge, the deflection of the annular diaphragm tends to zero, which implies infinite stiffness. At the scale factor-ideal *b/a* ratio of 34.6%, the annular diaphragm is 2.5 times as stiff as the plain diaphragm based on maximum deflection.

6.8.3 Fixed annular diaphragm with finite inside edge stiffness

The diaphragm in the sensor will operate with a finite thickness piezo film supported with finite stiffness. Hence the real diaphragm will operate between the cases of figure 6.8 and 6.10 dependent on the relative stiffness of the diaphragm and the piezo-film support.

These two scenarios have to be married into a reasonable model of the true diaphragm. The stiffness contributed by a round piezo film is:

$$k_{piezo} = \frac{E_{piezo} A_{piezo}}{L_{piezo}} \qquad (6.43)$$

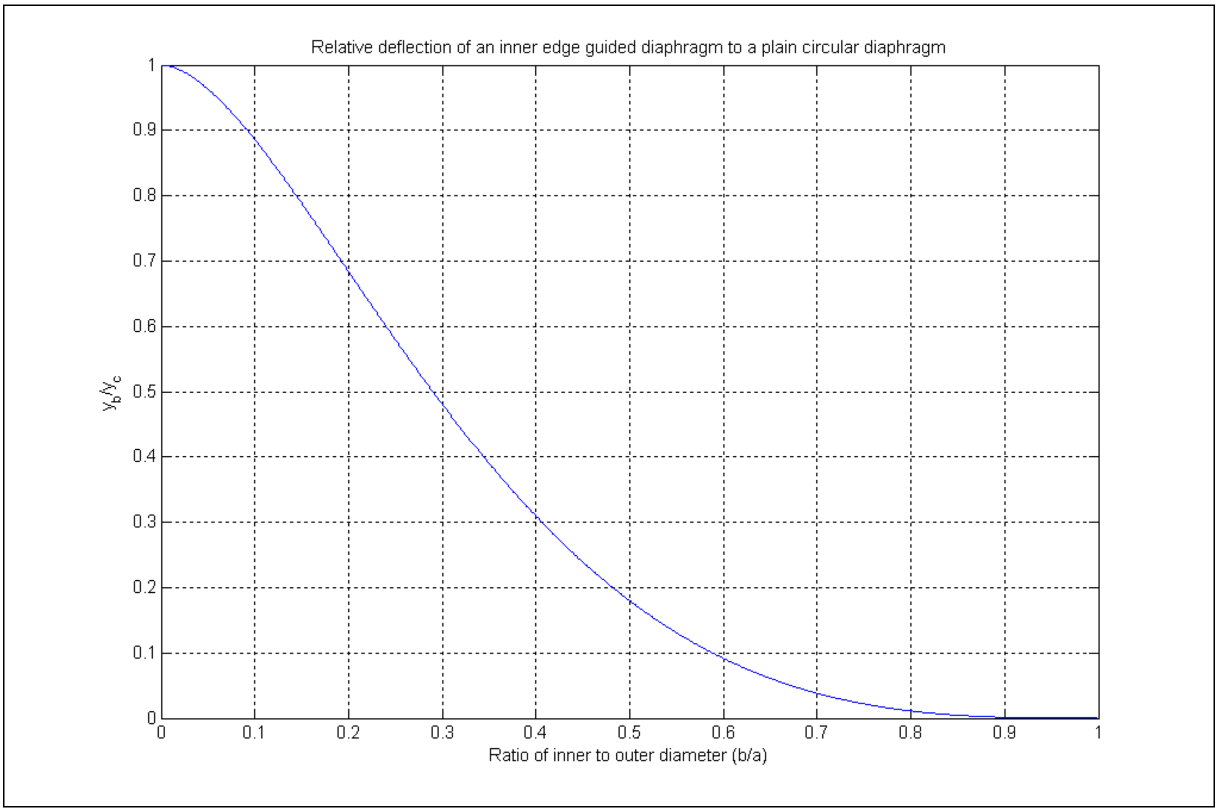

Figure 6.11: Relative stiffness of an annular inner edge guided to a plain diaphragm.

Similarly, the stiffness provided by the column supporting the piezo film is:

$$k_{\sup} = \frac{E_{\sup} A_{\sup}}{L_{\sup}} \tag{6.44}$$

The total stiffness resulting from these two separate entities is:

$$k_{pillar} = \left(\frac{1}{k_{\sup}} + \frac{1}{k_{piezo}} \right)^{-1} \tag{6.45}$$

For a pillar deflection of y_b the deflection attributable to the piezo film is:

$$y_{piezo} = \frac{y_b k_{\sup}}{k_{piezo}} \tag{6.46}$$

As in the case of the plain circular diaphragm, the annular diaphragm deflection shape has to be integrated into a volumetric deflection to make it of any use inside a simulation. The integration of the annular diaphragm deflection shape is quite a formidable task if done analytically. The describing equation is a massive polynomial with an integrand spread between elevation to various powers as well as natural logarithms. These functions were rather integrated numerically and a relation was found between the maximum diaphragm deflection and the volume required to make the diaphragm reach that deflection. The result is a case-specific formula, which is limited to a single *a/b*. To get a general formula out of the numerical integration, the volumes and deflections could also be fitted to the diaphragm constants. Curve fitting unfortunately has inherent errors.

A general formula is not required for simulation of the diaphragm because the designer is only interested in diaphragms that maximize scale factor and dynamic performance. An *a/b* ratio of 2.8916 is used for maximum scale factor, and the diaphragm outer diameter is varied to attain the required bandwidth. A scale factor maximized at an *a/b* of 2.8916 again assumes rigid piezo support (as in figure 6.8). This assumption is reasonable for the true diaphragm since this is the diaphragm support type pursued in the design. Finite support stiffness only affects the true *a/b* for maximum scale factor and not the accuracy of strain relations for the assumed *a/b*.

If a fixed ratio of *a/b* is used, the ratio of diaphragm deflection to volume becomes a constant for both diaphragms. Furthermore, the location of maximum deflection of a fixed-fixed annular diaphragm also becomes a fixed ratio of the outer diameter. The results of the numeric integration for a diaphragm with an *a/b* of 2.8916, accurate to 5 significant numbers are:

Table 6.1: Annular diaphragm relations when *a/b* = 2.8916.

DIAPHRAGM CASE AND VARIABLE CALCULATED	RESULT
Volumetric deflection of **fixed-guided** annular diaphragm vs. deflection	$Vol_{fg} = 1.5305\, y_{bfg}\, a^2$
Center deflection of **fixed-guided** annular diaphragm vs. pressure	$y_{bfg} = \dfrac{0.065556\, qa^4 \left(1-\nu^2\right)}{E_{dia} t^3}$
Position of maximum deflection in **fixed-fixed** diaphragm	$r\big\|_{y=y\max} = \dfrac{a}{1.5235}$
Volumetric deflection of **fixed-fixed** annular diaphragm vs. deflection	$Vol_{ff} = 1.4627\, y_{\max ff}\, a^2$
Ratio of fixed-fixed to fixed-guided volumetric deflection for identical diaphragm and pressure	$\dfrac{Vol_{fg}}{Vol_{ff}} = 11.839$
Support force generated by **fixed-fixed** diaphragm vs. volume deflected	$F_{bff} = \dfrac{13.297\, Vol_{ff}}{a^4}$
Support force generated by **fixed-fixed** diaphragm vs. pressure applied	$F_{bff} = 0.47194\, qa$

The formulae in table 6.1 is now used to derive relations of the true diaphragm, which is somewhere between the fixed-fixed and fixed-guided support cases. Note that the two diaphragms are still very much linear in all the relations obtained. This will again only apply for deflection below one half of the diaphragm thickness. The annular diaphragm meets the deflection linearity condition more easily (as opposed to the plain diaphragm) because the addition of the diaphragm support allows thicker diaphragms to be used. An assumption is now made that the support reaction generated by the diaphragm linearly diminishes to zero from the fixed-fixed to fixed-guided case, or that:

$$F_b = F_{bff} - \frac{F_{bff}\, y_b}{y_{bfg}} \tag{6.47}$$

where y_b is the inner edge diaphragm deflection and F_b the piezo support force. The subscript *ff* denotes the fixed-fixed diaphragm case, while *fg* denotes the fixed-guided case. The force in the support is also:

$$F_b = k_{pillar}\, y_b \tag{6.48}$$

Solving equations 6.47 and 6.48 simultaneously for the diaphragm inner edge deflection yields:

$$y_b = \frac{F_{bff}}{\left(k_{pillar} + F_{bff} \big/ y_{bfg}\right)} \tag{6.49}$$

The results of table 6.1 are substituted into equation 6.49 to yield:

$$y_b = \frac{0.51274 \ qa^2}{k_{pillar} + \left(\frac{7.8214 \ E_{dia} \ t^3}{a^2\left(1-\nu^2\right)} \right)} \tag{6.50}$$

Equation 6.50 is used directly in the sensor model to calculate the feedback pressure resulting from a diaphragm support deflection. The two terms in the denominator are the stiffness contributed by the support and diaphragm respectively. The relative stiffness of the diaphragm and its support is therefore:

$$\frac{k_{pil}}{k_{dia}} = \frac{0.12785 \ k_{pillar} a^2\left(1-\nu^2\right)}{E_{dia} t^3} \tag{6.51}$$

If the relative stiffness as defined in equation 6.51 is infinite, the fixed-fixed case applies and when it is zero, the fixed guided case applies. The last relation required to complete the model of the diaphragm is its volume displacement to deflection relation. The volume relations in table 6.1 is substituted into equation 6.49 to yield:

$$y_b = \frac{13.297 \ \ \mathrm{Vol}}{a^4\left(k_{pillar} + \frac{20.353}{a^2} \right)} \tag{6.52}$$

While the deflection due to pressure is dependant on the diaphragm stiffness, the deflection due to volume is not. This is because a volume displacement implies a specific deformation on the diaphragm.

6.8.4 Pressure contribution opposite the piezo bonded area

Previous equations assume that the differential pressure experienced by the diaphragm is only exerted on the annular area of the diaphragm beyond where the piezo sensor ends. This assumption is accurate when a piezo sensor and support is used on each side of the diaphragm. Only one piezo sensor will however be used in order to utilize the extra pressure area on the diaphragm area opposite the piezo support.

To account for the pressure on the opposite side of the piezo, the effect of this pressure is now derived separately. The equivalent stiffness of the diaphragm-piezo sensor-support combination is derived when the only input is the pressure on the diaphragm circular area smaller than the annular inner diameter. The pressure exerted on this area is shown in red in figure 6.12.

Because the piezo sensor negates its own side of the pressure, only half of the differential pressure is exerted on the piezo bonded region. The stiffness of the diaphragm to this pressure (in the absence of a piezo support) can be found from Young (2002) to be:

$$k_{dia} = \frac{4\pi \ E_{dia} \ t^3}{3a^2\left(1-\nu^2\right)} \tag{6.53}$$

Taking the diaphragm stiffness in parallel with the pillar stiffness yields:

$$k_{bonded} = k_{pillar} + k_{dia} \tag{6.54}$$

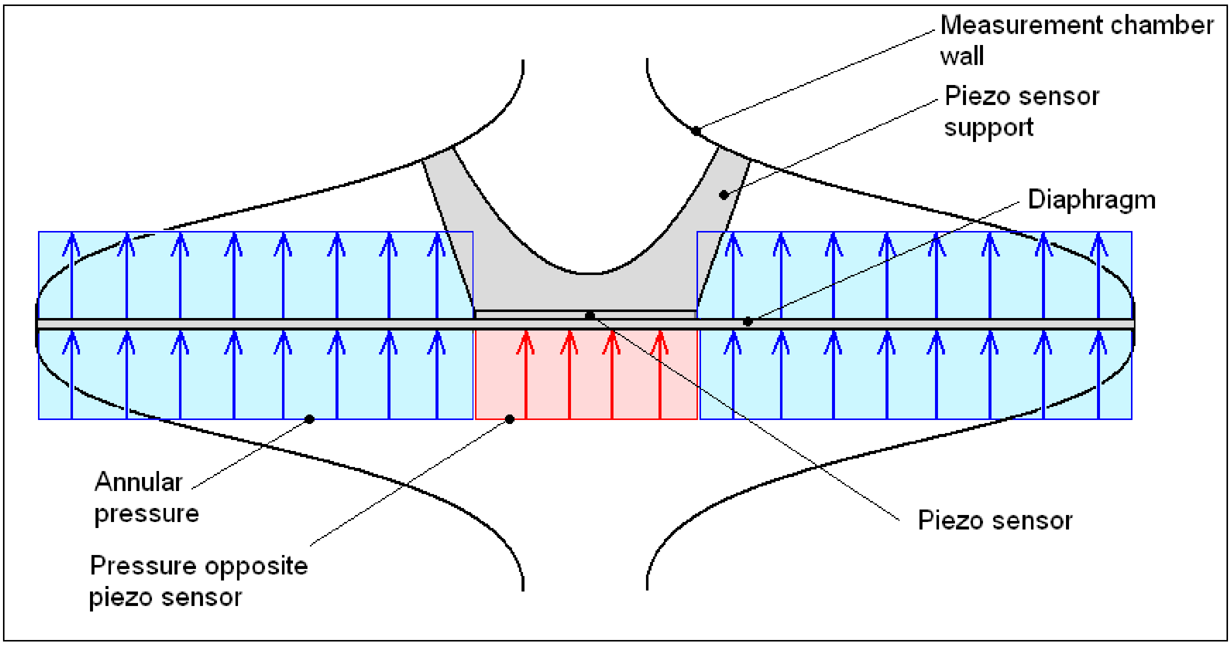

Figure 6.12: Schematic of diaphragm showing how pressure is applied in a piezo-type pressure sensor.

And the deflection the pillar experiences due to this pressure is:

$$y_{pillar} = \frac{q\pi\, b^2}{2k_{bonded}} \tag{6.55}$$

While the linearity assumption holds, this deflection is added to that resulting from the annular pressure. The contribution of this pressure is however generally small (about 10%), being roughly proportional to the fraction of the diaphragm covered by the piezo sensor.

6.9 Pressure transducer conclusions

The piezo-based transducer is a much stiffer alternative to the plain diaphragm, but introduces an unwanted transient response whereas the plain diaphragm has a flat frequency response. The use of a strain-gauged diaphragm is deemed less feasible than the piezo version for channels of a micro scale: The fluid volume required filling readily measured diaphragm deflections will require high flow if practical bandwidth is to be achieved. Larger sensors may make the ratio of channel width to diaphragm diameter more suitable for the use of the strain-gage concept. Many other pressure transducer concepts may also be viable for use in the sensor; the piezo-based transducer serves as a benchmark and a means of finding the potential of the sensor.

Chapter 7

Experimental verification of pressure theory

7.1 Introduction

In preceding chapters it has been shown that the sensor is diverse in the theory applied to its design. This document focuses only on the theory that lies central to the design function. At the heart of the design of the sensor lies the channel array, wherein most of the theory relevant to the sensor's design is concentrated. The channel array is a dynamic system in every sense: application of angular acceleration to the channels result in the generation of an unsteady differential pressure. This unsteady pressure differential results in unsteady flow. The starting flow would have been unsteady even if there were constant pressure, so the flow is unsteady not only due to the unsteady pressure, but is inherently so.

The flow response to pressure is approximately first order though, which is a non-oscillatory response. The most pronounced effect of the first order flow response is a large frequency response performance loss in the sensor as a whole. This is a price paid in favour of high sensor scale factor and is well characterized, partly by the clear limit set by the parabolic steady flow relation of Hagen and Poiseuille. The steady flow relations are analytically exact and have also been verified by experiment for diverse channel types and wall roughness. Experimentation on steady flow would be unnecessary, although experimentation on the transients of flow may prove useful.

The unsteady nature of the pressure generation is not as well understood as the flow. With stiff diaphragms, the pressure is very much oscillatory in nature due to reflections caused by the finite length of the channel and the theoretically negligible inherent damping of the pressure wave at low frequencies. This pressure oscillation is undesirable as it causes pressure noise in the order of magnitude of the pressures being measured. This is truer for inputs with high frequency output content, like step- or impulse inputs. If the differential pressure oscillations do not damp out, the sensor would have a noise floor many times that caused by electrical interference. Therefore, measures have to be taken to obtain a damping that is favourable for sensor operation. Due to these risks, the decision was taken to verify pressure generation experimentally.

The objectives of the experiment are:

1) Verification of the pressure generation theory. This includes pressure potential theory and pressure propagation theory.
2) Characterize the damping of a real system to approximate the damping to be expected in the sensor channels.
3) Explore possibilities for the addition of extra damping to the channels, and in particular the effect of free gas in the channels.
4) Explore the characteristics of the generated differential pressure by measuring the gage pressure at the two channel ends separately.
5) Confirm the ability of the fluid column to reject linear acceleration influence.

Due to the low volumetric deflections of contemporary pressure sensors, compressibility effects are isolated and the flow theory is not verified by this experiment. Even when significant air is contained in the channels, the compression of the air causes very small flow. This closely approximates the rigid body ends of the discrete model in figure 3.3.

7.2 Experiment apparatus

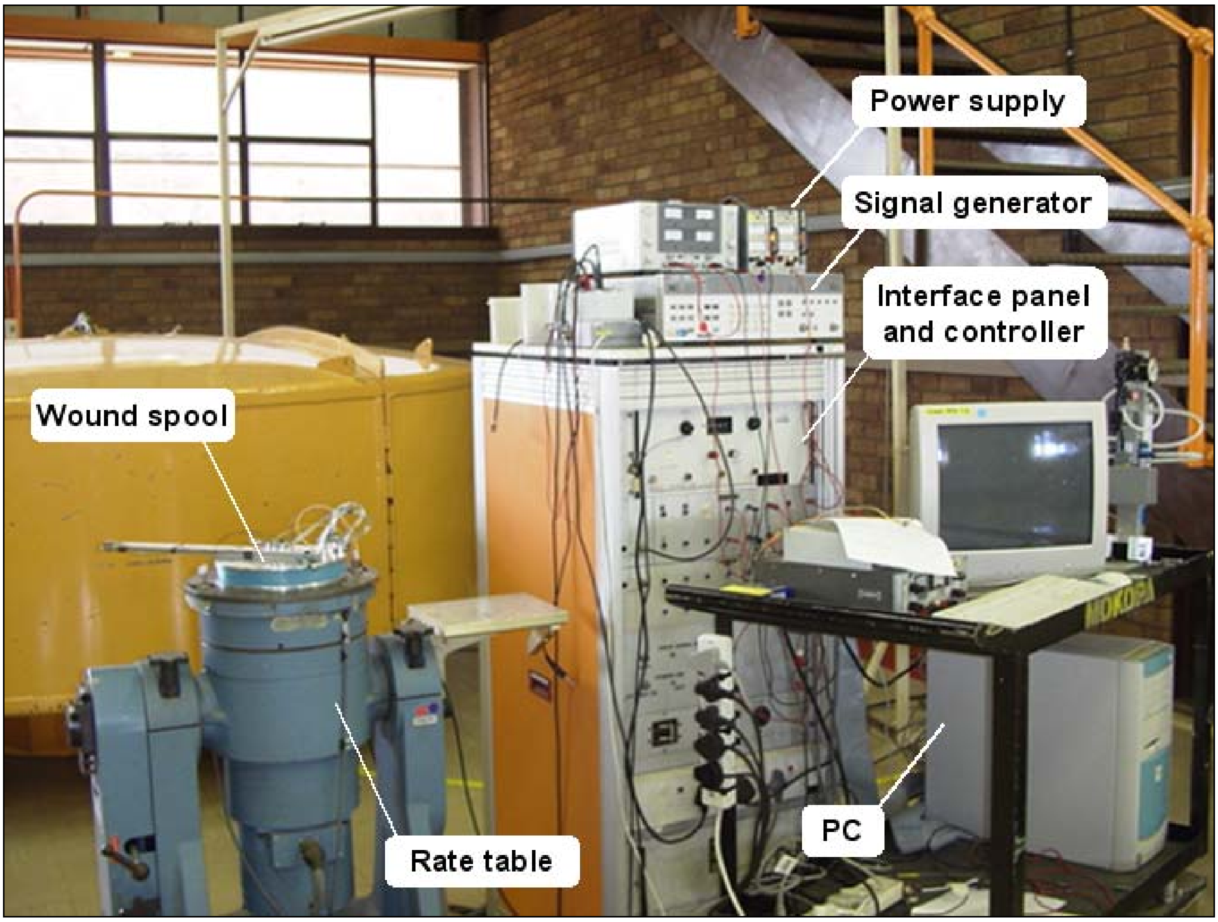

Figure 7.1: The experimental set-up.

Figure 7.1 shows the entire experimental set-up including the data recording equipment. A scaled-up version of a channel array was used to measure the pressure propagation properties.

The test hardware comprised of the following items:

1) Two separate PCB-mounted IC Sensors Model 1220 pressure sensors with analogue output is used. The two pressures are measured separately to better characterize the saturation of pressure drop on the low-pressure end. The available pressure range on each sensor is 100kPa and absolute pressure down to vacuum is measurable.
2) The channel array is built up out of pneumatic tubing of 3mm inner-diameter. This will make flow effects negligible since the flow diameter is large relative to the displacement volume of the pressure sensor.
3) Approximately 20m of tubing is reeled around a 200mm diameter spool that results in high pressures that are more conveniently measured than those in the envisaged sensor. Another 1.5m tube is reeled around the 20m tubing to verify effect of tube length and channel symmetry on the pressure.
4) A rate table is used as motive power to impose the required angular accelerations onto the spool. All signals and power were sent via the rate-table's slip rings.
5) A Hewlett Packard 3325B function generator was used when harmonic input was required to the rate-table.
6) A Humphrey LA45-0135-01, 20G linear accelerometer is placed on the end of a swing-beam to measure angular acceleration. Only one accelerometer was used, so the accelerometer could only measure angular acceleration that is centered on the spool.
7) The rate table's internal speed feedback is also available for processing. This signal is differentiated to obtain an angular acceleration measurement supplementary to that measured directly by the beam-mounted accelerometer.

8) DC power supplied to the sensors was provided with one dual supply for the sensor board and a separate single-supply for the accelerometer.
9) The pressure sensors are not compatible with water, so a buffer is needed to isolate the sensor from the water column. Hydraulic oil (Shell Tellus T15) is used for this purpose.
10) Diesel and water (but not mercury) is used as the working fluid, for the reason of safety. The loss of fluid density (and therefore scale factor) is compensated by the large tube length, and good motive power, which can provide high acceleration input.

Another disadvantage of using water and not mercury (besides the loss in density) is the difference in vapor pressure of the two fluids. The vapor pressure of mercury at 20°C is 1.1×10^{-3} Pa as opposed to the 2.337 kPa of water. When the fluid pressure drops below the vapor pressure, the liquid boils causing vapor bubbles in the channels. Bubbles in the fluid column damage the continuity in the fluid column and make the pressure propagation theory used here quite inapplicable. The use of water therefore limits the absolute pressure at the low-pressure end of the fluid column to a minimum of 2.337 kPa at 20°C.

Two measures exist to remedy this problem:

1) Pressurization of the fluid to avoid fluid evaporation. The range of the pressure sensor firstly limits the pressure in the channels. The next limit is the strength of the tube walls, which will start yielding at about 10 bar gage pressure. The same pump used to fill the tubing with the working fluid can be used to pre-pressurize the fluid. The pressure limit on the sensors unfortunately eliminates the pressurization option in this experiment.
2) Cooling of the water is also a means of lowering its vapor pressure. A constant fluid temperature is important for this experiment because the bulk modulus of water shifts appreciably with temperature. The whole system, including the rate table will therefore have to be cooled to a constant temperature if this option is taken. Care must also be taken not to freeze the water since this will also negate fluid column function.

Figure 7.2 shows a schematic layout of the experimental method. Some of these items are annotated in a close up photograph of the spool set-up in figure 7.3. The rate table is controlled to provide a constant rate of rotation (as the name implies). For this purpose, the table has a speed-based closed loop system operating from a tachometer for feedback. The table is also useful to effect accelerations that have good repeatability up to maximum of approximately 480rad/s^2 (27500°/ s^2). The table cannot realistically reproduce the customary test signals like step- or ramp-inputs, which means that the simulated indicial response is not of much use in verifying the theory's validity. Fortunately the system can be simulated for any acceleration input, the only requirement is that the true input is measured so that similarity is satisfied. The only drawback of not having a step or impulse input available (besides convenience) is that finite slope inputs do not excite the system as forcefully as those of infinite input acceleration slope. This means that not as many natural frequencies are excited by the input acceleration, and that system specific characteristics will be harder to identify. The "finger print" of the system is clearer with infinite slope acceleration inputs. In operation though, the sensor will not experience infinite jerk (time differential of acceleration) and even if it did, the higher frequency pressures would damp out very rapidly. This seems to make the necessity for fluid column characterization in such detail somewhat superfluous, but by neglecting this, the question of accuracy of the higher natural frequencies will be left unverified even if they are of less importance. The current measurement system however does not have the accuracy or bandwidth to measure these modes in any event.

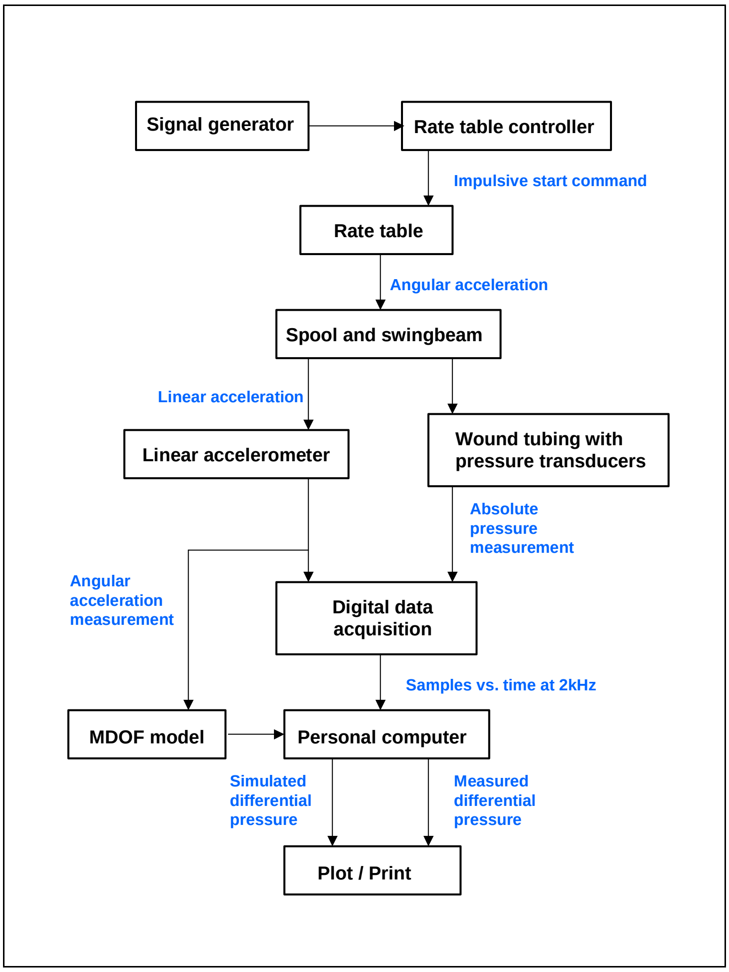

Figure 7.2: Schematic of experimental procedure.

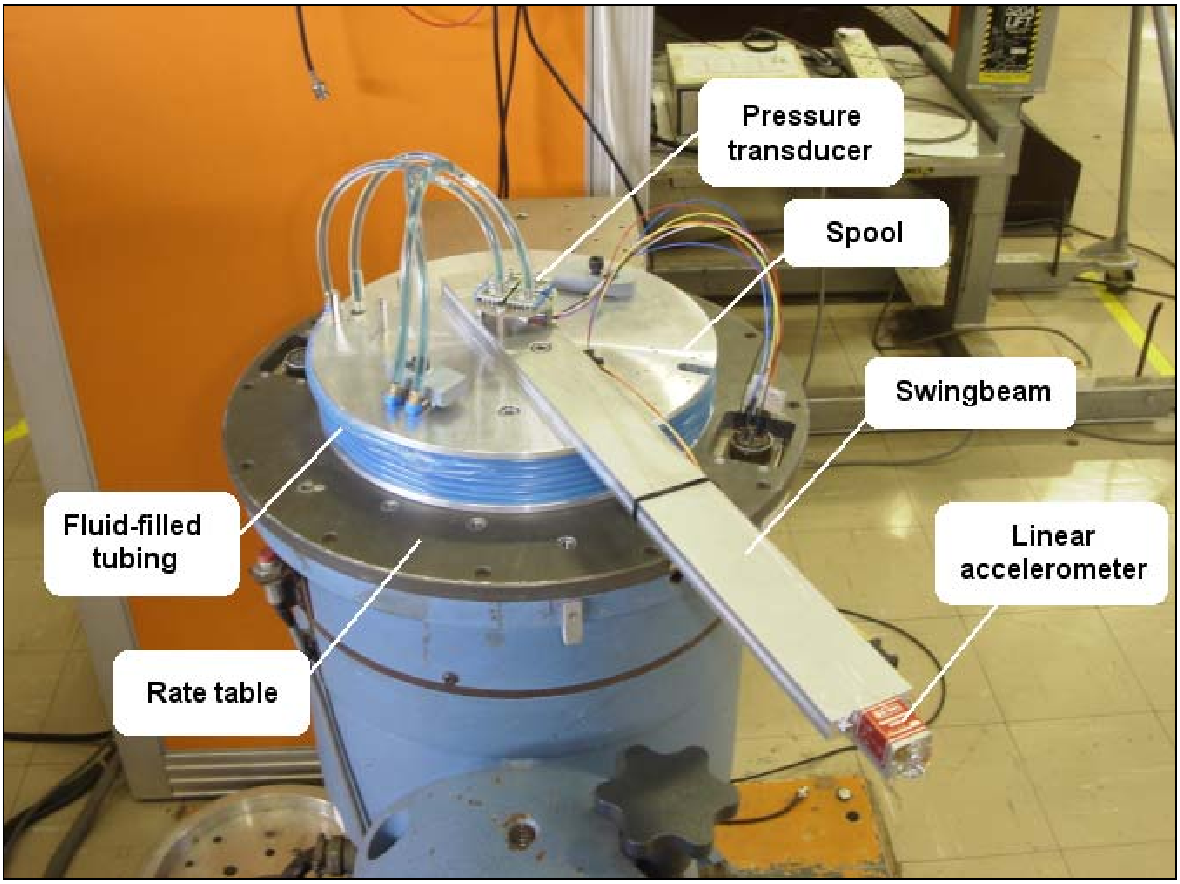

Figure 7.3: The rate table-top with spool, PCB mounted pressure sensors and wound tubing. The linear accelerometer is also shown at the end of the swing beam.

In order to test the whole frequency response, an infinite jerk input is required (like an acceleration step input). An acceleration step input is problematic to create because the inherent inductance of an electric motor limits the speed of change in current through the windings. This in turn imposes a minimum time for a change in torque, and so places an upper limit on the jerk imposed on the table by its motor. The maintenance of the angular acceleration step input will also be problematic after a certain time because of the maximum speed of the rate table motor. Another input that contains theoretically infinite rate is the impulse. A velocity impulse is maybe more practically realizable and can be approximated by a rigid collision although this also problematic, since an absolutely rigid material does not exist. If the swing-beam hits a stationary object it will deflect and undergo energy loss due to its inherent damping, thus making infinite jerk impossible. A compromise has to be made with the realities of nature and deal with large values of jerk and not infinite ones. For this experiment, only the rate table's acceleration was used as input (up to 480rad/s^2). The acceleration caused by the table can be indirectly adjusted to the desired level by changing the set rotation rate and letting the table accelerate from rest to the set speed.

7.2.1 Data recording equipment

All signals were sent single-ended via the slip rings of the rate table to an interface box. The signals are then fed differentially to a PC-based logging system. All data was sampled at 2kHz and recorded on PC hard disk with interface software written in Labview®.

7.3 Experimental corrections

7.3.1 Spiral shape corrections

The tubing used in the experiment is wound in radial levels – as one would wind a fishing line on its reel. This contrasts with the envisaged channel array that contains interconnected spirals on separate longitudinal levels. The difference between the two is the acceleration field experienced by the channel. The sensor channel experiences a field that increases along the channel for one wafer and decreases for the next wafer. If an Archimedes spiral is used throughout, a linear increase and decrease versus length along the channel results. This culminates in a deterministic triangular shaped acceleration field along the whole fluid column. This acceleration field will cause a symmetric pressure change on the two ends of the channels if an even number of wafers is used. The tubing installed in the experiment behaves more like a single wafer as it contains only one spiral from a radius of 100mm up to 120mm. The gage pressure generated will always be more at the tube end placed at the larger diameter. If a linearly increasing spiral is assumed, the tube end at 100mm will generate 100/220 = 45.45% of the total pressure and must therefore be multiplied by 1.1 to equalize the output. The tube end at 120mm will produce 55.45% and must be multiplied by 0.917 to obtain a symmetric output.

7.3.2 Centripetal acceleration correction

The MFCAA measures acceleration by transducing pressure in the center of the sensor. No centripetal acceleration effects are present across the diaphragm plane to influence differential pressure. The experiment unfortunately does not use an internal sensor, so centripetal acceleration has a significant effect. Provision is made to place the pressure sensors as close as possible to the tube ends to minimize centripetal acceleration effects, but a correction on the measured data is still necessary.

The centripetal acceleration experienced in an object rotating at constant speed ω, at a radius r from the center of rotation is:

$$a = \omega^2 r \tag{7.1}$$

If an arbitrary shaped fluid-filled channel rotates with its two ends at r_1 and r_2 with $r_1 < r_2$, then the pressure differential between the two points is:

$$\begin{aligned} \Delta P_{centri} &= \text{density x acceleration x length} \\ &= \rho \int_{r_1}^{r_2} a(r)\ dr \\ &= \rho \int_{r_1}^{r_2} \omega^2 r\ dr \\ &= \rho \left[\frac{\omega^2 r^2}{2} \right]_{r_1}^{r_2} \\ &= \frac{\rho \omega^2}{2} \left(r_2^2 - r_1^2 \right) \end{aligned} \tag{7.2}$$

The sensors are placed at lower radii than the two tube ends so the centripetally generated pressure is always added to the measured pressure to find the pressure at the spiral ends. Equation 7.2 requires accurate speed information to be implemented successfully; the internal tachometer of the rate table serves this purpose.

Equation 7.2 furthermore assumes constant speed input, hence the dynamic effects of centripetal acceleration is neglected. Placement of the pressure measuring PCB as close as possible to the tube spiral outputs minimizes the influence of centripetally generated pressures and makes calculation of dynamic influence unnecessary.

7.4 Experiment assembly

An important requirement of the fluid column is that no air bubbles are present inside the tubing. The tube wall is quite prone to the forming of bubbles when it fills with fluid. An air free tube is assured by circulating fluid through the whole system until all bubbles are pumped out. For this to succeed, the flow has to be high enough to entrain any bubbles. Inside a long tube this can be troublesome due to the high pressure required to sustain high flow (especially with the viscous liquids used). For a single layer of translucent tubing, a visual inspection would suffice to confirm the absence of air. In a long tube that is reeled in multiple layers no visual inspection for bubbles can be done, hence the measured data has to confirm fluid column continuity. Measuring the pressures at the tube ends separately aids in doing this. Section 7.4.1 shows the effect of free air on the measured pressures.

A further complication for the removal of air is that the pressure sensor cannot be bled to remove internal gas. The air inside the sensor is removed firstly by injecting as much as possible liquid deep into the sensor with a syringe. A filling tube containing more oil is now fitted on the sensor and the pressure on the tube open end dropped to below atmospheric. The air left inside the sensor expands due to the pressure drop and partially exits the sensor. The pressure in the tube is now suddenly increased to atmospheric level, which makes the expanded bubble inside the sensor break up, sending smaller bubbles up the tube. Doing this repeatedly helps remove air from the sensor. The sensor is known to be air free when the oil level in the filling sensor only changes by the internal sensor volumetric displacement when the open-end pressure is decreased.

If a boundary between two unmixable and discernable fluids exists (like oil and colored water) a quick test can be done to confirm the absence of gas in the system. In an air free tube, high angular accelerations in both directions should cause negligible movement of the fluid interface. High angular inputs can also coax the last air out of the sensor.

7.4.1 Impact of free air in channels

After the pressure corrections of section 7.3 are implemented, the outputs of the two pressure sensors should be symmetric. Symmetry of data is the foremost measure of the quality of the fluid column. The main culprits that cause an asymmetric output are free air in the fluid column and fluid column boiling. If the pressures at the sensors remain above the fluid vapor pressure, an asymmetric output implies the presence of free gas. An asymmetric output is shown in figure 7.4. The effect of the free air can clearly be seen on the symmetry. Not only the magnitudes are affected, but also the wave shapes.

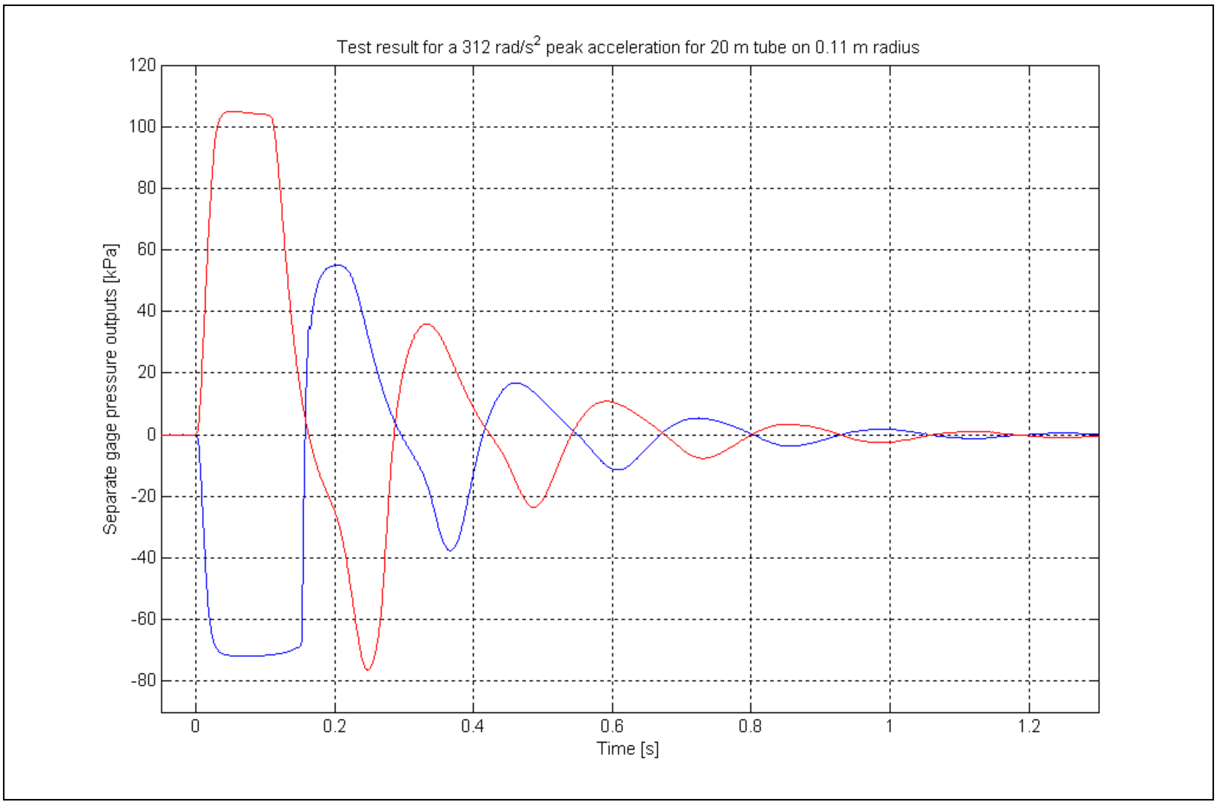

Figure 7.4: Typical asymmetric pressure output due to free gas in inertial fluid. The two column end pressures are measured separately.

Figure 7.5 combines the two gage outputs of figure 7.4 into a differential output and plots the output of an air free system for comparison. The system parameters are identical except that the one fluid column contains approximately 20ml air and the other none. At the start of the impulse, the two graphs are seen to follow the same path. The graphs diverge at the first crest, where the air-containing system forms a plateau while the air-free system does not. The compression of the air blunts the wave crests and causes an increased oscillatory motion in the channels. This seems contrary to what was expected in the theory, where a gas-filled accumulator was in fact proposed to add damping to the system. The increased oscillatory motion of the air-containing column in figure 7.5 is caused by the high compressibility of air coupled with a low flow system. If the channels had a smaller diameter so that significant flow is caused by the compression of air, the air-containing column would exhibit higher damping.

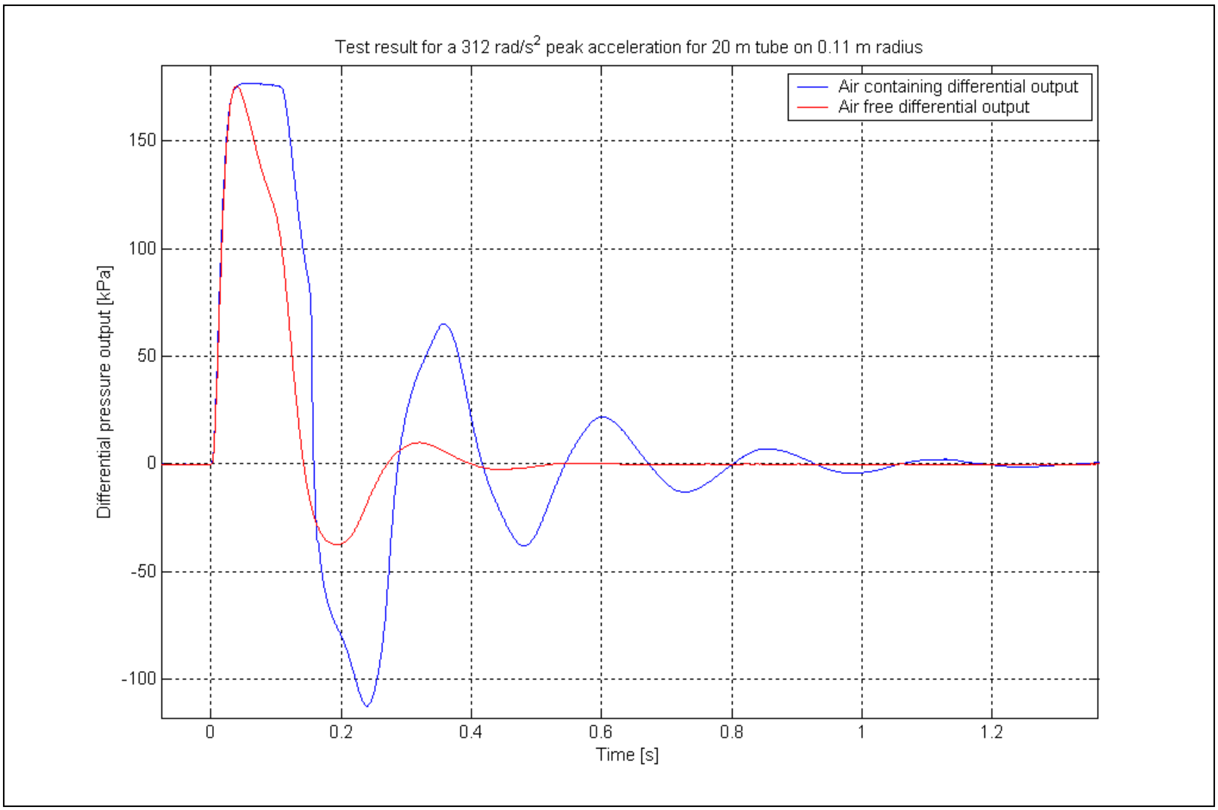

Figure 7.5: Comparison between air-free and air-containing fluid-column outputs.

7.4.2 Impact of radial offset

An important feature of an angular accelerometer is the rejection of linear acceleration inputs. Linear acceleration must have no influence whatsoever on the generated pressure. To test whether this is the case, the fluid column spool was placed increasingly offset to the center of the rate table (up to 209mm) in repeated test runs with the same fluid and the same angular acceleration imposed each time. No difference in measured pressures was recorded in the tests except minimal offsets (of 9% and lower) caused by centripetally generated pressures and variations in the angular inertia of the spool due to its offset on the rate table.

7.5 Results

Two tubing systems were tested. A 20m tube wound at a diameter varying between 0.2m - 0.24m and a shorter 1.5m tube wound at 0.24m. The shorter tube fills faster and the higher flow rate helps attain an air free fluid column.

The theoretical prediction is based on a 51 DOF model one-dimensional column as discussed in chapter 3. The measured acceleration input is slightly filtered with a zero phase digital filter, as the acceleration signal was noisier than the pressure signal. The physical properties of the tubing and working fluid are used to make an approximation of the modified bulk modulus to be used in the fluid column model. The system properties are:

Pressure potential (1.5 m tube): 0.174 Pas^2 /rad
Pressure potential (19.73 m tube): 2.17 Pas^2 /rad
Diesel bulk modulus at 20°C: 1500 - 1600 MPa
Diesel density 0.854 kg/m^3
Polyurethane tubing Young's modulus: 0.05 - 0.2 GPa
Tube inner diameter: 2.9mm
Tube wall thickness: 0.7 mm

The wound tubing is only positively anchored at its ends. Vulcanized silicon is used elsewhere on the tube for support. The anchoring constant c is expected to be close to the constant used for longitudinal constrainment. From equation 3.27:

$$\frac{1}{K'} = \frac{1}{K} + \frac{dc}{eE}$$

The expected modified bulk modulus for the tubing parameters quoted above is expected to fall between 13 and 51MPa. The other parameter that cannot be fixed with certainty before the start of the experiment is the fluid column damping. These variables are selected according to the best fit of the data, and should be within the limits calculated above. A series of data is fit only on the highest acceleration input test and then fixed for other tests with the same system.

Symmetry of the data is also evaluated for all experiments conducted and printed on the graphs. The symmetry is calculated on a comparison of the maximum pressure variation of the two sensors. The tests completed were all without free air present, so only tests with symmetries higher than 95% are used.

7.5.1 Short tube experimental results

All data is presented with the ideal pressure response plotted with the measured and predicted data. The ideal pressure response refers to the pressure yielded by an incompressible fluid inside a rigid tube. This imaginary pressure is directly proportional to the applied angular acceleration and is included as reference. The real pressure response will equal the ideal response in the steady state.

The fit parameters on all theoretical predictions in this section are:
Inter-mass damping: 0% of critical
Shear damping: 21% of critical
Modified bulk modulus: 29.73 MPa

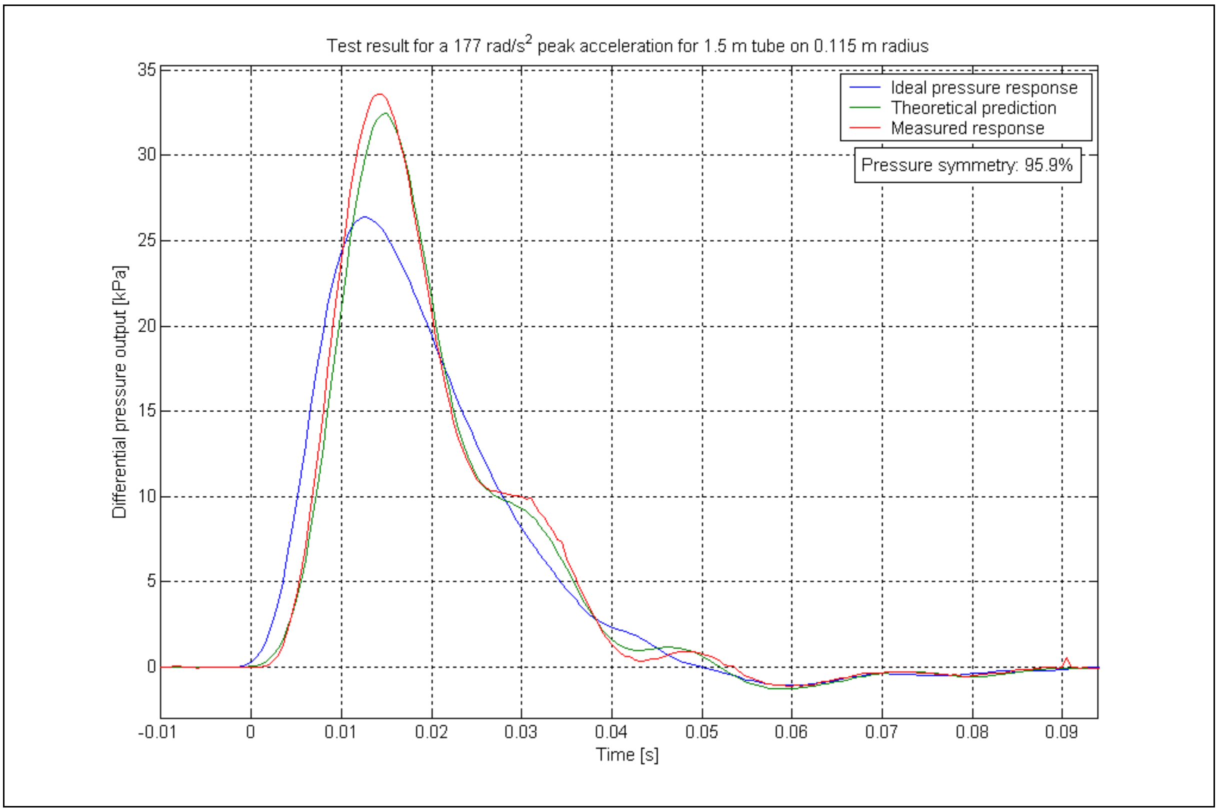

Figure 7.6: Test result in 1.5m long tube for acceleration to 200 °/s from rest in 50ms.

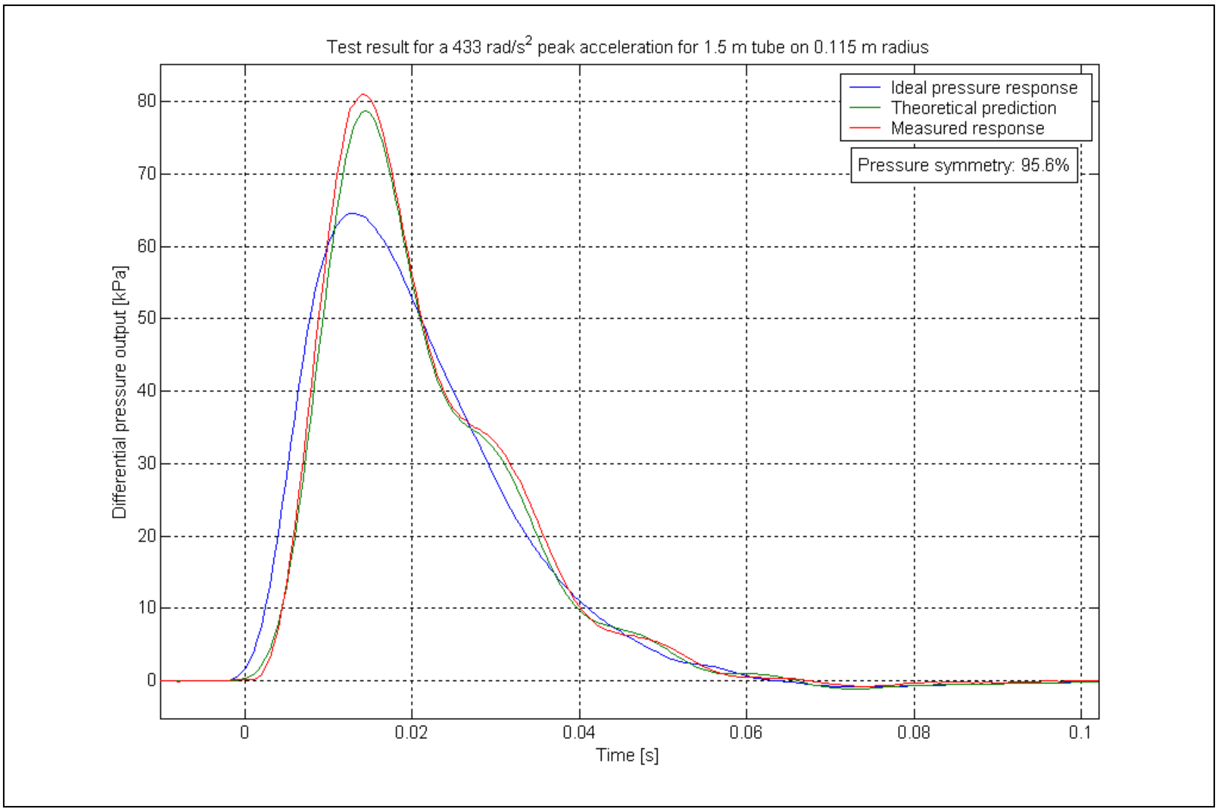

Figure 7.7: Test result in 1.5m long tube for acceleration to 600 °/s from rest in 60 ms.

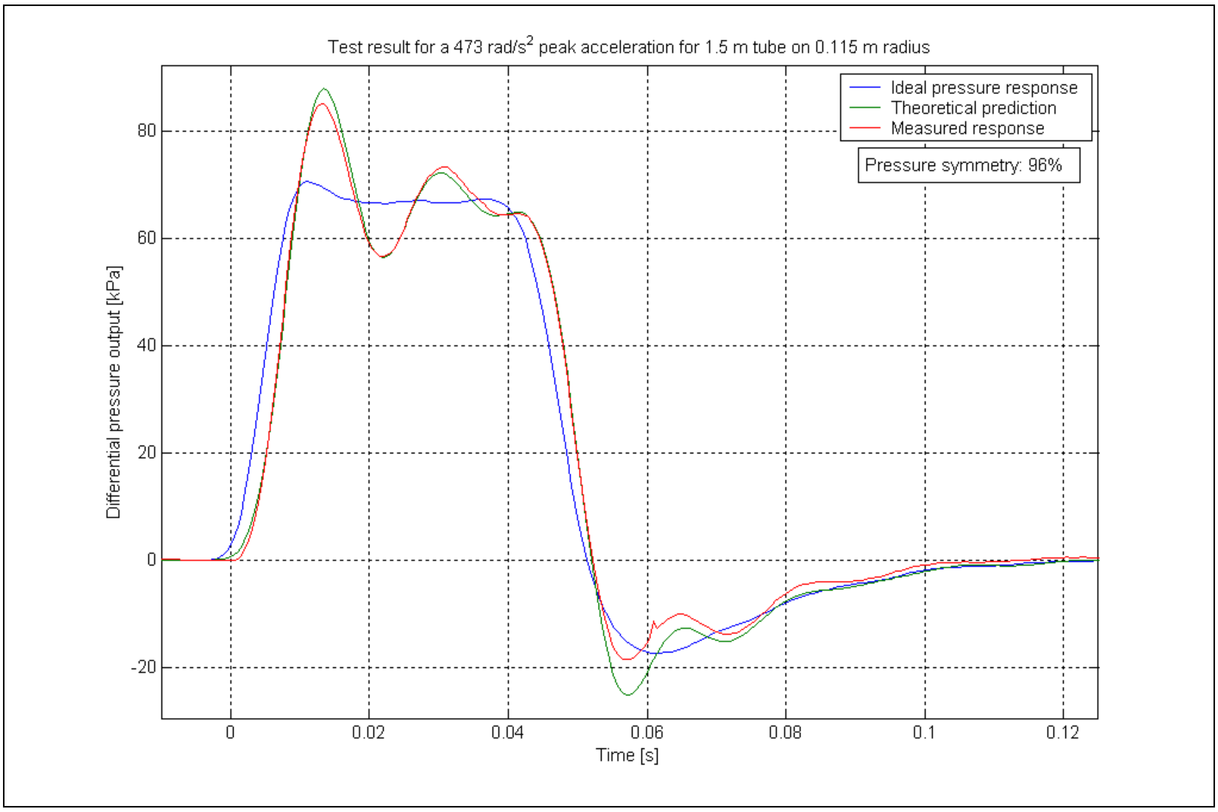

Figure 7.8: Test result in 1.5m long tube for acceleration to 900 °/s from rest in 50 ms.

7.5.2 Long tube experiment results

The fit parameters on all theoretical predictions in this section are:

Inter-mass damping: 2.4% of critical

Shear damping: 41% of critical
Modified bulk modulus: 25.15 MPa

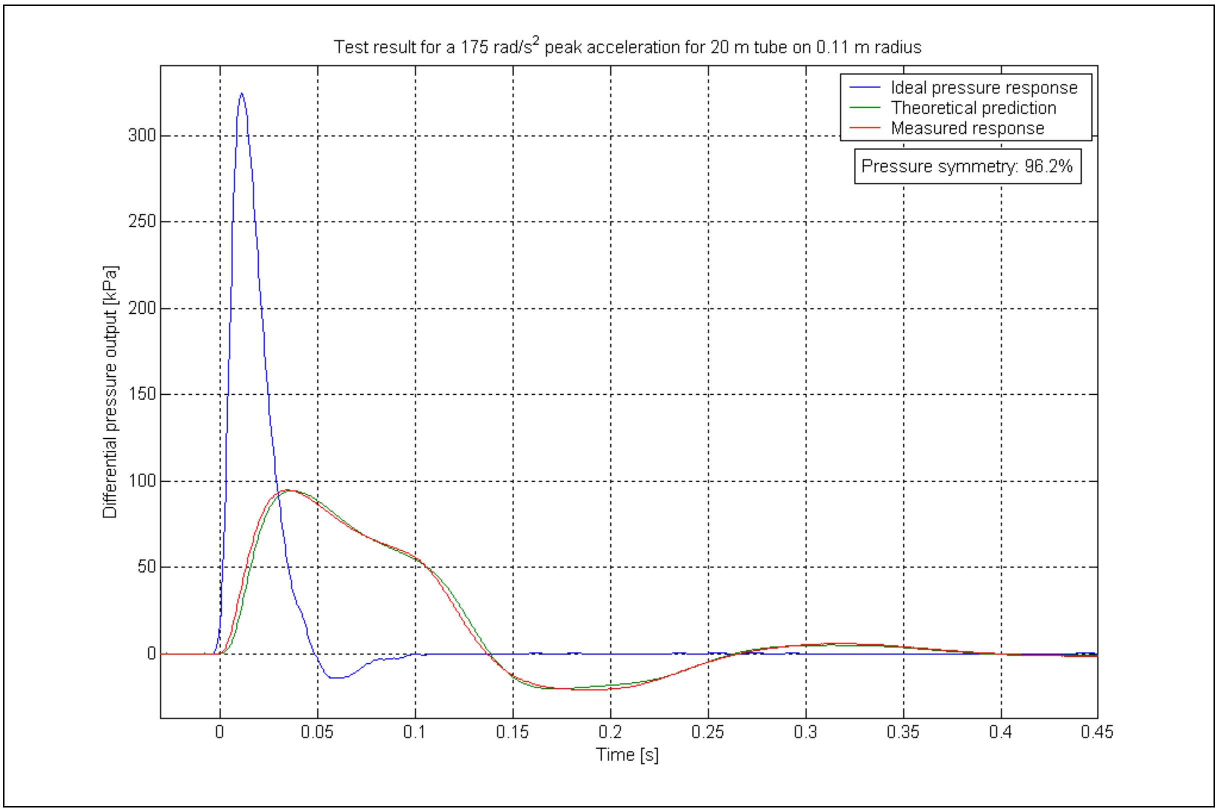

Figure 7.9: Test result in 20m long tube for acceleration to 200 °/s from rest in 50 ms.

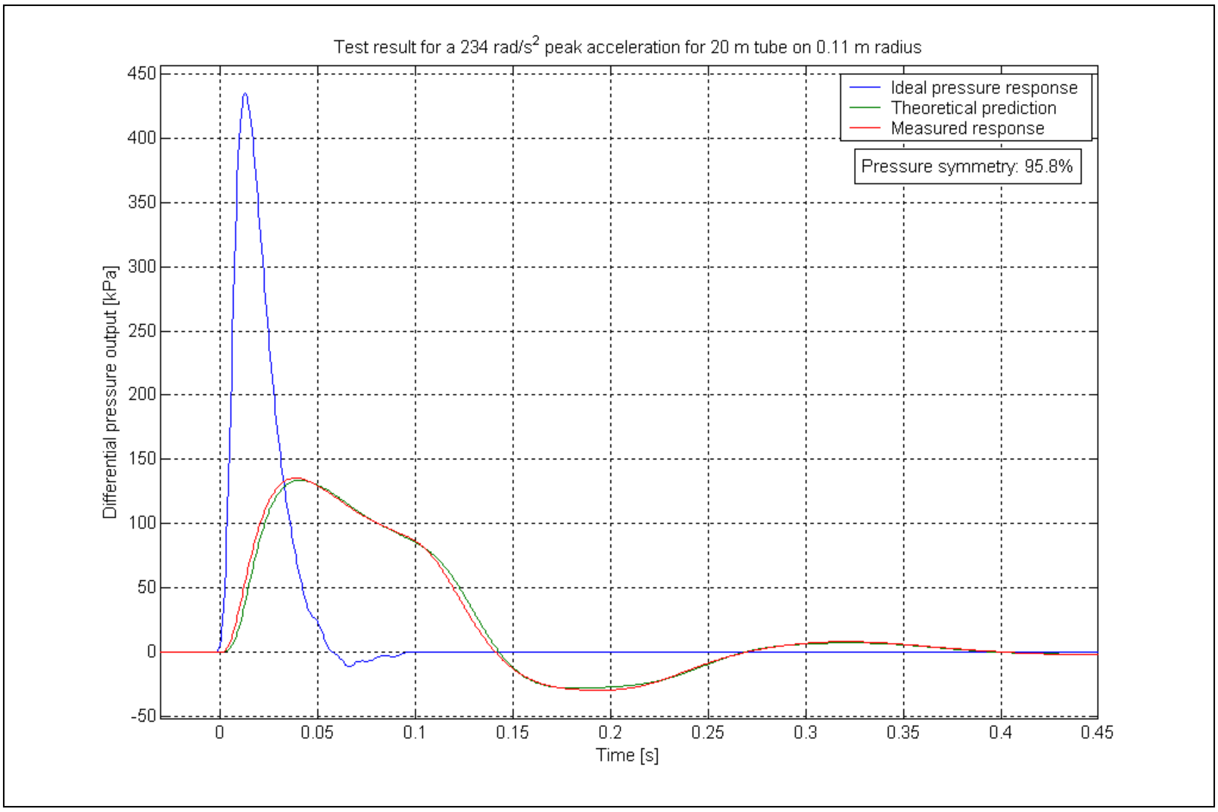

Figure 7.10: Test result in 20m long tube for acceleration to 300 °/s from rest in 60 ms.

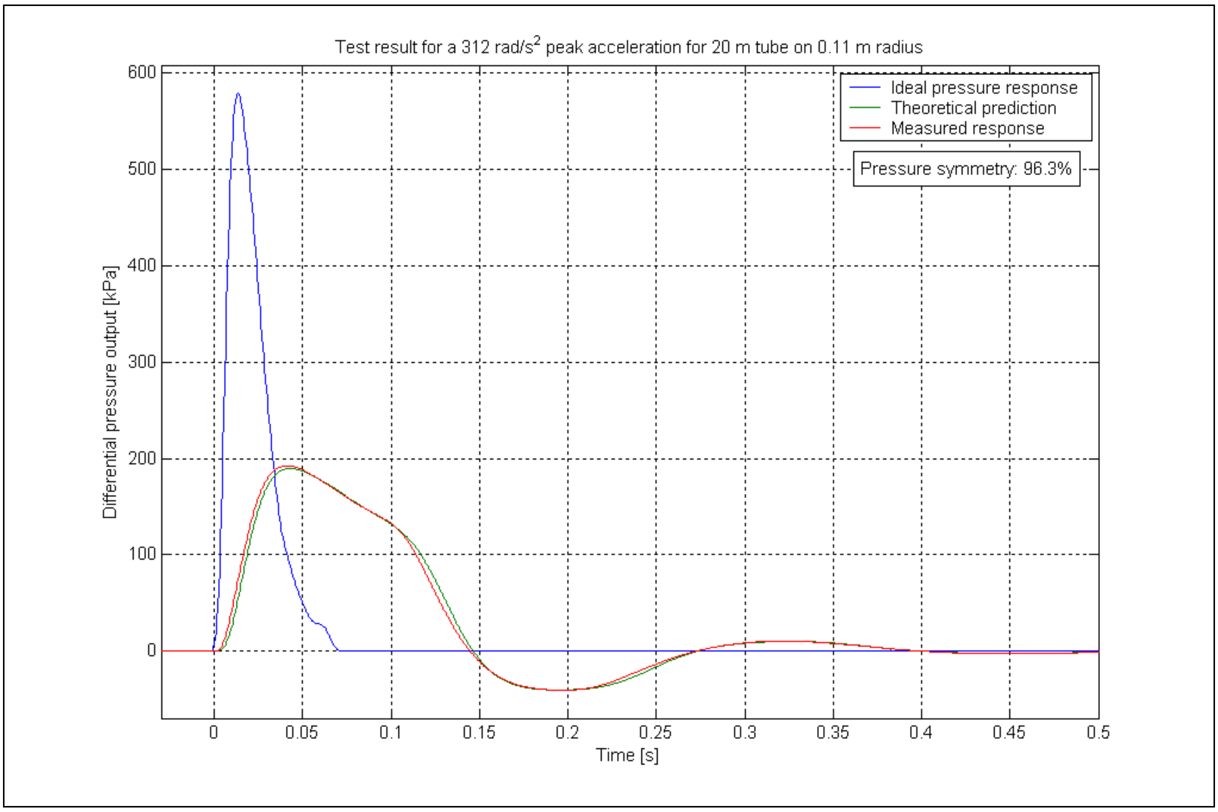

Figure 7.11: Test result in 1.5m long tube for acceleration to 450 °/s from rest in 70 ms.

7.6 Experimental observations

The fit is satisfactory with all constants within expected limits. Only the first two modes of wave motion are evident in the tests. In particular, the following is found:

1) The long tube bulk modulus is lower than the short tube. This is due to the large lengths of unconstrained tubing on the spool, which decreases the wave speed.
2) Shear damping dominates both sets of data. The fit only requires minute inter-mass damping, even with the long tubing. The wave damping predicted by Lord Rayleigh (see section 3.5.3) is clearly supplemented by other damping. The total level of damping increases with tube length, although not linearly. Not enough tube lengths were tested to obtain a better relation.
3) The short tube data fits better for lower acceleration inputs but the high acceleration result is still satisfactory. The low pressures generated sometimes exhibit a slightly jagged shape due to noise, especially in figures 7.6 and 7.8. The worst fit is obtained in figure 7.8. The reason for this may be attributed to the highly dynamic nature of this input, which causes non-linear damping or other effects not modeled by the MDOF pressure propagation model.
4) The predictions fit the 20m tests very well. The prime reason for this is the large pressures generated, which make the measurement errors less evident.
5) Tests performed with water show similar damping values to diesel. The lower viscosity of water cannot have an affect because negligible flow is present. The test done here therefore represents mostly the damping offered by the tubing material and is as such a lower limit.
6) The extrapolated damping at tube lengths approaching zero is 19% of critical. This damping cannot be attributed either to flow losses or channel wall damping because both of these loss types require tube length to have an effect.

7.7 Experiment conclusions

1) The fluid column model proposed in chapter 3 is an adequate model to use for predictions of fluid column characteristics in a micro-fluidic channel simulation. The experiment is not extensive enough to provide detailed information of the nature of pressure wave damping in the channels.
2) Free air in the fluid column will only add damping to the pressure wave if its presence causes significant flow. For a system with large channels the presence of free air adds oscillatory character to the wave.
3) The spiral rejects linear acceleration. The risk for cross-coupling in the MFCAA is therefore small.

Chapter 8

Sensor modeling and optimization

8.1 Introduction

This chapter integrates the mathematical models into a single model to simulate the functioning of the angular acceleration sensor. The aim of the sensor simulation is to synthesize all the work done on pressure generation and flow pressure loss in the channels into an analyzable unit for which optimization can be performed. After a complete sensor model is available the sensor characterization is first done for the 0Hz angular acceleration input case in order to find sensor scale factor and then the sensor dynamic characteristics are simulated. Lastly, the simulation parameters are optimized within practical limits (and assumptions made herein) to find a sensor design suitable for some known applications.

The aims of this chapter are:

1) Integration of sensor theory into a model that can accurately predict sensor performance.
2) Characterize the sensor constants qualitatively to gain an understanding of the mechanisms at work inside it.
3) Determine sensor potential by doing a sensor optimization for several existing applications and predict sensor performance for these scenarios.

8.2 Sensor simulation

The aim of the dynamic simulation is to determine holistically the effects of the variables governing the operation of the sensor. For the simulation of any unsteady influence in the sensor, a full dynamic simulation is required. The dynamic model of the sensor was built in Matlab® Simulink®. Figure 8.1 shows the highest level of the model.

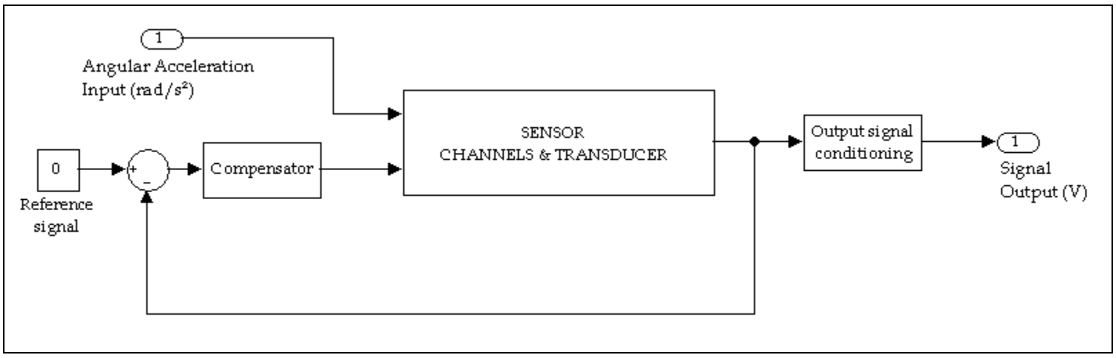

Figure 8.1: The sensor model top level.

The sensor as a whole is a single input/output system, like every other system in its composition. Angular acceleration is input to the sensor and a signal is the output, which may be conditioned or not. The sensor may also be assisted by a feedback system, in which case the negative of the output is fed back and compensated, before being applied to a sensor actuating system. The whole dynamical sensor system comprises of the following elements:

1) The environment of the sensor, which gives the desired acceleration input but also undesirable effects like temperature fluctuations, noise vibration and electromagnetic interference.

2) Sensor channels that constrain the fluid in a fashion that is favorable to maximum pressure generation at the pressure transducer. (This is covered in detail in chapters 2, 3 and 4, while its experimental verification is in chapter 7)
3) Sensor pressure transducer, which transforms the pressure generated in the sensor into an electrical signal for further processing. A simple system would consist of a strain-gaged diaphragm, although a stiffer system may be required in the form a piezo electrical transducer. (This is covered in chapter 6)
4) Output signal amplifier. Only the transducer charge amplifier is covered herein, but the sensor will probably contain more than one amplification stage.

The sensor model architecture is shown in figure 8.2. The subjects from previous chapters are included herein. Table 8.1 more specifically refers to the input/output relation governed, and what theory is used in which block. The systems in table 8.1 are all of the LTI variety. The model contains a trim block at the output to create normalized Bode plots and step responses according to the 0dB levels dictated by the sensor steady state performance, or scale factor (covered in section 8.4).

Table 8.1: Equation references for blocks used in sensor model.

Model Block	Input	Output	Formula used
Spiral-Helix channels	Angular acceleration (rad/s^2)	Pressure (Pa)	Multi-DOF state space model. Section 3.5.6
Unsteady flow calculation	Pressure (Pa)	Volume Flow (m^3/s)	Equation 5.22
Transducer stiffness	Transducer deflection (m)	Feedback pressure (Pa)	Equation 6.3 (plain) Equation 6.50 (piezo) Equation 6.55 (piezo)
Transducer Volumetric deflection	Volume flow (m^3)	Transducer deflection (m)	Equation 6.13 (plain) Equation 6.52 (piezo)
Strain-gage output	Transducer deflection (m)	Bridge output (V)	Equation 6.19
Charge amp. output	Transducer deflection (m)	Charge amp. Output (V)	Equation 6.34

8.2.1 Pressure to flow interaction modeling

At the heart of the sensor model lays the interaction of pressure generation to flow. The combination accurately approximates flow resulting from an applied acceleration (including flow losses) into the transfer function. Different approaches are available:

Cascaded pressure to flow architecture

The use of the state space method is convenient for the fast modeling of a high DOF system such as the fluid column. It does have a drawback though. The state space representation is best used as an LTI description of a system. This means that the matrices describing the system are fixed. No information can be fed from outside the system except the inputs defined inside the input matrix. This divorces the pressure propagation model from the flow model. The energy loss caused by flow cannot be fed back from the flow model after coding of the pressure model; the correct damping has to be entered beforehand as a constant. Such a model is simple and fast to simulate but may neglect the finer characteristics of the flow interaction with pressure propagation. The architecture of such a model is shown in figure 8.2. The model functions by means of addition of all pressure effects, and then calculating channel flow based on the net differential pressure on the diaphragm. Besides speed of calculation, this model is elegant in its implicit separation of the workings inside the sensor.

This enables the designer to easily tap into any signal (be it pressure, flow or deflection etc.) and so better identify the inter-dependence of the subsystems.

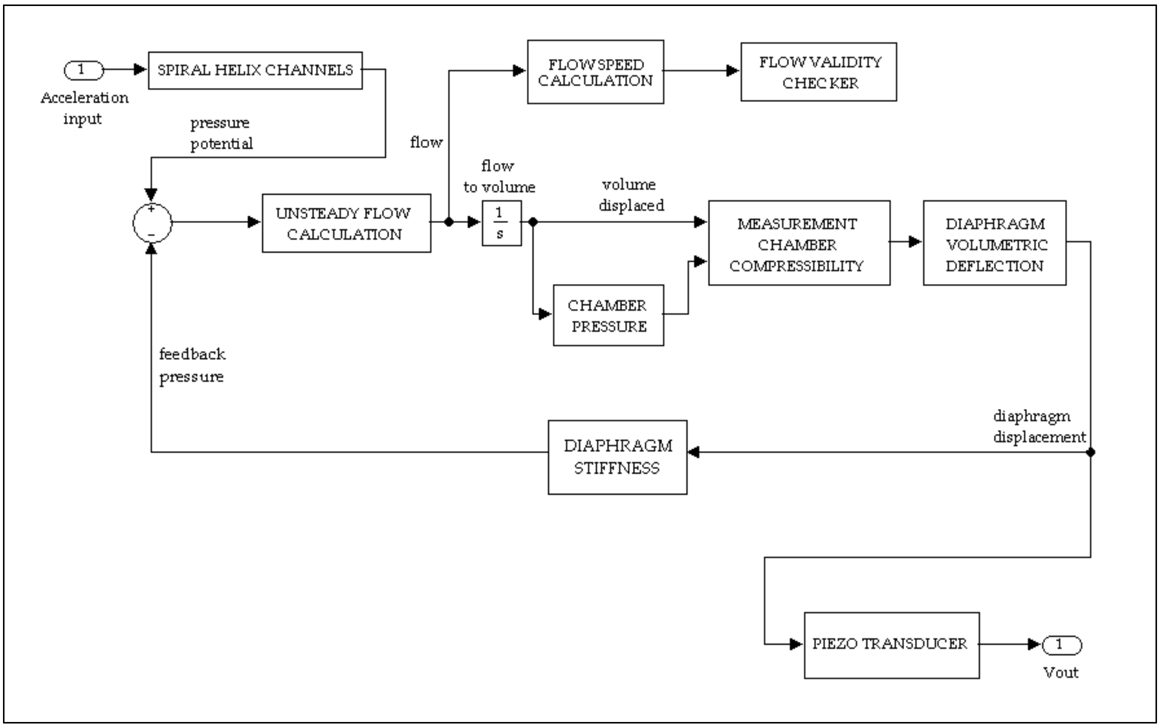

Figure 8.2: Sensor internal systems model architecture with cascaded pressure-to-flow loss model.

Chamber pressure is approximated to ascertain the fraction of the volume flow entering the measurement chamber that is lost due to fluid compressibility and the direct fluid pressure experienced by the diaphragm and piezo sensor. The measurement chamber is a large diameter cavity relative to the channels and the flow speed inside it can realistically be neglected. For zero flow (and neglecting gravity) the pressure will be constant everywhere inside the measurement chamber on one side of the diaphragm. The effect of gravity is negligible since it cannot generate differential pressure. Hence the pressure applied to the pressure transducer approximates the chamber pressure. According to Newton's third law, the pressure fed back from the pressure transducer equals the pressure applied to the diaphragm in the steady state, hence it follows that the feedback pressure is a good approximation of the chamber pressure. Taking the feedback pressure directly from the feedback leg unfortunately results in an algebraic loop that has to be solved with Newton's method, and this severely hampers solver performance. For this reason, a chamber pressure block is included to output a value identical to the pressure fed back to the adder. For time-based simulation, the system is solved with a Runge-Kutta or Dormand-Prince fixed step differential equation solver. Variable step methods (like Bogacki-Shampine) may improve solver performance, but is less robust in complex simulations.

Discrete flow architecture

Another option for the modeling of flow interaction on pressure generation is to furnish each fluid column degree of freedom in the state-space model with its own flow model. This is similar to doing a time-marching CFD analysis with compressibility effects included. The only difference is that the finite element system is modeled in one dimension only and has vastly shorter calculation time.

The subsystems are all unified in this model's architecture. A schematic of this model is shown in figure 8.3 The chamber compressibility spring is a lumped stiffness from the diaphragm and chamber fluid compressibility. The fluid column is modeled the same as before except that each fluid element receives its own flow loss model in addition to the customary Coulomb damping. Figure 8.3 models the sensor up to the transducer stiffness. The only element to be added to complete the sensor model is the transducer's deflection-to-signal transfer function. For the discrete flow model to be implemented an ordinary differential equation of the flow loss is required and is not implemented in the simulation used for optimization.

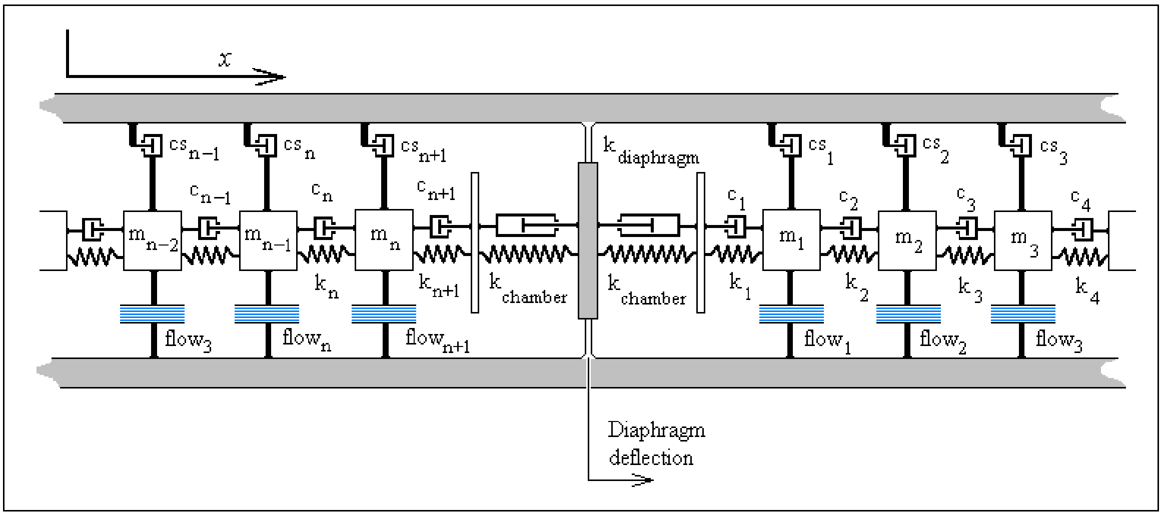

Figure 8.3: Unified model of sensor with finite element flow loss model.

8.3 Desired measurement system characteristics

The desired sensor characteristics is required in order for an optimization to commence because the MFCAA performance characteristics is at this stage an uncharted map of many variables. Having a general requirement narrows the number of methods of attack down significantly. The desired system performance is synonymous with the application, but the aim of a measurement system can be one of two classes according to Wright (1994):

1) Frequency reproducing measurement systems: This typically covers measurement systems that gather data for spectral density analyses. To reproduce the frequency content of a signal the system must have **a) a flat amplitude response** and **b) a linear Input/Output (IO) relationship.**

2) Wave shape reproducing measurement systems: To reproduce the waveshape is a more challenging task which adds a third requirement on the first two, namely that **the system must have a linear phase response.**

This totals three requirements of 1) flat magnitude response 2) IO linearity 3) linear phase response for a wave shape reproducing system. As a feedback sensor, the matter of IO linearity gains more priority but the other two can never fall by the wayside for any sensor.

These three characteristics are no mean feat to achieve. Even in fixed laboratory installations or pure electronic systems like amplifiers some compromises have to be made. Due to the varied types of transfer functions at work inside the MFCAA, the sensor has many idiosyncrasies and the three response requirements mean that an excellent match of all the sensor transfer functions has to be made. Simulation in a trial and error method to find this match will squander time, and the result will be dubious. The optimal solution has to be sought in a structured manner. The Optimization Toolbox ® by Matlab® is used to achieve this.

8.4 Sensor steady state characterization

In the design of the angular accelerometer, steady state characteristics of the sensor are obtainable without any simulation needed. Sensor scale factor, for example can be calculated without consideration of the dynamics of the system. In the case of the strain-gaged diaphragm, the sensor scale factor is easily found by taking all steady state gains of the system into account.

8.4.1 Strain-gaged diaphragm sensor scale factor

Multiplying all the steady state gains in figure 8.2 (via table 8.1) for the strain-gaged diaphragm sensor yields:

$$\chi_{str-gauge} = \frac{0.82\ V_{in}\rho\ h_{ang} R_0^2 \left(1-\nu^2\right)}{t^2 E_{dia}} \tag{8.1}$$

This shows the parameters influencing strain-gaged sensor's scale factor. As is almost always the case, equation 8.1 is a variable tradeoff. No variable can be adjusted to give greater scale factor without paying a price for it elsewhere in terms of dynamic performance or size of the sensor. The two variables h_{ang} and R_0 (the diaphragm outer diameter) have a mutually exclusive effect on another in equation 8.1. If h_{ang} is increased, R_0 has to decrease or the sensor will increase in size. Since most designs will have an upper limit for the sensor size, the mutual dependence of h_{ang} on R_0 for fixed sensor size is important. Optimum scale factor would be obtained where the product $h_{ang}R_0^2$ is maximized. Figure 8.4 relates this dependence if assumed that all sensor volume not assigned to the measurement chamber is utilized by the spiral and shows that as far as sensor scale factor is concerned, the chamber diameter should be 74% of the maximum spiral diameter. At this ratio the spiral efficiency is also very high, so the only possible justification to use another ratio would be dynamic performance. Of course, a larger chamber diameter as well as a longer spiral adversely affects sensor dynamic performance.

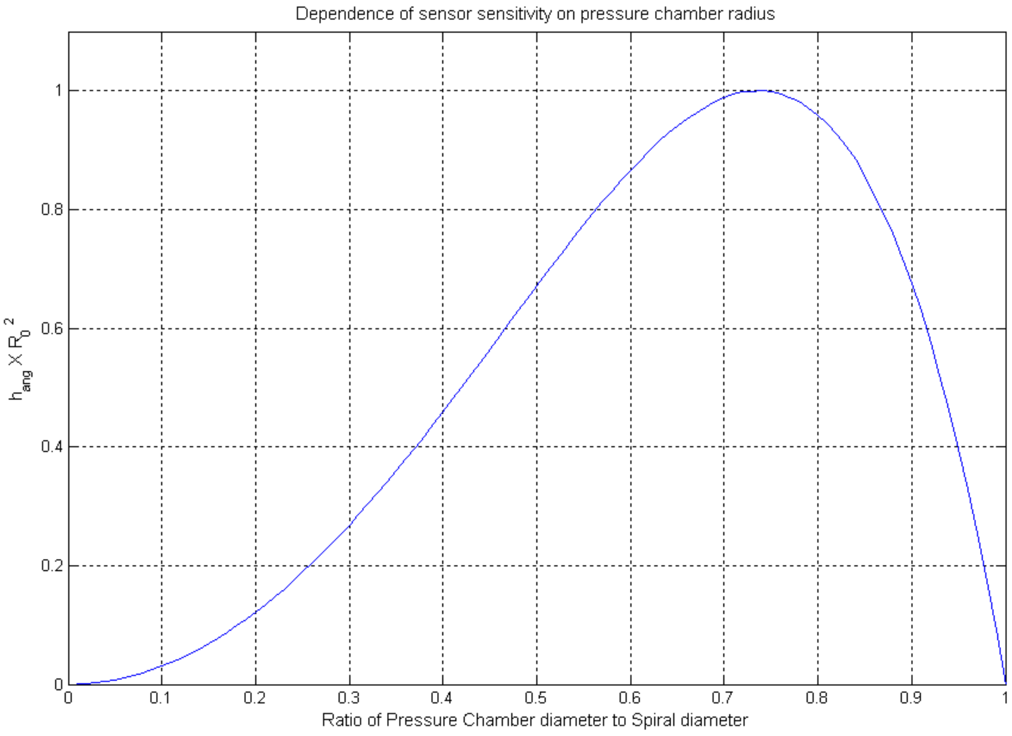

Figure 8.4: The effect of measurement chamber diameter on sensor scale factor.

The factor in equation 8.1 showing the influence of the channel pressure potential is h_{ang}. A plot of h_{ang} for channel widths below 500µm is shown in figure 8.5. For a fixed wafer annular area, the obtained pressure potential may also be described by equation 8.3.

$$h_{ang} = \frac{const}{b^2} \tag{8.2}$$

where b is the channel width. The increase in scale factor for smaller channel widths is clearly substantial.

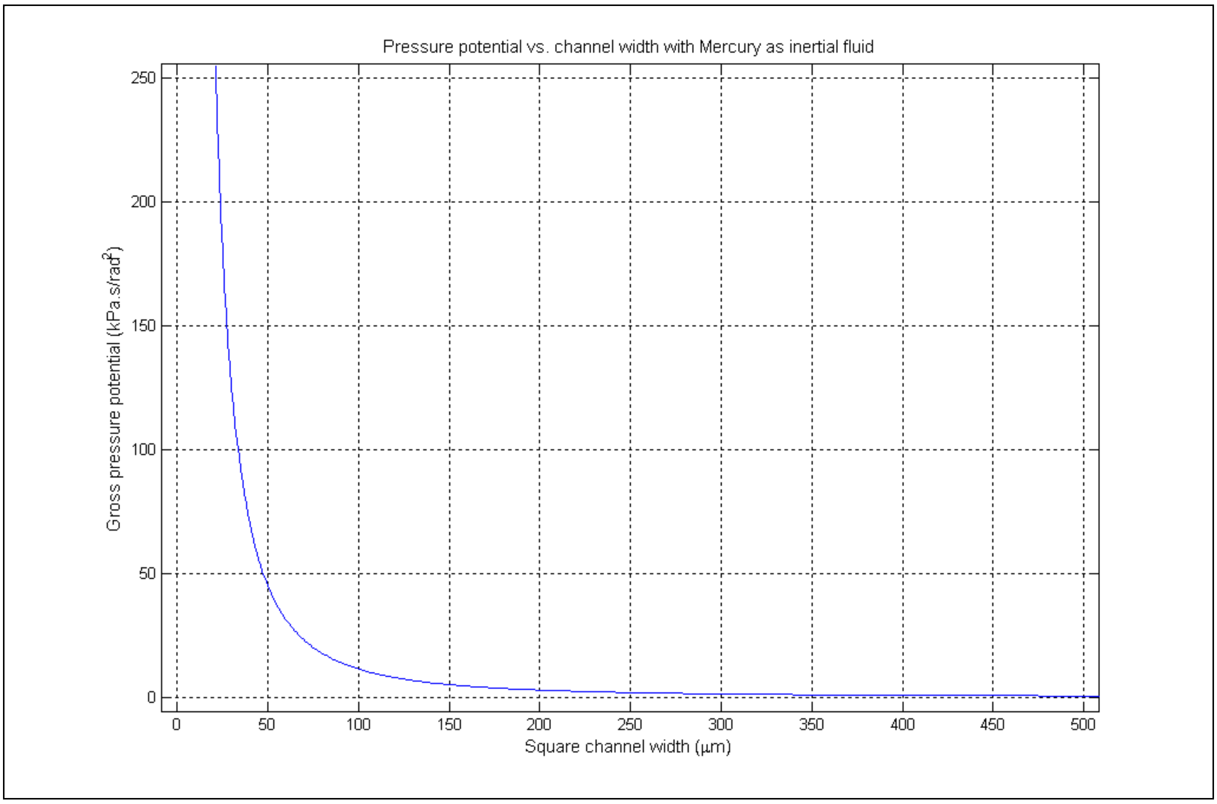

Figure 8.5: Gross steady state pressure generated for channels of square shape with widths smaller than 250 microns.

The relation displayed in figure 8.5 only realizes if the thickness of the wafers is adjusted to conform to the decreasing channel depth, and the number of wafers accordingly increased to construct a wafer stack of equal height. Differential pressures above 200kPa (at sea level) can only be linearly generated if boiling of the low-pressure fluid is prevented, by means of pre-pressurization.

Pressure in the region of two atmospheres seems ideal for measurement, even if a low accuracy pressure measurement technique is used. Unfortunately these are steady state pressures. The time required to fill the pressure transducer's volumetric deflection with a channel smaller than 100µm is not trivial. After taking the dynamics of the system into account, this rose-tinted picture may be expected to change. This is done in following sections.

8.4.2 Piezo sensor scale factor

The piezo-crystal sensor scale factor cannot be calculated by simply multiplying DC gains because a piezo-crystal has no DC response. Piezo scale factor is defined as peak output over peak input in the nominal scale factor range. The nominal scale factor range is above the *RC* cutoff point of the transducer and below the first resonance caused by the piezo-crystal's interaction with its support structure. The scale factor in the nominal piezo-crystal operating region is:

$$\chi_{piezo-nom} = \frac{\rho\ h_{ang}\ d_{piez} A_{\sup} E_{\sup}}{L_{\sup} C_{amp}} \left[\frac{0.51274 R_0^2}{\left(k_{pillar} + \frac{7.8214 \mathrm{E}_{\mathrm{dia}} t^3}{R_0^2 \left(1-\nu^2\right)} \right)} + \frac{A_{\sup}}{2\left(k_{pillar} + \frac{16\pi R_0^2 \mathrm{E}_{\mathrm{dia}} t^3}{3\left(1-\nu^2\right)} \right)} \right] \tag{8.3}$$

The first quotient in the block brackets represents the contribution of the annular differential pressure, while the second quotient in the block brackets represents the contribution of the pressure directly opposite the piezo sensor (as discussed in section 6.8.3). The nominal scale factor of the piezo transducer assumes that the appropriate frequency and magnitude effect is felt at the crystal and not only at the sensor input. This cannot be assumed lightly: the fluid column, channel flow and transducer stiffness all have dynamic effects on the input which now also have to be accounted for. This is the justification for a simulation to be written. The fact that a piezo-transducer has no steady state response forces the designer to account for all dynamic effects in order to obtain the true scale factor. The flat magnitude frequency band of the sensor magnitude response may not be the same as the flat magnitude response of the piezo crystal; the sensor as a whole is what matters. Printing the whole sensor transfer function on a page is unfortunately not feasible: just the fluid column transfer function alone for this simulation is a daunting Laplace rational function (depending on the number of DOFs included). Equation 8.3 is a suitable representation of the scale factor since it sets a 0dB baseline for normalization and relates all the important constants contributing toward the scale factor.

The scale factor dependence on chamber diameter does not hold quite as true for the piezo-based sensor because another R_0^2 is contained in the denominator. The contribution from the piezo support is also expressed by equation 8.3. The piezo film will in general be a very thin element, which causes it to be very stiff relative to its support. Where this is the case, the piezo film contribution to k_{pillar} will be negligible (see equation 6.45).

8.5 Sensor parameter assumptions

The sensor’s successful application depends on whether the pressure wave resulting from an angular acceleration disturbance can be damped out at the diaphragm. Characterization of the sensor is only sensible for such cases. Experiments done in polyurethane tubing has shown that considerable passive damping is present, proportional to the tube length, even in the absence of flow. For true control of the pressure wave damping, the sensor will have to be servoed. It comes as little surprise then that the current primary fluid-based angular accelerometer, the Fluid Rotor Angular Accelerometer (FRAA) patented by Statham (Hartzell, 1985) is also servoed, and that it is sensor damping that is controlled. The FRAA is still in use today. The damping problem in the MFCAA is more severe than the fluid rotor variant, because of the length of the fluid column, which might place significant resonances within the frequency of interest. The damping in a silicon-based channel will still be proportional to the fluid column length but probably smaller than that of the polyurethane tested in the experiment.

The following assumptions are made regarding the channels and wafer sensor's parameters:

1) The planform shape is assumed to be Archimedes’s spiral. For fine spirals, the other spiral types approach the characteristics of an Archimedes spiral. The simulation allows the use of any spiral mentioned in chapter 4.
2) The channel cross section is assumed to be square. This is in alignment with a shape that can be readily micromachined or microformed.

3) The depth of the channel is assumed to be two thirds of the wafer thickness.
4) The wafer stack height is 20mm with diameter also of 20mm. This places the MFCAA size in the same region as other MEMS sensors
5) The wafer stack annulus inside diameter is a variable input to the optimization. The stack outside diameter is 20mm.
6) A chamber of 14.8mm is used for the strain-gaged sensor, which in accordance with figure 8.4. This chamber diameter bypasses the value system and may not have desired dynamic performance. The choice of another diameter diaphragm also depends on the available gage size.
7) A measurement chamber as small as 1mm is allowed for the piezo based sensor. MEMS methods will therefore not only be employed in the fabrication of the channels, but also the transducer.
8) The fluid column contained in the channels is assumed to have at least 28 degrees of freedom. Less than 20 should be sufficient for most cases, and yet, processor performance is still satisfactory with a 55 DOF system. The challenge is that for long channels with high DOFs, the state-space system tends to become badly balanced. A routine ensuring the stability of the state space matrices are used to ascertain the maximum number of DOFs possible for a specific length channel. For long channeling this routine may bring the number of DOFs down to 23.
9) The working fluid is mercury.
10) For the optimization exercise a minimum shear damping of 10% of critical is used plus 1% per metre of channel length. No inter-mass damping is included. On further investigation of the nature of the damping inside silicon an improvement can be made on this damping assumption.
11) The piezo-crystal used in the transducer is a $100\mu m$ thick PZT5 (Lead Zirconate Titanate) with a piezoelectric charge constant of 374 pC/N in the d_{33} mode, 171 pC/N in the d_{31} mode and a Young's modulus of 85 GPa. High charge constant crystals (like Rochelle salt) may pose problems of poor tolerance to temperature or humidity.
12) The envisaged sensor is currently expected to be prototyped in silicon. Glass is also an option for the fabrication of microfluidic channels but with a Young's modulus of 48-83 GPa, it falls short of the stiffness of 168 GPa offered by polycrystalline silicon. Metal electroforming (using nickel) may reach in excess of 190 GPa.

8.6 Sensor dynamic characterization simulations

This section aims to describe the impact of the important trade-off variables on sensor dynamic performance. An optimum solution is not the objective here but rather a qualitative view on the most important sensor attributes.

8.6.1 Strain-gaged diaphragm dynamic characteristics

In chapter 6 the potential in polymers for use in diaphragms is mentioned as well as skepticism on strain-gage suitability for the sensor. Are the polymer diaphragms stiff enough though? A bode plot for a polymer diaphragm strain-gage is shown in figure 8.6.

The variables assumed here are:
Diaphragm thickness: 1.2mm (still using linear thin plate theory)
Diaphragm diameter: 14.8mm – not much smaller is feasible, due to the area required by a commercially available strain-gage.
Strain-gage resistance: 350Ω

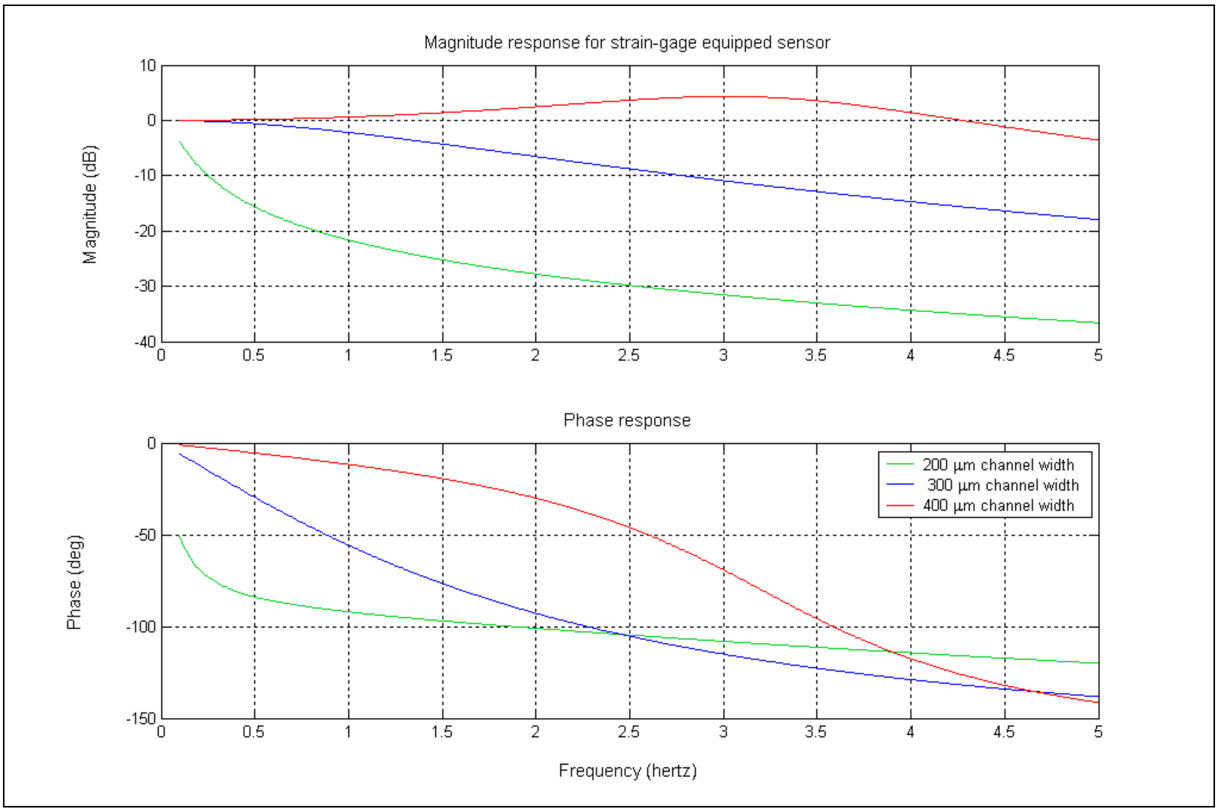

Figure 8.6: Bode plot for strain-gage equipped sensor with a thick polymer diaphragm.

The DC response is a big advantage of the strain-gage sensor, but the bandwidths attained are not of much use in many known applications. Bandwidths are low even with the large channel widths used. The problem is that the large volumetric diaphragm deflection takes too long to fill by the channel flow. This low performance is probably a disqualifier of the concept in the short term. More sensitive strain-gages like the piezo-resistive varieties are of course candidates to solve the problem. These gages again have their own drawbacks of which the greatest is poor temperature stability.

The optimization and characterization is continued only for the piezo-crystal. The possibility of using a strain-gage may be revisited if a smaller diameter transducer can be constructed or if higher scale factor gage is available. The plain circular diaphragm theory can also be used to investigate other transducer concepts further.

8.6.2 Piezo-based dynamic sensor characteristics

The piezo-based sensor offers greater promise than the strain-gaged sensor for performance in both scale factor and bandwidth. The piezo pressure sensor can be miniaturized into a very stiff transducer that leaves space for larger channels and so reach both higher scale factor and better dynamic performance. Most pressure transducer parameters were selected in chapter 6. The only parameter still to be selected is the diaphragm diameter. This parameter has large impact on all aspects of sensor performance because a smaller transducer possesses greater stiffness, but transmits smaller forces to the piezo-crystal. Miniaturization of the piezo-crystal poses an important challenge for the fulfillment of the potential of the MFCAA.

The parameters of diaphragm diameter (or transducer diameter), channel width and diaphragm thickness are the parameters that need to be selected in a trade-off exercise. In cases where the pressure transducer becomes very small and all other available space is used for the channel helix, the channel inside diameter will be at low efficiency radii. In this case the objective of maximum flow potential might make the helix inside diameter another variable to be optimized since it would no longer necessarily coincide with the diaphragm outer diameter.

All other parameters are directly dependent on these three parameters or are separately selectable, which are:

1) **Sensor size:** Constrained by available space in the envisaged application, this has large impact on sensor performance.
2) **Piezo support parameters**: These are mainly dependent on the measurement chamber diameter, except for the support length, which is always as short as manufacturable to attain stiffness.
3) **Piezo-film**: Due to its low thickness, the piezo material is selected for its charge generation properties more than stiffness or another criterion.
4) **Charge amplifier parameters:** The feedback capacitance is minimised for scale factor, while the resistance is maximised to achieve reasonable lower cut-off. Extreme resistance values, like the ones preferred here has a noise implication that must be managed by shielding of the feedback resistance, as well as filtering.

Before the sensor is optimised, the effect of the main trade-off variables is illustrated. The effect channel size has on all performance aspects of the sensor is key to its design. To promote illustration and understanding, the other variables in the study are assumed to be the following constants.

- The diaphragm diameter is set at 4mm, which equals the channel helix inside diameter.
- Diaphragm thickness is fixed at 500μm.

As may be expected, a smaller channel has a constricting effect on the sensor. The most pronounced result of varying channel widths is the sensor's bandwidth and damping. The plot in figure 8.7 was made for relatively large channels, which makes the piezo-crystal's nominal scale factor more apparent above the piezo cut-off frequency of 3Hz. The immense damping-effect that small channel width has on the sensor is also clear from figure 8.7. In large enough channels, the system has an oscillatory nature. The absence of DC response is evident since all the step responses decay to zero (not shown).

The effect of the piezo crystal's decaying output is made obvious by a low charge amplifier feedback resistance (of 10GΩ). The effect can be seen on the magnitude response as a fading low frequency output and on the phase plot as an apparent lead at low frequency. The remedy for both these phenomena is a large charge amplifier time constant (i.e. product R_f C_f).

The capacitance also has scale factor impact and is included into the trade-off. The resistance on the other hand is generally made as large as practicable, because the capacitance needs to be kept low for the sake of scale factor (which is not influenced by resistance). A prime motivation for the design of extremely high resistors is in fact the use of the piezoelectric transducer. In recent years processes have been developed (see Schweber 2001) that can produce resistors of 10TΩ (10×10^{12} Ω). In following optimization calculations a resistance value of 1TΩ is assumed. When a capacitance of 0.5pF is combined with this resistor, a cut-off frequency of 318mHz results. Lower cut-off frequencies are feasible by using larger capacitance at the expense of scale factor. The loss of DC response is therefore not a disqualifier of the piezo-electric transducer even if a low frequency design is envisaged.

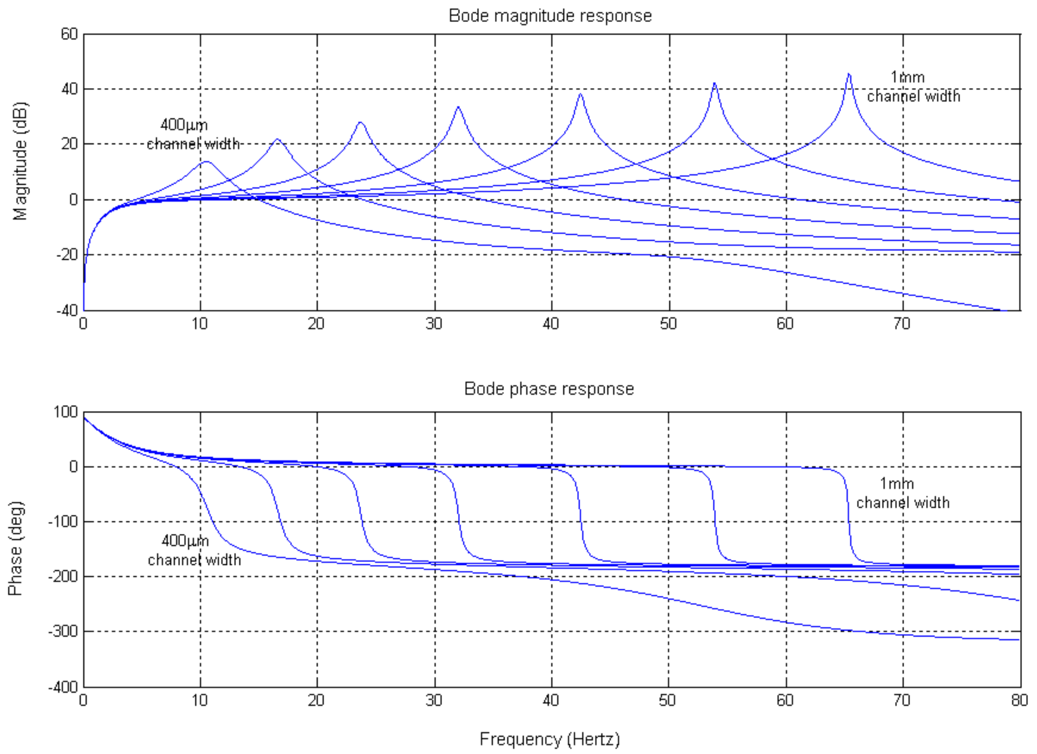

Figure 8.7: Bode plot showing the effect of increasing channel width from 400μm to 1mm in equal increments. Higher bandwidths correspond to larger channel width.

The response beyond the piezo lower cut-off and below the first resonance resembles a second order system closely. The fluid column resonances may be expected to make their appearance at higher frequencies, but it seems that the system could be approximated by a second order system, in the frequency range of interest at least. This is unfortunately not so. Figure 8.8 shows a plot with the same parameters except that the diaphragm diameter is halved to 2mm. The response now exhibits a damped resonance before the main resonance. The large impact that the smaller diaphragm has on the bandwidth is clear, the resonance frequencies have increased more than ten times while the diaphragm diameter has only halved. The transducer stiffness increases sharply when the diaphragm diameter is decreased.

The one and only resonance in figure 8.7 is a flow/diaphragm interaction mode, as is the second resonance in figure 8.8. This flow resonance frequency has increased in figure 8.8 (because of the smaller diaphragm) to lie beyond the first fluid column resonance, which forms the first peak of the figure 8.8 responses. The clearest indication of the flow resonance is the 180° phase drop at this frequency. This phase drop also applies for the flow resonance of figure 8.8 except that the proximity of the fluid column modes superimposes a waved phase response on the phase drop. The fluid column resonant frequencies cause ever-decreasing magnitude and phase fluctuations as frequency increases.

Figure 8.9 shows a bode plot on logarithmic axes with a 2mm diaphragm diameter that is 500μm thick. The 400-700μm plots are identical to those of figure 8.7. The log scale gives a more complete view of the Bode magnitude response. The response starts off with a 20dB per decade slope caused by the contribution of the piezo transducer. The response then reaches its apex with the flow response resonance and drops down before the fluid column resonances start. Only 45 of the infinite number of fluid column resonances are shown in figure 8.9. In a true plot the resonances would be visible all along the –80db per decade slope in ever-decreasing magnitudes. Each of the 45 resonances each represent one DOF, hence the discrete model contains 44 masses in the fluid column model. The other DOF is the housing. The damping effect of decreasing channel width is clearly illustrated. At 100μm the large damping eliminates any sign of resonance. The position of the flow resonance depends mainly on the diaphragm stiffness and fluid column cross-section area. The first fluid column resonance position depends on the wave speed in the working fluid and the length of the fluid column. In a sensor with a long enough channel, the cascade of fluid column resonances may start at lower frequencies than the flow resonance (as in the case in figure 8.8).

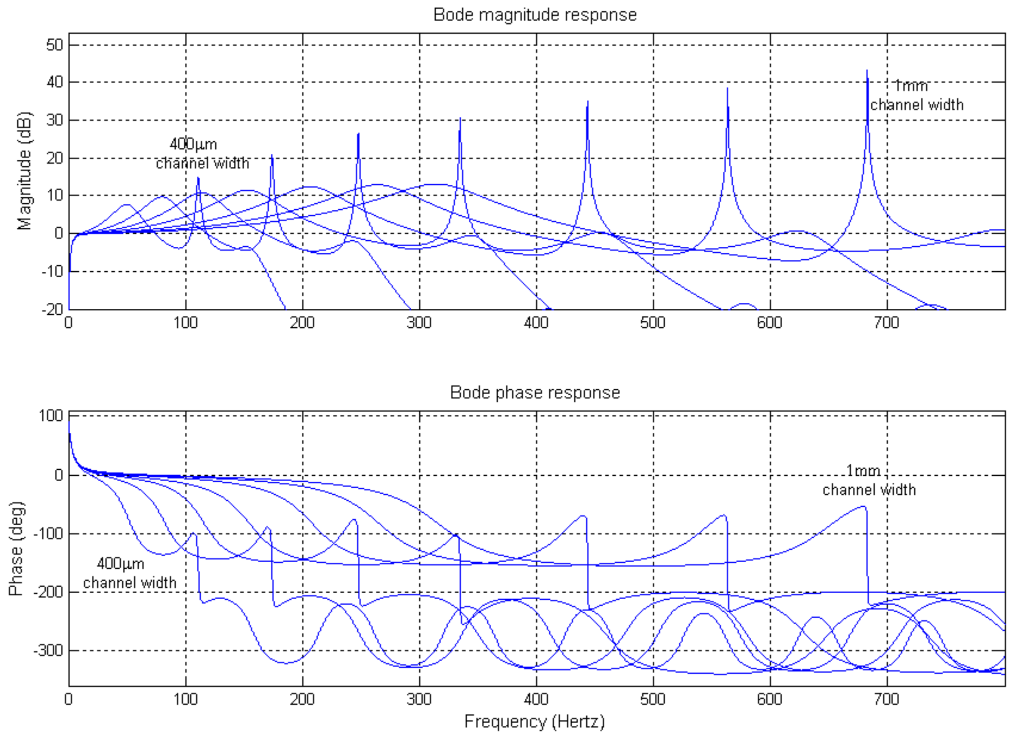

Figure 8.8: Bode plot showing the effect of increasing channel width from 400μm to 1mm in equal increments with a 2mm diaphragm.

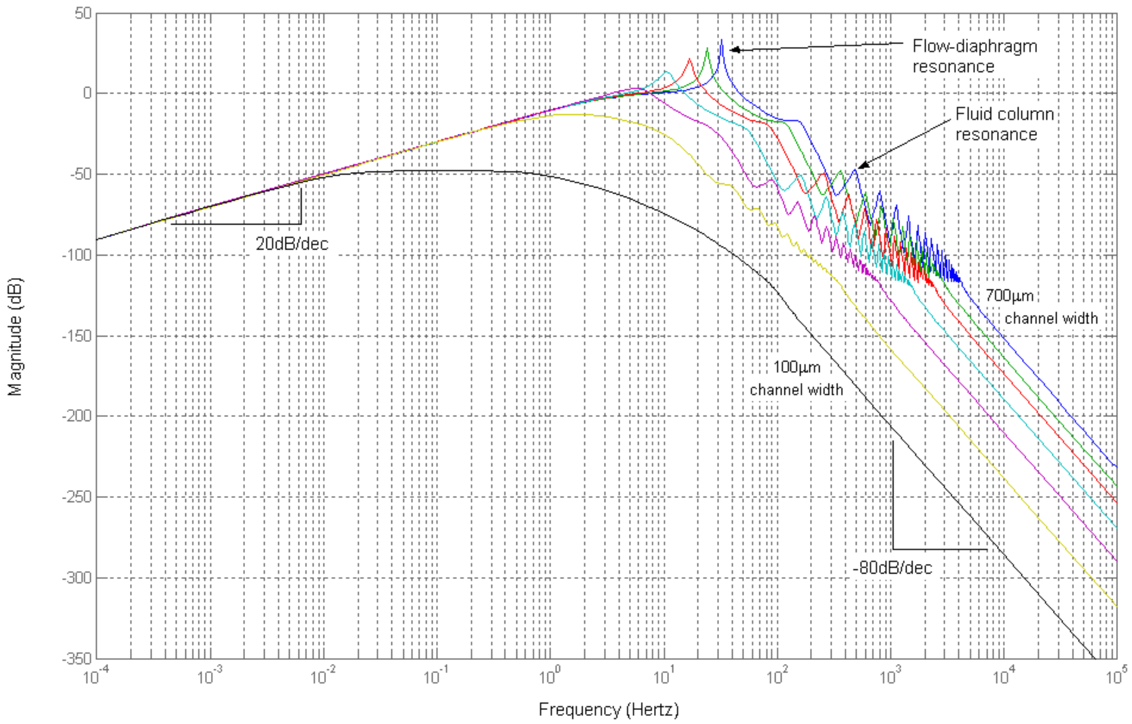

Figure 8.9: Bode plot showing the effect of increasing channel width from 100μm to 700μm in equal increments.

8.7 Sensor optimization

Preceding sections in this chapter serve to give the designer an illustration of the effect of adjusting sensor parameters within critical areas. To the objective of optimizing the sensor this is unfortunately of limited value. The interdependency of all the adjusted parameters is covered to a very limited extent by making a constant assumption for all parameters besides the one being adjusted. A true representation of the effect of changing all adjustable parameters is so multidimensional that it far surpasses the capabilities of visualization on a single illustration. This necessitates the use of an optimization algorithm to systematically seek out an optimum solution within the boundaries set for the sensor parameters.

Put in a more general way, optimization is the process of seeking of a set of system governing parameters,

$$x = [x_1 \quad x_2 \quad x_3 \ \ldots\ldots\ldots\ldots\ldots \ x_n]$$

which is in some way perceived to be optimal. The perception of the optimal solution is entirely according to the preference of the designer and his/her set of set of priorities (or value system). A simple representation of this set of priorities is a cost function, which is:

$$\text{Cost} = [w_1 y_1^{p1} + w_2 y_2^{p2} + w_3 y_3^{p3} \ \ldots\ldots\ldots\ldots\ldots\ldots \ w_n y_n^{pn}]$$

with w the weight assigned to each system output y. The power p of each output is positive to signify proportionality and negative for inverse proportionality. The powers may be any real number but the weights are only positive real numbers. The objective of the optimization algorithm is to find the parameters $\mathbf{x}$ that minimize the cost function. A system may have any number of outputs. The selection of important outputs is also the onus of the designer.

For the sensor, the following outputs were selected for entering into the cost function:

1) **Sensor scale factor**: The ability to reach high scale factor is one envisaged advantage of the MFCAA.
2) **Step input overshoot**: A common step input criterion, which is mostly dependent on damping.
3) **Step response speed**: For step responses, the 90% rise time is often used as a measure of the system step response speed.
4) **Steady state error after one second**: For sensors with very low bandwidth the sensor may not even reach steady state after one second. The response after one second is taken as steady state regardless of whether steady state has been reached or not because a sensor of such slow response will not qualify for use in any event.
5) **Bode magnitude resonance peak**: A consequence of the second order response contributed by flow interaction with the diaphragm. This peak is independent of those caused by the fluid column. A resonance peak inside the used frequency range of below 1dB may be satisfactory, but as small as possible is preferable.
6) **Bode magnitude –3dB bandwidth**: The standard measure of sensor bandwidth.
7) **Magnitude at half of –3dB bandwidth**: A measure of the flatness of the magnitude response. For a purely second order system this would be redundant but the MFCAA sometimes exhibits a drop in magnitude before rising for the resonant peak. An example of this is shown in figure 8.8.
8) **Bode phase -90° bandwidth**: Phase bandwidth is a variable commonly neglected in favor of magnitude bandwidth.
9) **Phase at half of -90° bandwidth**: A measure of the flatness of the phase response.

These criteria are portrayed in figure 8.10. The main difference between the strain-gaged diaphragm and the piezo-electric sensor is also shown. This difference is much less noted (and even negligible) for sufficiently high charge amplifier feedback resistances. Selected criteria are used in the cost function and a designer-selected weight is applied to each. This simplifies the objective function (entire sensor simulation) to output a single variable, namely the “cost”. The objective function output is now minimized by the optimization routine to find an optimum result.

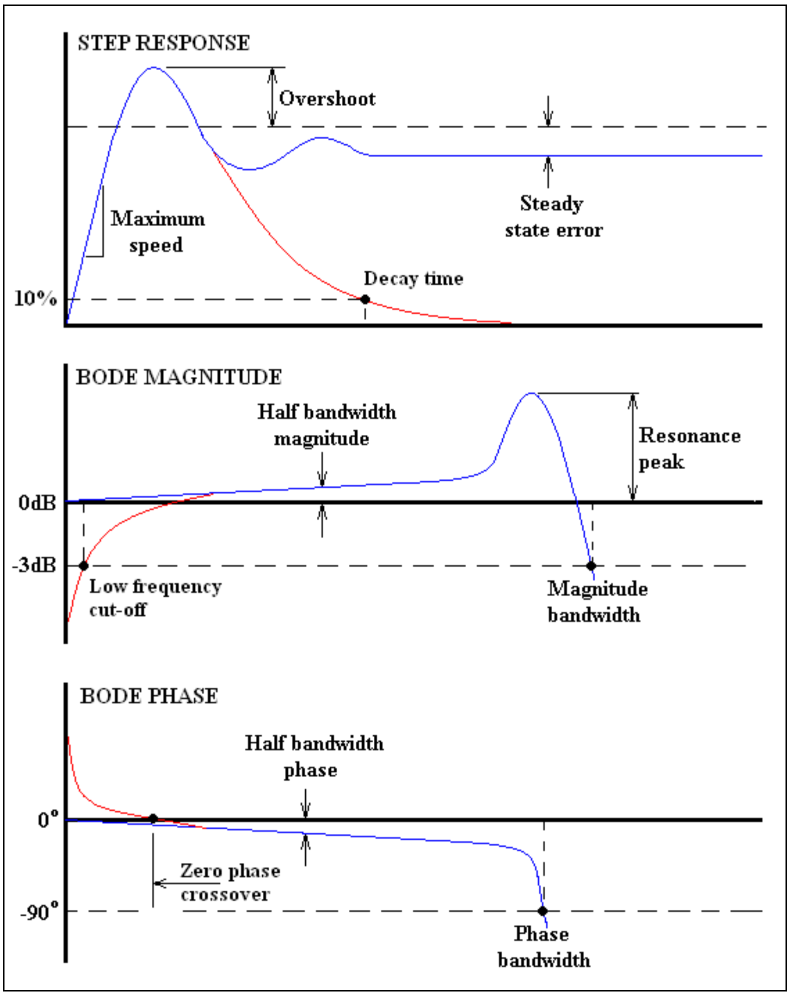

Figure 8.10: Typical performance criteria for a sensor. Blue denotes sensors with DC response and red for sensors without DC response.

The optimization routine starts from user-selected initial conditions and converges to a solution if it exists. The routine used here is the Kuhn-Tucker line search method. Figure 8.11 shows a schematic of the method followed to optimize the sensor with the use of a cost-function and the Kuhn-Tucker line search method. All optimization runs completed have the nominal sensor scale factor printed on the Bode diagram. The scale factor is referred from the zero dB level and is based on the piezo-crystal nominal scale factor. The printed scale factor is only illustrative of what scale factor is attained at the quoted charge amplifier feedback capacitance and resistance. The sensor resolution is still very dependent on the noise floor caused by various internal and external sources. The trade-off of the charge amplifier variables versus noise is still to be performed as part of the detail electronic design. Noise is though not beyond a significant measure of control and is also addressed by other passive measures like screening and filtering during the design.

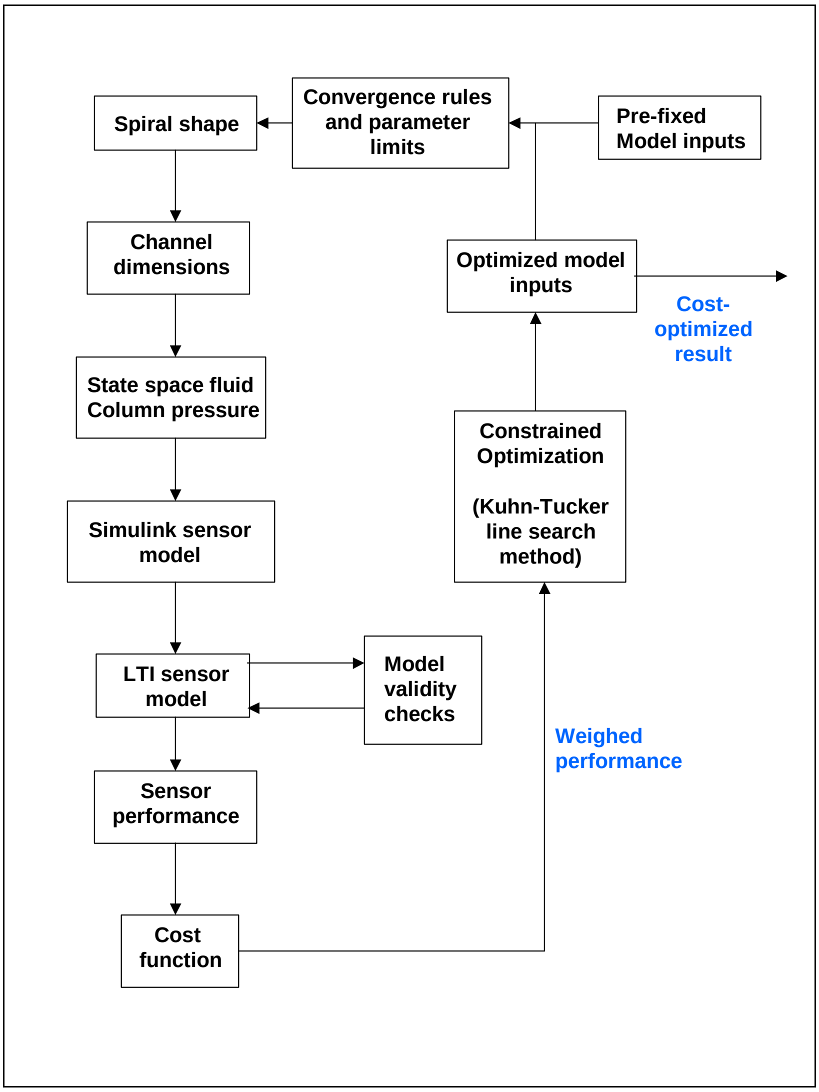

Figure 8.11: Schematic of optimization method.

8.7.1 Optimization constraints

The optimization inputs have to be constrained because all the simulation inputs represent real characteristics and as such are always a positive real numbers with an upper and lower bound. This complicates the optimization method somewhat because the routine requires a sufficient margin within to calculate a finite difference approximation of a derivative. The bounds therefore have to be widened somewhat for the sake of the routine, and results have to be checked for feasibility. The optimization was commenced for a sensor outside diameter and sensor height fixed at 20mm unless mentioned otherwise. Other limits as noted in table 8.2 were also imposed on the optimization routine.

The sensor simulation results in an elaborate function with many minima when a cost function is applied. These multiple minima degrade the quality of the optimization result because the routine tends to find only a local minimum and not the global minimum inside the optimization constraints. Various initial conditions therefore have to be tested to ascertain the quality of a result. Using an optimization routine exclusively for a design like this removes designer authority. Some fine-tuning of a response is therefore usually done around the obtained "optimum" result when a promising response is found.

Table 8.2: Constraints of optimization exercise

OPTIMIZATION CONSTRAINTS	Lower bound	Upper bound
Charge amp feedback capacitance	0.5 pF	100 μF
Channel width	50 μm	1 mm
Diaphragm thickness	50 μm	1 mm
Diaphragm diameter	1mm	9mm

8.7.2 High bandwidth application results

The bulk of inertial applications require a bandwidth up to approximately 50 Hz. For missile applications this requirement can reach 100Hz. Current MEMS vibrating structure gyroscopes perform in the 50Hz region. The design in this section aims to reach 50Hz bandwidth with the best possible scale factor and frequency shape. Figures 8.12 to 8.14 use a 0.5pF feedback capacitance and 1TΩ resistance, which results in a 0.318Hz cut-off.

This can be approached in two ways regarding the response shape. Figure 8.12 and 8.13 illustrates the two options. Figure 8.12 shows a response that increases monotonically inside the usable frequency range. The sensor usable frequency range is defined as the frequencies where the output of a harmonically excited sensor stays within 29% of the input. This is approximately between +2.2dB and –3dB. These limits are marked off on figure 8.13 and 8.15. By this definition, the bandwidth attained in figure 8.12 is 52Hz and in figure 8.13 it is 30Hz. The scale factor attained in figure 8.13 is far superior to that of figure 8.12, but the response is of lower quality almost reaching 2dB at 12Hz.

The phase response is also of higher quality in figure 8.12 showing barely any lag (5°) at 50 Hz, whereas considerable lag of 200° applies in figure 8.13 at the bandwidth frequency. The use of a frequency range where the flow resonance is the lowest frequency peak is therefore preferable unless in cases where scale factor is of utmost importance. One way of improving the frequency response of figure 8.13 is by means of feedback inside the sensor to improve the response. The $1\mu V/\sqrt{Hz}$ reference resolution is $6\mu rad/s^2$ for figure 18.12, which equals $3.44\text{x}10^{-4}\ ^\circ/s^2$. With a scale factor of $1178mVs^2/rad$, a noise level of $118\mu V$ can be tolerated to rival the 10^{-4} rad/s^2 accuracy of current angular accelerometers.

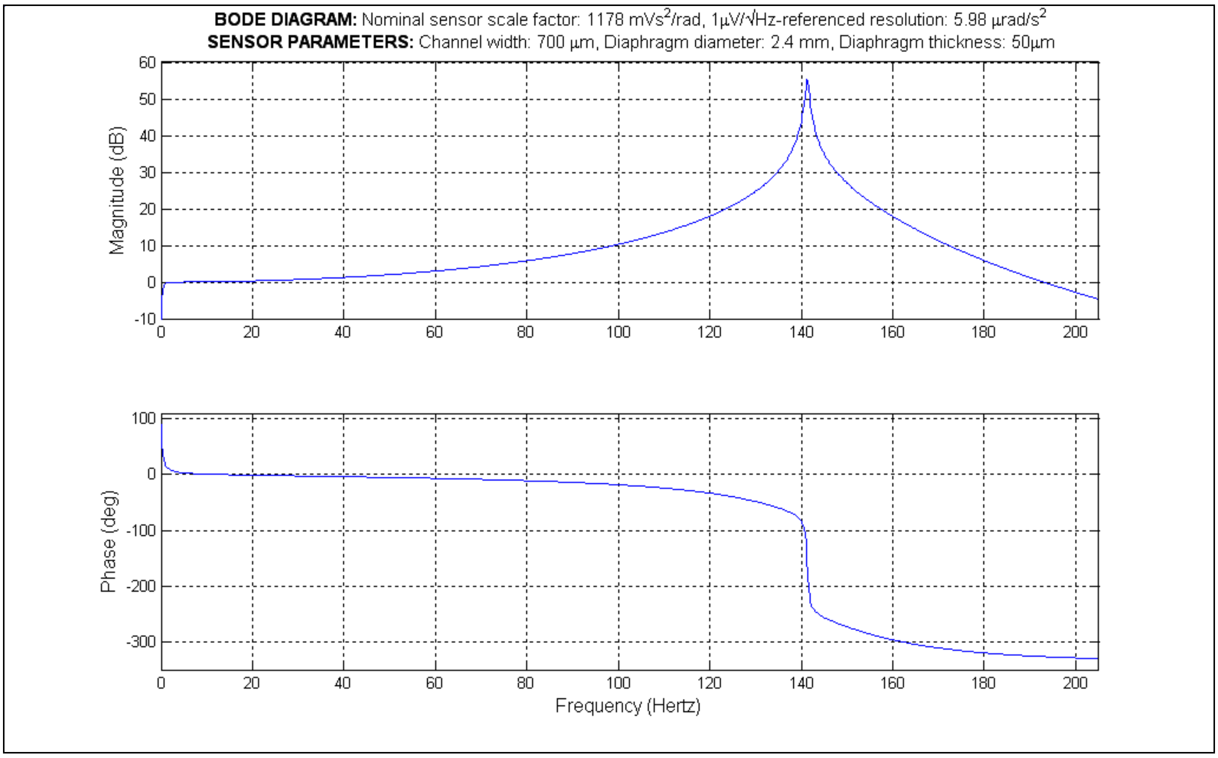

Figure 8.12: A monotone response design inside the usable frequency range for a 20∅ x 20mm sensor.

The effect of sensor diameter on sensor performance is expected to be large, but how large? Figure 8.14 shows a sensor also designed to measure up to 50Hz (like in figure 8.12) but the sensor diameter has been doubled to 40mm. The frequency response is seen to be almost identical to figure 8.12 up to 50Hz, while the scale factor has tripled to 3.5Vs²/rad. By also doubling the sensor height the scale factor can be quadrupled. The effect of sensor height is therefore not as dramatic as sensor diameter.

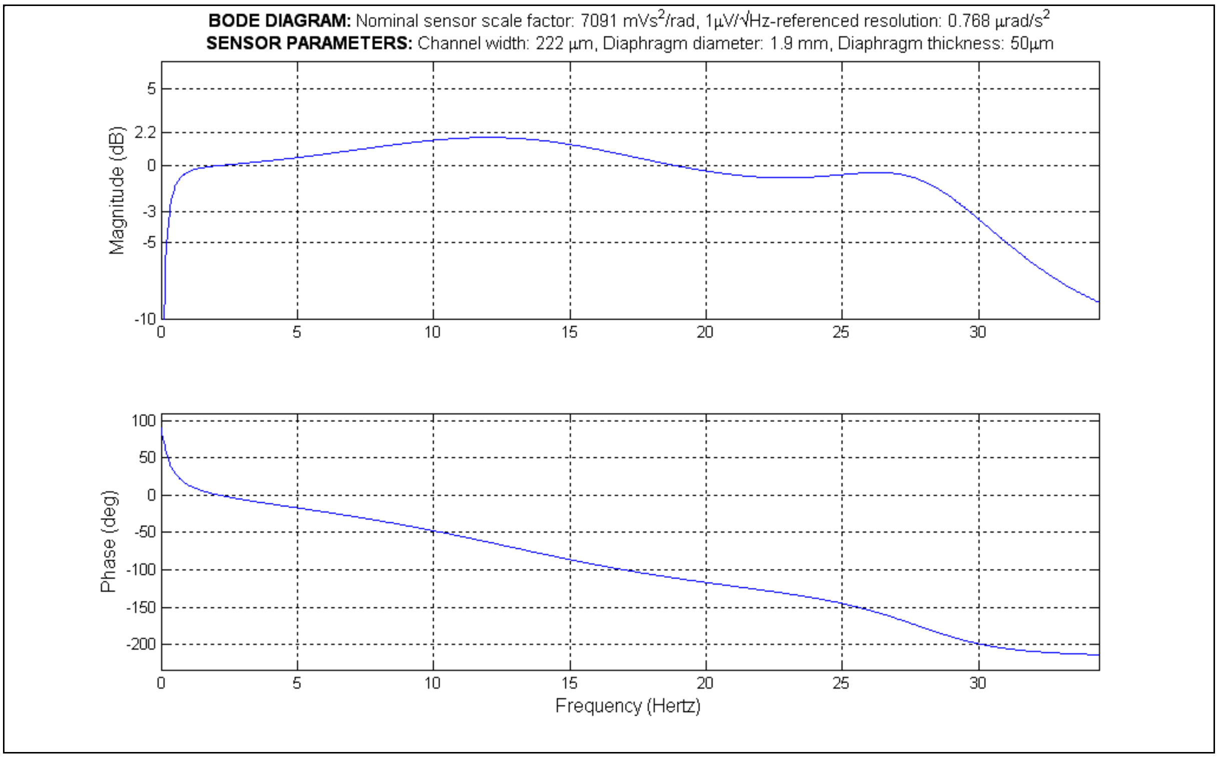

Figure 8.13: Design across the first two resonances for a 20∅ x 20mm sensor. The +2.2 dB and –3dB ticks represent the magnitude bandwidth limits.

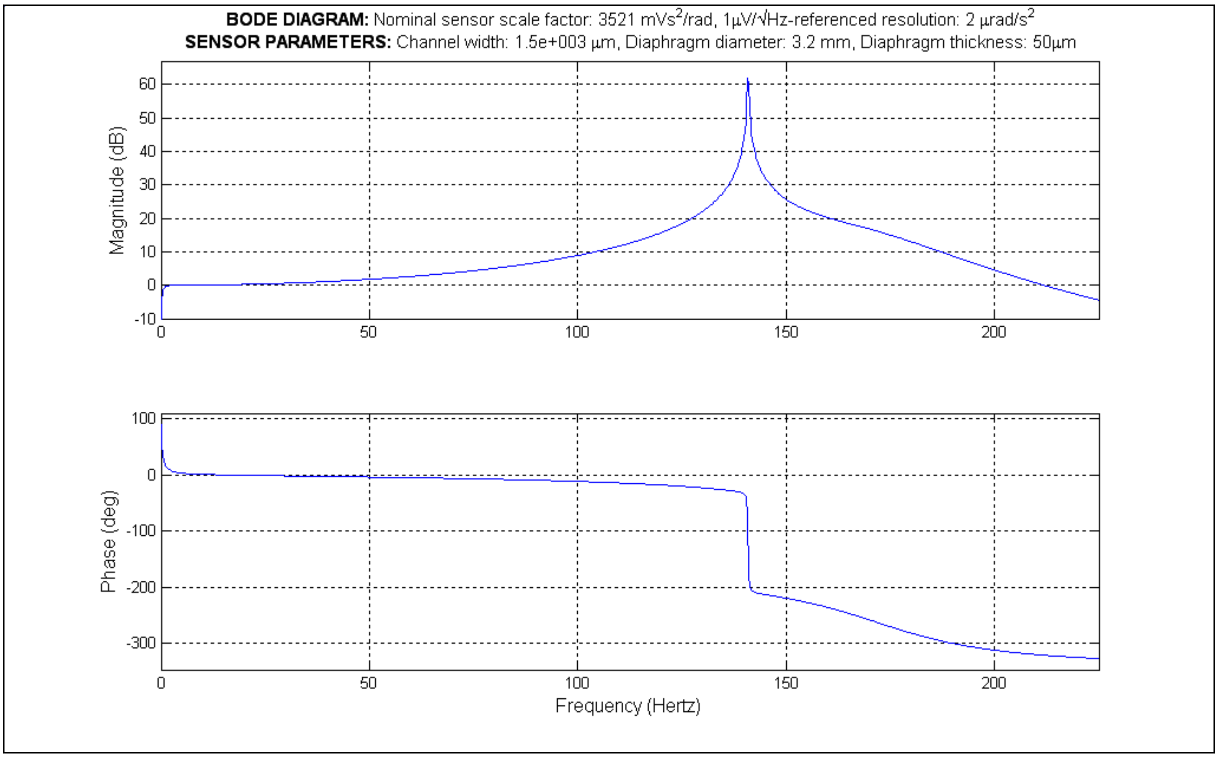

Figure 8.14: Response of 40∅ x 20mm sensor, designed for a bandwidth of 50Hz.

8.7.3 Low bandwidth application results

Low frequency applications exist mainly in the satellite industry. Telescopes and gradiometers make angular acceleration measurements in the region of 1Hz. The main limitation in using a piezo-based sensor for low frequencies is the cutoff frequency. A large feedback resistance and capacitance helps a lot to decrease the cutoff but a large capacitance decreases the sensor scale factor (see equation 8.2). A low frequency design leaves room for finer channeling and a larger diaphragm to attain scale factor but puts pressure on the capacitance to be increased, which again decreases scale factor. Higher resistance would solve the problem partially, but at 1TΩ the limit of achievable resistance is quite close. These limitations have the effect that low frequency designs do not excel quite as well as expected at high scale factor. Of course, the same capacitance used for a high bandwidth design can be inserted into a low-bandwidth design, but this causes proportionally large loss of the useful sensor frequency range. In the following simulation, the feedback capacitance is increased to 5pF, which decreases the cutoff frequency to 0.03Hz.

An example of a low-bandwidth design is shown in figure 8.15. This design again uses a 20∅ x 20mm size sensor. Although the bandwidth is only 10Hz, the quality of response is high with a peak of only 0.66dB. The phase response also exhibits good linearity. A high resolution even better than that of figure 8.14 is obtained, even though the scale factor has less than halved. This is due to the bandwidth of the sensor that has reduced. A smaller frequency of interest lowers the rms noise level and allows higher resolution.

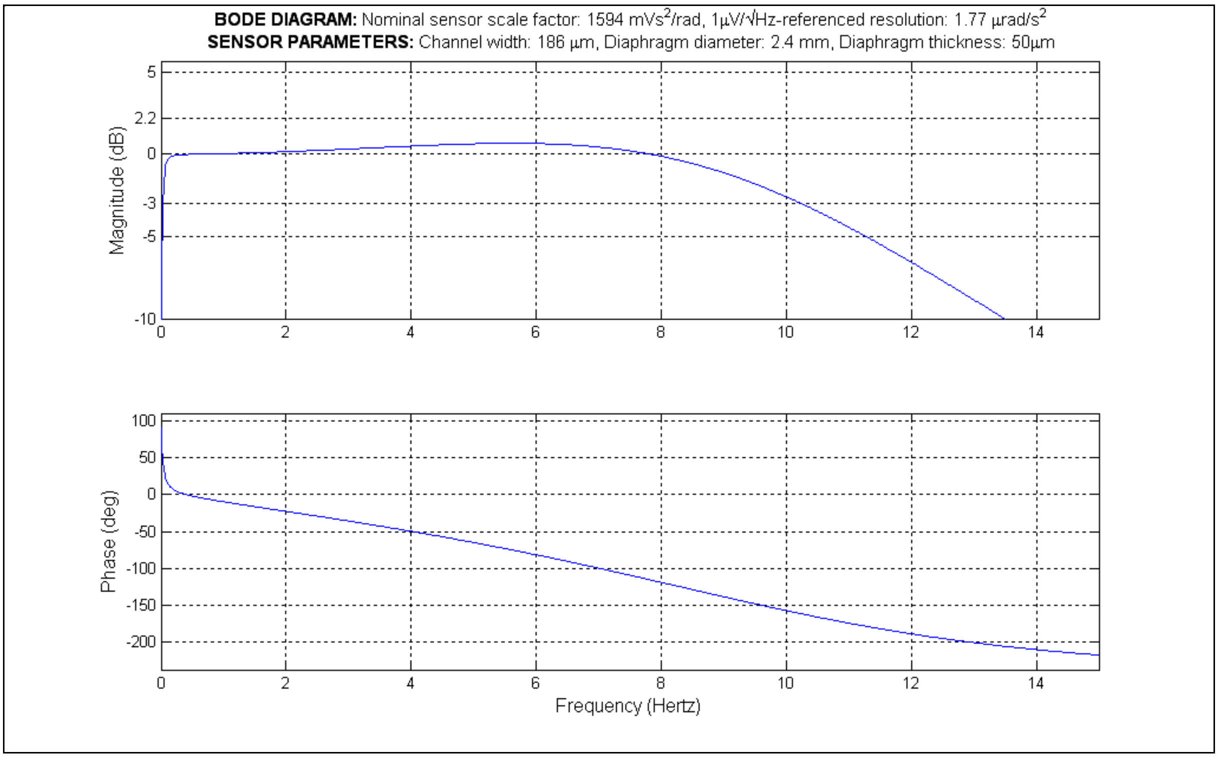

Figure 8.15: Low frequency sensor design using 5pF charge amplifier feedback capacitance with a 20∅ x 20mm sensor. The +2.2 dB and –3dB ticks represent the bandwidth limits.

Chapter 9

Conclusions

Theory has been developed for the design and simulation of the microfluidic channel angular accelerometer. The proposed sensor consists of a central differential pressure transducer fed by a channel system in the shape of a spiral-helix. The sensor's objective is to have superior angular acceleration scale factor in one sensitive axis with good cross-axis rejection capabilities.

The natural phenomena relevant to the functioning of the sensor are:

1) Pressure generated by the angular acceleration due to inertia of the working fluid: A discrete multi degree of freedom model is used in a state-space formulation to simulate pressure generation and propagation. The model is stiffness-corrected to have similar wave propagation characteristics to a real fluid column. The number of masses in the model is limited by computational power and matrix stability during eigenvalue calculation. Stability is improved by diagonalization of characteristic matrices and the number of DOFs is continually set to the maximum by monitoring matrices for stability in all simulations performed. The minimum number of modes included in the model is sufficient for simulation past the most optimistic range of operation for the sensor.
2) Flow inside the sensor channels caused by deflection of the pressure transducer: A first order transfer function is fitted on analytical unsteady flow theory. The transfer function is general to any size channel with large bending radii and accepts arbitrary pressure input. The transfer function is a good (though not exact) fit of the Newtonian laminar incompressible flow found inside the channels, and is customizable according to degree of flow development that is required. Since the sensor is expected to operate in a generally underdeveloped state of flow, the transfer function is fitted to the lowest Fourier number amenable to a first order response.
3) Deflection of the pressure transducer: A strain-gage based transducer and piezo-based transducer has been studied. The strain-gage pressure transducer uses a pressure rosette strain-gage bonded to a plain circular diaphragm. The strain gauge transducer does not show much promise for application inside the sensor. The main reason for this is the high volumetric deflection necessary for its use and the associated loss in sensor bandwidth. A piezo-based pressure transducer has greater potential. The piezo-based pressure transducer's diaphragm is modeled as a combination of an annular diaphragm fixed on all edges and a fixed outer-edge annular diaphragm that is guided on the inside edge, depending on the piezo support stiffness. The piezo crystal is modeled with a charge amplifier providing sensor output. Charge amplifier noise is not modeled directly, but sensor output is referenced against expected noise levels for sensor resolution approximation.

Various channel shapes have been studied to advance manufacturability of the sensor channels. The effect of the different channel schemes has been found to be minimal for channels of expected dimensional ratios.

Experimental verification was successfully performed on the pressure generation and propagation model by using a 200mm spool wound with 3mm fluid-filled polyurethane tubing. Tube lengths of 20m and 1.5m were evaluated with diesel and water as inertial fluids. The experiment also confirmed the high cross-axis rejection of the MFCAA and highlighted the risk and effect of free air inside the fluid column.

The theory was synthesized into a simulation of the entire sensor, which comprises of cascaded models of the various systems inside the sensor. Channel flow area and diaphragm diameter was shown the most important variables in the sensor's mechanical design both in terms of scale factor and bandwidth. The sensor contains one resonance associated with flow –diaphragm interaction. The frequency of this resonance depends mainly on the ratio of flow area to diaphragm area. Other resonances in the sensor are caused by the various fluid column modes; their frequencies depend mainly on the wave speed in the fluid and the fluid column length. A Kuhn-Tucker optimization routine was performed on the design variable, which pointed out feasible domains in the design variables. Multiple minima in the cost function of the sensor hampered the search of an absolute optimum in the design variables, but by doing various resetting of the initial conditions, satisfactory designs were found.

From the simulations done, the MFCAA shows potential to be a novel single-axis, solid-state angular accelerometer in the MEMS scale. The sensor should improve considerably on current MEMS technology in the area of scale factor and stability and fill a performance gap that currently exists in miniature angular accelerometry. The simulated achievable sensor scale factor is very high even in high bandwidth designs. For a 50Hz sensor (which is a common industry requirement) a scale factor of 1178 $\mathrm{mVs}^2/\mathrm{rad}$ is simulated as feasible if a low noise charge amplifier can be constructed with 0.5pF feedback capacitance and 1TΩ feedback resistance (resulting in a 0.318Hz low frequency cut-off). This claim can though only be verified by a prototype. Scale factor can be further improved by tuning of the resonances to fall within the bandwidth of the sensor for a frequency response quality compromise. The sensor offers a great size advantage on current non-MEMS high-accuracy angular accelerometers, being comparable to contemporary MEMS gyroscope designs. The channels used for a 20ΦX20 sensor is not extraordinarily small and should be readily micromachinable. The main miniaturization challenge expected is the pressure transducer with a diameter of as low as 1.8 mm.

The sensor offers the following advantages:

1) High angular acceleration scale factor and resolution.
2) Low cross-coupled sensitivity.
3) Low angular velocity sensitivity.
4) Small size and mass. Dimensions in the range of the British Aerospace Systems SiRRS rate gyro is expected. This compares favorably with other angular devices.
5) Very high reliability.
6) High shock resistance.
7) The expected MEMS features are quite large by 2005 standards and should be easy to micromachine. The aspect ratio of the channels is also low, which should simplify the manufacturing process. Laser ablation should be the most viable option for rapid prototyping of the sensor channels.
8) The sensor design is versatile and can be applied to a wide range of frequency applications.

and the following drawbacks:

1) Approximately 20 to 80 wafers may be used in the construction of the microfluidic channel system depending on the diameter of the diaphragm. This compounds the cost, and decreases the mass-manufacturability somewhat. This contrasts with the advantages gained by contemporary MEMS products.
2) Miniaturization of the sensor size has a noted negative effect on the scale factor.
3) The sensor currently has no DC response. Further investigation may provide other means of attaining DC response with different pressure transducer concepts.
4) The sensor uses mercury, a hazardous substance.
5) Internal mechanics requires a method to allow for thermal expansion of working fluid.

6) Sensor assembly will be a much more involved process than other existing MEMS sensors.

Recommendations on further work

The sensor simulation can be improved upon in the following respects:

1) A complete and realistic noise model of the sensor noise must still be constructed. This is the main shortcoming of the simulations done in this document, which leaves sensor performance parameters like resolution and drift still to be determined. This may only be feasible when the electronics layout has been conceptualized.
2) A single integrated state space model of the whole sensor will improve on the fluid column wave damping assumptions made above.
3) The modeling of the minor flow losses is completely neglected in this document. A CFD model used in a time marching scheme may be considered if high computing power is available.
4) The diaphragm theory may be expanded to the non-linear regime. The advantage to be gained by doing this is limited since the sensor linearity also degrades on such large diaphragm deflections.
5) A more general formulation of the piezo-based pressure sensor may be advantageous to investigate the effect other piezo to diaphragm size ratios on the sensor performance.
6) The sensor is modeled as an open-loop device. The addition of a feedback system in the sensor is still to be investigated and simulated.

With a view to a prototype, the following work is still to be done:

1) Sensor design for manufacturing. Wafer fabrication and bonding, pressure transducer fabrication and sensor assembly are matters addressed under this heading.
2) Electronics design. The bulk of the design is still to be completed. This document covers mainly the mechanical aspects of the sensor.
3) Sensor packaging is not addressed at all in this document. The main issues still to be dealt with here are interfacing, sensor protection and noise sensitivity.

References

Aerospace Industries Assosiation (1965) AIA report on standard gyro terminology. EETC Report No. 5, National Standards Assosiation, Washington D.C., U.S.A

Amptek Incorporated (publication date and author unknown) A225 and A250 Charge Sensitive Preamplifier and Shaping amplifier datasheets and application notes. http://www.amptek.com Last accessed 21 Feb. 2005

Anthony L. (1993) Modern inertial technology: navigation, guidance and control. Springer-Verlag, pp 38

Avramenko, A. A. (2001). Analysis of nonstationary incompressible flows in differently shaped channels on the basis of symmetries. Journal of Engineering Physics and Thermophysics, Vol. 74, No. 5, pp 1137-1153.

Bernardin D. (1999). Teoretical studies of some transient Couette flows of viscoelastic fluids in inertial devices. Journal of Non-Newtonian Fluid Mechanics, 1999, pp 1-30.

Beckwith, T. G., Marangoni R. D. and Lienhard V J. H. (1993). Mechanical measurements. Addison-Wesley Publishing Co. Reading, U.S.A.

Bèlanger, P. R. (1992). Estimation of angular velocity and acceleration from shaft encoder measurements. Proceedings of the IEEE Conference on Robotics and Automation, Nice, France, pp 585-592.

Bill, B. and Wicks, A. L. (1990). Measuring simultaneously translational and angular acceleration with the new Translational-Angular-Piezobeam (TAP) system. Sensors and Actuators, A: Physical, Vol. 21, Issue 1-3, pp 282-284.

Blevins, R. D. (1995). Formulas for natural frequency and mode shape. Krieger Publishing, Melbourne, Australia.

Brosnihan, T. J., Pisano A. P. and Howe, R. T. (1995). Surface micromachined angular accelerometer with force feedback. Proceedings of the ASME Dynamic Systems and Control Division. Vol 57-2, pp 941-947.

Burchett, B. T. and Costello, M. F. (2001). Specialized Kalman filtering for guided projectiles. AIAA, 39th Aerospace Sciences Meeting and Exhibit. Reno, U.S.A.

Canavan E. R., Paik, H. J. and Parke J. W. (1991). Superconducting six-axis accelerometer. IEEE Transactions on Magnetics. Vol. 27, No. 2, pp 3253-3256.

Cheshmehdoost, A., Jones, B. E. and O'Connor. B. (2001). Characteristics of a force transducer incorporating a mechanical DETF resonator. Sensors and Actuators A: Physical,Vol. 26, Issues 1-3, March 1991, pp 307-312.

Ellis, R. and Gulick, D. (1994). Calculus with analytical geometry. Fifth Edition, Harcourt Brace & Co, Orlando, U.S.A.

Evans, R. D. Jr. (1970). Development and testing of a triaxial angular accelerometer for high-performance aerospace vehicles. International Aerospace Instrumentation Symposium. Cranfield, U.K.

Friedland, B. (1986). Control System Design. McGraw-Hill, New York, U.S.A.

Gates, R. L. (1968). Inertial guidance systems. Howard W. Sams & Co, Indiana, U.S.A.

Gola, A. et al. (2000). A MEMS-based rotational accelerometer for HDD applications with 2.5rad/s^2 resolution and digital output.

http://microlab.unipv.it/~andrea/private/Conference/C53-ESSCIRC01_RotatSens.pdf, Last Accessed July 2004.

Hamamatsu Photonics K.K. Solid State Division (publication date and author unknown). Characteristics and use of Charge Amplifier. Technical Information SD-37, http://usa.hamamatsu.com Last accessed 21 Feb. 2005

Hancke G. P. and Viljoen C. F. T. (1990). The Microprocessor measurement of low values of rotational speed and rotation. IEEE Transactions on Instrumentation and Measurement, Vol. 39, No. 6, pp 1014-1017.

Hartzell, R. E. Jr. (1985). A high reliability, low cost, fluid inertia-angular accelerometer and its application in real time inertial coordinate frame of reference systems. Symposium Gyro Technology 1985, Stuttgart, Germany. AIAA Technical Library.

Hernden, C. (2000). Vibration cancellation using rotational accelerometer feedforward in HDDs. Data Storage.

Horowitz, P. and Hill, W. (1995). The Art of Electronics. Cambridge University Press, Cambridge, U.K.

Hulsing R. H. (1988). SCIRAS sensor – Sundstrand coriolis inertial rate and acceleration sensor. AIAA Technical Library, U.S.A.

Ingram, W.A.R. (2003). Inertial Sensors – An Industry and Strategic perspective. Kentron MEMS Symposium 25 March 2003, Denel Optronics, Irene, South Africa.

Kadhim, A. H., Babu T. K. M. and O' Kelly D., (1992). Measurement of steady-state and transient load-angle, angular velocity and acceleration using an optical encoder. IEEE Transactions on Instrumentation and Measurement. Vol. 41, No. 4, pp 486-489.

Kayton, M. and Fried, W. R. (1969). Avionics Navigation Systems. John Wiley & Sons, Inc, New York.

Kester, W. et al. (publication date unknown). Amplifiers for Signal Conditioning. http://www.analog.com Last accessed Feb. 21 2005

King, A. D. (1998). Inertial Navigation – Forty years of evolution. GEC Review Vol. 13, No. 3.

Kivrich, I. G. and Belkin, A. M. (1985). Automated aircraft navigation. (Russian book), AIAA Technical Library, U.S.A.

Insalaco, M. D., Kistler Corp. (2000). The art of fabricating a rotational accelerometer. Sensors magazine (www.sensorsmag.com), page last accessed June 2004.

Ladyzhenskaya, O. A. (1969). The mathematical theory of viscous incompressible flow. Gordon and Breach Science Publishers, New York, U.S.A.

Lassow, R. and Meydan, T. (1995). Angular accelerometer using amorphous wire. IEEE Transactions on Magnetics, Vol. 31, Issue 6, Part 1, pp 3179-3181.

Lawrence, A. (1993). Modern Inertial Technology – Navigation, guidance and control. Springer-Verlag, New-York, U.S.A.

Le Du, M. (1995). Optimal pointing stability achievement through isolation. AIAA Technical Library, U.S.A.

Listvin, A. V. et al. (1993). A passive fiber-optic accelerometer. AIAA Technical Library, U.S.A.

Marat-Mendez, R., Dias, C. J. and Marat-Mendez J. N. (1999). Measurement of the angular acceleration using a PVDF and a piezo-composite. Sensors and actuators, Vol. 76, pp 310-313.

McDonnel, K. G. (2001). Evaluation of an angular Accelerometer. Proceedings of the International Modal Analysis Conference – IMAC, Vol. 2, pp 1460-1466.

Minbang, L. and Pen, C. (1992). Precision fluid floated flywheel servo angular accelerometer. Proceedings of the International Instrumentation Symposium, April 26-30 1992, Las Vegas, U.S.A.

Mizuno at al. (1997). Silicon bulk micromachined accelerometer with simultaneous linear and angular sensitivity. International Conference on Solid-State Sensors and Actuators, June 16-19 1997, Chicago, U.S.A.

Merhav, S. (1996). Aerospace sensor systems and applications. Springer-Verlag, New-York, U.S.A.

Meydan, T. (1997). Recent trends in linear and angular accelerometers. Sensors and Actuators A: Physical, Vol. 59, Issues 1-3, pp 43-50.

Neusypin, A. K. (1991). Using angular acceleration transducers in inertial systems for increasing the accuracy of the gyrostabilized platform and the system as a whole. AIAA Technical Library, U.S.A.

Ogata, K., (1970). Modern Control Engineering. Prentice Hall, New Jersey, U.S.A.

Ovaska S. J. and Väliviita S. (1998). Angular acceleration measurement: A Review. IEEE Transactions on Instrumentation and Measurement, Vol. 47, No. 5, pp 1211-1217.

Pasanen, J., Vainio O. and Ovaska S. J. (1994). Predictive synchronization and restoration of corrupted velocity samples. Measurement, Vol. 13, pp 315-324.

Pickford, J. (1969). Analysis of surge. Macmillan and Co. Ltd, London, UK.

Purdy, D. (1979). Vibration measurement – an introduction to piezoceramic accelerometers. Noise Control Vibration Isolation. 10:140-142

Restivo, M. T., Gomes de Almeida, F. (2004). The use of eddy currents on the measurement of relative acceleration. Sensors and Actuators A, Vol. 113, pp 181-188.

Roszhart, T. et al. (2000). Development of a Micromachined Vibrating Beam Multisensor (MVBM) for tactical guidance and navigation purposes. AIAA Guidance, Navigation, and Control Conference and Exhibit, Denver, U.S.A.

Rubinow, S. I. and Keller, J. B. (1971). Wave propagation in a fluid filled tube. The Journal of the Acoustical Society of America, Vol. 50, Number 1 (part 2), pp 198-223.

Samoilescu, G. and Radhu, S. (2002). Stabilisers and stabilizing systems on ships. 8th International Conference, Constantin Brâncusi University Day, May 24-26m Târgu Jiu, Gorj, Romania.

Schlichting, H. (1968). Boundary-layer theory. McGraw-Hill, New-York, U.S.A.

Schweber B. (2001). Unique process takes your resistance to the max. EDN (5/24/2001) http://www.edn.com/article/CA84282.html Last accessed Feb. 22 2005

Shirron, P. J., Vol Moody, M. and Canavan, E. (1996). Development of a superconducting angular accelerometer. Proceedings of SPIE – The International Society for Optical Engineering. Vol. 2814, pp 187-196.

Slezkin, N. A. (1955). Dynamics of a viscous incompressible fluid. [in Russian], Moscow.

Schmidt, P. B. and Lorenz, R. D. (1992). Design principles and implementation of acceleration feedback to improve performance of DC drives. IEEE Transactions on Industrial Applications, Vol. 28, pp 594-599.

Statham, L. D. (1957). Angular Accelerometer. U.S. Patent #2,778,623 January 22, 1957.

Stieler, B. (1995). Inertial Navigation. AGARD, Aerospace navigation systems, AIAA Technical Library, U.S.A.

Stovall, S. H. (1997). Basic inertial navigation. Naval Air Warfare Center, Weapons Division, California, U.S.A.

Strutt, J. W. (Baron Rayleigh), (1945). The Theory of Sound. Dover Publ, New York.
Sydenham P. H., Hancock, N.H. and Thorn, R. (1989). Introduction to measurement science and engineering. New York: Wiley London: Chapman and Hall.

Szymanski, P. (1932). Quelques solutions exactes des équations de l'hydrodynamique du fluide visqueux dans le cas d'un tube cylindrique. Journal de mathématique pures et appliqués, Series 9.; also see the Proceedings on the International Congress on Applied Mechanics. Stockholm, Sweden.

Täubner, A. and von Martens, H. J. (1998). Measurement of angular accelerations, angular velocities and rotation angles by grating interferometry. Measurement: Journal of the International Measurement Confederation, Vol. 24, Issue 1, pp 21-32.

Tompkins, W. J. and Webster J. G. eds. (1988). Interfacing sensors to the IBM® PC. Prentice-Hall, New Jersey, U.S.A.

Udd, E., Watanabe, S. F. and Cahill R. F. (1985). Comparison of ring laser and fiber-optic gyro technology. AGARD Conference Proceedings No. 383, Guided Optical Structures in the Military Environment.

Urazhdin, S., Tessmer S. H. and Ashoori R. C. (2002). A simple low-dissipation amplifier for cryogenic scanning tunnelling microscopy. Review of Scientific Instruments, Vol. 73 number 2, pp 310-312.

Vainio, O. and Ovaska, S. J. (1997). A class of predictive analog filters for sensor signal processing and control instrumentation. IEEE Transactions in Industrial Electronics, Vol. 44, pp 565-570.

Vishay Measurements Group Technical Note TN-510 (1982) Diaphragm pressure transducers, Rayleigh, NC, USA

White, F. M. (1994). Fluid mechanics. Third Edition, McGraw-Hill, New-York, U.S.A.

Womersley R. J. (1955). Method for calculation of velocity, rate of flow and viscous drag in arteries when the pressure gradient is known. J. Physiol-London 127:553-563

Wrigley, W., Hollister, W. M. and Denhard, W. G. (1969). Gyroscopic Theory, Design, and Instrumentation. M.I.T Press, Cambridge, Massachusetts, U.S.A.

Wright, C. P. (1994). Applied measurement engineering. Englewood Cliffs, N.J. Prentice Hall, U.S.A.

Wylie, C. R. (1966). Advanced engineering mathematics. Third Edition, McGraw-Hill, New-York, U.S.A.

Young, W. C., Budynas, R. G. (2002). Roark's formulas for stress and strain. Seventh Ed. McGraw Hill, New York, U.S.A.

Appendix A

A.1 Pressure wave speed constants

Pressure wave speed constant per channel unit length (Φ/L, unit m^{-1}) versus number of masses in fluid column model. (See section 3.6.1)

Number of masses (N-1)	Wave speed constant/m (Φ/L)	Number of masses (N-1)	Wave speed constant/m (Φ/L)
2	0.450158158	74	0.013512499
4	0.24362384	76	0.013156958
6	0.164769322	78	0.012819646
8	0.124198356	80	0.012499197
10	0.099589274	82	0.012194376
12	0.083095555	84	0.011904068
14	0.071278799	86	0.01162726
16	0.06239965	88	0.011363033
18	0.055485069	90	0.011110547
20	0.049948612	92	0.010869037
22	0.045415935	94	0.010637803
24	0.041636925	96	0.010416202
26	0.038438145	98	0.010203645
28	0.035695555	100	0.009999589
30	0.033318105	102	0.009803534
32	0.031237452	104	0.009615019
34	0.029401303	106	0.009433617
36	0.027768964	108	0.009258933
38	0.026308296	110	0.0090906
40	0.024993575	112	0.008928279
42	0.023803974	114	0.008771652
44	0.022722445	116	0.008620426
46	0.021734906	118	0.008474326
48	0.020829615	120	0.008333095
50	0.01999671	122	0.008196495
52	0.019227845	124	0.0080643
54	0.018515907	126	0.007936302
56	0.017854801	128	0.007812304
58	0.017239272	130	0.007692121
60	0.016664763	132	0.007575579
62	0.016127307	134	0.007462516
64	0.015623431	136	0.007352778
66	0.015150085	138	0.00724622
68	0.014704575	140	0.007142707
70	0.014284515	142	0.00704211
72	0.013887787	144	0.006944307

Number of masses (N-1)	Sound constant/m (Φ/L)
146	0.006849183
148	0.00675663
150	0.006666545
152	0.00657883
154	0.006493394
156	0.006410148
158	0.00632901
160	0.0062499
162	0.006172743
164	0.006097468
166	0.006024006
168	0.005952294
170	0.005882269
172	0.005813873
174	0.005747048
176	0.005681743
178	0.005617905
180	0.005555485
182	0.005494437
184	0.005434717
186	0.00537628
188	0.005319087
190	0.005263098
192	0.005208275
194	0.005154583
196	0.005101986
198	0.005050452
200	0.004999949